University of Calgary

PRISM Repository **https://prism.ucalgary.ca**

The Vault Open Theses and Dissertations

2019-04-24

Geochemical Modeling of Oil-Brine-Rock Interactions during Brine-Dependent and Brine-CO2 Recovery Technique in Carbonate Petroleum Reservoirs

Awolayo, Adedapo Noah

Awolayo, A. N. (2019). Geochemical modeling of oil-brine-rock interactions during brine-dependent and brine-CO2 recovery technique in carbonate petroleum reservoirs (Doctoral thesis, University of Calgary, Calgary, Canada). Retrieved from https://prism.ucalgary.ca.
http://hdl.handle.net/1880/110237
Downloaded from PRISM Repository, University of Calgary

UNIVERSITY OF CALGARY

Geochemical Modeling of Oil-Brine-Rock Interactions during Brine-Dependent and Brine-CO_2 Recovery Technique in Carbonate Petroleum Reservoirs

by

Adedapo Noah Awolayo

A THESIS

SUBMITTED TO THE FACULTY OF GRADUATE STUDIES

IN PARTIAL FULFILMENT OF THE REQUIREMENTS FOR THE

DEGREE OF DOCTOR OF PHILOSOPHY

GRADUATE PROGRAM IN CHEMICAL AND PETROLEUM ENGINEERING

CALGARY, ALBERTA

APRIL 2019

© Adedapo Noah Awolayo 2019

Abstract

The brine-dependent recovery process involves the tweaking of the ionic composition and strength of the injected water compared to the initial *in-situ* brine to improve oil production. The type of brines used during the recovery process is often generated through the dilution or addition or removal of ions to/from the available injection water. The recovery process has seen much global research efforts in the past two decades because of its benefits over other oil recovery methods. In recent years, several studies, ranging from laboratory coreflood experiments to field trials, admit to the potential of recovering additional oil in sandstone and carbonate reservoirs and has been well explored on two frontlines, namely, brine dilution and compositional variation. However, many challenges have saddled the recovery process, such as disputes over the fundamental chemical mechanisms; difficulty with construction of a representative model to give reliable interpretation and prediction of the process; and these necessitate applicable solution.

Therefore, this study explores the formulation of theory based on experimentally observed behavior to couple equations of multicomponent transport and geochemical reactions. Mechanisms such as dispersion/diffusion, advection, instantaneous equilibrium reactions and non-equilibrium rate-controlled reactions are captured in the construction of the numerical models. The DLVO theory of surface forces was also applied to rationalize potential determining ion interactions and to evaluate the contribution of each force component to the wettability change in the oil-brine-rock system and the characteristic oil recovery improvement. The model was applied to interpret recently published results on the different approaches that have been explored in the application of brine-dependent recovery process in carbonate reservoir rocks. The focus being that identifying the dominant mechanisms responsible for the observed improved recovery will help substantiate the field application of the process.

Hence, the model was utilized to explore brine-dependent recovery application beyond the lateral propagation that could be achieved in 1D coreflood experiments by considering an areal propagation of a 2D large-scale model with similar properties as reported in the published experimental experiments. Analysis of sensitive parameters like thermodynamic constants, rock surface site density and area, the viable link between wettability alteration and oil recovery, mineralogical content variation, injection strategies and pore volumes, were carried out to

determine their influence on the process performance. Then, the model was extended to investigate the intrinsic oil-brine-rock interaction during a system of combining low saline brine and CO_2 injection.

The study demonstrates that injected brines, containing potential determining ions depleted in NaCl, are more effective at improving recovery when it, and wettability alteration is much more pronounced at high temperatures. It was also illustrated that potential determining ion concentrations play a more significant role as compared to brine salinity reduction. The magnitude of the contribution of the electrostatic force to sustaining a stable water film increases with decreasing ionic strength, either through reduction of NaCl, Ca^{2+} or brine dilution, or increasing SO_4^{2-} concentration. Mineral dissolution/precipitation is necessary for the pursuit of re-establishing equilibrium and should not be ignored in modeling different mineralogical carbonate rocks. The derived optimized thermodynamic parameters are demonstrated to be widely applicable. Although chalk and limestone differ by surface area and reactivity, the same thermodynamic parameters are applicable in modeling the recovery process in their respective reservoir rocks. There is a significant increase in relative injectivity for brine-CO_2 recovery mainly due to more exposure to a higher amount of CO_2-saturated-brine.

Overall, brine-dependent recovery is relatively inexpensive and environmentally friendly, offers more advantage than other chemical EOR methods in terms of operating costs, field implementation and environmental assessment, even though it might recover comparably less additional oil. Additionally, low saline brine can serve as pre-conditioner for other EOR methods, as most of the injected chemical/gas performs better under low saline brine.

Keywords: smart waterflooding; low salinity waterflooding; potential determining ions; interfacial mechanisms; carbonate rocks; wettability alteration; oil-brine-rock interactions, surface sorption and complexation, water film stability, geochemical modeling, low-salinity-water-CO_2

Preface

This thesis is submitted to the University of Calgary in partial fulfillment of the requirements for the degree of Doctor of Philosophy.

The work presented in this thesis was conducted at the Chemical and Petroleum Engineering Department, the University of Calgary and the computational facility was provided by Research & Development Division of Computer Modelling Group (CMG) Ltd., Calgary. Many of the numerical model development was carried out in CMG's compositional simulator GEM™. The substance of this thesis is the original work of the author and due reference and acknowledgement has been made, whenever necessary, to the work of others cited in this thesis. Dr. Hemanta Sarma was the main supervisor, and Dr. Long Nghiem from CMG was the co-supervisor.

The research work was funded by the University of Calgary, with additional financial support from *Vanier Canada Graduate Scholarship* and *Killam Memorial Trust*.

Acknowledgements

The Ph.D. journey is merely a rugged road filled with many dead-ends, often skimming the brink of uncertainty. One cannot always tell which path to take, let alone where one is headed. Enveloped with seemingly Herculean tasks, the only thrust forward is often powered by caffeine and the apprehension of quitting after going several miles down the road. However, just like Frodo had Sam, T'Challa (Black Panther) had Shuri, Django had Dr. Schultz, and Sherlock had Watson, the learning experience is that purportedly challenging pursuits have a better chance of success when one does not navigate unaccompanied. In that case, I am very appreciative to have so many people support me on this journey. It is one of the most electrifying and terrifying moments of my life, though it took about three (3) years in humans' time, it was about three hundred (300) years in my mind.

Thank you to my advisor Dr. Hemanta Sarma, who has been my mentor for the past five years. I am highly thankful for your willingness to provide the needed help each time I knocked on your door, irrespective of the time and day. The countless scholarships and awards I received would not have been possible without your great recommendations. I am also thankful that you gave me the privilege to be independent while pursuing the research objectives, helped me set boundaries for this research work and focus on writing these past few months. I would likely still be wandering if not for your encouragement. I would like to acknowledge my co-advisor, Dr. Long Nghiem of CMG, for your irreplaceable contributions and that you always made time to help me find answers to my many questions and granted me unrestricted access to CMG facilities to aid in completing this study within the stipulated timeline. I appreciate the time and effort both of my supervisors, Dr. Sarma and Dr. Nghiem, have expended on my behalf, in developing, analyzing, and solving the problems posed in the research statement. It is with certainty that, without their support and constant motivation, it would have been an extremely difficult journey.

A special thanks to my committee members, Dr. Ian Gates and Dr. Mingzhe Dong, and examiner, Dr. Laurence Lines, Dr. Zhangxing Chen and Dr. Seung Kam (Louisiana State University), for providing detailed and intuitive feedback that had a significant impact on the definitive version of this thesis. I am particularly grateful to Dr. Brij Maini for his constant support in providing me with great recommendations, especially for the prestigious Vanier Canadian Graduate Scholarship and Killam Memorial Pre-Doctoral Scholarship. He was part of my committee members until the last moment. I am also thankful to my candidacy examiners, Dr. Ayodeji Jeje and Dr. Gopal Achari for their valuable time and providing significant feedback to

improve this research study. Thank you to Dr. Alex De Visscher, now with Concordia University, for introducing me to countless opportunities at the department and for your support throughout the initial stages of the program, especially writing a great letter of support for Vanier Canadian Graduate Scholarship.

I appreciate the financial support from the prestigious *Vanier Canadian Graduate Scholarship* administered by the Government of Canada and *Killam Doctoral Memorial Scholarship* administered through the Killam Trusts Funds at the University of Calgary. I am thankful to Dr. Emre Gorucu of CMG for his many assistance with the simulation work and Dr. Vijay Shrivastava of CMG for his support and valuable comments on this research, and the R&D Department of CMG for providing the necessary facilities and conducive environment for the successful completion of this research work. A word of appreciation goes to every administrative staff of Faculty of Graduate Studies, Graduate Student Association and Department of Chemical and Petroleum Engineering, especially Suha Abusalim and Arthur de Vera, for their help in coordinating various academic logistical matters.

The Ph.D. is just a small part of my life, and I sincerely appreciate the support of my friends, here in Calgary and abroad, various dialogues and assistance made my studies even more enjoyable. The wonderful families that helped my family settle down and identify with us in Calgary, especially the Jaiyeolas, Okanlawons and Kunderts, thank you for your continual support. I would not have gotten this far without you all. Thank you to my loving parents and my parents-in-law. My parents, Olusola and Mojirade Awoloyo, have always been there to encourage my growth and development and support every decision I have made and direction I have taken about my education and career paths. Most importantly, thank you to my adorable wife, Adura Oluwaseyanu Awolayo, and our amazing princess, Zion Nifemi Awolayo, for providing unfailing support and encouragement. You have helped me carry the burden of this Doctoral program without protest, and I know you are just as glad as I am that this journey has finally come to an end.

Dedication

This thesis is dedicated to:

- the maker of heaven and earth, the creator of all that lives, the Almighty GOD
- my earthly gods, my parents, for their unconditional love and support and
- my loving wife and daughter.

Table of Contents

Preface iv
Acknowledgements v
Dedication vii
List of Tables xi
List of Figures and Illustrations xiii
List of Symbols, Abbreviations and Nomenclature xx
Chapter 1 Introduction 1
1.1 Problem Statement 1
1.2 Research Justification 6
1.3 Research Goals/Hypothesis 7
1.4 Research Objectives 8
1.5 Outline of the Dissertation 9
1.6 Publication 10
Chapter 2 Background and Integrative Review 12
2.1 Introduction 12
2.2 Laboratory Experimental Studies 13
2.2.1 Connate water content and saturation 16
2.2.2 Crude oil composition 18
2.2.3 Rock mineral composition 21
2.2.4 Temperature and pressure 24
2.2.5 Injected brine composition and salinity 28
2.3 Field Application Studies 34
2.4 Proposed Underlying Recovery Mechanisms 37
2.4.1 Rock dissolution 37
2.4.2 Multi-ion exchange (MIE) 39
2.4.3 Electrical double layer expansion (DLE) 41
2.5 Modeling of Brine-Dependent Recovery 43
2.5.1 Analytical approach 44
2.5.2 Numerical approach 46
2.5.2.1 Sandstone rocks. 46
2.5.2.2 Carbonate rocks. 51
2.6 Injection Water Issues and Remediation 55
2.7 Chapter Summary 60
Chapter 3 Surface Forces and Water Film Prediction 62
3.1 Introduction 62
3.2 Theory of Water Film Stability 65
3.3 Interaction Force and Energy Calculations 68
3.4 Zeta Potential Calculation 73

3.5 Water Chemistry Effect on Disjoining Pressure and Potential Barrier Height 77
3.6 Chapter Summary 83
Chapter 4 Reactive Transport Model Description and Validation....85
4.1 Introduction....85
4.2 Model Formulation 87
4.2.1 Hydrocarbon solubility 87
4.2.2 Aqueous-Species reactions 88
4.2.3 Aqueous-Minerals reactions 90
4.2.4 Carbonate rock system modeling 92
4.2.4.1 Surface sorption reactions....94
4.2.4.2 Surface complexation reactions. 99
4.3 Coupled Flow and Reaction Model 101
4.4 Summary of Experimental Data 107
4.5 Validation of Surface Sorption Model....110
4.5.1 Temperature-Dependent Competition between PDI cations:....110
4.5.2 Competition between PDI cations in the presence of PDI anion: 114
4.5.3 Competition between PDIs in the presence of oil 118
4.6 Validation of Surface Complexation Model....119
4.6.1 Surface chemistry prediction comparison with zeta potential experiments120
4.6.2 Comparison of surface chemistry prediction to single-phase flooding experiments 127
4.7 Chapter Summary 132
Chapter 5 Prediction of Brine-Dependent Recovery 134
5.1 Geochemical Interactions and Wettability Modification Relationship 134
5.2 Oil Recovery Prediction for Brine Dilution Approach....137
5.2.1 Simulation portfolio for different mineralogical carbonate rocks 142
5.2.2 Laboratory simulation results 145
5.2.2.1 Core material with calcite and dolomite minerals 145
5.2.2.2 Core material with calcite and anhydrite minerals. 149
5.2.2.3 Core material with calcite, dolomite, and anhydrite minerals 152
5.2.3 Field-scale simulation....154
5.3 Oil Recovery Prediction for Compositional Variation Approach 158
5.3.1 Laboratory scale simulation....160
5.3.1.1 Single−phase modeling. 160
5.3.1.2 Two-phase modeling....163
5.3.2 Field−scale modeling....166
5.4 Chapter Summary 170
Chapter 6 Prediction of Low-Salinity-Water-CO_2 Recovery Process 173
6.1 Introduction....173
6.2 Simulation of LSWCO_2 176

6.3 Chapter Summary 185
Chapter 7 Conclusions and Recommendations.....186
7.1 Conclusions.....186
7.2 Recommendations for Further Study.....187
Appendix A: Aqueous Reaction Thermodynamic Parameters 189
Appendix B: Supplementary Material (Journal Permission License).....190
References.....197
Curriculum Vitae 221

List of Tables

Table 2.1—Salinity and composition of formation water and seawater in different regions (adapted from [23, 57, 133, 134]) 17

Table 2.2—Summary of successful field implementations of brine-dependent recovery in sandstone and carbonate reservoirs (adapted from Awolayo *et al.* [62]) 36

Table 2.3—Summary of technology selection criteria, key attributes and capabilities of both current and emerging water treatment technologies (adapted from Ayirala and Yousef [235]) 59

Table 3.1—Approximate characteristic radii of ions in water [130, 246] 67

Table 3.2—Compositions of the brines used in the interaction force and energy calculations consisting of synthetic formation brine (FB) and natural Arabian Gulf seawater (SW), with their various versions. 71

Table 3.3—Rock-Brine and Oil-Brine zeta and surface potentials in aqueous electrolyte solutions at pH 8.4 75

Table 4.1—Reaction pathways considered during simulation, where > is the prefix for surface species 86

Table 4.2—Summary of core properties used in simulating different single-phase flow through experiments to retrieve thermodynamic parameters for intact carbonate rocks. 108

Table 4.3—Fluid compositions and properties used in the simulation. 109

Table 4.4—Surface reactions and summary of equilibrium constants at different temperatures. These values were obtained from the best-matched simulation run after conducting a series of simulation 112

Table 4.5—Reported stability constants for the rock−brine surface reactions at room temperature 120

Table 4.6—Optimized stability constants derived from fitting pulverized carbonate ζ-potential 122

Table 4.7—Optimized stability constants derived from fitting natural intact carbonate ζ-potential 126

Table 4.8—Corresponding equilibrium constants at various temperatures and pressure of 7 bar 129

Table 5.1—Reservoir core properties used for simulating the different core experiments. 142

Table 5.2—Fluid compositions and Properties used in the simulation 144

Table 5.3—Mineralogical content for various cases simulated 157

Table 5.4—Summary of fluid and core compositions and properties used in the simulation. Site capacity; was assumed as 3 sites/nm^2. I represents ionic strength and TDS represents total dissolved solids. 161

Table 5.5—Input parameters for the 2D synthetic simulation model 166

Table 6.1—Summary of fluid and core compositions and properties used in the LSBCO_2 simulation. The total dissolved solids is denoted as TDS, ionic strength (M) is denoted as I, reservoir oil is denoted as RO and injected gas is denoted as IG 177

List of Figures and Illustrations

Figure 2.1— R&D-to-Field sketch of the systematic investigation for brine-dependent recovery design and implementation (adapted from Sarma [126], Awolayo *et al.* [62]). 15

Figure 2.2—Effect of acid number (AN) on spontaneous imbibition of brine into chalk cores saturated with different crude oil (reproduced from Standnes and Austad [116] with permission). The imbibition rate and water-wetness decrease as the AN increases in the absence of initial water 20

Figure 2.3—Comparison between ζ–potential of chalk, calcite, limestone and dolomite in different brine at reservoir pH of 7 (*left*) and in 25 times diluted seawater at pH range 6 – 11 (*right*) (reproduced from Mahani *et al.* [120] with permission) 23

Figure 2.4—Comparison of spontaneous imbibition rates of PDIs in chalk conducted at 70, 100 and 130 °C with a back-pressure of 88 psi. Modified seawater without Ca^{2+} and Mg^{2+} was initially imbibed, and Mg^{2+} or Ca^{2+} was later added in a systematic variation of PDI concentrations (reproduced from Zhang *et al.* [32] with permission) 29

Figure 2.5—An illustration of the proposed mechanism of wettability alteration by "dissolution" showing an oil-wetting state with oil attachment before dissolution (*top*) and the water-wetting state after dissolution (*bottom*). (adapted from Hiorth *et al.* [47])..... 38

Figure 2.6—A schematic illustration of the proposed mechanism of wettability alteration by "MIE" in carbonate reservoirs showing the oil component displacement from the carbonate rock surface through PDIs competition. Original state (*left*), Low temperature state (*right upper*) and High temperature state above 100 °C (*left lower*) (adapted from Zhang *et al.* [32]) 40

Figure 2.7—An illustration of the proposed mechanism for wettability alteration by "DLE" in oil-brine-carbonate rock system with DLVO disjoining pressure showing transition from an oil wetting state (left *upper*) with crowded double layer-filled non-active ions (*right upper*) to water wetting state (*left lower*) with double-layer depleted non-active ions (*right lower*) (reproduced from Fathi *et al.* [38], Awolayo *et al.* [65])..... 42

Figure 3.1—Schematic illustration of the EDL and electrical potential at the rock–brine interface: The sketch shows the variation of electrical potential as a function of distance from the rock surface, partitioned by charged planes— inner Helmholtz plane (IHP), outer Helmholtz plane (OHP) and slipping plane. The potential developed within the EDL declines with distance linearly through the Stern layer, exponentially through the diffuse layer and drops to zero in the bulk electrolyte solution. The partial charge on the dangling surface ions left behind at the bulk solid is represented by ψb; ψo represents the potential of the surface; ψd stands for the potential at the Stern layer and ζ represents zeta potential. While σo and σd are the surface and diffuse layer charge density (C/m^2) respectively. The Stern layer potential difference is characterized by constant capacitance, Cs while the diffuse layer has variable capacitance, Cd. At plane $x = 0$, which corresponds to the hydrolysis layer, H and OH of the water molecules are chemibonded to the dangling surface ions. At $x < 0$, the potential is so high that attaching ions do not bond to the surface ions. The inner-Stern layer is characterized by $d1$ length; the outer-Stern layer is

characterized by d2 length, and the electrical double layer is characterized by κ-1 length, also known as Debye-Hückel screening length [130, 170]..... 64

Figure 3.2—Schematic of Oil-Brine-Rock system at different wettability conditions: oil-wetting (*top*) and water-wetting (*bottom*) states. Interfaces exhibit a very strong repulsion (Born repulsion) upon contact; the surface interaction energy curve shows two potential minima: a deep primary minimum appearing at a small separation distance and a shallow secondary minimum appearing at a larger separation distance..... 66

Figure 3.3—Individual contributions from van der Waals, electrical double layer and structural force (*left*) to the total disjoining pressure (*right*) as a function of the thickness of the water film layer for the oil-brine-rock system (seawater, composition listed in Table 3.2). The positive half of the disjoining pressure represents the repulsive force required to separate two interacting interfaces, which is dominated by electrical double layer and structural force; while the negative half represent the attraction dominated by van der Waals. Dotted line is for CSC, dashed line for LSA and solid line for CSP; while, dashed blue line is for non-retarded van der Waals force. Unit conversion 1 atm = 101.325 kPa. 69

Figure 3.4—Interaction energy with individual contributions from van der Waals—ωA and EDL—ωR (*left*) and the net interaction energy (*right*) as a function of dimensionless film thickness (κh at a value of 1 implies that the separation distance is equivalent to the EDL thickness, which is 0.342 nm for seawater). Considering figure on the left, since ωR varies exponentially with thickness (eq. 3.12) and ωA varies with the square of thickness (eq. 3.10), ωA surpasses ωR at short and long distances, thus producing attraction between the two interacting interfaces and energy barrier at intermediate distance..... 73

Figure 3.5—Comparison of calculated and measured ζ–potential of the oil-brine system as a function of pH and brine ionic strength for Moutray oil (*left-top*), Leduc oil (*right-top*) and ST86 oil (*right-bottom*). The markers are the experimental data; dashed lines represent calculations with $\Delta = 0.6\,\mathrm{nm}$ and solid lines for $\Delta = 1.0\,\mathrm{nm}$. Calculated surface potential for the oil-brine system (*right-bottom*) is shown with dash lines representing eq. 3.14 and solid lines for eq. 3.13. The ionic strength is expressed in terms of NaCl brine, experimental data from Buckley *et al.* [251] varies from 0.1M to 0.001M. The trend for 0.5M and 1M has been included for comparison of the increasing ζ–potential with increased salinity..... 76

Figure 3.6—Net disjoining pressure as a function of film thickness (*left*) and interaction energy as a function of dimensionless separation distance (*right*) between the interacting interfaces with SO_4^{2-} concentration (expressed as pSO4) in two different brine salinity (0.05M and 0.5M NaCl). The term pSO4 is equivalent to -log10SO42- , which implies that pSO4 reduces as the concentration of SO_4^{2-} increases, i.e., pSO4 of 1.9 equals 0.0117M (half SO_4^{2-} in natural seawater), 1.5 equals 0.0329M (same SO_4^{2-} as in natural seawater) and 1.0 equals 0.0969M (thrice SO_4^{2-} in natural seawater). The solid lines indicate curves for lower salinity (0.05M NaCl) and dash lines (0.5M NaCl) indicate curves for higher salinity. Unit conversion 1 atm = 101.325 kPa..... 78

Figure 3.7—Net disjoining pressure as a function of film thickness (*left*) and interaction energy as a function of the dimensionless separation distance between the interacting interfaces (*right*) with pCa in two different saline brines (0.5M and 2M NaCl). The pCa of 1.3 is

equivalent to 0.0495M (quadruple Ca^{2+} as in natural seawater), 2.0 is equivalent 0.0102M (same Ca^{2+} as in natural seawater), 2.6 is equivalent 0.002M and 2.8 is equivalent 0.0015M SO_4^{2-} concentration. Unit conversion 1 atm = 101.325 kPa 79

Figure 3.8—Relationship between net disjoining pressure as a function of film thickness (*left*), interaction energy as a function of the dimensionless separation distance between the interacting interfaces (*right*) and brine compositions derived from seawater with increasing SO_4^{2-} concentration. Unit conversion 1 atm = 101.325 kPa 80

Figure 3.9—Net disjoining pressure as a function of film thickness (*left*) and interaction energy as a function of the dimensionless separation distance between the interacting interfaces (*right*) for seawater-derived brines with increasing SO_4^{2-} concentration and same ionic strength (0.7850). Unit conversion 1 atm = 101.325 kPa 81

Figure 3.10—Net disjoining pressure as a function of film thickness (*left*) and interaction energy as a function of the dimensionless separation distance between the interacting interfaces (*right*) with varying brine dilutions derived from seawater. Unit conversion 1 atm = 101.325 kPa 82

Figure 4.1—Schematic representation of the cross-section of the surface layer. In the presence of water, carbonate surfaces are generally covered with surface hydroxyl groups 94

Figure 4.2—Simulated and experimental breakthrough curves of Ca^{2+} and Mg^{2+} from CF-M brine on limestone core 2-21 at various experimental temperatures: 20 °C (*top left*), 70 °C (*top right*), 100 °C (*bottom left*), and 130 °C (*bottom right*). Data points connote measured datasets, and solid-lines represent the model results; subscripts "exp" and "mod" in the legend are the experimental (Strand *et al.* [53]) and predicted values 111

Figure 4.3—Relationship of exchange and isotherm coefficients with temperature 112

Figure 4.4—Simulated surface fractions of Ca^{2+} (> CaX2) and Mg^{2+} (> MgX2) along the mid-section of the limestone core 2-21 at various experimental temperatures: 20 °C (*top left*), 70 °C (*top right*), 100 °C (*bottom left*), and 130 °C (*bottom right*) 113

Figure 4.5—Simulated and experimental breakthrough curves of Ca^{2+} and Mg^{2+} from CF-M brine on chalk core CM-1 23 °C (*left*) and 130 °C (*right*). Data points connote measured datasets from Zhang *et al.* [32], and lines represent the model results. 114

Figure 4.6—Simulated and experimental breakthrough curves of Ca^{2+}, Mg^{2+} and SO_4^{2-} at room temperature from SW-½M brine on limestone core 2-21 (*top left*), SW-M brine on chalk core ¼ (*bottom left*), and simulated surface fractions of Ca^{2+} (> CaX2), Mg^{2+} (> MgX2) and SO_4^{2-} (> XSO4-) along the core mid-section of the limestone core 2-21 (*top right*) and chalk core ¼ (*bottom right*). Data points connotes measured datasets from Strand *et al.* [53] as plotted in the *top left* panel and from Strand *et al.* [127] as plotted in the *top right* panel, lines represent the model results and the dotted lines represent the first attempt at modeling the experimental data 115

Figure 4.7—Flow chart algorithm used to investigate thermodynamic parameters 116

Figure 4.8—Simulated and experimental breakthrough curves of Ca^{2+}, Mg^{2+}, SCN^-, and SO_4^{2-} from SW-M brine on chalk core 7/1 at various experimental temperatures: 40 °C (*top left*),

70 °C (*top right*), 100 °C (*bottom left*), and 130 °C (*bottom right*). Experimental data are taken from Strand *et al.* [54]. 117

Figure 4.9—Simulated and experimental breakthrough curves of SCN^- and SO_4^{2-} at room temperature from SW-1T brine flood (*left*). Simulated surface fractions of Ca^{2+} (> CaX2), Mg^{2+} (> MgX2) and SO_4^{2-} (> XSO4-) along the mid-section (*right*), on aged chalk core LSSK#5 (with oil at S_{orm} = 0.29) and unaged chalk core SCC#1 (with no oil present). Data points connotes measured datasets (Fathi *et al.* [38]) and lines represent the model results. 119

Figure 4.10—Comparison of measured and predicted ζ-potential for all PDI concentrations and varying surface site densities (*top left*) and 3 sites/nm^2, showing the variation with PDIs (*top right*), the contrast between the prediction from this model and PHREEQC reaction module (*bottom left*). The solid black diagonal line is 1:1 zero error line, i.e. $\zeta\,\mathrm{i},\ \exp = \zeta\,\mathrm{i},\ \mathrm{mod}$, which shows the contrast between measured and predicted values. ζ-potential measured by Austad and colleagues [32, 55] with stepwise addition of $MgCl_2$, $CaCl_2$ or Na_2SO_4 to 0.573 M NaCl brine solution in 4 wt.% pulverized chalk suspension with pH maintained at 8.4, compared against the predicted ζ-potential from SCM with optimized stability constants for 3 sites/nm^2 as shown by solid lines (*bottom right*). The top (*squares* and *circles*) curves and data points is for Mg^{2+} and Ca^{2+} additions, respectively; the bottom (*diamonds*) curve and data points is for SO_4^{2-} additions. PHREEQC prediction was plotted in dotted lines. 123

Figure 4.11—Comparison of ζ-potential measured and predicted for PDI concentrations with optimized stability constants for surface site densities of 3 sites/nm^2 (*left*). ζ-potential predicted by optimized stability constants for intact rock compared against measured ζ-potential (*right*) by Alroudhan *et al.* [104] with PDI variations in 0.5M (*red lines and data points*) and 0.5M (*other colored lines aside red*) NaCl brine. EPM data for Ca^{2+} variation in 0.05M NaCl brine is plotted in "*light-blue*" on the right graph. The concentration is plotted in terms of negative logarithmic value (pPDI) instead of molar concentrations. The specific surface area was taken 0.29 m^2/g. The fixed pH of cation and anion variation was taken as 7.2 and 7.9, respectively. 125

Figure 4.12—Optimized ζ-potential predicted against measured ζ-potential for pH of 7.2 and 7.9 (*left*) and 7.9 and 8.1 (*right*) for PDI cations and anions additions, respectively. Experimental data are taken from Alroudhan *et al.* [104]. 126

Figure 4.13—Predicted compared against experimental breakthrough curves of SCN^-, Ca^{2+} and Mg^{2+} from CF-M brine flow through limestone core 2-21 at various experimental temperatures: 20 °C (*top left*), 70 °C (*top right*), 100 °C (*bottom left*), and 130 °C (*bottom right*). Experimental data are taken from Strand *et al.* [53]. 128

Figure 4.14—Predicted surface fractions of $>CO_3^-$, $>CO_3Ca^+$ and $>CO_3Mg^+$ along the mid-section of the limestone core 2-21 at various experimental temperatures: 20 °C (*top left*), 70 °C (*top right*), 100 °C (*bottom left*), and 130 °C (*bottom right*). 129

Figure 4.15—Predicted compared against experimental breakthrough curves of SCN^-, Ca^{2+} and Mg^{2+} from CF-M brine flow through chalk core (CM-1) at 20 °C (*top left*) and 130 °C (*top right*). Predicted surface fractions of $>CO_3^-$, $>CO_3Ca^+$ and $>CO_3Mg^+$ along the mid-

section of the core at 20 °C (*bottom left*) and 130 °C (*bottom right*). Experimental data are taken from Zhang *et al.* [32]. 130

Figure 4.16—Predicted and experimental breakthrough curves of SCN^- and SO_4^{2-} from SW-M brine flow through chalk core (7/1) at various experimental temperatures: 23 °C (*top left*), 70 °C (*top right*), 100 °C (*bottom left*), and 130 °C (*bottom right*). Experimental data are taken from Strand *et al.* [54]. 131

Figure 4.17—Predicted surface fractions of $>CaOH_2^+$, $>CaSO_4^-$, $>CaOH^0$, $>CO_3^-$, $>CO_3Ca^+$ and $>CO_3Mg^+$ along the mid-section of the limestone core (7/1) at various experimental temperatures: 23 °C (*top left*), 70 °C (*top right*), 100 °C (*bottom left*), and 130 °C (*bottom right*) 132

Figure 5.1—Relative permeabilities (*top panels*) and capillary pressure (*bottom panels*) used in simulating core flooding experiment of Chandrasekhar [275] (*left*), Austad *et al.* [48] (*middle*), Yousef *et al.* [57] (*right*). The solid lines with markers correspond to the relative permeability to oil while the solid lines without markers correspond to relative permeability to water. The initial flow functions (*set 1*) correspond to the initial wetting state, and the subsequent flow functions correspond to cases where the wetting state has shifted towards more water wetness. The changes in krj, Pc and sor values in *middle panel* is smaller than in *left panel* and *right panel* because the cores used by Austad *et al.* [48] is more water-wet than those used by Chandrasekhar [275] and Yousef *et al.* [57]... 143

Figure 5.2—Core flood experiment design Vertical (*left*) and Horizontal (*right*) simulation model..... 144

Figure 5.3—Simulated and experimental breakthrough curves of Mg^{2+}, Ca^{2+} and SO_4^{2-} (*left*) and Na^+ and Cl^- (*right*). Experimental data obtained from Chandrasekhar [275] 146

Figure 5.4—Sim A prediction at the center of the simulation domain for exchangeable fraction of Ca^{2+} (> CaX2), Mg^{2+} (> MgX2), free anionic site > NaX, and amount of SO_4^{2-} adsorbed (*left*); mineral volume alteration and simulated and experimental pH comparison (*right*) 146

Figure 5.5—Comparison between simulated and experimental oil recovery and pressure differential. Experimental data obtained from Chandrasekhar [275] 148

Figure 5.6—Comparison of predicted and experimental breakthrough curves of SO_4^{2-}, $Mg^{2+,}$ and Ca^{2+} (*left*) and oil recovery and pressure differential (*right*). Experimental data obtained from Austad *et al.* [48] 150

Figure 5.7—Sim A predictions at the center of the simulation domain for exchangeable fraction of Ca^{2+} (> CaX2), Mg^{2+} (> MgX2), free anionic site > NaX, and amount of SO_4^{2-} adsorbed (*left*); mineral volume alteration and pH (*right*)..... 151

Figure 5.8—Comparison between simulated and experimental oil recovery, and pressure differential (*left*). Simulated breakthrough curves of SO_4^{2-}, Mg^{2+}, and Ca^{2+} (*right*). Experimental data obtained from Yousef *et al.* [57]..... 153

Figure 5.9—Simulation results at the center of the simulation domain for an exchangeable fraction of Ca^{2+} (> CaX2) and Mg^{2+} (> MgX2), free anionic site > NaX, and amount of sulfate adsorbed (*left*); mineral volume alteration (*right*)..... 154

Figure 5.10—Simulation model for the quarter of a five-spot pattern used in this research showing oil saturation after about 1 PV injection (*left*) and grid-block - 60 × 60 × 1 with a block size of 3.35 m (*left*). The green dot at the upper-left corner is the producer while the injector is represented by the red dot at the lower-right. The diagonal blue line is the shortest streamline between the injector and producer, about 284 m long. 155

Figure 5.11—Predicted oil recovery and water cut for the quarter of a five-spot pattern with the different grid-block cells (900, 3600 and 10000) using core, flow and reaction parameters of Yousef *et al.* [57] 156

Figure 5.12—Profiles along the diagonal streamline of the quarter five-spot pattern for the different grid-block sizes after each injection cycle: adsorbed SO_4^{2-} (*left*) and free anionic surface site (*right*). 156

Fig. 5.13—Oil recovery and water cut fractions comparison of varying mineralogical contents with a collapsed view (*left*) and expanded view (*right*)..... 158

Figure 5.14—Water-oil relative permeability curves for *in-situ* and injected smart brines used in simulating the flooding experiments of S#42 (*left*) and S#9 (*right*). Broken lines indicate relative permeability to water and solid lines indicate relative permeability to oil. 160

Figure 5.15—Comparison between observed and simulated normalized breakthrough curves for all ions (*left*) and relative breakthrough curves for PDIs (*right*) during seawater flooding. Experimental data obtained from Chandrasekhar *et al.* [196]..... 162

Figure 5.16—Comparison between observed and simulated [a] normalized breakthrough curves for all ions (*left*) and relative breakthrough curves for PDIs (*right*) during seawater with $4xSO_4^{2-}$ flooding. Experimental data obtained from Chandrasekhar *et al.* [196]..... 162

Figure 5.17—Results of formation water, seawater and seawater with $4xSO_4^{2-}$ flooding sequence comparison between two-phase simulated and experimental oil recovery, and simulated mineral volume changes (*top left*); simulated and experimental effluent ions concentration of PDIs (*top right*); simulated surface and equivalent fractions of PDIs along the mid-section of core S#42 (*bottom left*) and simulated and experimental effluent ions concentration of Na^+ and Cl^- (*bottom right*). Data-points indicate measured datasets (Awolayo *et al.* [29]), broken lines indicate injection concentration, and solid lines indicate the simulation results..... 164

Figure 5.18—Prediction of formation water, seawater and seawater with $0.5xSO_4^{2-}$ flooding sequence: comparison between two-phase simulated and experimental oil recovery (*top left*); simulated and experimental effluent ions concentration of PDIs (*top right*); simulated surface and equivalent fractions of PDIs along the mid-section of core S#9 (*bottom left*); and simulated and experimental effluent ions concentration of Na^+ and Cl^- (*bottom right*). Experimental data obtained from Awolayo *et al.* [29]. 165

Figure 5.19—Simulation of 2-D synthetic quarter five-spot pattern with permeability distribution map (*top left*), porosity distribution map (*top right*) and permeability-porosity cross-plot (*bottom*) [277]. The block size is 15 ft. in every direction. The black dot at the upper-right corner is the producer, while the black dot with an arrow at the lower-left corner is the injector..... 167

Figure 5.20—Comparison of oil recoveries by formation water and seawater in secondary mode 168

Figure 5.21—Comparison of the evolution of water saturation during secondary injection mode of formation water, seawater and seawater with $4\times SO_4^{2-}$ 169

Figure 5.22—Evolution of equivalent fractions of unoccupied sites during secondary injection mode of seawater with $4\times SO_4^{2-}$ 169

Figure 5.23—Oil recovery comparison between secondary and tertiary injection mode of formation water and seawater (*left*), and formation water and seawater with $4xSO_4^{2-}$ (*right*) 170

Figure 6.1—CO_2 solubility in different brine salinity brine at 195 ºF (90.5 ºC) and a wide range of pressure using Li and Nghiem [287] solubility model in CMG WINPROP™ 175

Figure 6.2—Estimation of CO_2 MMP from slim tube simulations with different number of cells 178

Figure 6.3—Water-oil relative permeability curves (*left*) and gas-oil relative permeability curves (*right*) used in simulating the flooding experiments of Teklu *et al.* [88]. Broken lines indicate final-wetting state relative permeability and solid lines indicate initial wetting relative permeability 180

Figure 6.4—Comparison of experimental and simulated oil recovery and pressure differential. Experimental data obtained from Teklu *et al.* [88] 181

Figure 6.5—Simulation profiles at the mid-section of the flow domain for surface fractions of Ca^{2+} ($>CO_3Ca^+$), SO_4^{2-} ($>CaSO_4^-$) and Mg^{2+} ($>CO_3Mg^+$) and surface charge density (*left*) and fractional amounts of mineral volume alteration (*right*) 182

Figure 6.6—Predicted oil density and viscosity at the injection grid block (*left*); relative injectivity and the total amount of CO_2 dissolved in the aqueous brine solution (*right*).... 183

Figure 6.7—Predicted oil recovery for different injection schemes in a quarter of a five-spot pattern (*left*), comparison of injectivity and amount of dissolvable CO_2 (*top right*) and oil density and viscosity (*bottom right*). Here, carbonated water injection is compared with low saline brine and seawater injection in terms of oil recovery, injectivity and CO_2 solubility. 184

Figure 6.8—Predicted oil recovery comparison for $LSWACO_2$, conventional seawater WAG and normal waterflooding (*left*); comparison of their relative injectivity (*right*) 184

List of Symbols, Abbreviations and Nomenclature

Symbol	***Definition***
Abbreviations:	
AFM	atomic force microscopy
AN	acid number
ARDE	advection-reaction-dispersion equation
ASP	alkaline-surfactant-polymer
BN	base number
BPS	bond product sum
CEC	cation exchange capacity
CSC	constant surface charge
CSP	constant surface potential
DLE	electrical double layer expansion
DLVO	Derjaguin–Landau–Verwey–Overbeek
EDL	electrical double layer
EOR	enhanced oil recovery
EPM	electrophoretic mobility measurement
FB	formation brine
GOR	gas-oil ratio
HS	high salinity
IFT	interfacial tension
IG	Injected Gas
IHP	inner Helmholtz plane
LS	low salinity
LSA	linear superposition approximation
MIE	multi-ion exchange
NF	nanofiltration
NMR	nuclear magnetic resonance
OHP	outer Helmholtz plane
OOIP	original oil in place
PBE	Poisson-Boltzmann equation
PDE	partial differential equation
PDI	potential determining ions
ppm	part per million
PR-EOS	Peng-Robinson equation of state
RO	reverse osmosis
ROS	residual oil saturation
SCM	surface complexation model
SEM	scanning electron microscopy
SPM	streaming potential measurement
SRB	sulfate-reducing bacteria
SSM	surface sorption model

SW	seawater
SW/10	ten times diluted seawater
SW/2	Twice diluted seawater
SW/20	twenty times diluted seawater
SWCT	single well chemical tracer
WA	wettability alteration
WAG	water alternating gas

Notations:

a_i	activity of the *i*-th component
$\dot{a}_\iota$	ion size of the *i*-th component
$a_{(i)}$	activity of the *i*-th surface species
A	Hamaker constant
$\dot{A}_\beta$	reactive surface area
A_o	magnitude of the structural interaction
A_β	specific surface area of the mineral β
b	correction constant to the non-retarded Hamaker expression
$\dot{b}_\iota$	ion-specific parameter for the *i*-th component
C_s	Stern layer constant capacitance
C_d	diffuse layer variable capacitance
C_β	total concentration of dissolved ion components
d_o	decay length for the structural interaction
Da_β	Damköhler number for the mineral reaction β
D_{ij}	dispersion coefficients of the *i*-th component in the *j*-th phase
e	electronic charge
$E_{a\beta}$	activation energy
f_{ij}	fugacity of the *i*-th component in the *j*-th phase
h	water film thickness
H_i	Henry's constant for the *i*-th component
I	ionic strength
k_B	Boltzmann constant
k_{rl}	relative permeability to phase l
k_β	reaction rate constants
K_A	apparent stability constant
K_{ADS}	isotherm coefficient
$K_{eq,\alpha}$	equilibrium constant of the aqueous reaction α
$K_{eq,\beta}$	equilibrium constant of the mineral reaction β
$K_{ex,\delta}$	selectivity coefficients for the exchange reaction δ
K_{int}	intrinsic-reaction stability constant
L	characteristic flow length
m_i	molality of the *i*-th component
n	exponent

n	ionic density in the aqueous solution
$N_{[>i]}$	number of sorbed moles per unit volume
N_A	Avogadro's number
N_a	aqueous components
N_{aq}	total components in the aqueous phase
N_c	total number of soluble hydrocarbon components
N_{ex}	number of surface exchangeable species
N_{ia}	Primary aqueous components
N_m	mineral components
N_t	total number of components/species
P	pressure
P_{cow}	oil-water capillary pressure
q_i	molar rate of source/sink term for the *i*-th component
$Q_{ex,\delta}$	activity quotient for the exchange reaction δ
Q_α	activity product of the aqueous reaction α
Q_β	activity product of the mineral reaction β
r_β	rate of reaction
R	universal gas constant
R_{aq}	total number of aqueous reactions
R_{ex}	number of exchange reactions
R_i	residual function of the *i*-th component
R_m	number of mineral surface reactions
s_j	saturation of the *j*-th phase
S_d	site density
S_{or}	residual oil saturation to waterflood
S_{orw}	residual oil saturation
S_w	water saturation
S_w	water saturation
S_{wi}	irreducible water saturation
S_{wn}	normalized water saturation
T	absolute temperature
V_b	bulk volume
V_b	bulk volume
u_j	Darcy velocity of the *j*-th phase
y_{ij}	mole fractions of the *i*-th component in the *j*-th phase
z_i	ion valence
$\prod$	disjoining pressure
$\prod_D$	electrical double-layer forces
$\prod_S$	structural forces
$\prod_V$	London–van der Waals forces
$\mathcal{F}$	Faraday constant

Greek Letters:

α_o	power-law indices for oil
α_w	power-law indices for water
β_i	mole fractions of the surface sorbed species i
γ_i	activity coefficient of the *i*-th component
γ_{ro}	rock/oil interfacial energies
γ_{rb}	rock/brine interfacial energies
γ_{bo}	brine/oil interfacial energies
δ_s	total surface site capacity
Δ	shear/slip plane position
ε	dielectric constant of water
ε_0	free space permittivity
ζ	zeta
ζ	zeta potential
κ	Debye-Hückel reciprocal length
κh	dimensionless water film thickness
λ_c	interaction characteristic wavelength
μ_i	chemical potential of the *i*-th surface species
ν	transport velocity
$\nu_{i\alpha}$	stoichiometry coefficient of the *i*-th component in reaction α
$\nu_{i\delta}$	stoichiometry coefficient of specie i in exchange reaction δ
ξ_i	equivalent fractions of specie i
ξ_j	molar densities of the *j*-th phase
ρ_b	rock bulk density
σ_d	diffuse layer charge density
$\sigma_{i,eq}$	net moles per unit bulk volume due to equilibrium-controlled reactions
$\sigma_{i,m}$	net moles per unit bulk volume due to kinetic-controlled reactions
σ_o	surface layer charge density
ϕ	porosity
Φ_j	pressure potential of the *j*-th phase
χ	electrostatic interaction term (Boltzmann factor)
ψ	electrostatic potential
ψ_d	Stern layer potential
ψ_o	surface potential
ψ_r	reduced surface potential
ω	interpolation parameter
ω_A	van der Waals attraction energy
ω_R	double layer repulsion energy
Ω_β	saturation index

Chapter 1 Introduction

This Chapter presents a description of the research problem, discusses the justification and hypothesis proposed for this research, and lists the research objectives. The contents of each Chapter are also presented to provide an overview of this dissertation.

1.1 Problem Statement

The life cycle of petroleum reservoirs typically undergoes three modes of oil recovery: primary recovery utilizes the reservoir natural energy; secondary recovery mainly utilizes an injection of water or gas for maintenance of pressure; while tertiary or enhanced oil recovery (EOR) utilizes diverse forms of injection fluid [1, 2]. The recovery performance depends on several factors like fluid type, reservoir management, reservoir heterogeneity, and drive mechanisms [3]. Almost all light-to-medium gravity oil reservoirs go through a water injection cycle to produce some portions of the oil left behind after the depletion of the reservoir natural energy due to the ease of water injection, water availability, small capital investment, and operating costs among other benefits [4]. It is estimated that after the first two stages of production, the average oil recovery can only reach 10–50% of the original oil in place (OOIP) and a considerable amount remains trapped underground [5, 6].

Waterflooding has been widely used as a secondary recovery process to supplement the reservoir's natural energy and displaces more oil because of increased viscous force. Ever since the reported improved oil recovery as a result of the accidental water injection in some fields in Pithole City, Pennsylvania, waterflooding has been generally considered as a relatively low-cost and simple oil recovery technique used in recovering hydrocarbons left after primary recovery process [7]. Several researchers have made numerous attempts to investigate the fundamental mechanism to understand, design and optimize the displacement process [8, 9]. The driving mechanism of the injected brine was seen more like a physical process, and less attention was paid to the process chemistry. The nearest accessible water supply has always been sourced for water injection, which implies that seawater is often used for offshore applications. The brine is usually selected based on the project's economic evaluation along with its compatibility with existing formation water.

It was not until the late 1950s when some researchers noted an improved production after fresh water injection during core experiments, which they credited to sweep efficiency as a result of clay swelling and pore throat plugging [10, 11]. However, the process chemistry considering the quality of the injected brine has generated a lot of significant attention in the last three decades. This upsurge came by when Morrow's research group [12, 13, 14, 15, 16, 17] reported improved oil recovery in experiments conducted on clay-rich outcrop and Berea sandstone rocks. Meanwhile, the recovery process was only identified in carbonate rocks when an unexpected, remarkable success was reported during seawater injection into the Ekofisk mixed-wet fractured chalk reservoir, significantly leading to high oil recovery [18, 19, 20, 21]. Consequently, extensive research work at laboratory-scale and fairly at field-scale [22, 23, 24], in both sandstones [15, 25, 26] and carbonates [24, 27, 28, 29, 30, 31, 32, 33], confirmed that the process has a higher potential to improve oil recovery compared to conventional waterflooding.

Though many published studies showed a positive response, which translates into additional oil production as high as 30% in laboratory experiments and a decrease in residual oil saturation ranging from 2-50% in field trials, but a few others showed no significant benefit [34, 35, 36, 37, 38, 39, 40]. Despite this discrepancy, the brine-dependent recovery process has gained recognition as an emerging improved and enhanced oil recovery (I/EOR) technique to extract more oil in sandstone and carbonate reservoirs. The process has drawn industry attention not only because it is virtually identical to conventional waterflooding but also serves an upgrade as it delivers higher recovery and displacement efficiency. While the process necessitates additional surface facilities for water sourcing and disposal, it has more favourable economics and environmentally friendlier than other I/EOR techniques. This brine-dependent recovery technique is also referred to as "smart or low salinity waterflooding" by various researchers, "LoSal EOR" by BP [41], "Designer Waterflood" by Shell, and "Advanced Ion Management" by ExxonMobil [42].

In sandstone rocks, there are several requirements, like the presence of clay in the rock, polar components in oil, divalent/multicomponent ions in the formation water, that are necessary to observe an improved oil recovery [43]. Reduction of injected brine salinity, as low as 2000 ppm and as high as 7,000 ppm, and selective removal of divalent cations has proved successful,

whereas, carbonate rocks seem to be exempted from such requirements and approaches. The mineralogical differences between sandstone and carbonate rocks appear to dictate the performance of brine-dependent recovery in the different rocks. Different studies have shown that the recovery process is more complex in carbonate rocks than in sandstones [44]. The complexity is essentially because the bonding energy between the carboxylic component (RCOOH) of oil and carbonates is always higher than for sandstones. Hence, carbonate rocks are often characterized as mixed-wet to oil-wet, which is due to the collapse of the water film preventing the carboxylic component in the oil from adhering to the rock surface. In an oil-wet state, a higher negative capillary pressure is developed during conventional waterflooding. More oil is trapped as a result, ensuing in an ineffective displacement process due to low oil recovery and high water cut. However, the brine-dependent recovery process in the salinity range between 20,000–33,000 ppm has been reported to alter the carbonate rock wettability by restoring stability to the water film, thereby overcoming the negative capillary pressure and increasing water imbibition leading to higher recovery.

Despite its success, the recovery process has been explored on two major frontlines, each supported by experimental evidence of improved recovery [29]:

a. Reduction of injected brine salinity or ionic strength
    i. Brine dilution.
    ii. Reduction of water hardness (Ca^{2+} and Mg^{2+})
    iii. Non-active ions (Na^{+} and Cl^{-}) removal or reduction
b. Brine ion modification
    i. Potential determining ions (PDIs - SO_4^{2-}, Mg^{2+}, Ca^{2+}) concentrations
    ii. Surface interacting ions (PO_4^{3-} and BO_4^{3-}) concentration.

This study "brines with modified ions and not necessarily salinity change" are referred to as "*smart brines*" and "brines with reduced salinity" as "*low saline brines*". Brine-dependent recovery processes could also be combined with other recovery techniques such as chemical flooding or water alternating gas (WAG). However, a thorough understanding of the mechanisms at play during any recovery process is crucial for its successful implementation as well as reliable

production modeling, optimization and forecasting. The different frontlines as mentioned above that have been applied on carbonate rocks have led to the postulation of various mechanisms responsible for the improved oil recovery observed during its application. The widely acceptable mechanism among many researchers is wettability alteration, however, there is quite a debate as to the process by which the rock wetting state is changed by low saline/smart brine. Several different mechanisms have been proposed to justify the wettability as will be extensively discussed further in Chapter 2. Among the proposed mechanisms are reduction of interfacial tension [45, 46], mineral dissolution [31, 47, 48, 49], multi-ion exchange [32, 33, 44, 50, 51, 52, 53, 54, 55], and surface charge alteration/electrical double layer (EDL) expansion [27, 31, 56].

However, the decrease in interfacial tension (IFT) observed in several studies [45, 57, 58, 59, 60] was considerably less, which is not ample to cause such a high incremental recovery as compared to ultra-low values associated with gas-dependent recovery processes and alkaline flooding. Similar observations made by authors (such as Yousef *et al.* [31], Mahani *et al.* [56], Gupta *et al.* [61]) showed a small effect of injected brines on IFT, and no correlation could be established between the improved recovery and IFT. Hence, brine-dependent recovery influence on capillary forces is mainly seen in wettability alteration rather than IFT alteration. Several studies showed evidence to support rock dissolution mechanism, such as anhydrite dissolution contributing to the *in-situ* generation of sulfate as observed in produced brine [48, 49], increase in pressure drop resulting in fines migration [30, 36], improved connectivity between micropores and macropores during NMR experiments[31]. Contrarily, several researchers (such as Mahani *et al.* [56] and Chandrasekhar and Mohanty [27]) believed that mineral dissolution should be considered rather as a secondary recovery mechanism, relevant only at lab-scale and not field-scale.

Meanwhile, surface charge alteration indicates that the charge at the rock-brine interface is changed to less positive (which is strongly positive for calcite minerals) as compared to the negatively charge brine-oil interface. This alteration creates a repulsive electrostatic force that maintains a high disjoining pressure and expands the EDL. The water film thickness is related to the EDL, such that once the EDL expands, the thickness of the water film becomes stable and vice versa. The approach that involved ion modification and reduction or removal of monovalent salts

(consisting of Na^+ and Cl^-) has been proven to favorably decrease the rock-brine interfacial charge, creating repulsive forces necessary to expand the EDL [7, 38, 54, 56] . While the approach with brine dilution, where PDIs are relatively low, is presently debated to be due to surface charge alteration as the fundamental mechanism rather than dissolution [27, 56, 57].

A more comprehensive review of published research studies is presented in Chapter 2. However, from extensive research studies conducted thus far, it seems quite difficult to adjudicate which mechanism dominates, especially given that no consensus has been reached except that every proposed explanation has some form of wettability alteration [62]. The main cause for such could be because most result interpretation did not consider all factors influencing the oil-brine-rock interaction such brine content (connate and injected), rock mineralogy, oil type and structure, and temperature. During the recovery process, the already established equilibrium among oil, brine and rock is disturbed, and so it is envisaged that the underlying mechanisms behind this process would be related to a thorough geochemical interpretation of the process.

Reliable optimization of any recovery process requires the availability of a predictive tool. This tool is a necessity to understand the principal mechanisms driving the recovery process. For such a tool to be developed to simulate the recovery process, the mechanisms at play need to be well grasped. However, irrespective of not reaching a consensus over the proposed recovery mechanisms, few modeling works [47, 63, 64, 65, 66, 67, 68, 69, 70, 71, 72, 73, 74] have been performed to simulate pore-to-surface-scale mechanisms that have been proposed to explain the complex oil-brine-rock interactions. Most modeling attempts to present solutions to the mathematical equations describing brine-dependent recovery process have explored numerical approximations, while a few have attempted the application of analytical solutions [71, 72, 75, 76]. The bulk of the numerical black-oil models used salinity-dependent flow functions, while some of the compositional models used empirical correlations. Meanwhile, the complex interaction needs to be predicted by using either of surface sorption and complexation geochemical models that allows the investigation of rock mineralogical contents, brine compositions and polar oil materials, which are significant in electrostatic interactions at both rock−brine and oil−brine interfaces.

1.2 Research Justification

In recent times, with fluctuations in oil price, the cost of exploring new oil fields and unconventional oil becomes a very high-risk venture, fraught with uncertainties. Therefore, an approach to lessen such risks and uncertainties will be to target the residual oil in already discovered and proven reserves by developing cost-effective techniques/processes to improve recovery. The brine-dependent recovery process has proved effective in achieving such hurdle just as discussed above. However, many challenges have saddled the process which necessitates solution for prolific implementation:

- *Disputed fundamental chemical mechanisms*: As discussed above, conflicts exist among various researchers on the plausible mechanisms responsible for the observed improved recovery. Though wettability alteration has been agreed as the main effect, the path through which this is achieved remains disputed. The different proposed hypotheses are mineral alteration, surface charge alteration, multi-ion exchange and double layer expansion. Without a thorough understanding of the mechanisms at play, there will be a setback in its implementation. Therefore, this research is intended to develop a tool to closely evaluate the dominant chemical mechanism at play in the complex interactions among ion species in the aqueous, oil and rock surfaces.
- *Modeling challenges:* Different numerical modeling approaches have been used to evaluate this recovery technique. Few have extended black-oil models [68, 77, 78] by incorporating additional component in the aqueous phase without tracking the individual ionic species. Some tried empirical correlations and data matching, which is only peculiar to the condition where such correlations were developed [63, 79]. Few others assumed adsorption of a single wettability alteration agent to modify the flow functions**,** which is not enough to accurately capture the complexity of the process [64, 80]. Other two-phase models assumed either calcite dissolution or cation exchange [67, 69, 81], again not accounting for the interaction of hydrocarbon species with the brine and rock surface. Few compositional models developed either coupled a geochemical-transport model [82] with huge computation time or were designed for only sandstones [83]. There are others that used the surface complexation model

without applying thermodynamic parameters appropriate for natural reservoir rocks [70, 84]. There are simplified assumptions in many of these models that are not representative. It is therefore imperative to have a compositional multicomponent geochemical model that captures rock/brine/oil interaction with reliable interpretation and validation of reported experimental observations. The model should be able to perform fast and reliable numerical simulations of coreflood experiments as well as field scale studies. Also, the sensitivity of controlling parameters that could have a positive effect on oil recovery needs to be evaluated which could help provide equitable prediction at field-scale.

- *Benefits of combining brine-dependent recovery with other EOR techniques*: oil mobilization is improved through wettability alteration during the brine-dependent recovery process, and there are feasibilities of combining other processes which are capable of further reducing the capillary force responsible for oil trapping. Then, the combined system tends to benefit from the symbiotic effects of the combinations of the various processes. Encouraging results in carbonate reservoirs have been demonstrated through laboratory and numerical studies in low-salinity-water-CO_2 [83, 85, 86, 87, 88, 89], low-salinity-water-polymer flooding [90, 91, 92, 93], low-salinity-water-surfactant flooding [94, 95]. Hence, there is a need to further improve these processes.

1.3 Research Goals/Hypothesis

Based on existing literature, complexities in brine-dependent recovery in carbonates pose challenges to its field-scale application. However, certain questions that have come to mind with the work done so far will be addressed in this research. These questions are:

1. What are the dominant mechanisms at play considering the different approaches that are proven in carbonate reservoirs? How do these mechanisms interplay to achieve the reported experimental successes?
2. How realistic are these numerical models? Do they fully replicate the thermodynamic interaction between oil-brine-rock system during low saline/smart brine injection into carbonate reservoirs? How will the process behave in field-scale?

3. Many studies considered brine-CO_2 recovery, how will CO_2 perform in a low saline environment? What different injection approaches will excel using CO_2? How will the process behave in field-scale?

In this research study, "the hypothesis for the main underlying chemical mechanism behind brine-dependent recovery is wettability alteration from oil-wet towards water-wet". Its modeling can be quite challenging due to complex, coupled intra-aqueous, aqueous/oleic and aqueous/solid reactions. These reactions and transport of the resulting ions would have such a significant impact on oil recovery; hence, a robust model is required. Then, a native approach will be to distinguish various chemical interactions occurring because of the introduction of brine with a different composition into the core containing brine with compositions that is already in thermodynamic equilibrium with the core. Such would result in destabilization of the existing equilibrium state, triggering chemical reactions between ions in the aqueous phase as well as between ions in the aqueous and those dissolved or precipitated to the rock regarding mineral dissolution/precipitation and those attached to the rock surface due to various surface reactions. This fact, if proven, will lead to corresponding changes in the rock wetting nature as represented by flow functions like relative permeability and capillary pressure. The most important variable is the process-dependent interpolating parameter which captures wettability alteration through the interpolation of the flow functions as a function of different parameters as will be discussed later.

1.4 Research Objectives

Sequel to completing this study, which is to fill existing gaps in the literature, unravel the discrepancy between different studies, further implement representative modeling techniques and evaluate benefits of the brine-CO_2 recovery system, the following research objectives are proposed:

- In small scale, identifying the dominant chemical mechanisms behind the improved recovery observed during the brine-dependent recovery process and understanding the interplay between these mechanisms are the key objectives, on which other objectives rely. No reliable prediction or optimization can be achieved without this.

- Developing a comprehensive model that captures the dominant mechanisms and exploring different parameters relating the possible link between geochemical changes in the oil-brine-rock system. The model is employed to discuss recently published lab experiments where various experimental approaches in carbonates are proven.
- In large scale, evaluating low saline/smart waterflood beyond core-scale by extending recently published coreflood properties to a quarter of five-spot field model and comparing its performance under different operational and design strategies. Parametric sensitivity analysis is performed to highlight the impact of various variables.
- Developing a model that can capture oil recovery from the combination of low saline/smart brine and gas injection. Symbiotic benefits of low saline/smart brine and CO_2 is modeled, and different injection strategies are explored.

1.5 Outline of the Dissertation

This thesis describes the interpretation and validation of thermodynamic modeling of oil-brine-rock interactions during the brine-dependent and brine-CO_2 recovery for oil production enhancement in petroleum reservoirs. The scope of work extends from an extensive integrated review on systematic laboratory and field studies, interfacial mechanisms and modeling attempts to theoretical/numerical approaches to wettability evaluation at core-to-field scale based on the balance of the surface forces and geochemical modeling. The target of this work is to understand fluid physics during brine-dependent recovery, associate the dominant physics with rock wettability in terms of surface forces, predict the oil recovery and identify sensitive parameters that can influence the process performance. The rest of the thesis is structured as follows:

Chapter 2 presents an integrative literature review on the different systematic observations from laboratory experiments and field studies, taking into consideration the critical factors affecting the process performance. The proposed fundamental mechanisms with its associated contradiction and resolutions, as well as the major modeling attempts, including their potential challenges and lessons learned, were discussed. Besides, a summary of the major compatibility issues associated with the injection water and the possible remediation were presented. Chapter 3 discusses the theory of surface forces and water film stability, and mineral-scale investigation of wettability

alteration during brine-dependent recovery due to variation in PDI and NaCl concentrations, and brine dilution. The wetting state of carbonate rocks and the relationship of their wettability to oil recovery characteristics are also rationalized.

The description of the numerical model is given in Chapter 4 by presenting a general formulation of the system of mass action laws and flow equations for the reactive multiphase multicomponent transport applicable in multiple dimensions and describe the numerical approaches that are implemented in this modeling work. The model was validated using zeta potential and single-phase flow through experiments to acquire important thermodynamic parameters describing various surface reactions. Chapter 5 presents the investigation of the oil recovery characteristics by applying the numerical model developed in Chapter 4. The changes in oil recovery characteristics were described by developing a controlling parameter to alter flow functions as an indication of the wettability alteration process. Chapter 6 presents the investigation of the synergy between brine-dependent recovery and CO_2 flooding on improving oil recovery at both core-scale and field-scale. Finally, the major scientific findings of this study and several technical suggestions for future studies are presented in Chapter 7.

1.6 Publication

The work performed during this research study has led to several publications so far. The portions of the introductory text in Chapter 1 and the review of the systematic investigation of brine-dependent recovery presented in Chapter 2 have resulted in the following article:

> Adedapo Awolayo, Hemanta Sarma, and Long Nghiem. Brine-Dependent Recovery Processes in Carbonate and Sandstone Petroleum Reservoirs: Review of Laboratory-Field Studies, Interfacial Mechanisms and Modeling Attempts. *Energies*, 11 (11): 3020, 2018

A portion of Chapter 3 on surface chemistry and prediction of water film stability and the validation work on surface sorption model presented in Chapter 4 has been published as:

Adedapo Awolayo, Hemanta Sarma, and Long Nghiem. Modeling the characteristic thermodynamic interplay between potential determining ions during brine-dependent recovery process in carbonate rocks. *Fuel*, 224: 701–717, 2018.

The work presented in Chapter 4 on the development of the reactive transport modeling and part of the work presented in Chapter 5 on the prediction of brine-dilution dependent oil recovery approach led to the publication of the following article:

Adedapo Awolayo, Hemanta Sarma, and Long Nghiem. Thermodynamic Modeling of Brine Dilution-Dependent Recovery in Carbonate Rocks with Different Mineralogical Content. *Energy & Fuels*, 32: 8921–8943, 2018.

Part of the work presented in Chapter 5 on the prediction of brine-dependent oil recovery through composition-variation approach has been presented and included in the following conference proceedings:

Adedapo Awolayo, Hemanta Sarma, Long Nghiem and Emre Gorucu. A Geochemical Model for Investigation of Wettability Alteration during Brine-Dependent Flooding in Carbonate Reservoirs. *In: Proceedings of 2017 Abu Dhabi International Petroleum Exhibition & Conference* (*Paper SPE-188219*), Abu Dhabi, UAE, 13-16 November 2017.

The work presented in Chapter 4 on surface complexation modeling and validation and Chapter 6 on the prediction of the low-saline-water-CO_2 recovery process has been presented and included in the following conference proceedings:

Adedapo Awolayo, Hemanta Sarma, Long Nghiem and Emre Gorucu. Numerical Modeling of Fluid-Rock Interactions during Low-salinity-brine-CO_2 Flooding in Carbonate Reservoirs. *In: Proceedings of the 2019 SPE Reservoir Simulation Conference* (*Paper SPE-193815*), Galveston, Texas, April 10 - 11, 2019.

Chapter 2 Background and Integrative Review

This Chapter presents a comprehensive review on the established features and major progress made in the systematic investigation of brine-dependent recovery across the different scale of investigations from laboratory experiments to field studies, various proposed fundamental mechanisms, the major modeling attempts and water injection compatibility issues. Meanwhile, major attention is paid to studies conducted in carbonate rocks.

2.1 Introduction

As highlighted in Chapter 1, the brine-dependent recovery process has been explored on two major frontlines: ionic strength and composition modification [29]. For sandstone rocks, the presence of clay minerals and injected water salinity level as low as 2000 ppm and as high as 7,000 ppm gives optimum performance [96, 97, 98, 99, 100]. Meanwhile, a salinity range between 20,000–33,000 ppm appears to work well in carbonate rocks [44]. There were cases where the salinity range of 5,000–10,000 ppm resulted in improved oil recovery [30, 31, 36, 48, 101], but this has been attributed to the presence of dissolvable minerals [48, 102]. In addition, on the composition modification front, the process performance is optimum using injected water with less multivalent ions for sandstone reservoirs and more PDIs for carbonate reservoirs. PDIs are classified as those ions whose concentration in the aqueous solution controls the polarity and density of electrical charge on the mineral surface and influence interactions between oil and the rock surface [103].

Most experimental studies focused on, besides reporting oil recovery factors and residual oil saturation from displacement and imbibition tests, collection of a plethora of laboratory data (such as, produced brine composition and pH, pressure differential, water cut and breakthrough, contact angle/wettability index, zeta (ζ) potential, oil-brine interfacial tension, surface relaxation and adhesion, etc.) to explain the recovery mechanisms [29, 32, 54, 56, 57, 61, 104, 105, 106, 107, 108]. There have been inconsistencies in the report of many experimental studies. The major consensus reached is that “wettability alteration is considered as a consequence rather than as a cause of the processes” underlying brine-dependent recovery process. Several different mechanisms have been proposed to justify the wettability shift towards less oil-wetness; however,

there appears to be no unanimity about the recovery mechanism. Besides, some of the proposed mechanisms could only explain cases that showed a positive response and failed to explain cases with no significant benefit.

Few modeling attempts [47, 63, 64, 65, 66, 67, 68, 69, 70, 71, 72] have been made to simulate the proposed mechanisms to interpret the complex oil-brine-rock interactions, through the application of either numerical approximations or analytical solutions [71, 72, 75, 76]. Even so, a correct representation of the pertinent mechanisms in a mathematical model is required for an accurate prediction of fluid flow. Most modeling attempts to present solutions to the mathematical equations describing brine-dependent recovery process have explored numerical approximations, while a few have attempted the application of analytical solutions [71, 72, 75, 76]. The practical value of these models lies in the fact that they aid to improve interpretations of the process and help conduct fast sensitivity computations. This review addresses the subjects of current interests about comparing past and recent developments, and challenges of brine-dependent recovery processes in carbonate rocks. A detailed review highlighting the similarities and differences between the recovery process in sandstone and carbonate rocks is presented by Awolayo *et al.* [62].

2.2 Laboratory Experimental Studies

Ever since waterflooding has been introduced to recuperate hydrocarbons left after the primary recovery process, numerous attempts to investigate the fundamental mechanism have been made to understand, design and optimize the displacement process [8, 9]. The driving mechanism was then seen more like a physical process, and less attention was paid to the process chemistry. It was not until 1950 when some researchers [10, 11] noted an improved production after freshwater injection during core experiments, which they credited to sweep efficiency as a result of clay swelling and pore throat plugging. However, the process chemistry considering the quality of the injected brine did not generate significant attention until the 1990s. The earliest comprehensive study undertaken by Morrow and colleagues [13, 14, 15, 16, 109, 110] demonstrated the effect of oil-brine-rock interactions on improving oil recovery in a clay-rich rock formation and presented additional oil recovery from the brine-dependent process due to salinity gradient and wettability

shift. Since then, numerous studies have been conducted with most tests showing positive results [15, 23, 29, 30, 33, 38, 49, 52, 57, 60, 99, 100, 111, 112], while no response was observed in other tests [35, 36, 37, 38, 39, 40].

Because of the large size of subsurface rocks with diverse mineralogical contents occupied by complex reservoir fluids, systematic investigations are usually conducted at all levels (from the molecular scale to macro-scale, see Figure 2.1) in no particular order to completely understand and reliably predict subsurface processes. The scale of investigation often determines the type and degree of effects that are observed about gaining complete knowledge of the process. As such, a systematic investigation of brine-dependent recovery has been explored at the molecular scale (from atomic to nanometric level) through atomic force microscopy (AFM), scanning electron microscopy (SEM), nuclear magnetic resonance (NMR) and ζ–potential. At micro-scales, experiments (such as coreflooding, spontaneous imbibition, chromatographic and contact angle tests) typically investigate crude oil and brine flowing through or occupying pore spaces in the order of micrometres up to centimetres. Then, mechanisms and integrated effects can be further examined in a more magnified view at the macro-scale level through field trials and implementation.

Most of the laboratory evidence to support improvement in oil recovery during the brine-dependent process is mostly presented at different reservoir conditions through coreflood experiments (at micro-scale), in both secondary and tertiary mode, and augmented by spontaneous imbibition experiments. Some of the coreflood experiments are performed at low flooding velocity on short core samples, which often results in the erroneous estimation of residual oil saturation, because the fluid movement and production are susceptible to capillary end-effects [113]. Meanwhile, increasing the injection rates to reduce the capillary end-effects did not lead to remobilization of trapped oil in many studies [57, 114, 115], which emphasized the positive impacts of the injected brine on improved oil recovery. Spontaneous imbibition, on the other hand, is not only used to determine the initial wetting state but also to quantify the associated wettability changes when invading brine enters the pore-space [13, 116, 117]. It has been reported to yield higher imbibition rate and total oil production with the invading brine in both secondary and tertiary mode [13, 15,

50, 52, 102]. Moreover, for wettability assessment, a lower rate and smaller extent of imbibition often indicate oil-wetting nature, while higher rate and larger extent of imbibition are indicative of water-wetness [15]. Determination of the rock surface wettability inferred/directly measured through different techniques at both molecular and micro scales such as contact angle measurements [7, 30, 46, 57, 118], chromatographic test [32, 53, 54], electrokinetic (ζ-potential) measurements [104, 107, 119, 120, 121], NMR [57, 122, 123], AFM [106, 124, 125] , etc., has reported data consistent with a change to more water-wet conditions.

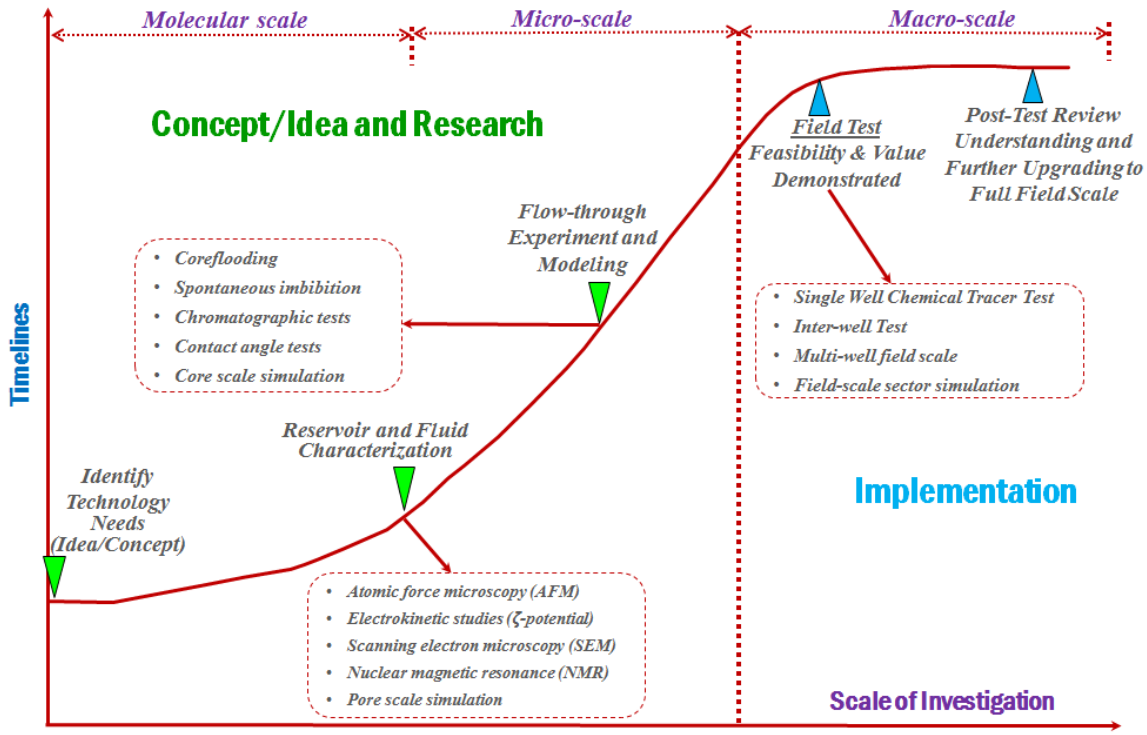

Figure 2.1— R&D-to-Field sketch of the systematic investigation for brine-dependent recovery design and implementation (adapted from Sarma [126], Awolayo *et al.* [62]).

The chromatographic test is a technique centred on the chromatographic partitioning of two water-soluble compounds, an adsorbing ion (like PDIs) and a non-adsorbing tracer ion (like SCN^-), with the aim to calculate the water-wet fraction after the rock samples are exposed to various brines. The ratio of the area between the relative effluent concentration of the two water-soluble compounds and the corresponding area of completely water-wet cores are then related to the wetting conditions (0 - oil-wet and 1 - water-wet) of the rock samples [127]. The contact angle

measurement is used to quantitatively express the degree of wetting when a solid surface is in contact with two fluids as measured through the denser fluid. The oil-wetting condition is often considered to be greater than 115°, water-wetting as less than 75° while intermediate/neutral wetting is considered to be between both extremes [128]. AFM is used to directly measure intermolecular adhesion forces between two surfaces by generating force-distance curves, which provide valuable information about hydrodynamic interactions between deformable surfaces, the nature of each force, surface energies and indirect clues of surface mineral chemistry [129]. The ζ-potential measurement is used to evaluate the electrokinetic behaviour of two interfaces in contact; the positive magnitude of one interface as compared to the negative magnitude of the other interface often result in electrostatic attraction between the two interfaces and consequently rupture the thin water film layer and lead to less water-wetness, and vice versa [130]. NMR is often based on T_2 relaxation time and surface relaxivity of fluid samples in a porous rock to determine different rock properties, especially pore occupancy and wettability because the relaxation time of the wetting phase is shorter than the bulk fluid phase [31, 122, 123]. These different scales of investigation have been well tested, though some were more tested compared to others, many of which will be discussed below.

Based on these previous studies, various aspects of the experimental method have been investigated, including reservoir and the injected brine parameters, to identify the optimum condition for brine-dependent process performance. The important parameters which have been given much attention in the literature in recent years, include the injection brine composition and ionic strength, connate water composition and saturation, rock type, clay content and type of clays present in the rock material, temperature, initial wettability of the rock surface, and crude oil composition and its acid/base number, as discussed below.

2.2.1 Connate water content and saturation

Most oil reservoirs initially contain formation water, which is highly saline and more often contains a high concentration of multivalent ions. Table 2.1 compares the variation in water compositions in different regions with successful brine-dependent recovery field application, such as the Endicott, Ekofisk and Arabian Gulf. The Ca^{2+} concentration is usually high in the formation

water and can be a factor of more than ten as compared to that of Mg^{2+} [131, 132]. The composition, salinity and saturation of the connate reservoir water can significantly influence the initial rock wetting state, which in turn based on its interactions with the injected water affects the efficiency of oil recovery.

Table 2.1—Salinity and composition of formation water and seawater in different regions (adapted from [23, 57, 133, 134])

Ions	**Seawater (ppm)**			**Formation water (ppm)**		
	Endicott	**Ekofisk North Sea**	**Arabian Gulf**	**Endicott**	**Ekofisk North Sea**	**Arabian Gulf**
Na^+	10812	10345	18043	11850	15748	59491
K^+	386	391	0	110	0	0
Ca^{2+}	402	521	652	320	9258	19040
Mg^{2+}	1265	1093	2159	48	607	2439
Ba^{2+}	0	0	0	7	0	0
Sr^{2+}	7	0	11	24	0	0
Fe^{2+}	0	0	0	10	0	0
Cl^-	18964	18719	31808	17275	42437	132060
HCO_3^-	147	122	119	2000	0	350
SO_4^{2-}	2645	2305	4450	63	0	354
CO_3^{2-}	0	0	27	0	0	0
TDS	34628	33498	57269	31707	68051	213734
Ionic Strength	0.688	0.659	1.146	0.541	1.453	4.317

It was documented that an increase in initial water saturation up to 34% leads to an increase in imbibition rate in Chalk as reported by Viksund *et al.* [135]. The authors claimed that the scaled imbibition curves for chalk in the absence of initial saturation closely agrees with that of sandstone rock. Strand *et al.* [53] reported twice the oil recovery observed using similar salinity brine in the core with the initial saturation of 9.1% than that of 14.8% initial water saturation, even though much of the improved recovery was attributed to the presence of sulfate in water injected into 14.8% water saturated cores. Similarly, Puntervold *et al.* [136] compared the effect of a range of initial water saturations (high – 30-50%, low – 10% and No water saturation – 0%) on oil recovery and observed that the cores became less water-wet as the water saturation decreases. The

wettability change led to a reduction in the imbibition rate, and it was proposed that at low water saturation, high oil saturation increases the amount of crude oil surface-active materials such that the oil can easily adsorb on the rock surface.

In a subsequent study, Puntervold *et al.* [137] observed no difference in oil recovery when two cores were initially saturated with deionized water at 22% and 10% water saturation, respectively and flooded with similar brines at 90 °C and 130 °C. The authors further proved through chromatographic tests and spontaneous imbibition that a small amount of sulfate in the formation brine can significantly improve the rock water wetness and oil recovery. A similar study conducted on Stevns outcrop chalk reported that when initial sulfate was removed from the core by flooding with distilled water prior to aging, the effect of sulfate on the oil recovery was greater compared with core plugs where the sulfate was initially present [138]. Furthermore, Shariatpanahi *et al.* [131] conducted additional studies on impacts of sulfate present in the initial brine on the initial wetting state and confirmed that increasing sulfate concentration to 2 mmol/L increased oil recovery and decreased water-wetness. The improvement in oil recovery and water-wetness was reported to increase as the aging temperature decreased (130 – 50 °C), while no noticeable improvement was observed as the sulfate concentration was increased beyond 2 mmol/L in the initial brine. In addition, Zhang *et al.* [50] reported that increasing Ca^{2+} concentration in the initial brine has a very marginal effect on the rock wetting condition. In a recent study by Shariatpanahi *et al.* [139], it was shown that increasing Ca^{2+} concentration decreased the water-wetness while Mg^{2+} in the formation brine makes the rock more water wet.

2.2.2 Crude oil composition

Crude oil usually contains both acids and bases that are ionizable and exhibit surface activity [140]. The ionizable acidic and basic surface-active groups of the crude oil form as a result of the presence of typical heteroelements (like nitrogen, oxygen, and sulfur) found in oil [141]. Petroleum bases are identified as heterocyclic aromatics with the nitrogen atom, quantified by base number (BN); while the number of carboxylic materials in crude oil is used in characterizing petroleum acids, quantified by acid number (AN). The carboxylic group and the nitrogen-containing bases, as mostly found in crude oil heavy end fractions, i.e. asphaltene and resins, plays such a vital role on

the rock initial wetting. The polarity and the chemical properties of crude oil as determined by its ionizable acidic and basic surface groups can influence rock wettability [142].

Various earlier studies [141, 143, 144, 145, 146] have described the role of heavy fractions, asphaltenes or acid and basic components in crude oil on rock wetting state. However, not all crude components have been reported to be influential in altering the preference of the rock towards oil wetting. Denekas *et al.* [141] presented that sandstones seem not to have any selective affinity for a specific type of polar product, as both the acidic and basic components of the crude oil alter the rock wettability. In contrast, the authors claimed that limestone rocks are more sensitive to basic products containing nitrogen. Many other authors [147, 148, 149] have given contradictory opinions about the above assertion that indicate the possibility of the chemisorption of the acid components (most notably naphthenic acids) of crude oils on the basic carbonate surface. The differences in opinions could be as a result of increased decarboxylation of carboxylic material in crude oil at elevated temperatures, catalyzed by the presence of formation itself ($CaCO_3$), and leading to a reduction in acid number compared to basic number over geological time [150].

In a different study, Standnes and Austad [116] reported that acid number is a crucial wettability factor for carbonate rocks as the imbibition rate and water-wetness was observed to decrease as the AN increased in the absence of initial water (see Figure 2.2). The authors did not observe any correlation between the imbibition rates and the asphaltene content and stated that the functional acid groups did not dominate the asphaltene fraction of the oil. In several tests performed on chalk wetting properties using oils with different AN (0.17 – 2.07 mg KOH/g) and synthetic seawater, an increased water-wetness as the AN decreased was reported by Zhang and Austad [151]. Austad *et al.* [48] also compared imbibition rate of limestone cores aged in two different crude oils, imbibed in formation water and reported that the imbibition rate decreased as the AN increased, while the contribution from BN was ignored. In a similar study, the imbibition rate was observed to increase further as the brine was switched to a brine of higher sulfate concentration with increased AN [152].

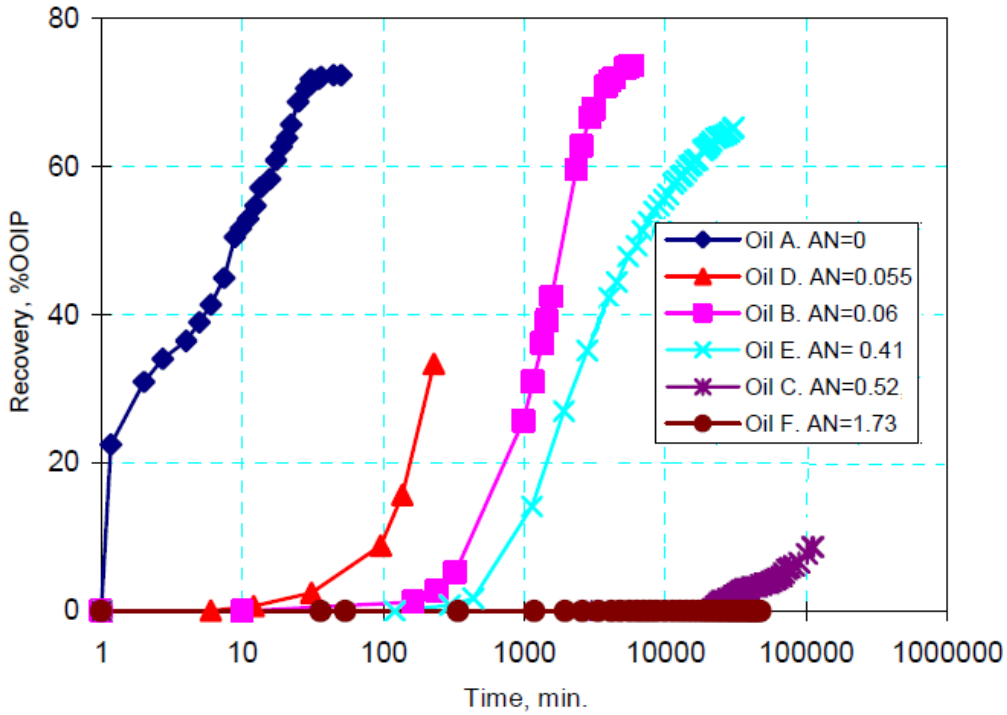

Figure 2.2—Effect of acid number (AN) on spontaneous imbibition of brine into chalk cores saturated with different crude oil (reproduced from Standnes and Austad [116] with permission). The imbibition rate and water-wetness decrease as the AN increases in the absence of initial water

A wider range of organic compounds was investigated for carbonate rock adsorption and wettability by Thomas *et al.* [153]. Fatty acids were observed to strongly and nearly irreversibly adsorb to the carbonate surface, whereas aromatic and branched carboxylates and long chain acids were moderately adsorbed and alcohols, amines, short-chain acids were weakly-adsorbed/non-adsorbed. It was also stated that the overall structure of the compound determined its adsorption strength, for example, the small size of the carboxyl group and long straight chains of the fatty acids lead to the formation of a closely-packed hydrophobic layer, thereby providing multiple attachment sites to stabilize the adsorption and make the carbonate surfaces oil-wet. Standnes and Austad [116] also claim that carboxyl groups are the most active polar functional groups of crude oil in adsorbing organic material onto the chalk surface. Several other authors [154, 155, 156, 157, 158] have shown that long-chain acids are the most effective among researched acidic species to alter the carbonate rock to a more oil-wet state. Despite that the effect of basic materials on wettability was not widely studied, Puntervold *et al.* [136], observed that an increase in the amount of natural bases led to decrease in water-wetness as AN was held constant. It was suggested that

the natural base forms a large molecular weight acid-base complex to be in equilibrium with the carboxylic materials in the oil, thereby preventing the carboxylates from adsorbing to the rock. In many of the discussed studies, it is well agreed that the AN and BN of the crude oil, associated with the presence of long chain acids, play a significant role in wettability alteration of carbonate surfaces.

2.2.3 Rock mineral composition

Different rock types have varying mineral compositions that affect the rock's surface area, grain structure, crystalline texture, and reactivity towards diverse ions in brines and this reflects the heterogeneous nature of the reservoir and difference in their responses towards brine-dependent recovery processes. Therefore, understanding the effect of rock properties as it influences the initial wetting state and response to brine-dependent recovery is essential for a valid comparison. Carbonate rocks are primarily composed of calcite ($CaCO_3$) and dolomite ($CaMg(CO_3)_2$), with a variety of other minerals like anhydrite/gypsum ($CaSO_4$), magnesite ($MgCO_3$), aragonite ($CaCO_3$), apatite (phosphate source), quartz, siderite ($FeCO_3$), evaporite, pyrite, etc. [159, 160]. Carbonate rocks often experience different post-depositional chemical/physical changes, which results in corresponding changes in rock properties, such as surface area, reactivity, permeability, porosity, faults, fractures, and wettability.

Studies by various authors (like [161, 162, 163]) have shown that mechanical properties (such as strength, yield and bulk modulus) of chalk is weakened (decreased) when flooded with seawater containing SO_4^{2-} ions, which can enhance compaction and cause a minor change in permeability as compared to distilled water and seawater without sulfate. The resulting large-scale heterogeneity often generates complex fluid flow paths, which has been shown to increase oil displacement through smart brine injection from the matrix blocks by well-connected induced fractures [164], compared with non-connected fractured cores. Meanwhile, it has been shown that the surface area and the reactivity towards PDIs in the injected brine vary for different carbonates.

Several parametric studies have demonstrated that chalk (a pure biogenic calcite) is highly reactive to PDIs as their adsorption can change the surface charge of the rock and alter rock wettability [32,

50, 51, 52, 54, 55, 127, 152, 165]. The degree of sulfate ions adsorption was found to be different depending on the chalk type [138, 161, 166] and proportional to the surface area of the specific chalk [161]. Further studies by Fathi *et al.* [38] suggested that NaCl-depleted seawater is more reactive to the chalk surface as its imbibition rate and ultimate oil recovery increased relative to ordinary seawater and further improvement was observed when NaCl–depleted seawater was spiked by sulfate [167], while increasing NaCl concentration led to a decrease in oil recovery. However, limestone, which is less homogeneous than chalk with smaller surface area, has been reported to have a similar affinity towards PDIs, although the reactivity is less than it is chalk [29, 53, 99, 112]. As for chalk, NaCl–depleted seawater appeared to be an even better wettability modifier in limestone than ordinary seawater [39, 112].

On the other hand, the injection of low saline brine in chalk cores did not result in additional recovery [36, 38, 48]. In the same study, Austad *et al.* [48] reported oil recovery improvement when limestone cores containing anhydrite was flooded with low saline brine. The study indicated that the improvement in oil recovery recorded by Yousef *et al.* [31] on limestone core was as a result of anhydrite dissolution that led to the *in-situ* generation of SO_4^{2-} ions. The authors claimed that the presence of anhydrite is essential for the success of brine-dependent recovery in cases where injected brine contains little/no SO_4^{2-} ions. Meanwhile, Romanuka *et al.* [101] conducted spontaneous imbibition experiments on limestone cores (primarily calcite) and showed that brine dilution contributed to an incremental recovery up to 2–4% OOIP, whereas NaCl–depleted seawater had no recovery benefit. Zahid *et al.* [36] also reported a substantial increase in oil recovery with diluted seawater on carbonate cores free of dolomite/anhydrite and suggested that rather than anhydrite dissolution, calcite mineral rock dissolution leading to fines migration was the plausible mechanism for the incremental recovery.

Dolomite core, which predominantly contains dolomite minerals, has been reported to have a similar surface reactivity towards PDIs in the injected brines, however, is weaker compared to chalk and limestone cores [101, 120, 139, 168]. Shariatpanahi *et al.* [139] reported that the presence of sulfate ions (either through the injected brine or anhydrite dissolution [101]) is essential to observe oil recovery benefits and the brine salinity was suggested to be low to increase

surface reactivity of dolomites to PDIs. The degree of improvement in oil recovery and wettability alteration has been observed to differ based on the mineral composition, grain structure, deposition and crystallographic origin of carbonate rocks [120]. In the study by Mahani *et al.* [120], it was observed that adhesion between carbonate rocks and oil varies in the following descending order: dolomite > calcite crystal > limestone > chalk for the same type of brine and oil, which signifies that rock surface reactivity is the reverse order (see Figure 2.3). Likewise, it was reported that limestone showed negative ζ–potential in all tested brines, while dolomite showed more positive ζ–potential, which was related to higher charge density on dolomite, because of the presence of Mg^{2+} in its crystalline lattice.

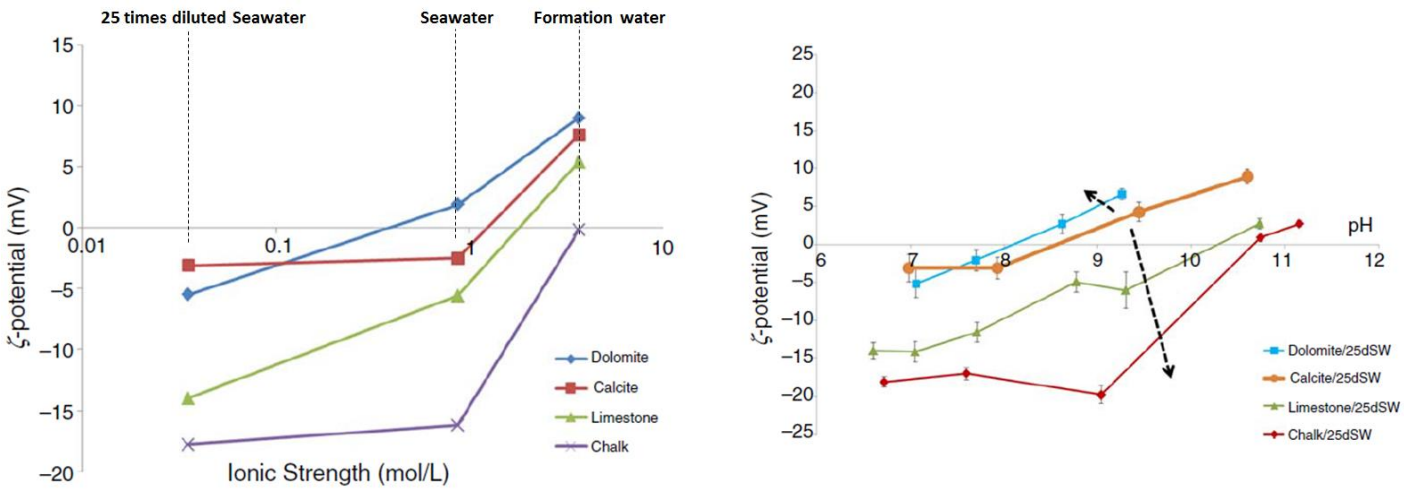

Figure 2.3—Comparison between ζ–potential of chalk, calcite, limestone and dolomite in different brine at reservoir pH of 7 (*left*) and in 25 times diluted seawater at pH range 6 – 11 (*right*) (reproduced from Mahani *et al.* [120] with permission)

Additionally, different types of outcrop chalk cores were reported to have a diverse degree of reactivity towards SO_4^{2-} ions with its associated oil recovery benefits due to their mineral depositions and compositional differences [138]. Outcrop limestone rocks acted completely different from reservoir limestone in wettability alteration studies, which showed that diverse sources of rock could influence the systematic investigation of brine–dependent recovery process. Two outcrop limestone rocks were tested, both showed water-wet conditions and appeared nonreactive towards PDIs as seawater flooding at high temperature couldn't modify the wettability

and improve oil recovery [169]. Contrary to outcrop limestones, outcrop dolomite responds to low saline/smart brine in the same way as reservoir dolomite cores [139].

In an electrokinetic study by Al Mahrouqi *et al.* [170], it was reported that natural carbonate yielded a more negative ζ–potential than synthetic calcite, due to the presence of impurities (such as clays, organic matter, anhydrite apatite, or quartz), which yield a negative ζ–potential compared to pure calcite. Similarly, it was reported that synthetic calcite and pre-aged calcite rock exhibited positive ζ–potential at low pH range and negative potential at a higher pH (above pH of 10), which was attributed to positive species (like Ca^{2+} and $CaHCO_3^+$) and negative species (like CO_3^{2-}) prevalence at the rock surface at lower and high pH respectively. Meanwhile, natural calcite and post-aged calcite rock exhibited negative ζ–potential, which was attributed to the organic material's adsorption on the calcite surface, giving it the negatively charge surface [171, 172].

2.2.4 Temperature and pressure

Due to the reactive nature of the brine-dependent recovery process, reservoir temperature is a key factor that affects the activation energy required for the chemical reaction at the oil–brine and brine−rock interfaces leading to the wettability alteration process. The influence of temperature can be categorized as two-folds, as it affects rock wettability through the interaction of oil polar organic compounds and the reactivity of ionic species in the brine or sensitivity of the ionic strength with the rock surface. Pressure is mostly identified to impact the oil polar organic compounds interaction with the rock surface due to changes in the solubility of the asphaltenic content of the crude oil. As the reservoir pressure reduces towards bubble point pressure, the asphaltene solubility decreases, resulting in surface precipitation and adsorption of the crude oil onto the rock surface [142, 173].

The thermal degradation of crude oil is more promoted in the presence of calcite as substantially greater amounts of a lower carbon number hydrocarbon is formed at high temperature [150]. Over geological time, the thermo-catalytic effect of calcite on the decomposition of carboxylic acids in crude oil will significantly result in a reduction in AN as the temperature increases. Because of the affinity of the carboxylic materials to carbonate surfaces compared to other polar materials that

are naturally present in crude oil, the AN strongly dictates the wettability state of carbonate rocks, which implies that the water-wetness increases as the temperature increases. This logic might explain the reason why high-temperature carbonate reservoirs appear to be more water-wet compared to low-temperature reservoirs, contrarily to most sandstone reservoirs [174]. However, Zhang and Austad [151] argued that the observation is not a temperature effect; rather it is the reduction in carboxylic acids. Typical reservoir examples mentioned by Zhang and Austad [151] in decreasing order of water wetness are: Yates dolomite Texas field (30 °C, AN – 1.0 mg KOH/g) > Valhall chalk North sea field (90 °C, AN – 0.3-0.5 mg KOH/g) > Ekofisk chalk North sea field (130 °C, AN – 0.1 mg KOH/g). It was further reported that cores aged at three different temperatures (40, 80 and 120 °C) with similar AN crude oil show insignificant differences in chromatographic wettability test, which suggests that aging temperature have a minor impact on chalk rock wettability, provided the oil–rock–brine system reaches chemical equilibrium during aging [151]. The authors claimed that decarboxylation is a slow process and cannot be achieved in the aging period considered in their experiments. Like observations made in sandstone rocks, aging temperature has been observed to affect the wetting conditions of carbonate surface aged at 25 and 50 °C [175]. The core aged at 50 °C was observed to reach an intermediate wetting state earlier compared to the core aged at 25 °C in a contact angle measurement conducted using a synthetic brine solution (1 wt.% NaCl). Another factor where temperature plays a role in brine-dependent recovery is the dependence of the reactivity of brine ionic species on temperature.

A systematic series of studies has been conducted by Austad and colleagues [33, 50, 52, 54, 55, 127] to investigate the effect of temperature on the activity of PDIs in the injected brine. The reactivity of SO_4^{2-} towards the chalk surface was observed to increase in a chromatographic wettability test due to increased sulfate adsorption as temperature increased from 20 – 130 °C, with a linear increase between 40 and 100 °C and drastic increase above 100 °C [33, 52]. The authors further support the improvement in water-wetness by reporting an increase in oil recovery by spontaneous imbibition as the temperature increases for experiments with the same sulfate concentration in the injected brine. The ultimate oil recovery from spontaneous imbibition of chalk cores at two different temperatures (100 and 130 °C) for a fixed condition (same oil AN, initial water and varying sulfate concentration in seawater) was observed to be smaller at 100°C

compared to 130 °C. It was stated that a further increase in the amount of sulfate in the imbibing brine at 100 °C could only partly compensate for the significant difference in recovery [55]. Strand *et al.* [54] investigated the effect of Ca^{2+} and SO_4^{2-} ions on wettability modification of chalk surfaces at varying temperatures (90 and 130 °C) and reported an increase in both imbibition rate and oil recovery as the temperature increased. The improvement in recovery was further verified through a chromatographic wettability test performed at varying temperature (23 – 130 °C), where adsorption of SO_4^{2-} and co-adsorption of Ca^{2+} increased as the temperature increased, while at any given Ca^{2+}/SO_4^{2-} ratio, sulfate adsorption as well as the front dispersion increases with temperature. It was also reported that beyond 100 °C the sulfate adsorption reduces as the Ca^{2+}/SO_4^{2-} ratio increases. The given explanation is that the solubility of $CaSO_4$ drastically reduces above 100 °C, possibly because of a decrease in hydrogen bonding between the sulfate ions and water molecules. Therefore, as the bond breaks, sulfate tends to leave the aqueous phase either by adsorption onto rock or precipitation of $CaSO_4$. With a decrease in solubility and increase in Ca^{2+} ion, sulfate will precipitate above 100 °C.

Zhang *et al.* [50] showed, in a similar study, that increasing Ca^{2+} concentration increased oil recovery as temperature increased from 70 to 100 °C and further when the temperature was increased to 130 °C, however, the impact was reduced and even vanished due to precipitation of $CaSO_4$. The overall theme in these studies [33, 52, 54, 55] is that higher affinity of sulfate observed at higher temperatures results in the displacement of the negatively charged carboxylic oil groups on the rock surface, alters the wettability to more water-wetness and increases the degree of the water-wetness. In another study conducted by Zhang et al. (2007), the interplay between Ca^{2+} and Mg^{2+} was investigated through the chromatographic wettability technique at different temperatures and reported that affinity of Ca^{2+} towards the chalk surface was higher compared to Mg^{2+} at low temperatures. However, Mg^{2+} strongly adsorbed and even substituted Ca^{2+} at higher temperatures, and the degree of substitution increased with temperature, with 70 °C appearing as the threshold temperature for Ca^{2+}/Mg^{2+} substitution. Besides, spontaneous imbibition experiments showed that adding Mg^{2+} ions resulted in a higher incremental oil recovery than by adding Ca^{2+} ions at 100 and 130 °C. The reactivity of Mg^{2+} observed at 130 °C significantly surpassed the effect of spiking sulfate in the injected brine with Ca^{2+}. It was then proposed that instead of Ca^{2+} co-adsorbing with

SO_4^{2-} at the chalk surface, Mg^{2+} becomes active and less hydrated at a higher temperature, and displaces Ca^{2+} to bound to the surface, because Mg^{2+} has a smaller ionic radius and larger hydrated radius compared to Ca^{2+} [32, 33, 51, 65]. An identical temperature-dependent interaction was reported between PDIs and limestone, though the reactivity was less than for chalk surfaces as previously mentioned [53, 112].

Another temperature-dependent effect was observed for the non-active salt (NaCl) on oil recovery by Fathi *et al.* [38] using NaCl-depleted seawater while maintaining the concentration of PDIs. It was reported that as the elevated temperature increased (from 100 – 120 °C), imbibition rate and oil recovery significantly increased for NaCl-depleted seawater compared to when NaCl was spiked four times in the seawater. In a later study, it was reported that spiking sulfate concentration in NaCl-depleted seawater increased oil recovery as the temperature increased (70 – 120 °C) while spiking Ca^{2+} above 100 °C did not result in additional recovery [167]. Like the electrokinetic study in sandstones, the measured ζ-potential of intact carbonate rocks in low saline brine environments was reported to increase with temperature; however, the pH remained constant irrespective of temperature or ionic strength. Instead, the equilibrium concentration of calcium resulting from carbonate dissolution was observed to increase as temperature increased with low saline brine and remained constant with high saline brine, while equilibrium concentration of other PDIs remained constant irrespective of temperature. Hence, the temperature dependence of the ζ-potential is correlated to have a Nernstian linear relationship with the temperature dependence of the equilibrium calcium concentration (PDI for the calcite surface) [103].

Similarly, Mahani *et al.* [176] reported that as temperature increases in the range of 25 – 70 °C for low saline brine, the oil and rock ζ–potentials shift towards the point of zero potential (either from more positive to less positive values or from more negative to less negative values). This shift with increasing temperature was negligible for higher salinity. The increasing trend of rock ζ–potentials towards a less negative value for low salinity brine was ascribed to more presence of divalent cations adsorbing to the rock surface. Meanwhile, for low saline brine injection that depended on the presence of the anhydrite minerals because of little/no sulfate ions in the injected brine, it has been shown that the dissolution of anhydrite decreases with temperature [48, 112]. While the

surface reactivity leading to wettability alteration as well as imbibition rate and ultimate oil recovery increases as temperature increases, which could somewhat be counterbalanced by a lesser amount of sulfate available for adsorption due to reduced dissolution. For this reason, Austad [134] proposed that the optimum temperature window for the success of low salinity brine injection is probably between 90 - 110 °C. In addition, Zhang and Sarma [30] studied the effect of lowering brine salinity and spiking SO_4^{2-} ions concentration on wettability alteration and oil recovery of reservoir limestone rocks at varying temperatures (70, 90, 120 °C). The authors argued that at 70 °C, lowering brine salinity is more efficient than increasing the SO_4^{2-} ions concentration, while at 90 and 120 °C, reducing brine salinity and increasing SO_4^{2-} concentration resulted in a similar magnitude of wettability alteration and higher oil recovery.

2.2.5 Injected brine composition and salinity

The effect of injected brine salinity and composition on wettability alteration and oil recovery improvement has been studied using both ionically-tuned and diluted versions of formation water or seawater (common injection water sources as shown in Table 2.1). Extensive laboratory studies, especially coreflooding and spontaneous imbibition, from carbonate cores have shown that increasing divalent ions (particularly PDIs, see Figure 2.4) and decreasing monovalent ion (Na^+ and Cl^-) concentrations in the injected brine lead to an increase in the rate and extent of oil recovery [32, 33, 38, 50, 52, 54, 55, 165]. The existence of an interdependent interaction among multivalent ions in brine (Ca^{2+}, Mg^{2+}, SO_4^{2-}, PO_4^{3-} and BO_3^{3-}) at the rock-brine interface has been emphasized that can bring the rock-brine interface into a new equilibrium state, thus improving water-wetness and recovery through various interfacial phenomena.

Earlier studies [52, 151, 165, 166] have shown that SO_4^{2-} can act as surface active agents that can lower the surface charge of carbonate surface, facilitate the removal of negatively charged polar components and change the contact angle to more water-wetness and improve oil recovery by spontaneous imbibition. A significant increase in oil recovery was observed as the SO_4^{2-} concentration in injected brine is increased from 0 to 4 times the concentration in ordinary seawater, and the affinity of SO_4^{2-} towards chalk surface is temperature dependent [52, 152]. The impact of sulfate, as a PDI and wettability modifier on increased oil recovery, has been well

examined and reported by other researchers (such as [27, 29, 30, 53, 101, 112, 177, 178]). Besides, several of these studies have proved that a high SO_4^{2-} concentration did not offer improved recovery; rather an upper limit existed beyond which no improved recovery could be observed [7, 46, 52, 138].

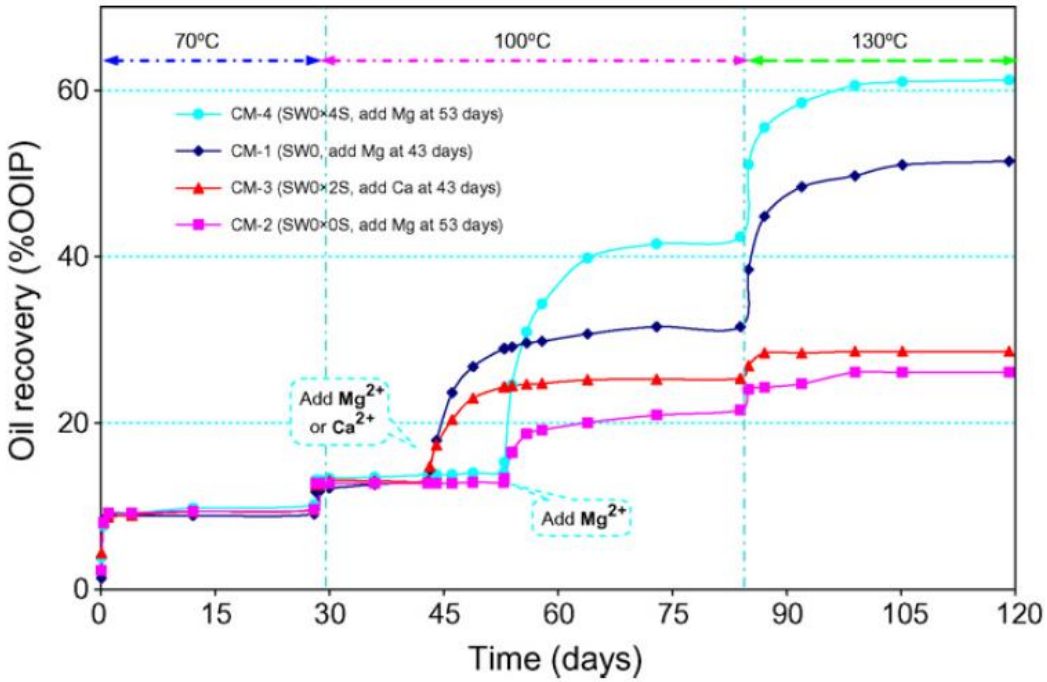

Figure 2.4—Comparison of spontaneous imbibition rates of PDIs in chalk conducted at 70, 100 and 130 °C with a back-pressure of 88 psi. Modified seawater without Ca^{2+} and Mg^{2+} was initially imbibed, and Mg^{2+} or Ca^{2+} was later added in a systematic variation of PDI concentrations (reproduced from Zhang *et al.* [32] with permission)

Similarly, Ca^{2+} and Mg^{2+} are considered to be active towards the carbonate rock surface [165]. Strand *et al.* [54] observed that the efficiency of the wettability alteration due to brine-dependent recovery is governed by the relative concentration of Ca^{2+} and SO_4^{2-} in the injected brine. The authors reported that increasing the Ca^{2+}/SO_4^{2-} ratio between 0.25 and 3 times the concentration in ordinary seawater led to increased adsorption of SO_4^{2-} but decreased as temperature exceeded 100°C. Zhang *et al.* [50] also presented spontaneous imbibition of oil as evidence to show the symbiotic interaction between Ca^{2+} and SO_4^{2-} and the temperature-dependency of the interaction. Increasing Ca^{2+} led to strong imbibition and increase in oil recovery, and beyond 100°C, the recovery is less due to precipitation of $CaSO_4$. According to these studies, SO_4^{2-} adsorbed onto the

chalk surface, lowers the positive surface charge resulting in lesser electrostatic repulsion. Meanwhile, Ca^{2+} would gain greater access to approach the surface to balance the electric charge as well as bind to the negatively charged oil acidic groups. This interaction helps to release the oil from the chalk surface.

On the other hand, Zhang *et al.* [32] presented ζ–potential experimental evidence to prove that Mg^{2+} has the potential to increase positive surface charge like Ca^{2+} and investigation of the interplay between Ca^{2+} and Mg^{2+} through a chromatographic test at different temperatures shows that Mg^{2+} substituted Ca^{2+}at higher temperatures. It was then proposed that instead of Ca^{2+} co-adsorbing with SO_4^{2-} at the chalk surface, Mg^{2+} becomes active and less hydrated at a higher temperature and displaces Ca^{2+} bound to the surface. In contact angle measurement, it was shown that SO_4^{2-} and Mg^{2+} were more efficient in altering wettability and improving oil recovery [7, 27, 30, 114]. The significant conclusion from the systematic series of studies conducted to investigate the impact of PDIs on oil recovery is that none of the PDIs could act alone in improving water-wetness, although in the different combinations, SO_4^{2-} was found to be present in the imbibing fluid [27, 30, 52].

The significance of polyatomic anions (e.g., phosphate−PO_4^{3-} and borate−BO_3^{3-}) as a possible replacement for sulfate has been investigated due to their higher ion valence to lower surface charge compared to sulfate SO_4^{2-}. Researchers at ExxonMobil [42, 61] found that replacing SO_4^{2-} in the injected brine by BO_3^{3-} in coreflooding experiments performed on several limestone and dolomite cores in tertiary mode resulted in higher recovery, whereas replacing with PO_4^{3-} gave even higher recovery. Meanwhile, softening the injected brine by depleting Ca^{2+} and Mg^{2+} in the formation water also resulted in an increase in recovery due to rock dissolution. In addition, Meng *et al.* [58] demonstrated that high concentration of PO_4^{3-} in the injected brine could induce larger contact angle alteration of limestone cores to a more water-wet condition, which was more pronounced when the brine was ten times diluted. However, the effect of polyatomic anions has not been further investigated due to the limitation of a higher likelihood of formation of precipitate that could potentially damage the reservoir.

Aside the PDIs, Na^+ and Cl^- have been identified as non-active ions that are indifferent toward carbonate surfaces. Fathi *et al.* [38] discovered that NaCl–depleted seawater gave a higher imbibition rate and recovery relative to seawater while spiking NaCl concentration in seawater by 4 times gave a lower recovery. Furthermore, chromatographic tests showed that the water-wet fraction further increased for chalk cores imbibed in NaCl–depleted seawater relative to seawater. In a later study, it was reported that spiking SO_4^{2-} concentration in NaCl–depleted seawater significantly increased recovery and water-wetness, however spiking Ca^{2+} had no significant effect because the experiments were conducted above 100°C [167]. Awolayo and Sarma [39] have also shown that NaCl–depleted seawater alters wettability towards more water-wetness relative to seawater in a contact angle measurement, which was supported by improved tertiary oil recovery in coreflooding experiments on limestone cores. These studies highlighted the impact both SO_4^{2-} and the indifferent ions (Na^+ and Cl^-) have on the injected brine to modify rock wettability. All charged surfaces in contact with brine will have an excess of ions close to the surface, which is usually called the double layer. If the double layer consists of a lot of ions not active in the wettability alteration process like NaCl, the access of the PDIs (Ca^{2+}, Mg^{2+} and SO_4^{2-}) to the surface is partly prevented. This approach of depleting NaCl from seawater results in total brine salinity reduction because of a high concentration of the indifferent ions in most brines. Another approach of reducing total salinity through brine dilution, which failed to work in chalk cores [38, 48, 101], has shown tremendous positive benefits in a series of experiments with middle-eastern limestone cores containing small amounts of anhydrite conducted by Yousef and colleagues [57, 102]. Seawater was diluted up to 100 times, and the sequential flooding experiments showed that the highest recovery was achieved by twice diluted seawater, followed by 10 times dilution, whereas 20 and 100 times dilution resulted in little/marginal recovery. The authors reported a total incremental recovery of up to 19% OOIP and indicated that surface charge alteration was more important than dissolution in the wettability alteration process.

Elsewhere, Austad *et al.* [48] injected sulfate-free diluted brine into carbonate cores containing anhydrite and reported an incremental recovery up to 5% OOIP. The authors explained that sulfate was continually generated in-situ because of anhydrite dissolution, which led to the wettability alteration process. Romanuka *et al.* [101] carried out spontaneous imbibition experiments on

different mineralogical carbonate cores with/without evaporites and showed that brine dilution contributed to an additional recovery of up to 20% OOIP. Zahid *et al.* [36] conducted another series of experiments on carbonate cores free of dolomite/anhydrite, and observed no incremental recovery at room temperature and reported additional recovery up to 18% OOIP at 90°C. The authors proposed fines migration and rock material dissolution as the plausible mechanisms for wettability alteration. Zhang and Sarma [30] and Chandrasekhar and Mohanty [27] observed that the multi-ion exchange between the active multivalent ions and mineral dissolution was the mechanism responsible for wettability alteration when the brine dilution approach was applied to middle-eastern carbonate cores. However, in a few other cases [39, 114] in limestones, very little or negligible results were observed during brine dilution. Results of lower/decrease in contact angle have also suggested that the wettability of carbonate rocks is altered by either a reduction in the brine salinity or increasing PDI concentrations [7, 27, 30, 31, 56, 58, 118].

Nyström *et al.* [179] carried out an electrokinetic study on the influence of the concentration of monovalent (Na^+) and multivalent (Ca^{2+}, Ba^{2+} and La^{3+}) cations on calcite particles. It was reported that Na^+ acted indifferent towards calcite surface, Ba^{2+} exhibited similar behaviour to that of Ca^{2+} but of greater magnitude as the ζ–potential increased with concentration, while La^{3+} exhibited an opposite trend to that of the other divalent cations. In a different study, Jackson and colleagues [104, 170] reported that both Ca^{2+} and Mg^{2+} exhibited identical behavior, linearly increasing the ζ–potential of intact limestones as their concentrations increased in the different NaCl brine solutions. While increasing SO_4^{2-} concentration reduced the magnitude of the ζ–potential, however, the gradient of the linear trend is observed to be lower than shown for both Ca^{2+} and Mg^{2+}. The gradient of the linear trend between ζ–potential and Ca^{2+}/SO_4^{2-} decreases with increasing brine salinity (NaCl), though at Ca^{2+} concentration, the ζ–potential becomes less sensitive to increase in brine salinity. The ζ–potential of natural carbonate was observed to linearly increase as the concentrations of indifferent ions (Na^+ and Cl^-) were increased. It was suggested that the presence of the indifferent ions could change the magnitude, but not the polarity of the ζ–potential [170]. It was shown that diluting seawater and adding SO_4^{2-} to seawater as a way of modifying the injected brine decreases the ζ–potential by double layer expansion and increasing negative charge on the calcite surface, which was correlated to incremental recovery [104].

Kasha *et al.* [168] observed similar trends for the PDIs with ζ–potential during an electrokinetic study on calcite and dolomite particles, though Mg^{2+} had a stronger effect on surface charges compared to Ca^{2+} in high salinity brines and suggested that the point of zero charge of carbonate rocks is not only a function of electrolyte pH but also PDI concentrations. Yousef *et al.* [102] demonstrated that ζ–potential of the rock-brine interface decreases as the brine salinity decreases and suggested that Ca^{2+} ions leave the rock surface in the form of mineral dissolution and enter the brine solution to re-establish chemical equilibrium. Jackson *et al.* [119] correlated improved oil recovery to ζ–potential of rock–brine and oil–brine interfaces using a reservoir limestone core, and different crude oils and brine solutions. The authors concluded that the potential for improved oil recovery by low saline brine injection is increased when both interfaces possess the same polarity (ζ–potential sign), such that the electrostatic repulsive force generated between the interfaces stabilizes the water film on the rock surface. It was suggested that for a negatively charged oil-water interface, diluting the brine salinity to produce a more negative/less positive rock–brine interface would be successful at improving oil recovery. While for a positively charged oil-water interface, increasing the rock–brine interface surface charge by increasing the PDI cation concentration would increase recovery, which would have been responsible for the failure of low saline brine to improve recovery in such cases.

Mahani *et al.* [56] investigated the importance of brine composition, salinity and pH on oil-brine-rock systems on different carbonate rock particles in different brine solutions. They observed positive ζ–potential for formation water, negative for seawater, and more negative for diluted seawater, which increased with increase in pH in the range 6.5 – 11. The low saline brine was influenced by a large shift in ζ–potential with pH because of the presence of fewer concentrations of PDIs compared to the concentration of H^+ and OH^-, which means any changes in later ion concentrations, would strongly impact the EDL and ζ–potential. The changes in rock-brine ζ–potential from positive to more negative was consistent with the observed decrease in contact angle and concluded that these changes are predominantly due to phenomena occurring at the rock–brine interface and to a lesser extent at the oil–brine interface. Meanwhile, the authors further claimed that pH does not directly control the ζ–potential, but rather equilibrium concentration of Ca^{2+}, because of the established relationship between ζ–potential and concentration of Ca^{2+}.

Other experimental evidence such as NMR has been used to test the hypothesis of improved water-wetness by low saline brine injection. Yousef *et al.* [57] performed NMR measurements on reservoir limestone cores, before and after low saline brine treatment, and reported a significant shift in T_2 distribution and surface relaxation by various versions of diluted brines. The influence of pore cleaning was also investigated to solely ascertain the observed shift in T_2 distribution to brine dilution. An improvement in connectivity among macro and micropores as a result of rock dissolution was associated with the observed shift. In contrast, in an NMR experiment conducted with different diluted seawaters, Zahid *et al.* [36] observed no significant changes in surface relaxation and no shift in T_2 distribution.

2.3 Field Application Studies

Promising achievements from laboratory studies have been the background for some pilot scale field trials of brine-dependent recovery process during the past years. The encouraging feature of the systematic experimental studies, as discussed in the previous section, has been reflected in the observations from several near-wellbore tests (like log-inject-log and single well chemical tracer (SWCT)), inter-well scale tests and multi-well field scale, which emphasize on the overall consistency between laboratory and field observations, as summarized in Table 2.2 for sandstone and carbonate reservoirs. However, there are a few field-scale projects in carbonate reservoirs that are reported in the literature. The fractured chalk Ekofisk reservoir, North Sea, has been flooded with seawater since 1987 following a successful waterflood pilot [19, 180]. Over the first three years, oil production steadily increased from 70,000 – 140,000 barrels/day, with an increasing trend and after ten years production level reached 290,000 barrels/day. The significant increase in oil rates has been accompanied by a drop in producing gas-oil ratio (GOR) and reduced water breakthrough [20, 181]. About two-thirds of the increase in production was ascribed to seawater injection response and the recent prognosis estimated recovery to be slightly above 50% of OOIP [18, 51, 134, 181]. The tremendous success recorded till date shows the potential for seawater to improve water-wetness of chalk through spontaneous imbibition and viscous displacement. This positive response seen in Ekofisk stimulated interest to investigate the potential of brine-dependent recovery in the fractured chalk Valhall field, North Sea.

A single injector waterflood pilot test was implemented by early 1990 to evaluate the potential of seawater injection, and its success recommended the feasibility of an economic waterflood scheme. Seawater injection only began in 2006, and the response revealed a varying performance in different parts of the reservoir. Some wells showed no oil production benefit with rapid water breakthrough and increase in water-cut, while others showed an increase in oil production, decrease in GOR and reduced water cut [182, 183]. This regional response was attributed to matrix/fracture dominance on water movement. A systematic study conducted by Webb *et al.* [177] on Valhall core showed that seawater improved water-wetness and oil recovery significantly compared with formation water. A further comparison between both brine-dependent field applications revealed that seawater injection performed less for Valhall as compared to Ekofisk. The difference in performance was ascribed to temperature and wetting conditions, as the wettability alteration process is temperature-dependent. The deeper Ekofisk field reservoir (130 ˚C) has a significantly higher reservoir temperature than Valhall (90 ˚C) [184]. Besides, Ekofisk field is more oil-wet compared to Valhall field as reflected by the acid numbers of their crude oils, about 0.35 and 0.1 mg KOH/g for Valhall and Ekofisk, respectively [51, 184].

The above-listed field projects have majorly explored the ionic composition modification, while the only field application of ionic salinity reduction was reported in Saudi Arabia Upper Jurassic carbonate reservoirs by Yousef and co-workers [24, 31]. Yousef *et al.* [24] reported two field trials with two single well chemical tracer (SWCT) tests using various dilutions of field seawater. The distance of investigation for the SWCT was considered as up to 20 ft. around the wellbore. For well A, a slug of seawater and twice diluted seawater was sequentially injected, while for well B, a slug of seawater, twice diluted and ten-times diluted seawater was sequentially injected and after each injection cycle, three different tracers were injected to estimate the residual oil saturation (ROS). They observed from the two field trials that diluted seawater gave 7% ROS reduction at well A beyond conventional seawater injection. While at well B, 3% reduction in ROS beyond conventional seawater was achieved by twice-diluted seawater and a further 3% reduction beyond twice-diluted seawater was achieved by ten-times diluted seawater injection. They concluded that the total reductions in ROS from well A and B are comparable and the field trials are in agreement with their previous experimental studies [31].

Table 2.2—Summary of successful field implementations of brine-dependent recovery in sandstone and carbonate reservoirs (adapted from Awolayo *et al.* [62])

Authors	Field attributes	Reservoir Temp. (°C)	Formation || Injected brine (ppm)	Benefits
Sandstone reservoirs				
Webb *et al.* [185]	Giant Middle Eastern clastic Clay: <5%	77	220000 || 3000	25 – 50 % ROS reduction
McGuire *et al.* [23]	Alaska North Slope Prudhoe Bay field	66	23000 || 3000	8 % ROS reduction and 18% incremental recovery
	Distance of Investigation: 12.8-13.9ft, 8.5-8.7ft, and 15 ft.	103	7000 || 2200	4 % ROS reduction and 8% incremental recovery
	Endicott Field Clay: 7%	99	28000 || 1500	9 % ROS reduction and 19% incremental recovery
Seccombe *et al.* [186]	Endicott Field	99		
	Clay: 7%		28000 || 1500	9 % ROS reduction
	Clay: 12%		28000 || 10	11 % ROS reduction
	Clay: 14%		28000 || 180	17 % ROS reduction
Lager *et al.* [41]	Alaskan Oil Field		16640 || 2600	2% ROS reduction
Vledder *et al.* [187]	Omar Oil Field (Isba) Clay: 0.5-4%		90000 || 500	10-15 % incremental recovery
Al-Qattan *et al.* [188]	Burgan Oil field (Wara formation) Distance of Investigation: 15ft	54 - 57	148000 || 692	3% ROS reduction
Callegaro, et al. [22, 189]	North African Brown Field Distance of Investigation: 13ft	76	39000 || 1000	5-11 % ROS reduction
Akhmetgareev and Khisamov [190]	Pervomaiskoye		252738 || 848	5-9 % incremental recovery
Carbonate reservoirs				
Austad [134]	Ekofisk reservoir, North Sea	130	68050 || 33498	Ultimate recovery above 50% of OOIP with two-thirds ascribed to seawater injection
Barkved *et al.* [182], Griffin *et al.* [183]	Valhall field, North Sea	90		Increase in oil production, decrease in GOR and reduced water cut
Yousef *et al.* [24]	Saudi Arabia Upper Jurassic	100	57670 || 5767	7 % ROS reduction
			57670 || 28835 || 5767	6 % ROS reduction

2.4 Proposed Underlying Recovery Mechanisms

Considering the huge number of research studies, several physicochemical recovery mechanisms have been proposed, while the majority of the observed trends attributed the primary cause to wettability modification, either to a more water-wetting or mixed wetting state [34, 46, 77, 191] by varying PDIs and/or decreasing injected brine salinity. There is a lack of consensus on the prevalent mechanism responsible for changing the wettability. This is because of the complex nature of the oil-brine-rock interaction, as well as several conflicting observations from various suggested mechanisms. It is quite apparent from these studies that either there are several mechanisms synergistically involved to increase the oil recovery or the right mechanism has not yet been identified. However, the inclination of this research study based on reviewed papers is that the primary cause of improved oil recovery is directly or indirectly linked to the wettability alteration.

2.4.1 Rock dissolution

The rock dissolution theory postulates that reduced concentration of PDIs (such as Ca^{2+}, Mg^{2+} and SO_4^{2-}) in the injected brine compared to the initial high saline brine disturbed the existing equilibrium and causes dissolution of these PDI source-rock minerals like $CaCO_3$, $CaMg(CO_3)_2$ and $CaSO_4$, thereby re-establishing a new equilibrium with the injected brine. During this process, the release of adsorbed polar components accompanies the dissolved minerals, which consequently result in increased water-wetness and improved oil recovery as illustrated in Figure 2.5. This concept was proposed by Hiorth *et al.* [47] through geochemical thermodynamic modelling of various experimental studies (such as spontaneous imbibition and electrokinetic tests, see [32, 50, 54, 55, 192]) on chalk that the surface charge dependence of disjoining pressure could not describe the oil recovery improvement observed in relation to pore water chemistry and temperature. They argued that PDI cations would promote oil wetting because they increased the rock surface charge while SO_4^{2-} did not show the strong temperature-dependence that was observed in many studies. Then, they reiterated that due to the calcite surface being thermodynamically unstable, dissolution occurs, and the amount dissolved correlates linearly with the improved production, particularly when the calcite was preferentially dissolved exactly where the oil wets the calcite. In a study with

limestone cores, Yousef et al. [31, 57] attributed the improved connectivity between micropores and macropores during NMR experiments on low saline brine injection at reservoir conditions to the microscopic dissolution of anhydrite. Austad *et al.* [48] injected sulphate-free diluted brine into limestone cores containing anhydrite and reported an incremental recovery of 5% OOIP. They explained that sulphate was continually generated *in-situ* because of anhydrite dissolution, and this led to the wettability alteration process. Several other experimental studies have ascribed the observed improved recovery in carbonates during low saline brine injection to rock dissolutions of different minerals [27, 36, 49, 61].

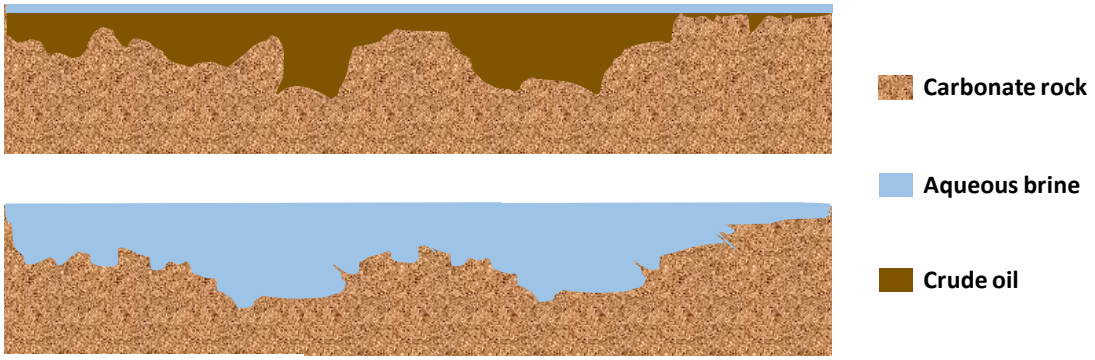

Figure 2.5—An illustration of the proposed mechanism of wettability alteration by "dissolution" showing an oil-wetting state with oil attachment before dissolution (*top*) and the water-wetting state after dissolution (*bottom*). (adapted from Hiorth *et al.* [47])

Austad *et al.* [193] strongly opposed the calcite dissolution mechanism proposed by Hiorth *et al.* [47] by questioning the applicability of the geochemical model to calculate the chemical equilibrium between calcite and seawater and the corresponding compositions at the considered temperature range. It was argued that calcite dissolution is contradictory to published experimental results, where it was discussed that an increase in aqueous Ca^{2+} increases oil recovery and will suppress chalk dissolution due to common ion effect, which means that decreased dissolution increases oil recovery, and then at high temperature, there is no increase in oil recovery with increased dissolution. Furthermore, it was argued that wettability alteration does not depend on the bulk mineral dissolution due to buffering of aqueous solution and equilibration at field-scale. This implied mineral dissolution is not considered to be contributing at a reservoir scale, hence ranked as a secondary cause [56, 120, 194, 195]. Despite these studies, Awolayo *et al.* [159] claimed, by using a geochemical model to predict performance history of low saline brine injection

into different rock minerals, that the interplay between mineral dissolution and surface charge alteration is vital to the improved recovery, and their relative contribution depends on brine composition, mineral constituents, and temperature. Aqueous pH was also reported to be controlled by the interaction between injected brine and minerals present, majorly the resultant effect of mineral dissolution and precipitation. The authors concluded that mineral dissolution/precipitation could not be exempted in modelling low saline brine injection at both core and field scale as it affects the concentrations of the PDIs available to adsorb.

2.4.2 Multi-ion exchange (MIE)

The pristine structure of carbonate mineral surfaces is composed of metal ions (such as Ca^{2+}, Mg^{2+}, etc.) coordinated to oxygen atoms from carbon atoms (such as CO_3^{2-}). Because of the reactive nature of the carbonate mineral surface, the surface is hydrated by the dissociation of chemisorbed water molecules resulting in a surface composed of hydroxylated cationic sites and protonated anionic sites, which are stabilized by the dissociated hydroxyl ions (OH^-) and protons (H^+) respectively. The stabilization of the surface site depends on the brine composition as well as the pH. At pH below 6-8, the excess H^+ ions and probable dissolution will make the positively charged cationic sites dominate and the overall surface positively charged. Meanwhile at a high enough pH, excess OH^- ions will change the surface to more negative charge. In representative reservoir conditions, carbonate rock surface is positively charged in the pH range (6.5 – 7.5) of the surrounding high saline formation brine (consisting low concentration of negatively charged ions like CO_3^{2-} and SO_4^{2-} and high amount of positively charged Ca^{2+}) while the polar components of oil have a predominantly negative surface charge, resulting in a high bonding energy between polar carboxylic materials and carbonates [53]. The adsorption of the negatively charged carboxylic component of crude oil onto the mineral surface causes a change in the rock wettability (preferentially oil/mixed-wet).

Under the influence of modified brine with more PDIs, SO_4^{2-} competes with the polar component, and adsorb onto the carbonate rock surface, lowering the rock surface charge. This creates an electrostatic repulsion and causes the bond between the rock-brine interface and oil-brine interface to rupture. Then, Ca^{2+} ions are co-adsorbed to the rock surface and its excess concentration at the

site bind to the negatively charged carboxylic groups in oil and release the oil in the form of Ca^{2+}-carboxylate complexes, resulting in improved water-wetness and oil recovery (Figure 2.6). This mechanism is analogous to the MIE described by Lager *et al.* [111] for sandstone reservoirs, except for sandstone rocks, the organic material or organo-metallic complexes that are attached to the clay minerals in the presence of divalent cations in high saline formation brine, are removed and replaced during injection of low saline brine by cationic ion exchange of un-complexed cations at the clay surface. The MIE was first proposed by Austad and colleagues [32, 33, 44, 50, 51, 52, 53, 54, 55] in different carbonate rocks and several others have presented evidence to support this mechanism [27, 28]. As discussed earlier, the temperature seems to influence the activity of these PDIs. At higher temperature (above 100C), Mg^{2+} has higher activity and could substitute Ca^{2+} at the rock surface and cause the oil to be released as Ca^{2+}-complexes. This mechanism has also been linked with rock dissolution as sufficient SO_4^{2-} is produced by dissolution of anhydrite while Mg^{2+} is produced by dolomite dissolution. Similarly, this mechanism is somewhat related to DLE as will be discussed below.

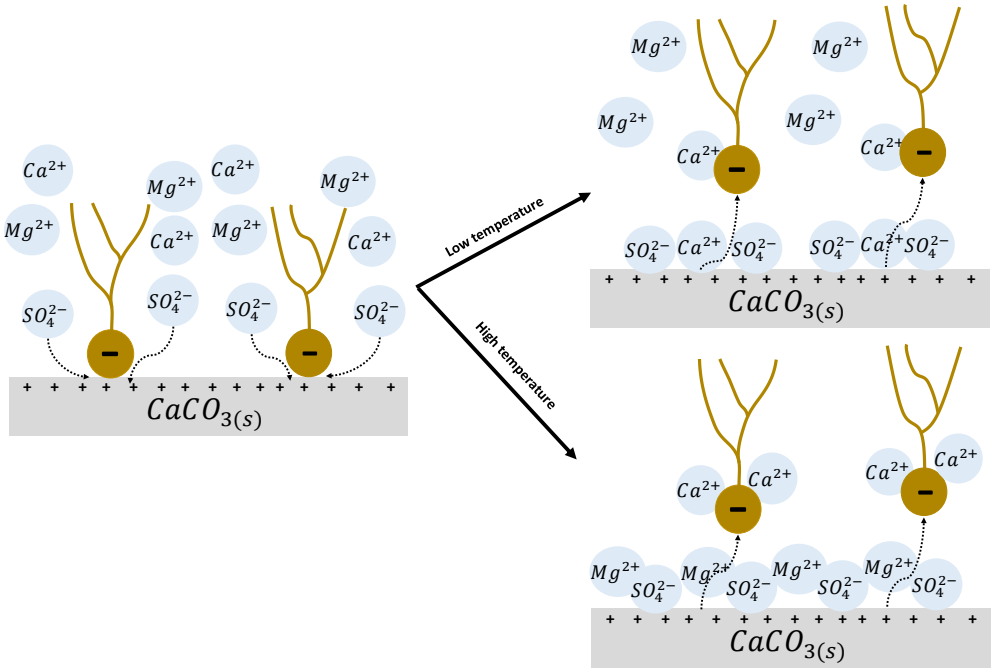

Figure 2.6—A schematic illustration of the proposed mechanism of wettability alteration by "MIE" in carbonate reservoirs showing the oil component displacement from the carbonate rock surface through PDIs competition. Original state (*left*), Low temperature state (*right upper*) and High temperature state above 100 °C (*left lower*) (adapted from Zhang *et al.* [32])

2.4.3 Electrical double layer expansion (DLE)

Electrostatic interaction is considered because the rock, brines, and crude oil, all contain charged ions and based on Derjaguin–Landau–Verwey–Overbeek (DLVO) theory, the electrostatic interactions acting on the oil-brine-rock system, comprising of the rock-brine and oil-brine interfaces, leads to the development of the EDL. The concept of electrical double layer expansion (DLE) was first suggested by Ligthelm *et al.* [99] in sandstone reservoirs as they argued that MIE was a secondary cause that decreases ionic strength and valence rather than a primary cause to wettability alteration. EDL expansion increases the electrostatic repulsion between rock-brine and oil-brine interfaces, resulting in higher and/or positive disjoining pressure, creating a thicker and more stable water film layer and resulting in more water-wet conditions (see Figure 2.7). Many authors describe this as "surface charge alteration" mechanism, which involves altering the rock surface charge to create more electrostatic repulsive forces between the two interfaces and alter rock wettability toward water-wetness [29, 31, 120, 159, 196]. Monovalent ions consisting of Na^+ and Cl^- have been considered as non-reactive towards the rock surface, which implies that they do not partake in the interaction at the carbonate surface within the Stern layer but are very sensitive in the outer diffuse layer, and they might regulate the admittance of the PDIs onto the rock surface [38, 112, 167].

At the initial reservoir conditions, the high saline formation brine contains relatively lower PDIs compared to the high concentration of NaCl, which implies that the initial positive charge at the rock-brine interface is maintained and much of Na^+ and Cl^- are retained at the diffuse layer. This arrangement will hinder the PDIs from interacting with the surface of the rock and electrostatic attraction (low/negative disjoining pressure) between the two interfaces and thinning of the water film layer. A significant change to the water chemistry will create much better access through the double layer and enable the PDIs to attach specifically in the Stern layer or via the intermolecular coordination of water molecules, altering the surface charge at the interface. NaCl-depleted brine has been shown to reduce the concentration of non-active ions in this layer so that the PDIs could enter easily to the surface (Figure 2.7). In this context, the rock-surface charge is reduced or even reversed towards negative from its initial condition of positive charge [128, 197]. Such interaction

can release adsorbed oil acidic components from the surface sites because of the more stable water film layer that is developed due to a lesser attraction (higher disjoining pressure) between the two interfaces. This logic was first proposed in chalk by Fathi and colleagues [38, 167] and later in limestone rocks [39, 112].

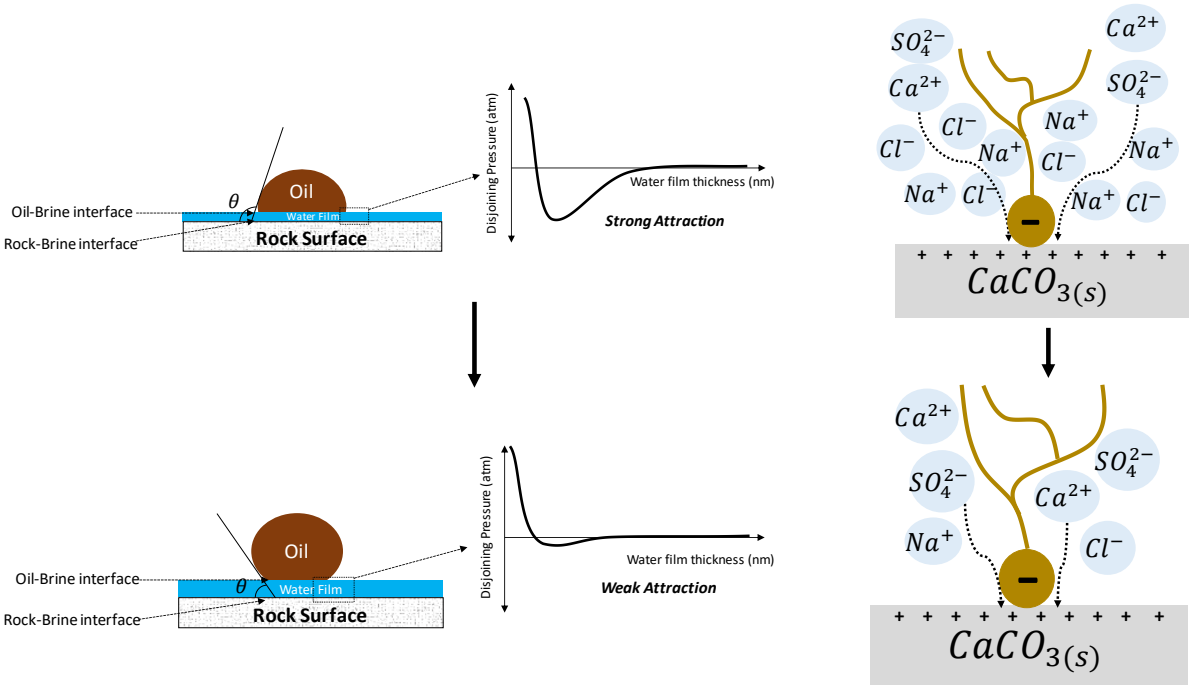

Figure 2.7—An illustration of the proposed mechanism for wettability alteration by "DLE" in oil-brine-carbonate rock system with DLVO disjoining pressure showing transition from an oil wetting state (left *upper*) with crowded double layer-filled non-active ions (*right upper*) to water wetting state (*left lower*) with double-layer depleted non-active ions (*right lower*) (reproduced from Fathi *et al.* [38], Awolayo *et al.* [65])

In addition, Yousef *et al.* [57] associated wettability changes to surface charge alteration in combination with rock dissolution through electrokinetic and NMR analysis. NMR showed fast surface relaxation and ζ–potential shifted towards more negative with a successive dilution of seawater. Alroudhan *et al.* [104] also observed a shift towards more negative when injected brine was diluted or SO_4^{2-} was added to the injected brine. They confirmed that both cases could improve oil recovery by altering the surface charge and expanding the EDL. Similarly, Mahani *et al.* [56] conducted ζ–potential and contact angle measurements on different carbonate rocks and stated that the observed wettability changes and improved recovery are primarily driven by surface-charge alteration due to electrostatic interactions between crude oil and rock. Moreover, the phenomena

are predominantly occurring at the rock-brine interface. In place of sorption of SO_4^{2-} to the rock surface, Brady and Thyne [198] suggested, based on work of Goldberg and Forster [199] that maximum boron sorption to calcite occurs at a pH of 9.5, that BO_4^{3-} can coordinate with calcite positive surface site [$>CaOH_2^+$], locally decrease the charge to decrease oil adhesion through an electrostatic attraction bridge and thicken the water film layer. In the same way, PO_4^{3-} can also link and reduce oil adhesion, which was observed by Sø *et al.* [200]. At relatively low concentrations, PO_4^{3-} can electrostatically sorb to calcite surfaces to convert the positively charged surface sites into neutral/negative, whereas at high concentrations, it can precipitate as calcium phosphate. These studies further acknowledge the improved recovery observed and water wetness using PO_4^{3-} and BO_4^{3-} by various researchers and their likelihood to precipitate at higher concentrations [42, 58, 61].

2.5 Modeling of Brine-Dependent Recovery

Reliable optimization of any recovery process requires the availability of a predictive tool, which is a necessity to understand completely the principal mechanisms driving the recovery process. For such a tool to be developed to simulate the recovery process, the mechanisms at play need to be well grasped. However, despite various inconsistencies in the process mechanisms, several attempts have been made to model this process and outlined below are the relevant works done thus far. The phenomena of fluid flow during the brine-dependent recovery process are often mathematically described by a partial differential equation (PDE) or a system of several PDEs, with associated boundary and initial conditions. The PDE describing process can be solved either analytically or numerically. Majorly, the PDE solution is linked to the observed improved recovery by considering the influence of capillary forces as a driver for wettability alteration, particularly, an increase in flow oil functions (e.g. relative permeability, capillary pressure and residual oil saturation and a corresponding decrease in water flow functions, are used to calculate the flow of each phase. Here, the methodologies and application of analytical and numerical approaches that are often made in modeling the brine-dependent recovery process in sandstone and carbonate reservoirs are summarized.

2.5.1 Analytical approach

Most of the recent modeling efforts have attempted capturing the brine-dependent recovery process through numerical approximations, and as far as one can tell from the literature, very few studies have explored the application of analytical solutions. The reason is because analytical solutions are often applied to many practical problems of fluid flow, with certain simplifying conditions, involving insufficient experimental data that could justify the use of a numerical model. Besides, analytical solutions can guide in the design of experiments and benchmark the numerical models. In addition, the practical advantage of analytical solutions lies in the fact that they offer quick estimation, improve interpretations and are useful in conducting sensitivity analysis and computations of different displacement behavior for different injection brine salinity and compositions.

Lemon *et al.* [201] captured the fine migration effects and permeability reduction by providing a simple analytical induced-fines migration model to justify improved oil production associated with low saline brine injection. The authors implemented a modified particle-detachment model, which considered maximum retention function as related to the ratio of detaching and attaching torques, into the quasi-2D Dietz model for waterflooding in a layered-cake reservoir and was validated using single flow laboratory coreflooding experiments. They suggested that fines migration effects on oil recovery are more pronounced with increased viscosity ratio and reservoir heterogeneity. Zeinijahromi *et al.* [72] opined that this model considered single-phase environment with mobilization caused by an increase in flow velocity and extended the model to capture 3D modeling of fines-assisted waterflooding by introducing two-phase flow equations with fines lifting and migration in the aqueous phase and fines size-exclusion. The fines lifting are caused by water salinity changes and the alterations in particle equilibrium by changes in both fluid velocity and salinity were captured, resulting in the reduction of relative permeability to water. The model typically involved integrating fines migration and permeability reduction into a two-phase black-oil model and was used to model fines-assisted waterflooding in two heterogeneous formations. It was highlighted that induced-fines migration was more effective in improving sweep efficiency for large-scale heterogeneity with highly correlated flow paths. This model has been applied to

interpreting and predicting fines-assisted waterflooding in many oil fields (such as Pervomaiskoye, Zichebashskoe, and Bastrykskoye fields) in Russia [190, 202, 203]. On the other hand, Borazjani *et al.* [76] extended this model by simultaneously accounting for wettability alteration and fines mobilization, migration, and straining, solved by using splitting procedure for hyperbolic systems. It was proposed that wettability alteration reduces residual oil and increased oil displacement from the swept area, while induced-fines migration with permeability reduction in the swept area decreased water flux and diverts the injected brine to unswept zones. The collective effects were observed to improve oil recovery much more than their individual effects.

Venkatraman *et al.* [71] used the hyperbolic theory of conservation laws to develop analytical solutions to the Riemann problem to explain the displacement process observed during fluid flow and cation exchange reactions between flowing aqueous phase and solid sandstone phase. The analytical solutions were used to predict effluent profiles of specific cases of three heterovalent cations (Na^+, Ca^{2+} and Mg^{2+}) and an anion (Cl^-) for any constant initial and injection brine composition by using mass equilibrium action laws, charge conservation equation and the cation exchange capacity equation. The number and nature of shocks or rarefaction waves in the displacement as well as when they occur was predicted to a reasonable accuracy, which becomes increasingly complex as the number of cations in the system increases. The theoretical predictions compared well with experimental data available at both the laboratory scale and the field scale and showed reasonable agreement with numerical model predictions, developed using finite differences. Awolayo and Sarma [75] derived an analytical expression based on the advection-reaction-dispersion equation (ARDE) theory for 1-D single-phase flow, which considered linear adsorption (retardation) to capture changes between ions in the aqueous phase and stationary solid phase in terms of sorption and surface complexation reactions. The model was used to replicate histories of effluent ions from single-phase experiments and the reactivity of PDIs towards carbonate rock surface was emphasized. The authors also predicted the breakthrough composition of different ions during oil-brine displacement experiments and stated that the wettability change was observed with high retardation for PDIs, which resulted in improved oil recovery. Various researchers have created a theoretical model based on the DLVO theory of surface forces to estimate the rock surface wettability through the stability of the water film layer separating the

rock and oil phase. The theoretical model evaluates the stability of the film by calculating disjoining pressure isotherm and interaction potential that influences the water film thickness and the energy barrier needed to be overcome to rupture the water film [65, 121, 176, 178, 204, 205, 206, 207]. Alshakhs and Kovscek [178] further estimated contact angle from the disjoining pressure and compared with that from contact angle measurements.

2.5.2 Numerical approach

As discussed above, analytical solutions are often difficult to obtain because of several complexities that might be encountered during many practical applications of fluid flow in porous media. The shapes of the reservoir boundaries might be irregular, the dependent variables in the governing equations, initial and boundary conditions might be space-variant and non-uniformly distributed, while the sink/source term in the governing equations might be a non-analytic function. Hence, the numerical technique provides a convenient, flexible, and sophisticated tool for solving fluid flow problems in complex realistic situations as it is the case for brine-dependent recovery, which combines multiple mechanisms. These mechanisms include processes such as convection, advection, diffusion/dispersion, sorption (adsorption/ion-exchange), surface complexation, mineral reactions, zero/first order production, and decay. The widely used numerical modeling method for brine-dependent recovery is based on black-oil and compositional reservoir simulation with or without coupling either of these two types of models: the surface sorption models (SSMs) and surface complexation models (SCMs). The SSM captures sorption reactions like adsorption, ion-exchange, where the electrical interaction is integrated into the equilibrium constants for the reactions and SCM captures similar surface reactions, except the sorption process depends on the interaction surface charges that are simultaneously calculated with the surface species.

2.5.2.1 Sandstone rocks.

Jerauld *et al.* [68] made the earliest attempt to model brine-dependent recovery process in sandstone reservoir through the adoption of the existing waterflood model. They implemented the fractional flow theory to describe the process and treated salt as a single-lumped component in the aqueous phase. The relative permeability and capillary pressure were considered a function of

salinity, such that wettability alteration was initiated through interpolation between the two relative permeability and capillary pressure sets (one at water-wet and the other at oil-wet set) within the salinity thresholds. The residual oil saturation was also made a linear function of salinity, which is used in calculating the interpolating parameter as expressed in the eqs. 2.1 – 2.4. They were successful in simulating coreflood experiments as well as other single-well tests.

$$k_{rl} = \omega {k_{rl}}^{HS}(S_{wn}) + (1-\omega){k_{rl}}^{LS}(S_{wn}) \tag{2.1}$$

$$P_{cow} = \omega {P_{cow}}^{HS}(S_{wn}) + (1-\omega){P_{cow}}^{LS}(S_{wn}) \tag{2.2}$$

$$\omega = \frac{S_{or} - {S_{or}}^{LS}}{{S_{or}}^{HS} - {S_{or}}^{LS}} \tag{2.3}$$

$$S_{wn} = \frac{S_w - S_{wi}}{1 - S_{or} - S_{wi}} \tag{2.4}$$

where k_{rl} is the relative permeability to phase l, n is an exponent, which has a value of 0 for current set, HS for high salinity set and LS for low salinity set, ω is the interpolation parameter, S_{wn} is the normalized water saturation, P_{cow} is the oil-water capillary pressure, S_{or} is the residual oil saturation to waterflood, S_w is the water saturation and S_{wi} is the irreducible water saturation. Tripathi and Mohanty [208] extended Jerauld *et al.* [68]'s work to studying the flow instability related to wettability alteration using a 1-D Buckley-Leveret analytical model excluding the effect of capillary pressure. They identified two saturation shocks for the considered low saline waterflood case, one of which was associated with adverse mobility. This was supported by viscous fingering theory and 2-D numerical simulation.

Wu and Bai [78] tried to model the process in both porous and fractured reservoirs. They treated salt as a pseudo component in the aqueous phase, which was subjected to advection and diffusion, as well as adsorption on the mineral surface. Similar to Jerauld *et al.* [68], their model expressed the dependency of relative permeability, capillary pressure and residual oil saturation on salinity. The residual oil saturation and contact angle were interpolated between two sets of residual oil saturation and contact angle data using the total salt concentration, which was used to evaluate only the oil relative permeability and capillary pressure respectively eq. 2.1 and 2.2. They simulated a hypothetical case to compare the low saline waterflood with conventional waterflood.

Al-adasani *et al.* [77] extended Wu and Bai [78]'s work by generating different correlations for residual oil saturation, contact angle and IFT as a function of salt concentration. These correlations were used to evaluate the oil relative permeability, water relative permeability, and capillary pressure. They successfully simulated a series of experimental data and concluded that the increase in oil relative permeability because of wettability change was the core element of the modeling approach. However, at weakly water-wet conditions, improved recovery is controlled by low capillary pressure.

Omekeh *et al.* [43] were the first to construct a more comprehensive model that takes into consideration the geochemical interpretation of low saline waterflood process in sandstones. They formulated a Buckley-Leveret two-phase model that accounted for MIE as the sole explanation for wettability alteration. The MIE was expressed using Gapon convention where cations are involved in a fast exchange process with the negative clay surface (eq. 2.5). They proposed modeling the transition between two relative permeability sets by using a weighting function which considered the amount of divalent cations (Ca^{2+} and Mg^{2+}) desorbed from the mineral surface. The model was successfully used to do several sensitivity checks on Berea sandstone cores using brines with different ion compositions. They observed the sensitivity of the desorption fronts speed to the injected brine composition and oil recovery to the composition of the formation water relative to the injected brine composition. They later coupled mineral dissolution into the model [69]. They obtained a good agreement between the model and experimental recovery and effluent concentration from a reported North Sea coreflood experiment.

$$1/2\, Ca^{2+} + Na - X \rightleftarrows Na^{+} + Ca_{1/2} - X \qquad (2.5)$$

$$1/2\, Mg^{2+} + Na - X \rightleftarrows Na^{+} + Mg_{1/2} - X$$

Similarly, Dang *et al.* [66] used CMG GEM^{TM}, a compositional simulator of Computer Modeling Group, to simulate low saline brine injection in sandstones by constructing a comprehensive multi-phase multi-component geochemical model. In their work, the multi-ion exchange was expressed using Gaines–Thomas convention as highlighted in eq. 2.6. They modeled the transition between the two-relative permeability sets as a function of equivalent Ca^{2+} fraction on the mineral surface, which was contrary to Omekeh *et al.* [43]'s viewpoint with regards to recovery mechanism in

sandstones. However, wettability alteration was captured as they successfully simulated coreflood experiments conducted on cores from the North Sea and Texas reservoirs [40, 209]. They validated the model by obtaining good agreement between experimental and model effluent ion concentrations, effluent pH and recovery. Besides, they extended the model to capture the combination of brine-dependent recovery and CO_2 flood [83]. They observed that such combination is a very promising recovery technique that promoted the synergy between the two processes in ensuring the capillary force is fully captured via wettability and IFT alteration.

$$Na^{+} + 1/2\, Ca - X_2 \rightleftarrows 1/2\, Ca^{2+} + Na - X \tag{2.6}$$
$$Na^{2+} + 1/2\, Mg - X_2 \rightleftarrows 1/2\, Mg^{2+} + Na - X$$

Korrani *et al.* [82] coupled a geochemical package and compositional simulator to obtain an integrated tool in UTCOMP-IPHREEQC capable of executing a geochemical-based modeling of complex processes like low saline brine injection, alkaline-surfactant-polymer (ASP) flooding and formation damage with sensitivity to hydrocarbon interactions. They modeled the transition from oil-wet to the water-wet region by considering different interpolation parameters, like total ionic strength and ion exchange through organometallic components surface complexation. The model was then used in matching histories of produced ions as well as the oil recovery of coreflood experiments and the Endicott field trial conducted by BP [41].

Brady and colleagues [206, 210, 211] constructed a batch SCM for sandstones having two surface charge sites; namely, clay edge and basal plane. Meanwhile, the charges at these sites are controlled by pH-dependent protonation/deprotonation reactions at the clay edge and heterovalent substitution in the lattice of the basal plane. Four electrostatic attraction bridges were identified as important in modifying rock wettability. At pH<5.5, [>Al:SiO^{-}↔$^{+}$HN<] and [>AlOH$_2^{+}$↔$^{-}$OOC<] attraction bridges are dominant while at higher pH, [>Al:SiO^{-}↔$^{+}$CaOOC<] attraction bridge dominates while [>Al:SiOCa^{+}↔$^{-}$OOC<] attraction bridge only important at pH>8. The authors showed that low Ca^{2+} injected brine, and low saline brine can both decrease [>Al:SiO^{-}↔$^{+}$CaOOC<] attraction bridge at higher pH and explained that at low acid numbers, low saline brine can decrease , [>Al:SiO^{-}↔$^{+}$HN<] and [>AlOH$_2^{+}$↔$^{-}$OOC<] attraction bridges, resulting in improved recovery [210]. It was also identified that, for kaolinite-containing

sandstones, an increase in Ca^{2+} will decrease oil adhesion by filling the exchange basal plane sites Ca^{2+} and increase oil adhesion by increasing [$^{+}$CaOOC<] species at the kaolinite edge site. They revealed that the ratio of edge to basal plane exposure is critical to determining the mechanism of oil adhesion to kaolinite-containing sandstones [211]. The bond product sum (BPS) of oil interaction with kaolinite edge, which is the sum of the four electrostatic attraction bridges, was also suggested to be a simple means to estimate mutual electrostatic adhesion between the surface charges of oil and kaolinite edge sites [206]. The BPS would equal to zero with no likelihood of electrostatic adhesion when both oil and mineral surfaces only contain negatively charged species, resulting in water-wetness. While the BPS would be high when both oil and mineral surfaces contain oppositely charged species and the potential for electrostatic adhesion would be high. This logic was used to interpret why the Snorre field (BN = 1.1 and AN = 0.02 mg KOH/g oil) showed very little positive response to low saline brine [35].

Elakneswaran *et al.* [212] further extend Brady's work by coupling SCMs and mineral dissolution/precipitation and showed that mineral equilibrium showed a notable positive effect on oil desorption and improved oil recovery. They also emphasized that pH, Ca^{2+} and Mg^{2+} significantly influenced electrostatic interaction at both rock-brine and oil-brine interfaces and oil desorption increased with the dilution of injected brines. Erzuah *et al.* [213] compares BPS from Brady *et al.* [206]'s SCMs work with flotation techniques in the presence of high saline formation brine and showed that the presence of divalent cations increased oil adhesion through cation bridging to kaolinite and quartz surfaces, reflected by the high BPS through [>Al:SiO^{-}↔$^{+}$CaOOC<] and [>Al:SiO^{-}↔$^{+}$MgOOC<] bridges, and high concentration of oil-wet particles from flotation tests. In addition, Lima *et al.* [214] developed a pore-scale model by coupling SCM with the generalized Poisson-Boltzmann equation to compute local disjoining pressures and contact angle and their dependence on brine salinity and pH. The contact angle was then incorporated in Brook Corey's formula to obtain the relative permeability functions for various low saline brine injection scenarios. Meanwhile, Korrani and Jerauld [215] showed that BPS failed to predict wettability change as instead of decreasing, it increased as wettability moves towards more water-wet state, and suggested that stability number (a dimensionless group defined

as the ratio of electrostatic to van der Waals force) gave a better prediction of coreflood experiments and the Endicott field trial conducted by BP [41].

2.5.2.2 Carbonate rocks.

Similar to modeling attempts in sandstones, there have been quite a few modeling studies conducted on carbonate rocks. Hiorth *et al.* [47] were the first to attempt to develop a model to better understand the published experimental results, especially in chalk formations. They coupled bulk aqueous, SCM with two sites ($>Ca^+$ and $>CO_3^-$) and mineral reactions in a geochemical model, calculated the surface speciation, charge, and potential with temperature and tried to calculate the water film stability and oil wettability, the result of which was compared with spontaneous imbibition experiments on Stevns Klint outcrop chalk. They found that the negatively charged surface promotes water-wetness, while the positively charged surface promotes oil-wetness. They reported that the experimental observation could not be fully explained by surface potential changes and only calcite dissolution could account for the improved recovery. They concluded that the unstable equilibrium that resulted in calcite dissolution has a strong dependence on temperature and pH conditions.

Yu *et al.* [80] presented a 1-D two-phase model to simulate a waterflood spontaneous imbibition tests conducted on core plugs from Stevns Klint Chalk formation. They considered a wettability alteration [WA] agent (sulfate ions) as the second component in the aqueous phase, which was used along with the adsorption isotherm to imitate the transition between the two-relative permeability and capillary pressure sets representing the oil-wetting and water-wetting state. The model accounted for molecular diffusion, capillary force, gravity and adsorption. However, it did not capture the influence of WA agent adsorption on rock permeability and porosity. A reasonable match was achieved between the model and experimental results. They emphasized dynamic and fixed wettability alteration, with the dynamic alteration depending on the salt concentration to capture the gradual transition period and gave a better match.

Evje *et al.* [216] constructed a 1-D model to describe water-rock interactions by coupling convection-diffusion equations with geochemical (equilibrium and non-equilibrium) reaction

equations relevant for chalk weakening effects essential to carbonate reservoirs. The model's result agreed with experimental profiles for measured effluent concentrations when a solution of $MgCl_2$ was injected into a chalk core initially saturated with pure water at an elevated temperature of 130 °C. Mineral non-equilibrium reactions in the form of $MgCO_3$ precipitation and $CaCO_3$ dissolution were the main components of the water-rock interactions used in matching. Similarly, Evje and Hiorth [67] proposed a 1-D mathematical two-phase model coupled with geochemical reaction equations for a modified brine-flood spontaneous imbibition (SI) experiment conducted on chalk core plugs. Dynamic wettability alteration was introduced by using changes in mineral composition as interpolating parameters between two sets of flow functions relating to oil-wet and water-wet conditions. The effects of varying temperature, sulfate and magnesium ion concentrations observed in SI experiments by Zhang *et al.* [32] were simulated, but not reproduced. They envisaged that mineral dissolution detaches the oil attached to oil-wet sites and gradually shifts rock wetness in a water-wet direction, which favors improved oil mobilization.

Andersen *et al.* [64] extended the model developed for chalk by accounting for transport effects like advection, dispersion, soluble hydrocarbon components, aqueous complexation, cation exchange and mineral alteration. The geochemical model was used to reproduce the measured effluent of flooding experiments performed at 130 °C. In another work, Andersen and Evje [81] developed a two-phase geochemical model to interpret possible chemical mechanisms responsible for brine-dependent oil recovery observed in the variation of sulfate and calcium ions at 70 °C in chalk formation [32, 55]. They incorporated ion exchange processes that accounted for sulfate adsorption to the free site at the surface and modeled the transition from oil-wet tothe water-wet region by considering different interpolation parameters like sulfate adsorption, calcite dissolution and anhydrite precipitation. A similar weighting function as used by Evje *et al.* [216] was used for the transition between the sets of flow functions representing oil-wet and water-wet curves, except that adsorption of sulfate was incorporated to increase CEC. They concluded that only sulfate adsorption, coupled with surface calcium activity, was responsible for the observed experimental results at 70 °C.

Al-Shalabi *et al.* [217] developed a two-phase flow model using UTCHEM, chemical compositional flow simulator developed at The University of Texas at Austin, to study the mechanisms responsible for brine dilution in carbonate reservoirs through data matching. They attempted to simulate the injection of seawater and its different dilutions in experimental studies conducted by Yousef *et al.* [31]. They used different scaling parameters to account for wettability alteration by interpolating between the two sets of relative permeabilities and residual oil saturation. They concluded that simulation was quite sensitive to the transition between the two sets of oil flow functions. In another work, Al-Shalabi *et al.* [63] used an empirical correlation between contact angle and salinity as the interpolating parameter to tune residual oil saturation and reported that contact angles gave a better option. Then curve fitting using the contact angle was used to obtain the oil relative permeability and Corey exponent. The model was used to obtain a good match on coreflood experiments [27, 102].

Al-Shalabi *et al.* [79] built a geochemical model using Gibbs free energy to correlate residual oil saturation and oil flow function and compared results from UTCHEM and PHREEQC (a geochemical module from the United States Geological Survey) to emphasize the effect of the activity coefficient. The same experimental studies were matched with emphasis on the dominant mechanism for wettability alteration as surface charge alteration and anhydrite dissolution [218]. However, it is essential to state that empirical correlation is only valid under the given experimental conditions and non-predictive under different conditions. Korrani *et al.* [219] also extended the usage of their integrated UTCOMP-IPHREEQC to simulate observations made during brine dilution experiments by Chandrasekhar and Mohanty [27]. The authors used the amount of calcite dissolved as the transition between oil and water-wet flow functions coupled with implicitly included surface complexation reactions. The model gave a good match of oil recovery, pH and breakthrough curves and emphasized that calcite dissolution and surface reactions are mandatory to capture improved oil recovery. Nevertheless, there was high computation time due to the coupled simulator.

Brady and colleagues [198, 211] constructed another batch SCM for carbonates and stated that the carbonate surface charge is largely controlled by sorption of Ca^{2+} and CO_3^{2-}, rather than pH. The

authors used the calculated surface speciation to consider individual coordination between calcite and oil at 25−130 °C. They identified several possible electrostatic attraction bridges. The strongest oil-calcite attraction bridge at reservoir pH is considered as [$>CaOH_2^+ \leftrightarrow {}^-OOC<$], which could be reduced by increasing Ca^{2+} and/or Mg^{2+} to reverse the charge of [$<COO^-$] specie, and/or increasing SO_4^{2-} to coordinate with [$>CaOH_2^+$] and eliminate the positive charge to produce a negative surface. The model was used to predict the injection of various versions of diluted brines used in the experimental study by Yousef *et al.* [31] on limestone rocks. The authors claimed that the decreased salinity decreased the oil-calcite BPS, which resulted in reduced oil adhesion and increased oil recovery; however diminishing returns was observed beyond ten times dilution.

Qiao *et al.* [70] developed a multiphase multicomponent reactive transport model that captured the SCMs of surface reactions among carboxylic groups, cations, and sulfate. The model was used to interpret the oil recovery from the spontaneous imbibition experiments conducted on chalk by using brine with selective removal of non-active ions [38]. The water-wetting fractions, controlled by the proportion of the carboxylic group desorbed from the surface sites, were used as the interpolating parameter to transit between the two sets of capillary pressure, relative permeability, and residual oil saturations. The model showed good consistency with experimental observations, and through sensitivity studies, they concluded that ion species, ionic strength and parameters, like oil acidity, reaction equilibrium constants, total surface sites and diffusion coefficient, play such a key role in the wettability alteration mechanisms. They extended the model by including limestone mineral dissolution/precipitation reactions [84]. Here, the interpolation was carried out using surface concentrations of desorbed carboxylic acid. They introduced changes in surface potential in the equilibrium constant calculations. The model was consistent with experimental observations using brine dilution approach on limestone [31, 48, 53] and chalk outcrop [38].

Mahani *et al.* [120] developed a batch SCM to elucidate and correlate ζ-potential results under varying brine salinity (synthetic seawater, with 25 and 100 times dilution) and pH conditions. They made changes to the reaction of SO_4^- with the calcite sites to match the ζ-potential results and observed that ζ-potential increased with pH, which was caused by the formation of surface species coordinating with the PDIs. Brine dilution was observed to lead to more negative surface charge

due to the resultant effect of an increase in the concentration of negatively charged species, decrease in positively charged species concentration and formation of neutral species. As the surface charge is modified, the wetting condition is influenced towards improved water-wetness. Eftekhari *et al.* [220] developed an SCM reactive transport model to derive the reaction equilibrium constant for natural carbonates by using a non-linear optimization technique to fit the model with ζ-potential and single-phase breakthrough curves data on intact chalk cores. The authors used the tuned model to suggest a correlation existing between the remaining oil in several chalk imbibition tests and [$>CaOH_2^+ \leftrightarrow {}^-OOC<$], which was estimated with equilibrium constants analogous to aqueous acid-base reactions.

Awolayo *et al.* [65] developed a reactive transport model considering adsorption and ion exchange and obtained temperature-dependent equilibrium constants for the two reactions by fitting with the single-phase breakthrough curves of different ions, temperature and intact carbonate minerals. The optimized model was used to simulate oil recovery and breakthrough curves from different experiments. In another study, the contribution of dissolution and precipitation of different minerals as they contribute to the distribution of PDIs available for surface sorption were captured and simulated. The fraction of the free surface sites that could adhere to oil was observed to reduce as the brine salinity reduced and sulfate concentration in injected water increased, which was used to transit between two sets of flow functions [159, 207].

2.6 Injection Water Issues and Remediation

In most published literature, it is evident that the properties of the formation fluids vary depending on different parameters, including mineral diagenesis, its pressure and temperature history and the other complex alterations experienced as reservoir fluid flow and mix over geological time [221]. As a result, typical formation water is highly saline and enriched in divalent ions. Sandstone formation water often contains an abundance of Ba^{2+} and Sr^{2+} cations, while carbonate and calcite-cemented sandstone formations usually contain a substantial amount of Ca^{2+} and Mg^{2+} cations [222]. Seawater is also rich in ions (higher SO_4^{2-} than in formation fluids) that form from marine sediments and water evaporation. These two fluids are the major sources of water injected (diluted seawater or formation water) during brine-dependent recovery, and the mixing of both

incompatible fluids can result in precipitation/scaling. The precipitate/scale arises when the natural state of the reservoir fluid system is disturbed to the extent that the solubility limits of some of its components are exceeded. As such, calcium sulfate (anhydrite) precipitates in carbonate and calcite-cemented sandstone formations [223], while barium sulfate (barite) and strontium sulfate (Celestine) precipitates can be readily formed in sandstone formations.

The scale precipitation of these minerals has a complicated dependency on variables like temperature and pressure; for instance, calcium carbonate scales, the most common oil field scale, precipitate because of pressure changes while sodium chloride (halite) scale forms similarly from highly saline brines encountering large temperature drops. The scale formed at near-wellbore region or in the reservoir cause plugging/flow restrictions, resulting in a porosity and permeability reduction and could reduce the waterflood scheme effectiveness, when formed close to an injection well. Those formed at near-wellbore are easily removed through acidizing while those formed in the formation are difficult to remove. Meanwhile, scales formed in the production tubing lower the production rate by reducing the flowing area and increasing the pipe surface roughness [222]. Romanuka *et al.* [101] proposed that injecting brine, with a high concentration of surface-interacting ions (like SO_4^{2-}, PO_4^{3-}, and BO_3^{3-}) into a formation containing divalent cations such as Ba^{2+} and Sr^{2+}, will increase the tendency for scale precipitation in the production lines, at near-wellbore region or in the reservoir.

Another major issue is the presence of sulfate-reducing bacteria (SRB), which feeds on sulfate sources to oxidize organic materials to hydrogen sulfide (H_2S) in the form of anaerobic respiration. The produced H_2S is highly toxic and corrosive, which can cause severe handling and safety problems in oilfield operations at a very low concentration. The H_2S is also slightly soluble in both oil and water phase that can turn sweet oil into sour oil, which is expensive to refine. Fine migration and mechanic compaction are other issues encountered during brine-dependent recovery, which are because of weakened rock structure. Clay swelling has been reported to be associated with brine dependent recovery in sandstone reservoir, which resulted in fines production and/or reduction in permeability or increase in pressure drop. Meanwhile, mechanical compaction has been mostly observed in chalk reservoirs, which is because of reduced mechanical strength of the

chalk. The weakening of chalk is caused by the replacement of Ca^{2+} at the biogenic chalk surface by Mg^{2+} in the injected water through chemical substitution at elevated temperatures. After water breakthrough, another environmental issue might be the content of the produced water, which will include an added cost for treating the water. The produced water from reservoir undergoing brine dependent recovery process will contain a low concentration of PDIs because of their adsorption to the rock. Hence, injecting an appropriate mixture of this produced water and freshly prepared-injection water has been proposed to also trigger wettability alteration and better recovery [224].

Even though preceding issues exist, success reported in various brine dependent recovery projects conducted in many fields (notably Alaska and the North Sea) for years did not report much encounter with precipitation/scaling, souring and fines production, except compaction which was prevalent in North Sea Chalk reservoirs. Various authors have highlighted optimum sulfate concentration to avoid precipitation of sulfate scales. Furthermore, in any waterflood project, the choice of water treatment method is a key factor that significantly affects project success. Treatment and reinjection of produced brine have been reported to be possibly cheaper than its transportation and disposal [225, 226, 227]. Desalination is the water treatment process readily used to remove selected dissolved ions in water to provide safe drinking water and treated injection water for improving oil recovery. There are two main methods for water treatment/desalination: thermal-based, which involves heating the feed water and collecting the condensed vapor from the distillation column and membrane-based, which involves applying pressure to force the water feed through the member, thereby leaving the selective salts. Membrane-based methods are often preferred over the thermal methods due to space limitation and energy requirements [228]. The two widely used membrane-based desalination methods are nanofiltration (NF) and reverse osmosis (RO), which is often used as either standalone or hybrid configuration. During the nanofiltration process, the divalent ions are selectively removed, decreasing water hardness, and leading to monovalent-ion rich effluent water (permeate stream), and divalent ion-rich rejected water (retentate stream). Meanwhile, in the reverse osmosis process, both monovalent and divalent ions are selectively removed to reduce the permeate stream water salinity. Essentially the permeate stream water from RO is fresh with negligible amounts of salt, and this is possible because RO has a much tighter pore size than NF.

Several published patents [229, 230, 231, 232, 233] have been proposed that the desired water quality can be generated through the blending of the effluent permeate streams from the different NF/RO application (standalone, hybrid configuration either parallel or series and plurality) schemes to satisfy brine-dependent recovery requirements in sandstone reservoirs. As such, Yousef and Ayirala [234] proposed a desalination optimization technique based on a parallel configuration of NF/RO that blends both the permeate and retentate water streams to cover the entire range of ionic salinity and composition appropriate for both sandstone and carbonate rocks, which also considered the minimization/prevention of clay swelling, reservoir souring, corrosion and aerobic bacterial issues. The authors emphasized that the availability of these multiple water streams provides the flexibility of customizing the desired ionic content and salinity not just for brine-dependent recovery process but also as a good pre-conditioner for combining with other EOR applications such as miscible gas flood, carbonated waterflood, polymer flood, ASP flood, and as boiler feed water in thermal floods.

Meanwhile, Ayirala and Yousef [235] recently reviewed different chemical extraction and desalination technologies and reported that current desalination technology has limitations to treat high saline water and produced water. They claimed that no current proven commercial technology could selectively remove specific ions in one step to optimally meet the desired water requirement, but a combination of all current technologies. Forward osmosis and membrane distillation are reported to offer cost-effective potential alternatives to reverse osmosis with the availability of low-grade waste heat and well suited to treat very high salinity water. Dynamic vapour recompression and Carrier-Gas extraction are identified as well suited to treat high saline water, and hyper-saline produced water from oil and gas production for zero liquid discharge. This is critically important in locations where disposal facilities are not available, which can become an effective water management strategy during field implementation by converting the produced water into the desired water quality for reinjection. However, the two technologies are reportedly not cost-effective for water desalination, and their footprints and energy requirements are not well defined as they are still in the development stage. The comparison of the features and capability of all current and emerging water desalination technology are given in Table 2.3.

Table 2.3—Summary of technology selection criteria, key attributes and capabilities of both current and emerging water treatment technologies (adapted from Ayirala and Yousef [235])

Water treatment process	Desalination Methods	Technology Maturity	Selective ion removal	Treatment Capability		Comparable features
				High saline water	Produced water	
Nanofiltration	Membrane-based	High	Yes	No	No	• water recovery efficiency of 90-99%: • More open pores leading to higher flux: • Low operation pressure and energy consumption over RO
Reverse Osmosis	Membrane-based	High	No	No	No	• Minimal footprint and energy requirement: • cost effective as its widely used with water recovery efficiency greater than 99%
Chemical Precipitation	Pretreatment	Medium - High	Yes	No	No	• Remove scaling and fouling in desalination pre-treatment • Upfront chemical costs and additional facility requirements for sludge handling and disposal
Salt Extraction	Pretreatment	Low	Maybe	Yes	Maybe	• No scaling and lower energy requirements: • details on cost and chemical solvents not well known
Forward Osmosis	Membrane-based	Low - Medium	No	Yes	Yes	• Lower energy requirements: • cost-effective compared to widely-used desalination method: • can treat high-saline water:
Membrane Distillation	Combo Membrane & thermal based	Medium	No	Yes	No	• Cost-effective compared to widely-used desalination method: • can treat high-saline water: • low-grade waste heat requirements
Carrier-Gas Extraction	Humidification / Dehumidification	Medium	No	Yes	Yes	• Provide zero liquid discharge solution up to 85-90% water recoveries: • treating both high saline water and produced water: • non-cost-effective compared to widely-used desalination method: • footprints and energy requirements not well-defined:
Dynamic Vapor Recompression	Thermal-based	Medium	Maybe	Yes	Yes	• Minimal pre-treatment and no scaling: • provide zero liquid discharge solution up to 97% water recoveries: • treating both high saline water and produced water: • non-cost-effective compared to widely-used desalination method: • costs, footprints and energy requirements not well-defined

2.7 Chapter Summary

This Chapter presents a comprehensive review of the systematic investigation of brine-dependent recovery through all level of investigations of oil-brine-rock systems. The discussion covers how different techniques have been exploited to interpret and predict the process efficiency while highlighting various contradictions posed. From laboratory and field-scale studies, brine-dependent recovery has resulted in substantial improvement in recovery, though the magnitude observed at field scale is minimal compared to that observed in laboratory experiments. It takes less injection water volume to achieve considerably incremental recovery in field scale than in the laboratory, which makes the application of the process more enticing. The improvement in recovery was shown to vary depending on brine content (connate and injected), rock mineralogy, oil type and structure, and temperature. Wettability alteration is widely accepted as the consequence of the brine-dependent recovery process, while no consensus exists on the probable cause/mechanism, which might be due to experiments conducted and reported at varying conditions. Despite these challenges, analytical and numerical models have been utilized to further interpret and predict the process performance.

Based on this review, it can be inferred that the injected brine should contain PDIs, depleted in NaCl, and wettability alteration is much more effective at high temperatures. There is however a limit to which increasing the SO_4^{2-} concentration with increasing temperature can improve oil recovery; as high SO_4^{2-} concentrations at a high temperature can result in $CaSO_4$ precipitation and oil recovery reduction. Aside chalk cores, SO_4^{2-} and Mg^{2+} can be generated *in-situ* due to the dissolution of anhydrite and dolomite leading to improved oil recovery, which depends on the injected brine content and reservoir rock temperature. The concentration of these PDIs in the formation water is also critical to observing improved oil recovery, which implies that the concentration of PDIs plays a more significant role, compared to brine salinity reduction. Overall, the composition of the formation water needs to be critically examined before designing the injected brine content to prevent chances of reservoir/wellbore damage and maximize oil production.

The effect of different minerals on the performance of brine-dependent recovery has been well investigated in carbonate rocks with high degree of repeatability and the observed trend is that presence of different kind of minerals helps the two approaches of ionic strength, and composition modification performs better through the *in-situ* generation of PDIs. Improving on the development of the analytical models can be quite difficult, because of the complexity of the process mechanisms. The bulk of the numerical black-oil models used salinity-dependent flow functions, while some of the compositional models used empirical correlations. Meanwhile, the complex interaction can be well represented by the using surface sorption and complexation geochemical models, which allows the investigation of rock mineralogical contents, brine compositions and polar oil materials, which are significant in electrostatic interactions at both rock−brine and oil−brine interfaces. However, if DLE is to be accepted as the cause of wettability alteration, then SCM would be the ultimate approach at generating a numerical model to predict the process performance at all level of investigation. Another area for further investigation will be to obtain thermodynamic parameters describing the surface sorption, and complexation models for natural rocks, instead of the current practise of applying aqueous thermodynamic parameters. It is also critical that the premise through which wettability alteration occur as reflected by the interpolation parameters used in the simulation is identified with a high confidence level before being considered in modeling to avoid contradictions.

Finally, brine-dependent recovery is relatively inexpensive and environmentally friendly, particularly with various emerging cost-effective water treatment technologies. It has more advantage than other chemical EOR methods in terms of operating costs, field implementation and environmental assessment, even though it might recover comparably less additional oil. Meanwhile, modification of the injected brine composition (like adding more PDIs) can be more expensive than brine dilution. The recovery benefits from both approaches can further outweigh any potential damages that could be caused to the reservoir or near-wellbore region. Additionally, low saline brine can serve as pre-conditioner for other EOR methods, as most of the injected chemical/gas performs better under low saline brine.

Chapter 3 Surface Forces and Water Film Prediction

This Chapter proposed that the geochemical interactions acting between the two interacting interfaces (rock−brine and oil−brine) in a three-phase system launch various intermolecular forces that govern the rock surface wettability. Therefore, a theoretical DLVO model was utilized to discuss the significance of the nature and magnitude of interaction force and energy between the interacting interfaces on rock wettability condition. The measured ζ–potentials at respective brine concentrations and pH, from individually-sourced experiments, were used as model inputs.

3.1 Introduction

A major thrust in various research efforts on brine–dependent recovery has been to tweak and optimize the brine chemistry that delivers more effective and efficient oil-brine-rock interactions leading to improved oil recovery. The effectiveness of the recovery process is mostly governed by the composition of flowing fluids in the porous media and the mass transfer between such flowing (aqueous/oleic) fluids and the immobile (rock) phase. To date, a significant volume of research studies has been conducted to resolve pending arguments about the applicability of the process in sandstones; however, research on carbonates reservoirs still lies in its emerging phase [44, 62]. Results from most experimental studies in carbonate rocks (for example, displacement tests, spontaneous imbibition, contact angle, NMR, ζ–potential, effluent analysis tests) point to the ability of the process to shift rock wettability towards water wetness as the principal fundamental mechanism.

However, there appears to be no unanimity as to how the wettability alteration occurs, and hence, this remains a gray area and needs to be studied. A review of mechanisms that influence wettability changes has been presented in Chapter 2, including electrostatic interactions between rock-brine and oil-brine interfaces, multi-ion exchanges between surface PDIs, rock mineral alteration in terms of dissolution/precipitation, complexation between oil phase components, multivalent ions and rock surface [7, 30, 32, 48, 56, 57, 236]. It is important to note that the magnitude of the forces existing between reservoir fluids (with their dissolved constituents) and the rock surface often controls wettability. Hence, the wettability changes can only be fully understood by considering a

detailed account of the intermolecular interactions between fluids in contact with the rock surfaces [237].

Moreover, many of these mechanisms combine to launch various interfacial phenomena occurring concurrently during fluid flow in porous rock. These phenomena involve intermolecular forces acting on the oil-brine-rock system, which is composed of rock-brine and oil-brine interfaces interacting through the water film layer. A significant feature of these interfaces is the electrical charge separation that occurs at the interface, and this plays a decisive role in the stability of the water film. The probable origin of the electrical charge separation at the interface could be due to either or a combination of the following: surface functional groups ionization, specific/preferential adsorption/desorption of ions, isomorphic substitution at the crystal lattice, and electron accumulation/depletion. Meanwhile, at the interface between a charged surface and an electrolyte solution, an electrical potential is developed such that the surface charge is neutralized via columbic interaction with oppositely charged ions (counter-ions) attracted to the surface from the adjacent solution. Subsequently, layers of ions are developed separating the charged surface from the bulk solution in a special arrangement known as the electrical double layer (EDL; shown in Figure 3.1).

The first region next to the charged surface is the Stern layer with a typical thickness of 1 nm; the counter-ions are specifically attached in the inner Stern layer defined by the inner Helmholtz plane (IHP). The hydrated counter-ions that do not specifically attach are in the outer Stern layer (also defined by outer Helmholtz plane – OHP). The second layer, known as the diffuse layer, contains ions of the same sign (co-ions) and counter-ions that are loosely associated with the surface and move freely under the influence of thermal motion and electric attraction [130, 170, 238, 239]. The diffuse layer has a thickness between 1 to 500 nm depending on the surface charge and the ionic strength of the aqueous solution. The ions in this layer are present to ensure electrical neutrality of the EDL, at any circumstances that the Stern layer failed to neutralize the surface charge. The diffuse layer extends from the OHP to a point where ions in the bulk electrolyte solution do not feel the electric attraction, and the thickness of this diffuse layer is termed Debye length (κ^{-1}). The shear or slipping plane, to which measured ζ–potentials are attributed, are often displaced by

a distance Δ from the OHP into the diffuse layer [240]. This specific distance is unknown and generally used as an adjustable parameter to fit ζ–potential data, within 0.245 - l nm has been reported [104, 197, 241, 242]. The distribution of ions in the region displaced by the distance Δ in the diffuse layer (see region I in Figure 3.1) is not influenced by tangential stress arising from bulk fluid flow while ions in the second region (see region II in Figure 3.1) of the diffuse layer are distributed based on fthe low of the bulk fluid.

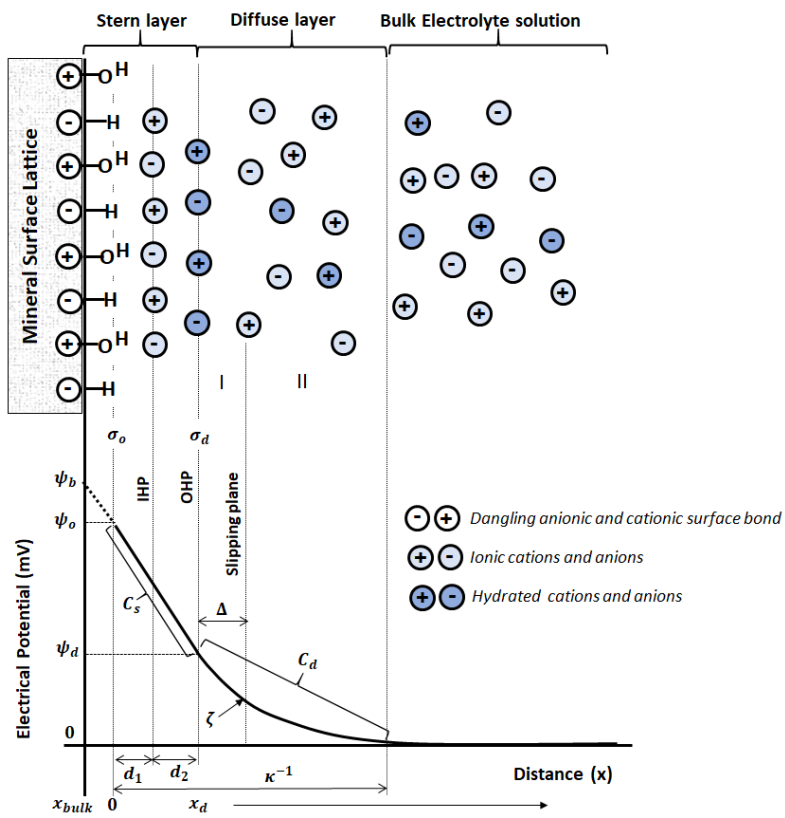

Figure 3.1—Schematic illustration of the EDL and electrical potential at the rock–brine interface: The sketch shows the variation of electrical potential as a function of distance from the rock surface, partitioned by charged planes— inner Helmholtz plane (IHP), outer Helmholtz plane (OHP) and slipping plane. The potential developed within the EDL declines with distance linearly through the Stern layer, exponentially through the diffuse layer and drops to zero in the bulk electrolyte solution. The partial charge on the dangling surface ions left behind at the bulk solid is represented by ψ_b; ψ_o represents the potential of the surface; ψ_d stands for the potential at the Stern layer and ζ represents zeta potential. While σ_o and σ_d are the surface and diffuse layer charge density (C/m^2) respectively. The Stern layer potential difference is characterized by constant capacitance, C_s while the diffuse layer has variable capacitance, C_d. At plane $x = 0$, which corresponds to the hydrolysis layer, H and OH of the water molecules are chemibonded to the dangling surface ions. At $x < 0$, the potential is so high that attaching ions do not bond to the surface ions. The inner-Stern layer is characterized by d_1 length; the outer-Stern layer is characterized by d_2 length, and the electrical double layer is characterized by κ^{-1} length, also known as Debye-Hückel screening length [130, 170].

3.2 Theory of Water Film Stability

When two interfaces approach and interact with each other, the distance separating them is considered to influence the energy of the oil-brine-rock system and as a result, the stability of the water-film layer between the interfaces. These interactions are mostly dictated by the resultant effect of the intermolecular forces considered as disjoining pressure. The disjoining pressure is the system Gibbs free energy change per unit area with a corresponding change in distance, which is also a measure of the force that separates the cross-sectional area of the two interfaces. Typically, a low or negative disjoining pressure will attract the two interfaces, destabilize and eventually weaken the water-film layer to cause polar components in the oil to interact directly with the rock and reverse the wettability towards oil-wetness, as in Figure 3.2. On the contrary, a high or positive disjoining pressure would indicate an energy barrier that would be too high for the interface to overcome (Figure 3.2), thereby thickening the water-film layer [130, 243]. Then, the water film becomes stable and the rock surface water-wet. The wettability shift towards water-wetness observed during brine-dependent recovery can then be associated with maintaining a stable water-film by increasing the disjoining pressure between the interfaces.

The three main force components of the disjoining pressure are Van der Waals, structural and electrostatic as described by the DLVO theory. This theory was mainly introduced to evaluate the stability of the colloid system to withstand aggregation due to the net contribution of attractive van der Waals forces and repulsive electrostatic forces generated by ions in the vicinity of charged colloidal surface in an electrolyte solution. The theory has been further extended to describe the stability of wetting film in the oil-brine-rock system (Buckley et al., 1989 and Hirasaki, 1991). The summation of the three surface forces is expressed as total disjoining pressure of the water film layer. These forces have diverse impacts at short (very close to molecular contact, <1 nm) and long (less than 100 nm) separation distances [130, 243]. Schematic representation of the disjoining pressure isotherm in an oil-brine-rock system is shown in Figure 3.2 as a function of the water-film thickness. Here, both van der Waals and electrostatic forces account for interactions among counter-ions, the charged surface and the ions beyond the OHP, whereas, structural forces account for the orientation of the charged surface within the hydrolysis layer (see Figure 3.1).

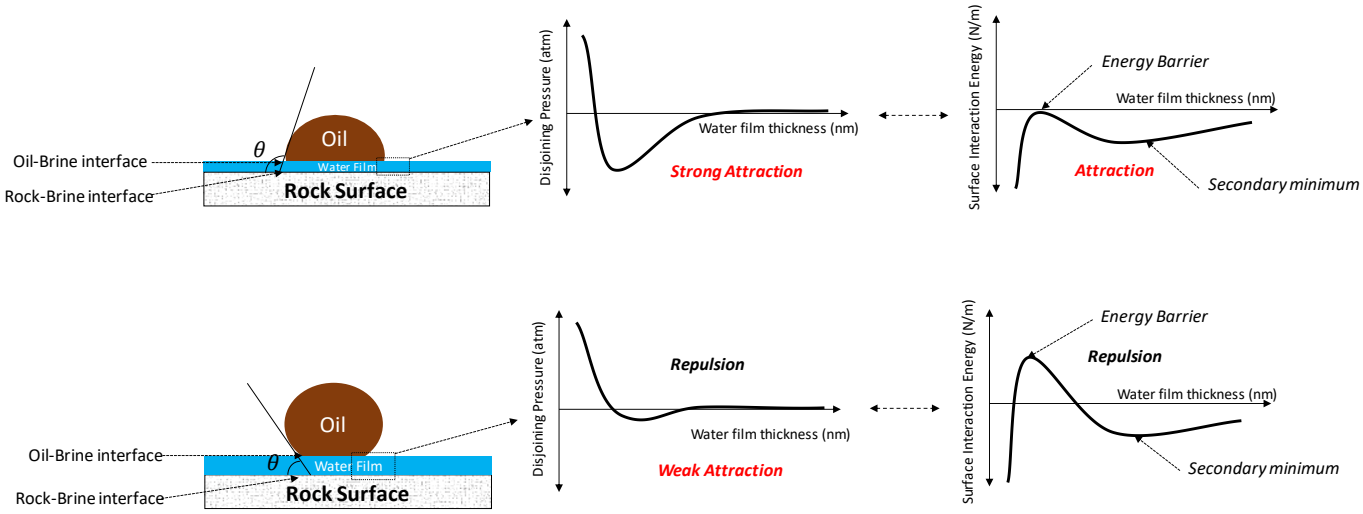

Figure 3.2—Schematic of Oil-Brine-Rock system at different wettability conditions: oil-wetting (*top*) and water-wetting (*bottom*) states. Interfaces exhibit a very strong repulsion (Born repulsion) upon contact; the surface interaction energy curve shows two potential minima: a deep primary minimum appearing at a small separation distance and a shallow secondary minimum appearing at a larger separation distance.

The Van der Waals force components are always present to describe the interactions between all atoms and molecules and are central in all phenomena involving intermolecular forces at small and large separations. Their contribution to disjoining pressure may be repulsive or attractive as dictated by Hamaker constant. Hamaker constants are experimentally obtained or theoretically calculated from dielectric constants, refractive indices and absorption frequencies of the interacting medium [243]. Generally, van der Waals forces are usually attractive because of positive Hamaker constant as the dielectric constant and refractive index of the intervening medium (water) are generally higher and lower respectively than those of the interacting media (oil and rock), respectively. When the dielectric properties of the intervening medium are intermediate between that for the two interacting media, the Hamaker constant will be negative, resulting in repulsion, which will act to thicken the water film to raise its energy barrier [130, 243].

The electrostatic force components are effectively long ranged because electrostatic interaction is weaker near to the charged surface in a polar medium due to the high dielectric constant and the electro-neutrality requirement. They are rather stronger in the diffuse layer beyond the OHP as a result of two different additional forces exerted by the excess counter-ions in the double layer, creating an electrical potential gradient within the EDL. The additional osmotic pressure is exerted

towards the charged surface and in the opposite direction acting outwardly from the charged surface is the other force, known as Maxwell's stress [130, 243]. The double layer forces are repulsive when both interfaces have the same sign, which is beneficial to a stable water film layer, and it is attractive when both have opposite signs, leading to a thin water film layer. In this context, the rock-brine interface is positively charged while the oil-brine interface is negatively charged. The consequence of this opposite charge is the development of an attractive double layer forces between the two interfaces, which drift towards bringing the two interfaces together and the formation of a thin water film layer. At this stage, the water film layer ruptures such that oil directly contacts the rock surface [244].

The structural force components are short-range forces induced by the intermolecular coordination of water molecules near the molecular contact of the rock-brine interface. Likewise, counterions are often attached to the charged surface in fully-hydrated, partially-hydrated, or dehydrated state, depending on their location in the Stern layer [130, 243]. Cations and anions, in aqueous solution, can have several water molecules orientationally bound to them, and the hydrated radius of cations is higher than that of anions with the same valency. Typical ions in pore water of petroleum reservoir rocks with their respective radii are given in Table 3.1. The water molecules often order themselves at the surface charge forming the hydrolysis plane in the Stern layer. X-ray reflectivity data presented by Geissbühler *et al.* [245] shows a laterally ordering of the water layer adsorbed to calcite surface. This type of molecular ordering creates hydration forces resulting in the formation of a thin water film layer, which limits water film thickness from complete rupture. Most often, the repulsive structural and electrostatic force tends to counterbalance the very attractive van der Waals force.

Table 3.1—Approximate characteristic radii of ions in water [130, 246]

Ions	**Na^+**	**K^+**	**Ca^{2+}**	**Mg^{2+}**	**Al^{3+}**	**Cl^-**	**OH^-**	**SO_4^{2-}**	**PO_4^{3-}**
Ionic radius (nm)	0.095	0.133	0.099	0.065	0.050	0.181	0.176	0.290	0.223
Hydrated radius (nm)	0.358	0.331	0.412	0.428	0.480	0.332	0.300	0.379	0.339

3.3 Interaction Force and Energy Calculations

The three main contributors to the total disjoining pressure acting between the two interfaces are London van der Waals, electrostatic, and structural forces. Figure 3.3 shows a comparison between the three forces as a function of the water film thickness. A brief introduction of these force components has been presented earlier, and their calculation procedures are presented below through the DLVO theory. As earlier mentioned, the stability of the wetting film on the rock and competition among oil and brine to wet the rock surface is strongly governed by the force balance present among non-wetting and wetting phase, and the rock surface. Hence, the net interaction force can be expressed as:

$$\prod(h) = \prod_V(h) + \prod_D(h) + \prod_S(h) \tag{3.1}$$

where $\prod$, $\prod_V$, $\prod_S$, $\prod_D$ and h are the disjoining pressure of the intermolecular interactions, London–van der Waals forces, structural forces, electrical double-layer forces, and the separation distance (signifying water film thickness) between the two interfaces respectively. The contribution from the van der Waals force between two parallel bodies is calculated using a simple approximation based on Lifshitz theory as given below:

$$\prod_V(h) = -\frac{A}{6\pi h^3} \tag{3.2}$$

where A is the Hamaker constant of the oil-brine-rock system. However, van der Waals interaction can be lessened owing to retardation caused when the separation distance existing between these interfaces becomes comparable with the London frequency electromagnetic wavelength during the time of propagation [247] . Hence, the retarded van der Waals force is expressed as:

$$\prod_V(h) = -\frac{A}{12\pi h^3}\left(\frac{3b\frac{h}{\lambda_c} + 2}{\left(1 + b\frac{h}{\lambda_c}\right)^2}\right) \tag{3.3}$$

where λ_c is the interaction characteristic wavelength (often assumed as 100 nm [247]) and b is the correction constant to the non-retarded Hamaker expression (a fitting value of 5.32 is often used [247]). Meanwhile, the Hamaker constant can be calculated as by assuming pairwise summation and geometric mean interactions:

$$A = [A_s{}^{1/2} - A_w{}^{1/2}][A_o{}^{1/2} - A_w{}^{1/2}] \tag{3.4}$$

where subscripts s, w and o indicate Hamaker constant for single component pairs of calcite, water and oil in vacuum. Using values of A_s, A_w, and A_o of 0.101, 0.037 and 0.06 aJ (attojoules) respectively [130, 248], eq. 3.4 yielded Hamaker constant of 0.0066 aJ for the oil-brine-rock system interactions. The comparison between the retarded (solid blue line) and non-retarded (dashed blue line) van der Waals attractive force is shown in Figure 3.3, the reduced interaction was not very significant, notwithstanding retarded van der Waals attractive force expression was used in the rest of the interacting force and energy calculations in this study.

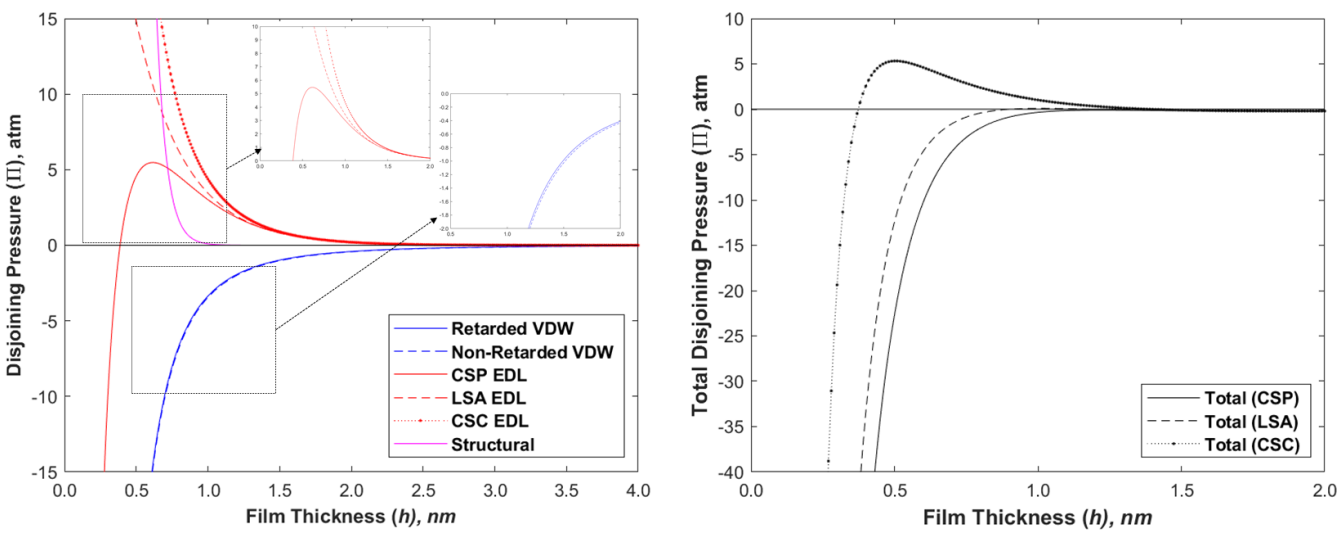

Figure 3.3—Individual contributions from van der Waals, electrical double layer and structural force (*left*) to the total disjoining pressure (*right*) as a function of the thickness of the water film layer for the oil-brine-rock system (seawater, composition listed in Table 3.2). The positive half of the disjoining pressure represents the repulsive force required to separate two interacting interfaces, which is dominated by electrical double layer and structural force; while the negative half represent the attraction dominated by van der Waals. Dotted line is for CSC, dashed line for LSA and solid line for CSP; while, dashed blue line is for non-retarded van der Waals force. Unit conversion 1 atm = 101.325 kPa.

The contribution from electrostatic forces can be obtained from the solution to the nonlinear Poisson-Boltzmann equation (PBE), which is quite complicated, involving elliptical integrals and requires numerical solutions. The general one-dimensional form of the PBE is expressed as:

$$\frac{d^2\psi}{dh^2} = -\frac{e}{\varepsilon\varepsilon_0}\sum_{i=1}^{N} z_i n_i \, e^{-\frac{z_i e \psi}{k_B T}} \tag{3.5}$$

where ψ is the electrostatic potential (mV), e is the electronic charge (1.602×10^{-19} C), ε is the water dielectric constant (temperature-dependent correlation by [249]), ε_0 is the free space permittivity (8.854×10^{-12} C^2/J.m), k_B is the Boltzmann constant (1.381×10^{-23} J/K), T is the absolute temperature (K), z_i and n_i are the *i-th* ionic mobile species valence and bulk concentration and the summation term sums up all concentration of cations and anions around the charged surface. However, it is more convenient to use approximate analytical solutions of the linearized PBE rather than the complicated numerical approaches, especially for low surface potentials ($|\psi_r| \ll 1$). These solutions are easily obtained for different boundary conditions — the constant surface potential (CSP) or the constant surface charge (CSC) as presented by eq. 3.6. At smaller separation distance, CSP underestimates while CSC overestimates the interactions between the interfaces due to charge regulation when the interacting interfaces approach each other. Generally, neither the potential nor charge remain constant as the two interfaces approach each other and this forces the true exact solution to lie somewhere between both solution limits [130, 250].

$$\prod_D(h) = nk_BT\left(\frac{2\psi_{r1}\psi_{r2}\cosh\kappa h \pm [\psi_{r1}^2 + \psi_{r2}^2]}{\sinh^2\kappa h}\right) \tag{3.6}$$

where ψ_{r1} and ψ_{r2} are the reduced surface potential for the rock-brine and oil-brine interfaces respectively, (i.e. $\psi_r = e\psi_o/k_BT$), κ is the Debye-Hückel reciprocal length (estimated as $\kappa = \sqrt{2000e^2n/\varepsilon\varepsilon_0k_BT}$), ψ_o is the surface potential (mV), n is the ionic density in the aqueous solution ($n = N_AI$), where N_A is the Avogadro's number (6.022×10^{23} /mol.) and I is the ionic strength (mol/kg water, also referred to as M) of the aqueous solution. While the plus sign in eq. 3.6 applies for CSC and the minus sign applies for CSP. On the other hand, linear superposition approximation (LSA) is the widely used asymptotic form for high surface potential cases, which holds irrespective of the type of boundary conditions (either CSP or CSC) on the interacting surfaces and gives intermediate results between CSP and CSC at smaller separation distances. Meanwhile, at large separation distances, all interactions merge and are well described by the three solutions as shown in Figure 3.3.

$$\prod_D(h) = 64nk_BT\gamma_1\gamma_2e^{-\kappa h} \tag{3.7}$$

where $\gamma = tanh\left(\frac{\psi_r}{4}\right)$. The last contribution to disjoining pressure is estimated from structural interaction, which has been found to decay exponentially as:

$$\prod_S(h) = A_o e^{-\frac{h}{d_o}} \tag{3.8}$$

where A_o and d_o are the magnitude and decay length for the structural interaction. This interaction has been extensively studied for only mica and, silica surfaces and those of calcite surfaces are not known. Meanwhile, a sharply rising model of magnitude 148038 atm and decay length of 0.05 nm [243] was assumed to estimate the structural force presented in Figure 3.3. The disjoining pressure contribution from van der Waals and structural forces are always considered fixed because they are insensitive to variations in brine salinity, composition, and solution pH [130]. However, in this current study, the contribution from structural force to the disjoining pressure was considered zero (i.e., $\prod_S(h) = 0$) for all pH values and brine concentrations. The total disjoining pressure for all the three cases of electrostatic interaction with retarded van der Waals attractive force is presented in Figure 3.3 for seawater brine concentration The LSA expression is seen to give intermediate results between those of CSP and CSC.

Table 3.2—Compositions of the brines used in the interaction force and energy calculations consisting of synthetic formation brine (FB) and natural Arabian Gulf seawater (SW), with their various versions.

Ions (M)	**FB**	**SW**	**SW/2**	**SW/10**	**SW/20**	**SW2S**	**SW3S**	**SW4S**
Na^+	2.0066	0.5660	0.2830	0.0566	0.0283	0.6320	0.6980	0.7640
Ca^{2+}	0.4200	0.0120	0.0060	0.0012	0.0006	0.0120	0.0120	0.0120
Mg^{2+}	0.0700	0.0500	0.045	0.045	0.045	0.0500	0.0500	0.0500
HCO_3^-	0	0	0	0	0	0	0	0
Cl^-	2.9800	0.6240	0.3120	0.0624	0.0312	0.6240	0.6240	0.6240
SO_4^{2-}	0.0033	0.0330	0.0165	0.0033	0.0016	0.0660	0.0990	0.1320
TDS (g/L)	170.63	40.001	20.000	4.0001	2.0000	44.688	49.375	54.062
Ionic Strength	3.4799	0.7850	0.3925	0.0785	0.0393	0.8840	0.9830	1.0820
pH	7.15	8	8	8	8	8	8	8

The various dilutions of seawater considered are twice diluted seawater (SW/2), ten times diluted seawater (SW/10), and twenty times diluted seawater (SW/20). The concentration of SO_4^{2-} was also varied in the seawater, SW2S implies seawater with twice SO_4^{2-}, SW3S implies seawater with thrice SO_4^{2-} and SW4S implies seawater with quadruple SO_4^{2-}. Sources: Data retrieved from Alroudhan *et al.* [104].

On the other hand, the interaction energy per unit area can be obtained by taking integration of interacting force (disjoining pressure) with respect to film thickness in the direction normal to that of the interacting interfaces [250]. The resulting equation can be used to estimate the energy barrier needed to achieve a thicker water film or the stability of the water film layer. As shown in Figure 3.2, similar to the surface interaction energy generated as a result of interacting force plays a vital role in determining the stability of the water film layer, hence rock wettability. The main components are the van der Waals energy of attraction (ω_A) and double layer energy of repulsion (ω_R). Depending on the surface potential of the interfaces and brine concentration, ω_R can dominate over ω_A, thereby creating a potential energy barrier. When the magnitude of this barrier height is large enough as compared to the thermal energy of the interacting interfaces, the interfaces are not able to overcome the barrier and, no overlapping can be achieved. However, when ω_A surpasses ω_R as a result of double layer contraction, the interfaces can overlap to fall into the primary minimum by van der Waals energy, resulting in oil-wetness.

$$\omega(h) = \omega_A(h) + \omega_R(h) = \int_{\infty}^{h} -\prod_V(h)\, dh + \int_{\infty}^{h} -\prod_V(h)\, dh \tag{3.9}$$

The retarded van der Waals interacting surface energy per unit area between two interfaces separated by distance h can be calculated as:

$$\omega_A(h) = -\frac{A}{12\pi h^2}\left(\frac{1}{1 + b\frac{h}{\lambda_c}}\right) \tag{3.10}$$

While for double layer energy of repulsion, it can be expressed, similar to the disjoining pressure, by CSP, CSC and LSA as given by eqs. 3.11 (the plus sign applies to CSC, and the minus sign applies to CSP) and 3.12 respectively. The individual interaction energy calculations are also compared in Figure 3.4, while the LSA approach showed intermediate results between CSP and CSC.

$$\omega_R(h) = \frac{nk_BT}{\kappa}[2\psi_{r1}\psi_{r2}\, csch\, \kappa h \pm (\psi_{r1}^2 + \psi_{r2}^2)(coth\, \kappa h - 1)] \tag{3.11}$$

$$\omega_R(h) = \frac{64nk_BT}{\kappa}\gamma_1\gamma_2 e^{-\kappa h} \tag{3.12}$$

where κh is the dimensionless thickness of the water film between the interacting interfaces. Based on the comparisons shown in Figures 3.3 and 3.4 for CSP, LSA and CSC interaction forces and energy, respectively, this study was focused on using a simplistic approach considering the analytical solution for the linear superposition approximation to estimate the double-layer interaction forces and energies.

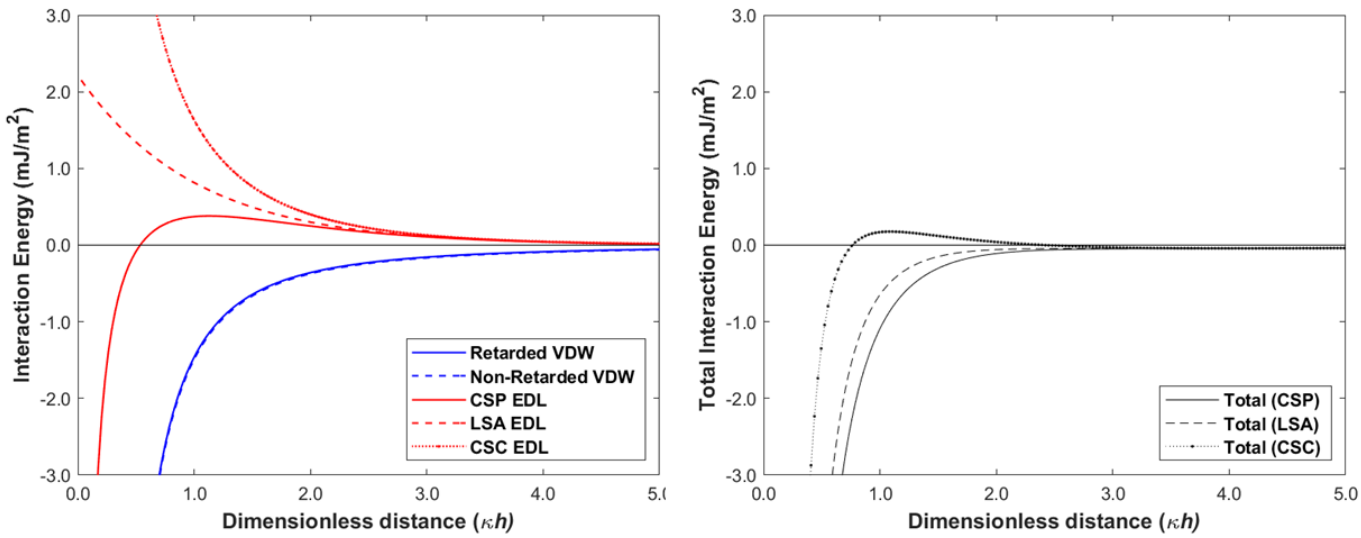

Figure 3.4—Interaction energy with individual contributions from van der Waals—ω_A and EDL—ω_R (*left*) and the net interaction energy (*right*) as a function of dimensionless film thickness (κh at a value of 1 implies that the separation distance is equivalent to the EDL thickness, which is 0.342 nm for seawater). Considering figure on the left, since ω_R varies exponentially with thickness (eq. 3.12) and ω_A varies with the square of thickness (eq. 3.10), ω_A surpasses ω_R at short and long distances, thus producing attraction between the two interacting interfaces and energy barrier at intermediate distance.

3.4 Zeta Potential Calculation

Zeta potentials are often measured in the laboratory through two major electrokinetic measuring technique: streaming potential measurement (SPM) and electrophoretic mobility measurement (EPM). SPM determines the ζ–potential by measuring the streaming potential induced by the flow of the electrolyte across the intact sample, while EPM determines the ζ–potential by measuring the electrophoretic mobility of the rock suspension. The surface and ζ–potential, at any distance Δ from the surface in the diffuse layer, are related nearly exponentially (eq. 3.13) or exactly exponentially (eq. 3.14) by considering Gouy-Chapman theory as below.

$$\zeta = \psi_o(\Delta) = \frac{2k_BT}{e}\ln\frac{1+\gamma\, e^{-\kappa\Delta}}{1-\gamma\, e^{-\kappa\Delta}} \tag{3.13}$$

The expression in eq. 3.13 assumes that the slip plane is located at distance Δ from the surface (OHP) into the diffuse layer, where ζ is the zeta potential. The simple form of eq. 3.13 can be expressed by the solution of the linearized PBE describing the electrical potential distribution for the condition of small charge density or low surface potentials ($|\psi_r| \ll 1$) [242]:

$$\zeta = \psi_o(\Delta) = \psi_o e^{-\kappa\Delta} \tag{3.14}$$

The expression in eq. 3.14 shows that ζ–potential decays from ψ_o at the surface to ψ_o/e at $\Delta = \kappa^{-1}$ (i.e., wall of the electrical double layer). In many cases, it is assumed that the slipping plane and OHP are identical, which considers that the surface is locally flat, and it implies that laboratory measured ζ–potential of rock-brine and oil-brine interfaces represent their surface potentials, $\psi_o = \zeta$. Alroudhan *et al.* [104] compared the differences between the two ζ-potential measuring techniques for rock-brine interface and reported that the shear plane corresponds to the Stern plane for EPM, which implies that $\Delta = 0$ and $\zeta = \psi_o$, while it was found out that Δ =0.245 nm for SPM and eq. 3.14 remains valid to obtain ζ–potential from surface potential. However, in this study, the surface potential for the rock-brine interface are calculated using eq. 3.14 by taking the slip plane distance as 0.245 nm as obtained with the experimental data from [54, 104] as listed in Table 3.3.

However, for the oil-brine interface, an approach used by Buckley *et al.* [251] was adapted to replicate their experimental data. Based on the ionizable surface-group model by Takamura and Chow [197], the charge at the oil-brine interface develops because of the dissociation of carboxyl groups, which indicates that the relative concentration of charges at the oil-brine surface sites depends on the relative concentration of protons (H^+) in solution. This means that H^+ behaves as PDI towards the oil-brine surface, and therefore, it is very common to plot surface or ζ–potential as a function of pH, with the isoelectric point often quoted as a pH value. As such, the chemical potentials at this interface depend upon only temperature and pressure so that the surface potential are related to the activity of H^+ ion with a Nernstian form of:

$$\Delta\psi_o = -2.303\frac{k_BT}{e}\Delta pH \tag{3.15}$$

where $p \equiv -log_{10}$ and considering the pH at the isoelectric point (pH_{iep}), eq. 3.15 can be expressed as:

$$\psi_o = -2.303\frac{k_B T}{e}\left(pH - pH_{ip}\right) \tag{3.16}$$

Table 3.3—Rock-Brine and Oil-Brine zeta and surface potentials in aqueous electrolyte solutions at pH 8.4

Brine Sample	**Zeta (ζ) Potentials (mV)**		**Surface (ψ_o) Potentials (mV)** [c]	
	Rock-Brine [a]	**Oil-Brine** [b]	**Rock-Brine**	**Oil-Brine**
FW	0.8020	-0.1031	3.6104	-15.9596
SW	-6.7120	-3.8824	-13.7144	-45.0747
SW/2	-8.0000	-10.1345	-13.2594	-61.0742
SW/10	-9.2740	-37.8385	-11.6252	-100.059
SW/20	-9.2980	-53.3352	-10.9089	-116.918
SW2S	-8.1690	-3.1785	-17.4374	-42.4395
SW3S	-9.1740	-2.6310	-20.4090	-40.1189
SW4S	-9.4980	-2.1982	-21.9767	-38.0519

Sources: [a] Data retrieved from Alroudhan *et al.* [104] and [b] Calculated based on data retrieved from Buckley *et al.* [251]. [c] Surface potential was calculated from ζ–potential values using eq. 3.13 with $\Delta = 0.245$ nm for Rock-Brine interface and $\Delta = 0.6$ nm for Oil-Brine interface.

Based on this approach of combining eqs. 3.13 and 3.16, a slip plane distance (Δ) of 1.0 nm was used to replicate the measured ζ–potential of Moutray (Texas), Leduc (Alberta) and ST86 (North sea) crude oil samples tested by Buckley *et al.* [251] compared to 0.6 nm stated in their work and the pH_{iep} was taken similar to their work as 3.4, 4.75 and 3.4, respectively. The Moutray crude was speculated to have a lesser total number of surface-active groups at its oil-brine interface due to having less negative ζ–potential as compared with Leduc and ST86 crude oils, even though it has a higher acid number (0.26 mg KOH/g) compared to the latter (both with 0.15 mg KOH/g). Overall, the ζ–potential reduces as the brine salinity reduces. As shown in Figure 3.5, the attempt to match the experimental datasets based on proposed approach with Δ = 0.6 nm failed and could only be better matched by using 1.0 nm, out of which Moutray crude gave a better match. Further analysis in this section is conducted using Moutray crude because it also has comparable properties (viscosity — 5.23 cP and density — 838 kg/m^3) to crude oil that is used in subsequent Chapters. Hence, ζ–potential of Moutray crude was converted to the surface potential through eqs. 3.13 and

3.14, with Δ taken as 0.6 nm as predicted by Buckley *et al.* [251] to be the slip plane distance. The comparison of eqs. 3.13 and 3.14 shown in Figure 3.5 confirms that eq. 3.14 holds only at low potential ($|\psi_r| \ll 1$) as there are no significant difference in the predicted potentials. In contrast, at high potential, eq. 3.14 largely underestimates the potential and any attempt to use the equation to describe surface potential at high potential will result in huge error. For this reason, eq. 3.13 was used for oil-brine interfacial calculations and either of the equations work for rock-brine interfacial calculations because they are low potential as tabulated in Table 3.3.

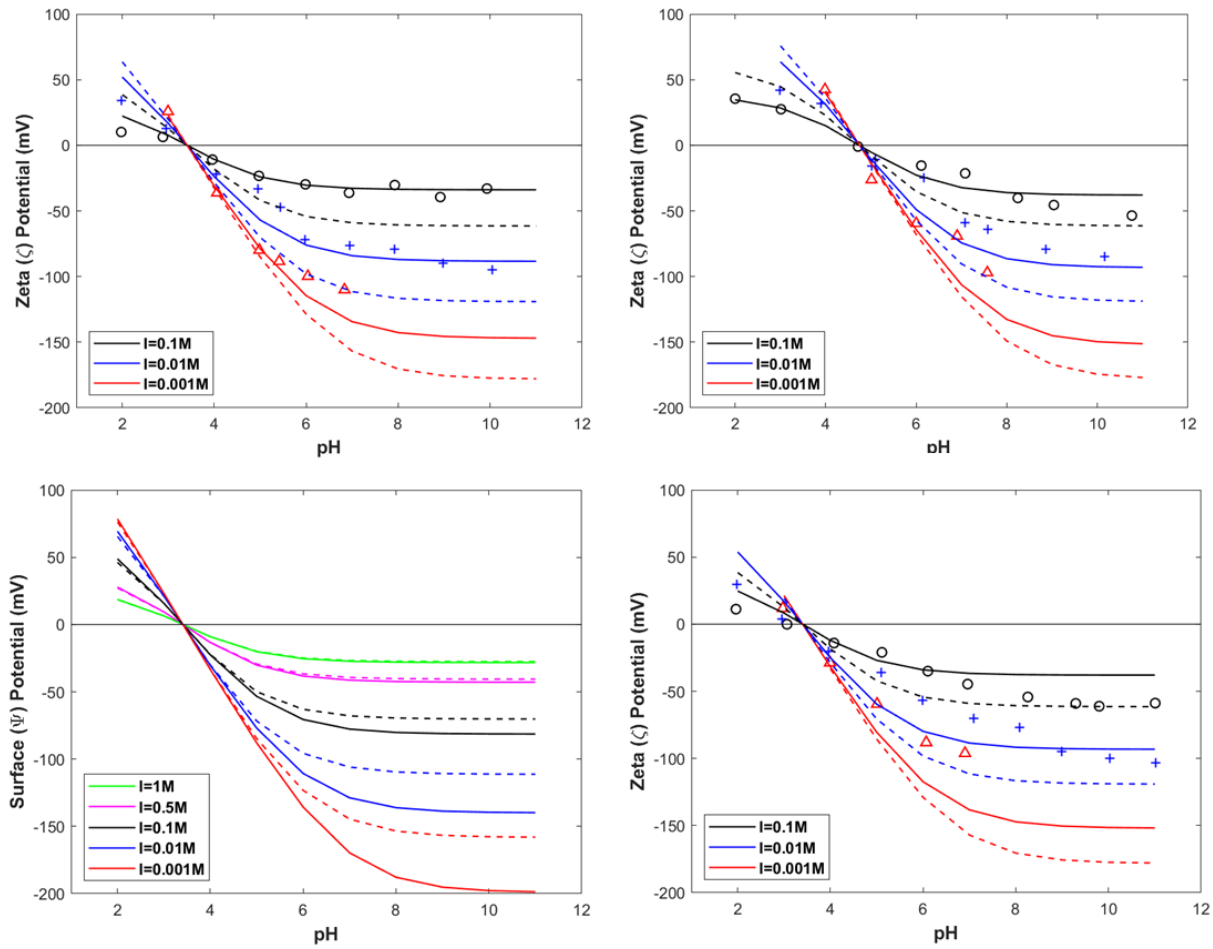

Figure 3.5—Comparison of calculated and measured ζ–potential of the oil-brine system as a function of pH and brine ionic strength for Moutray oil (*left-top*), Leduc oil (*right-top*) and ST86 oil (*right-bottom*). The markers are the experimental data; dashed lines represent calculations with $\Delta = 0.6$ nm and solid lines for $\Delta = 1.0$ nm. Calculated surface potential for the oil-brine system (*right-bottom*) is shown with dash lines representing eq. 3.14 and solid lines for eq. 3.13. The ionic strength is expressed in terms of NaCl brine, experimental data from Buckley *et al.* [251] varies from 0.1M to 0.001M. The trend for 0.5M and 1M has been included for comparison of the increasing ζ–potential with increased salinity.

3.5 Water Chemistry Effect on Disjoining Pressure and Potential Barrier Height

The net disjoining pressure and interaction energy of the water film between the rock and oil surfaces was calculated at ambient temperature using eqs. 3.1 and 3.9, respectively, using the rock-brine and oil-brine ζ–potential pairs at a typical reservoir pH range of 7.1 – 8 (see Table 3.3). The disjoining pressure has been estimated as a function of the film thickness, while the interaction energy was estimated as a function of the dimensionless separation distance. Figures 3.6 – 3.10 shows the total disjoining pressure and interaction energy for brines used in the study to evaluate the significance of PDIs and brine dilution on the stability of the water film layer. For all cases, the disjoining pressure becomes negative for film thickness lesser than 0.75nm due to the dominant effect of the attractive van der Waals force component over small separation distances. The peak of interaction energy curve is known as the potential barrier height, which gives the amount of energy per unit area in mJ/m^2 that the interacting interface needs to overcome to become attracted. This energy barrier is observed to be within a dimensionless distance of 1, when the separation distance is equivalent to κ^{-1}. The net disjoining pressure and interaction energy in initial formation brine was found to be negative, indicating a high attraction between the two interfaces, thereby resulting into an oil-wetting state. This is consistent with the observations that carbonate reservoirs are often mixed-wettability or oil-wet, and that the rock surfaces in carbonate reservoirs containing typical formation brine often possess a positive ζ–potential. The ζ–potential of the rock in crude oil was not measured, but the dependence of oil-brine ζ–potential with ionic strength as presented by Buckley *et al.* [251] was used in this work. The oil-brine interface has a negative ζ–potential, which becomes less negative as the brine ionic strength increases (see Figure 3.5).

Alroudhan *et al.* [104] reported that the ζ–potential of an intact carbonate rock in NaCl brine becomes increasingly negative and decreasingly negative with increasing SO_4^{2-} and Ca^{2+} concentration, respectively. The behavior was reported to show a linear trend, though, the ζ–potential of the rock remained negative irrespective of the SO_4^{2-}, while Mg^{2+} behaved identically with Ca^{2+}. As seen in Figure 3.6, the disjoining pressure shifted to more positive values with increased SO_4^{2-} concentration in the two different NaCl brines. Similarly, the interaction energy shifted to more positive, thereby increasing the energy barrier needed to be overcome for the

interacting interfaces to attract/overlap. Considering the EDL thickness, when the dimensionless distance is 1, the higher the SO_4^{2-} concentration the higher is the potential barrier height created between the interfaces. The shift became more pronounced over a larger proportion of the water layer as the salinity of the brine was reduced from 0.5M to 0.05M. Because the energy barrier increases as SO_4^{2-} concentration increases, it becomes harder for the interacting interfaces to attract due to formation of a more stable and thick wetting-water film, which enhances the rock wettability towards a more water-wetting tendency. At such distances away in the bulk electrolyte solution, where the interaction energy or disjoining pressure becomes zero or less as captured in Figure 3.6, the two interfaces would not have the tendency to attract because of the thick water film.

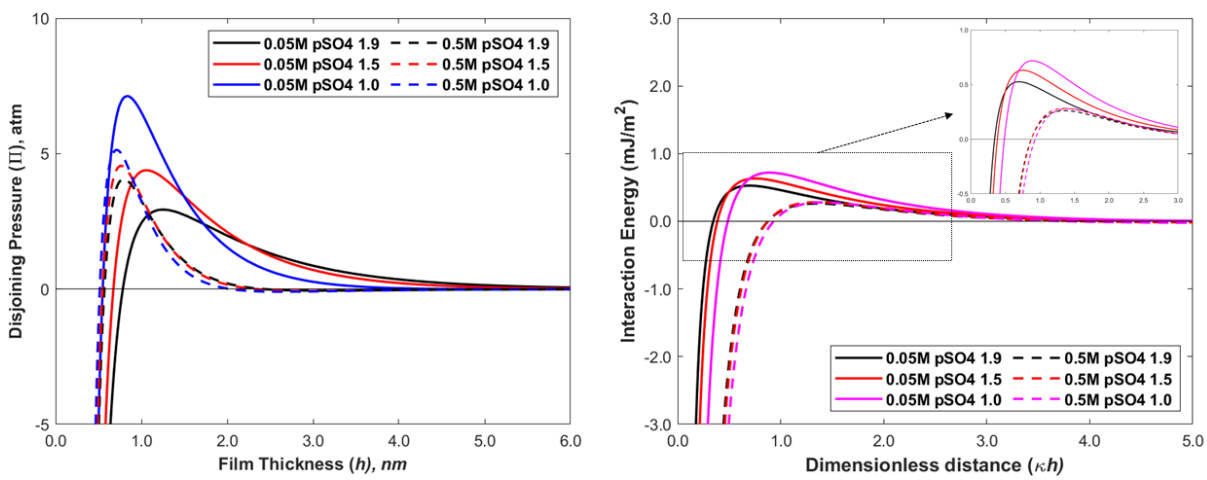

Figure 3.6—Net disjoining pressure as a function of film thickness (*left*) and interaction energy as a function of dimensionless separation distance (*right*) between the interacting interfaces with SO_4^{2-} concentration (expressed as pSO4) in two different brine salinity (0.05M and 0.5M NaCl). The term pSO4 is equivalent to $-\log_{10}[SO_4^{2-}]$, which implies that pSO4 reduces as the concentration of SO_4^{2-} increases, i.e., pSO4 of 1.9 equals 0.0117M (half SO_4^{2-} in natural seawater), 1.5 equals 0.0329M (same SO_4^{2-} as in natural seawater) and 1.0 equals 0.0969M (thrice SO_4^{2-} in natural seawater). The solid lines indicate curves for lower salinity (0.05M NaCl) and dash lines (0.5M NaCl) indicate curves for higher salinity. Unit conversion 1 atm = 101.325 kPa

In contrast, the disjoining pressure monotonically shifts to less positive/more negative as the Ca^{2+} concentration increases in the different NaCl brines shown in Figure 3.7. At low Ca^{2+} concentration, the energy barrier peaked and weakened towards the primary minimum as the concentration further increases, which would result in more attraction and enhances the rock wettability alteration toward a more oil-wetting state. The disjoining pressure and interaction

energy profiles are negative for high saline brine (2M NaCl) and monotonically decrease as Ca^{2+} concentration increases. From this discussion, it is obvious to acknowledge that increasing SO_4^{2-}, decreasing Ca^{2+}/Mg^{2+} and reducing NaCl concentration are capable of increasing the tendency to achieve more stable and thick water film to improve rock water-wetness. This is similar to many observations made by various authors that alteration of these ions in the injected brines is capable of improving the oil recovery. Similarly, Awolayo *et al.* [65] stated that unstable water films are instigated as the ratio of $[SO_4^{2-}]/[Ca^{2+}]$ reduces, which will bring the oil and rock together, resulting in the rock to be preferentially oil-wet. Whereas, some other studies (like Zhang *et al.* [50] and Zhang *et al.* [32]) have shown that increasing the concentration of Ca^{2+}/Mg^{2+} leads to improved water-wetness and oil recovery, contrary to above observations. This is because the oil-brine interface considered in this study is negatively charged, however, in cases where the interface is positively charged, modifying the ζ–potential of the rock-brine interface to yield more positive values by increasing concentration of Ca^{2+}/Mg^{2+} can result in improved recovery as presented by Jackson *et al.* [119]. As earlier stated, when the ζ–potential of the two interacting interfaces possesses the same polarity, then the electrical double layer force becomes repulsive, so the disjoining pressure and energy barrier shifts to more positive, stabilizing the water film and reversing the wettability towards water-wetness.

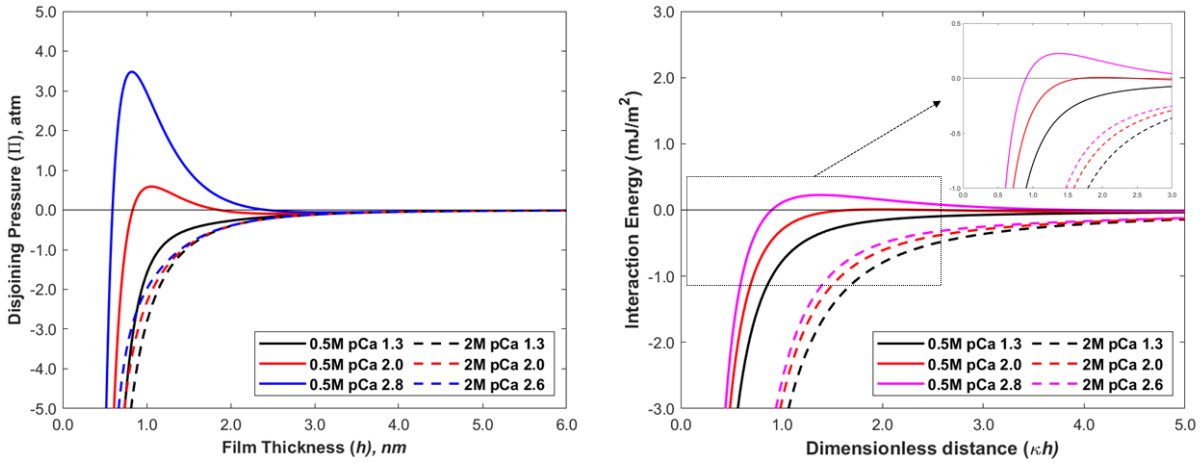

Figure 3.7—Net disjoining pressure as a function of film thickness (*left*) and interaction energy as a function of the dimensionless separation distance between the interacting interfaces (*right*) with pCa in two different saline brines (0.5M and 2M NaCl). The pCa of 1.3 is equivalent to 0.0495M (quadruple Ca^{2+} as in natural seawater), 2.0 is equivalent 0.0102M (same Ca^{2+} as in natural seawater), 2.6 is equivalent 0.002M and 2.8 is equivalent 0.0015M SO_4^{2-} concentration. Unit conversion 1 atm = 101.325 kPa

Furthermore, the variation of SO_4^{2-} concentration in typical natural field seawater was considered, which has been shown by various authors to change rock wettability towards more water-wetness and improve oil recovery. As presented in Figure 3.8, the net disjoining pressure shifted to more positive as SO_4^{2-} concentration increased in the seawater, though the magnitude was lesser compared to what was reported in NaCl brines due to the increased electrostatic screening as a result of higher salinity. The interaction energy also shifted to less negative/more positive, resulting in increased potential barrier height as SO_4^{2-} concentration is increased. It was expected that quadrupled SO_4^{2-} (SW4S) should outperform thrice SO_4^{2-} (SW3S), however, as ionic strength increased (from 0.983 to 1.082; see Table 3.2), which would impact the oil-brine interface charge, it causes the potential repulsive barrier to shift outward and weakened as compared to SW3S. This was corroborated by adjusting the NaCl concentrations of SW2S, SW3S and SW4S in Table 3.2 to maintain similar ionic strength as SW. Then, same rock-brine ζ–potential was used, assuming that it is mainly a function of SO_4^{2-} concentration and oil-brine ζ–potential was similar for all cases as a result of same ionic strength.

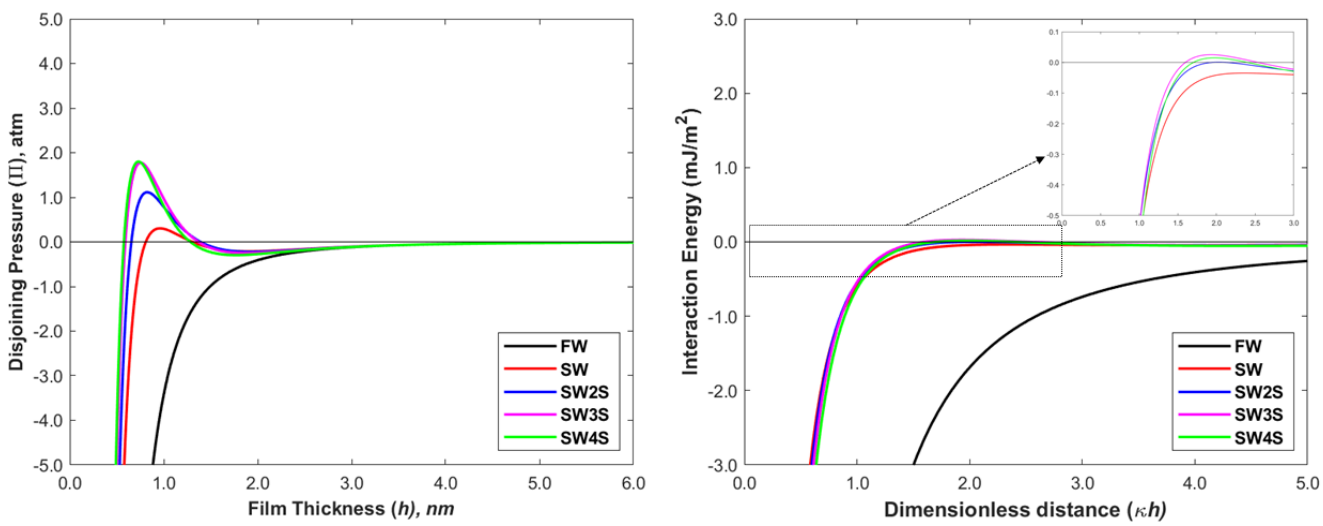

Figure 3.8—Relationship between net disjoining pressure as a function of film thickness (*left*), interaction energy as a function of the dimensionless separation distance between the interacting interfaces (*right*) and brine compositions derived from seawater with increasing SO_4^{2-} concentration. Unit conversion 1 atm = 101.325 kPa

The net disjoining pressure and interaction energy are presented in Figure 3.9; there is a distinct difference between predictions made here compared to that of Figure 3.8. The disjoining pressure

shifted more upward and outward covering larger proportion of the pore surfaces due to increased SO_4^{2-} concentration in natural seawater. The magnitude of the potential energy barrier height was even higher as a result of increased SO_4^{2-}. Thus, injecting brine with a higher sulfate concentration has the tendency to create higher energy barrier that can increase repulsion between the interacting interfaces and alter the wettability towards water-wetness. During typical displacement experiments, such as that investigated by several authors [7, 46, 52, 138], as will be discussed in subsequent Chapters, in which formation brine was replaced by seawater and then sequence of various seawater-derived brines (such as SW2S, SW3S and SW4S). The ζ–potential at the rock-brine interface in formation brine was positive, becomes negative in contact with seawater and more negative as various seawater-derived brines comes in contact with the rock. Consequently, the electrostatic force becomes repulsive and increases in magnitude, leading to a higher disjoining pressure and potential barrier height, and increasingly stable water film layer. The wettability is altered towards more water-wet conditions; oil previously adsorbed on the rock surfaces is released and incremental oil recovery can be observed.

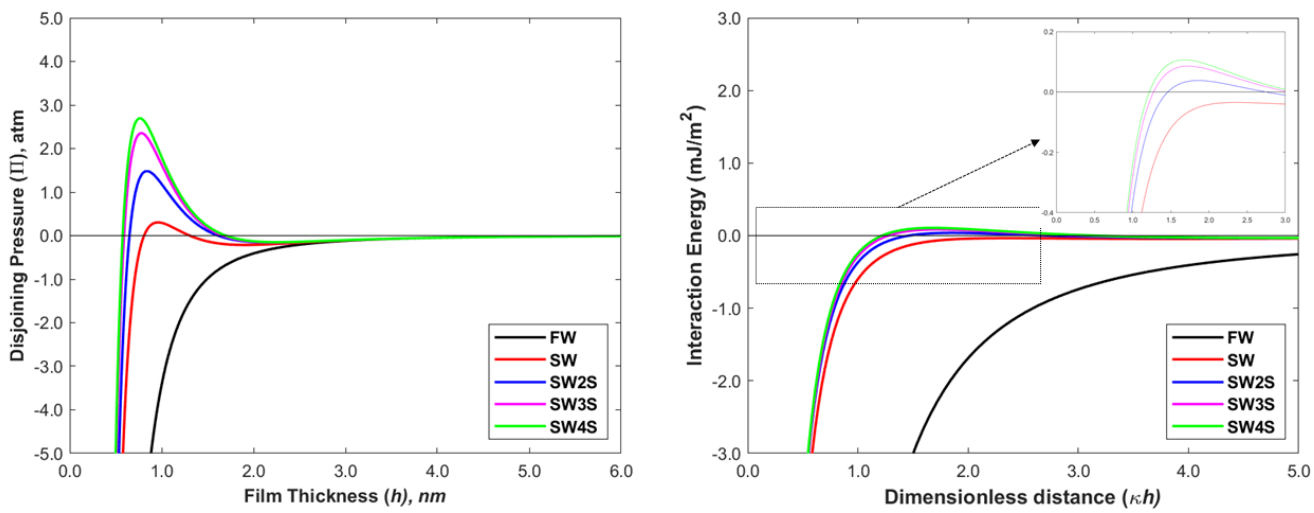

Figure 3.9—Net disjoining pressure as a function of film thickness (*left*) and interaction energy as a function of the dimensionless separation distance between the interacting interfaces (*right*) for seawater-derived brines with increasing SO_4^{2-} concentration and same ionic strength (0.7850). Unit conversion 1 atm = 101.325 kPa

Another consideration for typical natural field seawater is the reduction of brine salinity through brine dilution. The net disjoining pressure and interaction energy calculation for the variation

dilutions of seawater is presented in Figure 3.10. The trend that appears suggests the ζ–potential decreases as the brine salinity is reduced and disjoining pressure shifts to more positive and outward, which develops more stable water films over a large separation distance. The potential barrier height was also higher covering a larger proportion as brine salinity reduces. It is well established that reduction in ionic strength can expand the double layer thickness, due to reduced electrostatic screening and thereby causing an outward increase in disjoining pressure. This more positive shift would result in the reduction of the attractive forces that enhances wettability changes towards a more water-wetting state in a displacement process involving sequential dilutions of injected brine.

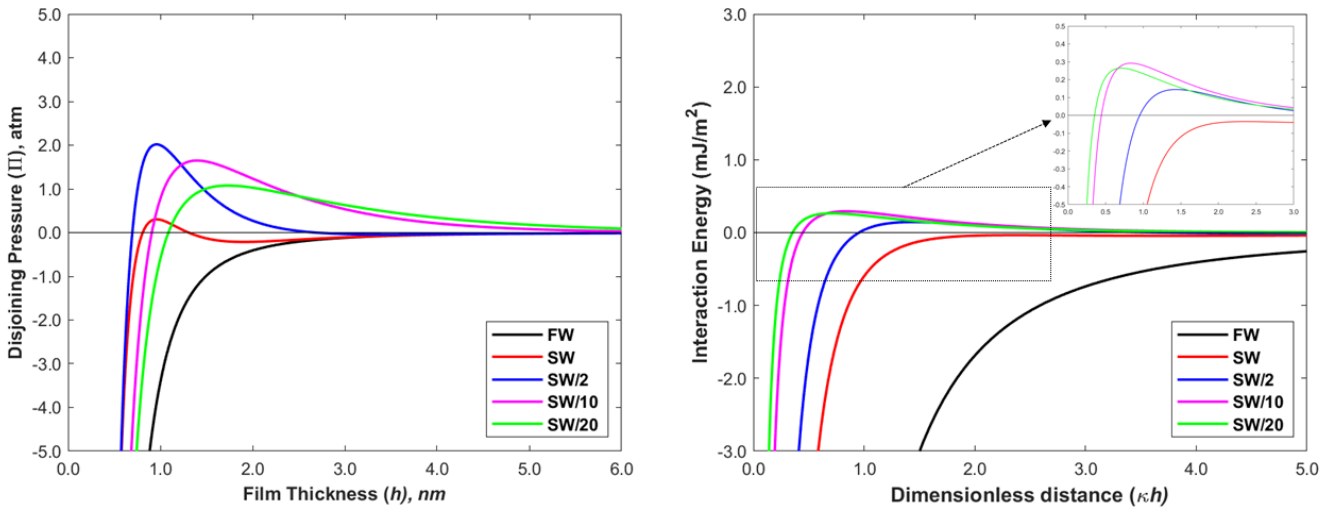

Figure 3.10—Net disjoining pressure as a function of film thickness (*left*) and interaction energy as a function of the dimensionless separation distance between the interacting interfaces (*right*) with varying brine dilutions derived from seawater. Unit conversion 1 atm = 101.325 kPa

For such displacement experiments, in which formation brine is replaced by seawater and then various dilutions of seawater, the magnitude of the repulsive electrostatic force increases, leading to a higher disjoining pressure and potential energy across a larger proportion, thereby increasingly stabilizing the water film. Many experiments carried out with the approach of diluting the injected brine has been successful, however, in cases with no success, Jackson *et al.* [119] demonstrated that the diluting the injected brines in the presence of positively charged oil-brine interface, which would lead to less positive/more negative ζ–potential at the rock-brine interface, will increase the magnitude of the attractive electrostatic force, leading to a more negative disjoining pressure and

lower the energy barrier to primary minimum. This will increasingly thin and rupture the water film. Reducing the NaCl and/or Ca^{2+} concentration in the injected brine has a similar effect to simple dilution as discussed above because varying their concentration changes the ζ–potential of the rock-brine interface, thus affecting the electrostatic contribution to the disjoining pressure and potential barrier height. However, changes in ζ–potential in response to changes in NaCl concentration were more pronounced for the experimental dataset investigated here than the changes in ζ–potential observed during conventional brine dilution. Thus, improved oil recovery would be more pronounced.

3.6 Chapter Summary

In this Chapter, the improved recovery associated with brine-dependent recovery has been rationalized at the surface-scale by considering changes to rock wettability due to the stability of the water film layer that wets and separates the rock surface from the oil phase. The DLVO theory for colloidal surfaces has been applied in linking wettability changes to the stability of the water film layer. The stability of this wetting film depends on the disjoining pressure and the energy barrier height developed from interaction energy calculation. The interaction force or disjoining pressure is the net contributions from van der Waals, electrostatic and structural forces, however contribution from structural forces was not included here as little is known about their existence at carbonate rock surfaces. The contribution from the attractive Van der Waals force to the interaction force/energy is always negative, which acts to destabilize the water film. Meanwhile, the contribution of the electrostatic force can be either positive or negative depending upon the ζ–potential of the interface, which is influenced by pH, brine compositions and mineral contents.

The disjoining pressure relates to the presence and thickness of water film separating the coming together of rock and oil. While the energy barrier height predicted from the interaction energy per unit area relates to the potential energy required to compress the double layer and thin the water film. The interacting interfaces become more attracted because of negative disjoining pressure and primary minimum interaction energy between the two interfaces. This would mean more oil-wetting or less water-wetting state. Meanwhile, the less negative the interaction forces and energies become, the higher are the repulsion between the two interfaces. This potentially creates an energy

barrier, which needs to be overcome for the interacting interfaces to attract. This would mean a less oil-wet or more water-wet system.

The DLVO predicts attraction between the interacting interfaces that implies oil-wet tendency as expected for carbonate rocks containing typical formation brine. The magnitude of the contribution of the electrostatic force increases with decreasing ionic strength, either through reduction of NaCl, Ca^{2+} or brine dilution, and/or increasing SO_4^{2-} concentration, which improves the trend/profile towards less attraction or more repulsion. The energy barrier required to be overcome for the interfaces to attract increases as a result, which can reverse the pre-existing oil-wetting condition as increased electrostatic repulsion generate a more stable water film between the two interfaces and consequently, improve the oil recovery as widely documented in literature. The surface forces/energies integration is the hidden features of the PDI interaction at the interfaces, which is well captured in the numerical model, presented in subsequent Chapters, to predict wettability alteration and the associated improved oil recovery.

Chapter 4 Reactive Transport Model Description and Validation

In this Chapter, the approach used to develop a reactive transport model, incorporating the interfacial phenomena responsible for improved recovery, obtain the numerical scheme and validate the model using independently-sourced experimental data were described.

4.1 Introduction

In previous Chapters, many interfacial phenomena that are observed during brine-dependent recovery process were discussed. More importantly, it was established that a combination of all these phenomena is involved in improving oil production as observed from the available experimental data. However, surface forces/energies developed from electrostatic interaction seemed to be very critical. Hence, the focus in this Chapter is to state the reactions describing these electrostatic interactions and formulate equations coupling their effect with fluid transport equations. During low saline/smart brine injection, the thermodynamic equilibrium existing among the ion species dissolved in the water film layer, ion species adsorbed on the rock surface and the ion species that form the rock matrix are disturbed. This triggers a reaction involving connate-waterflood mixing, mineral dissolution/precipitation, surface sorption and complexation, while trying to establish a new equilibrium state, and favorably alters rock wettability from an initial oil-wetting state to a water-wetting state and improves oil recovery.

The modeling of reactive components transport can be quite tedious without simplified assumptions, and the only way to solve these equations is through numerical approximations. In this case, the formulation of this model considers a porous rock initially saturated with crude oil and formation brine. The rock is assumed to comprise of different minerals responsive to the injected brine composition. Injecting brine of different salinities and compositions than those of the initial brine often disturbs the existing thermodynamic equilibrium. As the process becomes intense, it is expected that both the flow functions and reservoir rock parameters are transformed. Therefore, the sets of equations that depict this recovery process involve the transport of species by bulk phase advection, dispersion/diffusion, phase equilibrium reactions between gaseous, oleic and aqueous phases, equilibrium and rate dependent reactions between solid and aqueous phase.

Table 4.1—Reaction pathways considered during simulation, where > is the prefix for surface species

Hydrocarbon solubility	
$CO_{2(o)} \Leftrightarrow CO_{2(g)} \Leftrightarrow CO_{2(aq)}$	$(R1)$
$CO_{2(aq)} + H_2O \Leftrightarrow H^+ + HCO_3{}^-$	$(R2)$
Aqueous reactions	
$H_2O \Leftrightarrow H^+ + OH^-$	$(R3)$
$HCO_3{}^- \Leftrightarrow H^+ + CO_3^{2-}$	$(R4)$
$CaSO_4 \Leftrightarrow Ca^{2+} + SO_4{}^{2-}$	$(R5)$
$MgSO_4 \Leftrightarrow Mg^{2+} + SO_4{}^{2-}$	$(R6)$
$NaSO_4{}^- \Leftrightarrow Na^+ + SO_4{}^{2-}$	$(R7)$
$CaCO_3 + H^+ \Leftrightarrow Ca^{2+} + HCO_3{}^-$	$(R8)$
$MgCO_3 + H^+ \Leftrightarrow Mg^{2+} + HCO_3{}^-$	$(R9)$
$CaHCO_3{}^+ \Leftrightarrow Ca^{2+} + HCO_3{}^-$	$(R10)$
$MgHCO_3{}^+ \Leftrightarrow Mg^{2+} + HCO_3{}^-$	$(R11)$
$NaHCO_3{}^+ \Leftrightarrow Na^+ + HCO_3{}^-$	$(R12)$
Mineral reactions	
$Calcite + H^+ \Leftrightarrow Ca^{2+} + HCO_3{}^-$	$(R13)$
$Dolomite + 2H^+ \Leftrightarrow Ca^{2+} + 2HCO_3{}^- + Mg^{2+}$	$(R14)$
$Anhydrite + H^+ \Leftrightarrow Ca^{2+} + SO_4{}^{2-}$	$(R15)$
Surface adsorption reactions	
$> X^+ + SO_4{}^{2-} \Leftrightarrow \quad > XSO_4{}^-$	$(R16)$
Surface ion exchange reactions	
$Na^+ + \frac{1}{2} > CaX_2 \Leftrightarrow \frac{1}{2} Ca^{2+} + > NaX$	$(R17)$
$Na^+ + \frac{1}{2} > MgX_2 \Leftrightarrow \frac{1}{2} Mg^{2+} + > NaX$	$(R18)$
Surface complexation reactions	
$> CO_3H^o \quad \Leftrightarrow \quad > CO_3{}^- + \quad H^+$	$(R19)$
$> CaOH^o \; + \quad H^+ \quad \Leftrightarrow \quad > CaOH_2^+$	$(R20)$
$> CO_3H^o \; + \quad Ca^{2+} \quad \Leftrightarrow \quad > CO_3Ca^+ \; + \quad H^+$	$(R21)$
$> CO_3H^o \; + \quad Mg^{2+} \quad \Leftrightarrow \quad > CO_3Mg^+ + \quad H^+$	$(R22)$
$> CaOH_2^+ \; + \quad SO_4^{2-} \quad \Leftrightarrow \quad > CaSO_4^- \; + H_2O$	$(R23)$
$> CaOH_2^+ \; + \quad CO_3^{2-} \quad \Leftrightarrow \quad > CaCO_3^- \; + H_2O$	$(R24)$

The typical chemical reactions considered in this model are summarized in Table 4.1.

4.2 Model Formulation

The descriptions of the equations and assumptions are highlighted below.

4.2.1 Hydrocarbon solubility

Oil and gas are mixtures of different hydrocarbon and non-hydrocarbon components, whereas some hydrocarbons are soluble in the aqueous phases. The dissolution rates of these soluble hydrocarbon components are fast and presumed to be in thermodynamic equilibrium at a specific pressure, composition, and temperature. Their solubilities are modeled using the phase equilibrium concept, which necessitates that, in a mixture of N_c hydrocarbon components when an oleic phase, a gaseous phase and aqueous phase coexist, each component must maintain equal fugacity in all phases. For example, CO_2 at equilibrium (in reaction R1 of Table 4.1) possesses equal fugacity in all three phases as shown in eq. 4.1.

$$f_{ig}(P, y_{ig}, T) \equiv f_{io}(P, y_{io}, T) \equiv f_{iw}(P, y_{iw}, T) \qquad for\ i = 1, \ldots\ldots, N_c \tag{4.1}$$

where f_{ij} and y_{ij} are the fugacity (kPa) and mole fractions of the i-th component in the j-th phase, P is the pressure (kPa) and N_c is the total number of soluble hydrocarbon components. The fugacities f_{ig} and f_{io} are computed from the equation of state, in this case, Peng-Robinson (PR-EOS) using the following expression:

$$\ln\frac{f_i}{y_i P} = \frac{b_i}{b_m}(Z-1) - \ln(Z-B) - \frac{A}{B(\delta_1-\delta_2)}\left(\frac{2\sum_{k=1}^{N_c} y_i\sqrt{\alpha_i\alpha_k}(1-d_{ik})}{a_m} - \frac{b_i}{b_m}\right)\ln\left(\frac{Z+\delta_2 B}{Z+\delta_1 B}\right) \tag{4.2}$$

with

$$a_m = \sum_{i=1}^{N_c}\sum_{k=1}^{N_c} y_i y_j\sqrt{\alpha_i\alpha_k}(1-d_{ik}) \quad ; \quad b_m = \sum_{i=1}^{N_c} y_i b_i \quad ; \quad A = \frac{a_m P}{(RT)^2} \quad ; \quad B = \frac{b_m P}{RT}$$

where b_i and α_i are the two pure components EOS parameters for the i-th component related to molecule size and measure of attractive forces between molecules respectively; Z is the compressibility factor; δ_1 and δ_2 are EOS constants, where $\delta_1 = 1+\sqrt{2}$ and $\delta_2 = 1-\sqrt{2}$ for PR-EOS. While f_{iaq} is computed through Henry's law, as in eq. 4.3 [252, 253]:

$$f_{iw} = y_{iw} H_i \qquad for\ i = 1, \ldots\ldots, N_c \qquad (4.3)$$

where H_i is the Henry's constant for the i-th component. For three-phase flash calculation, the equilibrium equations (eq. 4.1) are often written in terms of equilibrium ratios (K_i) as:

$$R_i = \ln K_{ig} + \ln \frac{f_{ig}}{y_{ig} P} - \ln \frac{f_{io}}{y_{io} P} = 0 \qquad for\ i = 1, \ldots\ldots, N_c \qquad (4.4)$$

$$R_i = \ln K_{iaq} + \ln \frac{f_{iaq}}{y_{iaq} P} - \ln \frac{f_{io}}{y_{io} P} = 0 \qquad for\ i = 1, \ldots\ldots, N_c \qquad (4.5)$$

where R_i is the expression for the residual function of the i-th component. The hydrocarbon components in the oleic, gaseous, and aqueous phases can be derived from the phase calculation such that the following moles summation is achieved:

$$N_i = N_{io} + N_{ig} + N_{iaq} \qquad for\ i = 1, \ldots\ldots, N_c \qquad (4.6)$$

4.2.2 Aqueous-Species reactions

These are fast and homogenous chemical reactions occurring among components in the aqueous phase and are modeled with an equilibrium mass action law using the stoichiometry approach. The total components (N_{aq}) in the aqueous phase consist of N_c soluble hydrocarbon components plus components (N_a) that only exist in the aqueous phase. These aqueous components are further divided into primary (independent) and secondary (dependent) components, which are defined as (N_{ia}) and $(N_a - N_{ia})$ respectively. A typical example is shown in reaction R8 of Table 4.1 involving the dissociation of $CaCO_3$, where individual primary species $(H^+,\ Ca^{2+})$ are linked with secondary species $(CaCO_3,\ HCO_3{}^-)$ in a chemical reaction by an equilibrium constant K_{eq}. For chemical reactions in thermodynamic equilibrium, the rate of the forward reactions is equivalent to that of the backward reactions:

$$Q_\alpha - K_{eq,\alpha} = 0 \qquad for\ \alpha = 1, \ldots\ldots, R_{aq} \qquad (4.7)$$

where Q_α and $K_{eq,\alpha}$ are the activity product and equilibrium constant of the aqueous reaction α respectively and R_{aq} is the total number of aqueous reactions. The activity product can be expressed as:

$$Q_\alpha = \prod_{i=1}^{N_{aq}} (a_i)^{\nu_{i\alpha}} \qquad for\ \alpha = 1, \ldots\ldots, R_{aq} \qquad (4.8)$$

where a_i is the activity of the *i*-th component, $\nu_{i\alpha}$ is the stoichiometry coefficient of the *i*-th component in reaction *α,* and N_{aq} is the total number of components in the aqueous phase. The equilibrium constant values are tabulated as a function of temperature in several geochemical databases [254, 255, 256]. Alternatively, the values are calculated using an analytical polynomial expression (eq. 4.9) to define the temperature dependence of the equilibrium constants.

$$\log K_{eq} = A_0 + A_1 T + \frac{A_2}{T} + A_3 \log T + \frac{A_4}{T^2} + A_5 T^2 \qquad (4.9)$$

where T is the absolute temperature (K) and $A_0 \ldots\ldots A_5$ are the empirical parameters that can be found in several databases for various chemical reactions (see Appendix A). The activity of each component i is related to its molality as follows:

$$a_i = \gamma_i m_i \qquad for\ i = 1, \ldots\ldots, N_{aq} \qquad (4.10)$$

where γ_i and m_i are the activity coefficient (kg-water/mol.) and molality (mol./kg-water) of the *i*-th component. The activity coefficients, γ_i, for ideal solutions can be taken as unity. This implies that the activities of such species are equal to their molalities. For solutions that deviate from the ideal conditions, this model considers the WATEQ Debye-Hückel equation, also known as B.dot activity model [257], to compute the activity coefficients as presented below.

$$\log \gamma_i = -\frac{A(T) z_i^2 \sqrt{I}}{1 + \dot{a_\iota} B(T) \sqrt{I}} + \dot{b_\iota} I \qquad for\ i = 1, \ldots\ldots, N_{aq} \qquad (4.11)$$

where $A(T)$ and $B(T)$ are the temperature-dependent parameters, $\dot{a_\iota}$, z_i and $\dot{b_\iota}$ are the ion size, ion valence and ion-specific parameter for the *i*-th component respectively, and *I* is the ionic strength (mol./kg water) of the solution, which can be estimated as $I = \frac{1}{2}\sum_{i=1}^{N_{aq}} z_i^2 m_i$. In this model, the aqueous reactions mainly explored the most relevant aqueous complexes that can be formed between Na^+, SO_4^{2-}, HCO_3^-, Mg^{2+} and Ca^{2+} through reactions R2-R12 in Table 4.1. Their formations are more pronounced at high temperatures and can significantly affect the activity of the PDIs towards the rock surface sites. Higher concentrations of non-active ions in the imbibing

brine will result in higher ionic strength and lower activity coefficients of aqueous components especially the PDIs involved in the surface sorption reactions.

4.2.3 Aqueous-Minerals reactions

These are slow and heterogeneous reactions involving aqueous and mineral components. These reactions somehow influence the distribution of the aqueous components across the characteristic length and time-scale. The magnitude of their effects is determined by the Damköhler number, which dictates whether the reaction is modeled by either a kinetic-rate law or an equilibrium law. Damköhler number (Da) is the ratio of the reaction rates to the transport rates (eq. 4.12) and mostly depends on reaction rate constants, characteristic flow distance and transport velocity.

$$Da_{\beta} = \frac{Lk_{\beta}\dot{A}_{\beta}}{\nu C_{\beta}} \qquad for\ \beta = 1, \ldots\ldots, R_m \qquad (4.12)$$

where L is characteristic flow length (m), k_{β} is the reaction rate constants (mol./m^{2}s), $\dot{A}_{\beta}$ is the reactive surface area (m^2/m^3), ν is the transport velocity (m/s) and C_{β} is the total concentration of dissolved ion components (mol./m^3). At very high Damköhler numbers ($Da \gg 1$), the reaction rate is large, and reaction becomes instantaneous, which means that equilibrium concentration is achieved before the flux distribution of components. Meanwhile, at very low Damköhler numbers ($Da \ll 1$), fluid transport occurs faster than mineral reactions, which means that the components distribution is similar to that of inert chemical or molecule (tracer). Intermediate values of Damköhler numbers are of particular interest in this study, as they represent a non-ideal system where component distributions are influenced by these reaction sets. A quick estimation of Da for reaction R13 in Table 4.1, for the different waterfloods considered in this study, shows that Da is less than unity. Moreover, in many published studies, a few of which will be discussed in subsequent Chapters, some of the PDIs reached their injected level after more than 1 PV and others never returned. For this reason, mineral reactions are modeled as rate-dependent reactions.

Most often, the mineral components (N_m) are not in thermodynamic equilibrium with the aqueous components, which inevitably result in either mineral dissolution or precipitation. Reaction R13

shows an example of calcite dissolution/precipitation, where a mineral component $(Calcite)$ is involved in a reaction with only aqueous components $(CO_2,\ HCO_3^-,\ H^+)$ and no other mineral components. The law of mass action governing such reactions is written based on transition state theory as stated as:

$$r_\beta = k_\beta \dot{A}_\beta \left(1 - \frac{Q_\beta}{K_{eq,\beta}}\right) \qquad for\ \beta = 1, \ldots\ldots, R_m \qquad (4.13)$$

where r_β is the rate of reaction (mol./m^{3}s), Q_β is the activity product, R_m is the number of mineral surface reactions and $K_{eq,\beta}$ is the equilibrium constant. The activity product, Q_β, for the reaction, β, is similar to that expressed in eq. 4.8, except that activities of mineral species equal unity. The equilibrium constant values, K_{eq} for aqueous mineral reaction, β are also well documented in the different geochemical databases (see Appendix A). The natural log of the last term in the bracket in eq. 4.13 is also known as the *saturation index*, $\Omega_\beta = log\left(Q_\beta / K_{eq,\beta}\right)$, and indicates the deviation of the reaction from equilibrium. If $\Omega_\beta > 0$, the aqueous solution is supersaturated leading to mineral precipitation characterized by positive reaction rate. While for $\Omega_\beta < 0$, the aqueous solution is under-saturated leading to mineral dissolution, which is also characterized by negative reaction rate. At equilibrium, the saturation index and the reaction rate is equal to zero, $\Omega_\beta = 0$. Most often the rate constants in eq. 4.13 are always reported at a reference temperature, T_0 which can be converted to any temperature, T using the modified Arrhenius' equation below:

$$k_\beta = k_{\beta,0} exp\left(-\frac{E_{a\beta}}{R}\left[\frac{1}{T} - \frac{1}{T_0}\right]\right) \qquad (4.14)$$

where $k_{\beta,0}$ is the reaction rate constants for mineral surface reaction β at the reference temperature T_0 (mol./m^{2}s) and $E_{a\beta}$ is the activation energy (J/mol.). In this model, the inclusion of reaction R13-R15 is contingent on the dominant minerals in carbonate rocks — calcite, as well as other important minerals that can be found together in a typical carbonate reservoir. More importantly, calcite dissolution serves as an essential source/sink for Ca^{2+} components and buffers aqueous pH. Other viable sources/sinks for Ca^{2+} are dolomite and anhydrite dissolution, which are also considered as a source/sink for Mg^{2+} and SO_4^{2-} components respectively. Nghiem *et al.* [252]

proposed that some properties of the rock, such as reactive surface area ($\dot{A}_{\beta}$), porosity and permeability, changes as the mineral dissolves or precipitates. The equation employed in making the necessary adjustments at each time step can be found in Dang *et al.* [66], Nghiem *et al.* [252].

4.2.4 Carbonate rock system modeling

As discussed in Chapter 2, extensive laboratory studies on chalk, dolomite and limestone outcrop and reservoir cores have established the existence of an interdependent interaction among multivalent ions in brine (Ca^{2+}, Mg^{2+}, and SO_4^{2-} in addition to CO_3^{2-}, though they are of lower concentration in most reservoir fluids, and PO_4^{3-} and BO_3^{3-}) at the rock-brine interface. Such interactions can bring an existing oil−brine−rock system into a new equilibrium system during the introduction of low saline/smart brine, which in turns favorably cause the rock-brine interface to become less positively charged and repel the negatively charged oil-brine interface.

At the oil-brine interface, the polarity of crude oil is associated with the presence of acidic and basic surface groups dictating the rock wettability. The dominance of either of the surface groups is pH-dependent and determines the charge at the interface. At low pH (pH<3.5) the basic group is protonated at the interface resulting in a positively charged interface. Meanwhile, as pH increases, the acid group becomes deprotonated dropping the surface charge below zero and resulting in a strongly negatively charged interface at higher pH [197, 210, 251, 258]. The surface charge of the oil-brine interface is often strongly negative at the typical reservoir pH ranging from 7 to 9. Various studies have shown that the carboxylic acids mostly dominate the acidic groups while long-chain carboxylic acids are responsible for reversing surface wettability towards oil-wetness compared to short-chain acids [154, 251].

At the initial reservoir condition, the formation brine contains relatively lower PDI concentrations compared to Na and Cl, which implies that the initial positive charge at the rock-brine interface is maintained for pure calcite rock. This results in attraction (low/negative disjoining pressure) between the two interfaces and thin water film layer. Thus, oil acidic components majorly occupy the rock surface sites, and PDIs compete with the oil components for the surface sites. A significant change to the water chemistry enables the PDIs to attach specifically in the Stern layer or via the

intermolecular coordination of water molecules, altering the surface charge at the interface. In this context, the rock-surface charge is reduced or even reversed towards negative from its initial condition of positive charge [128, 197]. Such interaction can release adsorbed oil acidic components from the surface sites because of the more stable water film layer that is developed due to a lesser attraction (higher disjoining pressure) between the two interfaces.

The thermodynamic model for carbonates-aqueous interface postulates the formation of two primary surface sites, present in equal numbers (having a 1:1 stoichiometry) upon hydration of the calcite surface. Calcite contains an equal number of calcium (Ca^{2+}) and carbonate (CO_3^{2-}) ions held together by ionic bonding to ensure electrical neutrality. On fresh calcite surface exposed to water, the Ca^{2+} and CO_3^{2-} sites are coordinated to oxygen atoms (OH^-) and dissociated protons (H^+) groups from the chemisorbed water molecules (Figure 4.1). This originates from the assumption that during hydration of calcite mineral surface, the oxygen atoms of chemisorbed water molecules fill the vacant coordination sites of the surface cations (Ca^{2+}). Meanwhile, the surface anions (CO_3^{2-}) are stabilized by the transfer of dissociated protons from the chemisorbed water molecules. The hydroxylation of the Ca^{2+} surface site and the protonation of the CO_3^{2-} surface site create two primary surface sites: hydroxylated cation site ($>CaOH^o$) and protonated anion site ($>CO_3H^o$) at the hydrated calcite surface as evident through observations made from X-ray photoelectron and infrared spectroscopic measurements [238, 239, 259, 260]. Calcite surface in contact with aqueous solution develops electric charges due to reactions between the surface and aqueous components dissolved in an electrolyte solution. The resulting electric potential at the OHP and similarly the ζ–potential, as described in Chapter 3, are controlled by the PDIs adsorption in the Stern layer [238, 239]. There are two possible approaches of modeling PDIs reaction in the Stern layer, which are the surface sorption models (SSMs) and surface complexation models (SCMs). The SSM is a more simplistic approach that captures the MIE mechanisms by considering sorption reactions like adsorption, ion-exchange, where the electrical interaction is integrated into the reaction equilibrium constants, while SCM captures DLE mechanism and similar surface reactions as SSM, except that the sorption process depends on the interaction surface charges and electrical potential, which are simultaneously calculated with the surface components.

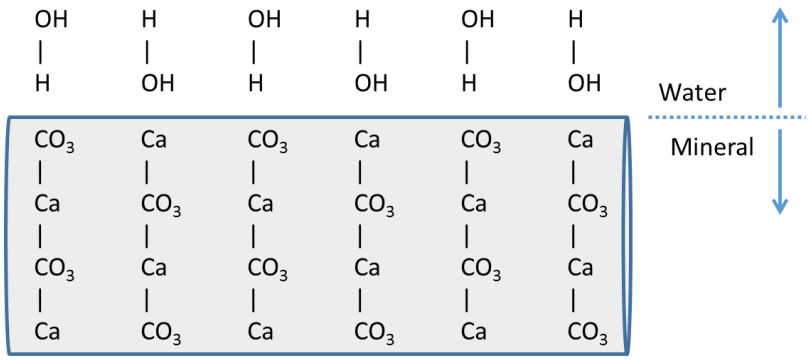

Figure 4.1—Schematic representation of the cross-section of the surface layer. In the presence of water, carbonate surfaces are generally covered with surface hydroxyl groups

4.2.4.1 Surface sorption reactions

Sorption involves reactions between aqueous components and the surface, often considered as a fast reaction process and controls the interactions at the fluid-rock interface during the early stages of flooding experiment. As previously mentioned, carbonate rocks are predominantly composed of calcite mineral, with large surface area and typically of high reactivity. A considerable amount of aqueous components can sorb to the rock surface site, having an equal number of positively (cationic $->X^{+}$) and negatively (anionic $->X^{-}$) charged surface sites, in a 1:1 stoichiometry [261]. The constant capacity of the carbonate surface sites can be obtained as:

$$\delta_s = \frac{S_d}{N_A} \tag{4.15}$$

where S_d is the site density, i.e. number of surface sites per unit area of the chalk surface and has been estimated to be between 2 and 8 sites/nm^2 for carbonate rocks [261, 262], N_A is the Avogadro's constant (6.022×10^{23} sites/mol.) and δ_s is the total surface site capacity in mol./m^2 or eq/m^2 (assuming 1 mol. ≡ 1 eq.), typically between 3.32 and 13.28 μmol../m^2 for the estimated site density. A large value of surface site capacity indicates that the surface could accommodate substantial amounts of adsorbed components, which can strongly influence the distribution of aqueous components.

The choice of specific aqueous components interacting with the surface sites is based on the remarks made from published studies. Various delays observed in some specific produced ions

concentration profiles during coreflood experiments were indications that such ions had sorbed to the surface site. In this regard, Ca^{2+}, Mg^{2+} and SO_4^{2-} have been documented to be the PDIs towards the surface site during the sorption process. Injection of brines that has the tendency to decrease surface electrostatic charges will enable the oil to desorb. The surface components of these PDIs were considered by combining equilibrium adsorption and ion exchange reactions (reaction R16-R18 in Table 4.1) to replicate the complex interactions at the aqueous-rock interface.

Adsorbed-Species Reactions: Active anions like sulfate ions can adsorb to the surface cationic sites and reduce the surface charge to a more negative magnitude. With lesser charge at the surface site, the electrostatic attractions between the negatively charged carboxylic components in the oil and the surface sites are reduced, such that oil could be easily desorbed. In this regard, a surface reaction in the form of reaction R16 was considered, where the surface cationic site is brought in contact with the sulfate component in the aqueous solution, resulting into a surface complex ($>XSO_4^-$). Hence, the mass action equation can be expressed as:

$$K_A = \frac{a_{(>XSO_4^-)}}{a_{(>X^+)} \quad a_{SO_4^{2-}}} \tag{4.16}$$

where $a_{(i)}$ is the activity of the *i*-th surface species and K_A is the apparent stability constant. Surface equilibrium reactions are often characterized by apparent-reaction stability constants due to the difficulty in the direct quantification of interfacial activities of free species and surface complexes through experiments [263]. The attraction or repulsion of aqueous components from the carbonate surface site is triggered by the columbic interaction between the components and the charged surface sites. The interaction reflects the amount of electrostatic work needed to transport these components via the interfacial potential gradient. This gradient exists because of ion transfer between the bulk solution and the surface sites. Therefore, the apparent-reaction stability constant of a surface complex is related to its intrinsic-reaction stability constant by:

$$K_A = K_{int}\, \chi \tag{4.17}$$

where K_{int} is the intrinsic-reaction stability constant and χ is the electrostatic interaction term (Boltzman factor) and can be expressed as:

$$\chi = exp\left(\frac{-z\mathcal{F}\psi_o}{RT}\right) \tag{4.18}$$

where $\mathcal{F}$ is the Faraday constant (96490 C/mol.), R is the universal gas constant (8.3143 J/mol./K) and z is the net charge over the reaction of the surface complex (which is -2 for reaction R16 in Table 4.1). The surface and ζ-potential, at any distance Δ from the shear plane in the diffuse layer, is related by the simple form of linearized PBE as discussed in Chapter 3: $\zeta = \psi_o(\Delta) = \psi_o e^{-\kappa\Delta}$. The reciprocal Debye length which determines the size of the double layer is referred to as κ and is related to ionic strength via $\kappa = \sqrt{2000\mathcal{F}^2 I/\varepsilon\varepsilon_0 RT}$. As discussed in Chapter 3, most electrical potential drop occurs in the diffuse layer, which implies that the system can be approximated by assuming $\psi_o = \psi_d$. Meanwhile, the surface charge density, σ_o must be balanced by the double layer charge density, σ_d to ensure electrical neutrality at the interface and thus, a direct relationship exist between surface potential and surface charge given by Grahame equation, which is derived from the Gouy-Chapman theory [130], as follows;

$$\sigma_o = -\sigma_d = \sqrt{8000\varepsilon\varepsilon_0 RTI}\, sinh\left(\frac{z_w\mathcal{F}\psi_o}{2RT}\right) \tag{4.19}$$

where σ_o and σ_d are the surface and diffuse layer charge density (the charge per unit area of the surface site, C/m^2), respectively, ε is the dielectric constant of water, ε_0 is the permittivity of the free space (8.854×10^{-12} C^2/J/m), and z_w is the charge on the background solute (often assumed to be unity). The dielectric constant of water, ε varies with temperature and brine ionic strength. The variation with temperature is from 78.5 at 25 °C to 50 at 130 °C using the empirical correlation derived by Malmberg and Maryott [249] as: $\varepsilon = 87.74 - 0.4008T + 9.4 \times 10^{-4}T^2 - 1.41 \times 10^{-6}T^3$, in this empirical expression T is the temperature in °C. The capacity for the positive calcium surface sites is considered as the anion exchange capacity and can be obtained in mol/kg through:

$$AEC = \delta_s A_\beta \tag{4.20}$$

where A_β is the specific surface area of the mineral (m^2/kg). For surface equilibrium reactions, surface species activities are replaced by surface species concentration and can be expressed in terms of the surface species mole fractions:

$$\beta_i = \frac{N_{[>i]}}{\delta_s A_\beta \rho_b} \tag{4.21}$$

where β_i is the mole fractions of the surface sorbed species i, ρ_b is the rock bulk density (kg/m^3) and $N_{[>i]}$ is the number of sorbed moles per unit volume (mol./m^3) of the i-th surface species. For the surface cationic sites, the summation of the mole fractions of the free and the occupied site species must be equal to one.

$$\sum_i \beta_i = \beta_{(>X^+)} + \beta_{(>XSO_4^-)} = 1 \tag{4.22}$$

The electrostatic term in eq. 4.18 accounts for the interactions of the ions with the charged surface, such that the mass action equation in eq. 4.16 can be rewritten with surface mole fractions for the surface complex as.

$$K_{int} = \frac{\beta_{(>XSO_4^-)}}{\beta_{(>X^+)} \ a_{SO_4^{2-}}} \chi^{-1} \tag{4.23}$$

Combining eqs. 4.22 and 4.23, eq. 4.24 can be obtained as:

$$\frac{1 + K_{int}\, \chi \ a_{SO_4^{2-}}}{K_{int}\, \chi \ a_{SO_4^{2-}}} \beta_{(>XSO_4^-)} = 1 \tag{4.24}$$

Considering a constant surface potential, the fraction of surface sites covered with SO_4^{2-} can be rewritten as eq. 4.25 such that the electrostatic term is lumped into the isotherm coefficient, K_{ADS}. Whereas the fraction of the surface sites that are free and not covered can be estimated by inserting the solution of eq. 4.25 into eq. 4.26.

$$\beta_{(>XSO_4^-)} = \frac{K_{ADS} \ a_{SO_4^{2-}}}{1 + K_{ADS} \ a_{SO_4^{2-}}} \tag{4.25}$$

$$R = \beta_{(>XSO_4^-)} - \frac{K_{ADS} \ a_{SO_4^{2-}}}{1 + K_{ADS} \ a_{SO_4^{2-}}}$$

Exchangeable-Species Reactions: These types of reactions occur when a charged surface achieves local electrical charge balance by accumulating a particular amount of charge. Then, the exchangeable species (N_{ex}) attached to the surface sites exist in equilibrium with those species in the neighboring aqueous phase. As discussed above, the adsorption of sulfate reduces the surface

charge to allow the surface anionic sites to adsorb a given amount of equivalence of cations from the aqueous phase. Thus, the exchange-species reaction equation is regarded as one exchangeable species replacing another exchangeable species. This exchangeable-species reaction formulation follows the Gaines-Thomas Convention as given by Appelo and Postma [264] for clay mineral (reactions R17 and R18), supposing that Mg^{2+}, Ca^{2+}, and Na^{+} are all involved in the reactions. These reactions are characterized by selectivity coefficients, K_{exch}, like chemical equilibrium constants in aqueous species reactions, such that similar equilibrium conditions must be satisfied:

$$K_{ex,\delta} = Q_{ex,\delta} = \prod_{i=1}^{N_{ex}+N_{aq}} (a_i)^{\nu_{i\delta}} \qquad for\ \delta = 1, \ldots\ldots, R_{ex} \tag{4.26}$$

where $K_{ex,\delta}$ and $Q_{ex,\delta}$ are the selectivity coefficients and activity quotient for the exchange reaction δ, N_{ex} is the number of surface exchangeable species, R_{ex} is the number of exchange reactions, and $\nu_{i\delta}$ is the stoichiometry coefficient of specie i in exchange reaction δ. The selectivity coefficients values, K_{exch}, for the surface sites are uncertain unlike for clay surface sites. Using the mass action law, the selectivity coefficients for the exchanged reactions R17 and R18 can be written as:

$$K_{Na\backslash Ca} = \frac{a_{(>NaX)}\ \left[a_{Ca^{2+}}\right]^{0.5}}{\left[a_{(>CaX_2)}\right]^{0.5}\ a_{Na^{+}}} \tag{4.27}$$

$$K_{Na\backslash Mg} = \frac{a_{(>NaX)}\ \left[a_{Mg^{2+}}\right]^{0.5}}{\left[a_{(>MgX_2)}\right]^{0.5}\ a_{Na^{+}}} \tag{4.28}$$

From eqs. 4.27 and 4.28, the activities of the aqueous species can be easily computed using eq. 4.10, whereas since Gaines-Thomas Convention was used for the exchange reaction formulations, the equivalent fractions, ξ_i, are considered as the activities of the exchangeable species. Thus, the selectivity coefficients can be rewritten as:

$$K_{N\backslash Ca} = \frac{\xi_{(>NaX)}\gamma_{Ca}^{0.5} m_{Ca}^{0.5}}{\xi_{(>CaX_2)}^{0.5}\gamma_{Na} m_{Na}} \tag{4.30}$$

$$K_{Na\backslash Mg} = \frac{\xi_{(>NaX)}\gamma_{Mg}^{0.5} m_{Mg}^{0.5}}{\xi_{(>MgX_2)}^{0.5}\gamma_{Na} m_{Na}} \tag{4.31}$$

The surface site has a constant capacity that is known as cation exchange capacity (CEC). This exchangeable capacity is denoted as the capacity of equivalents per unit rock pore volume, and the unit is eq. /m^3 bulk rock

$$CEC = \delta_s A_\beta \frac{\rho_b(1-\phi)}{\phi} = \frac{1}{\phi}\sum_{i=1}^{N_{ex}} z_i N_{(i-X)} = \frac{1}{\phi}\left(N_{(>NaX)} + 2N_{(>CaX_2)} + 2N_{(>MgX_2)}\right) \tag{4.32}$$

where ϕ is the porosity and z_i is the ion valency for species i (PDI in this context). Thus, the equivalent fractions of individual exchangeable species can be calculated as follows, while their sum should equal unity:

$$\sum_{i=1}^{N_{ex}} \xi_i = \xi_{(>NaX)} + \xi_{(>CaX_2)} + \xi_{(>MgX_2)} = \frac{N_{(>NaX)}}{\phi CEC} + \frac{2N_{(>CaX_2)}}{\phi CEC} + \frac{2N_{(>MgX_2)}}{\phi CEC} = 1 \tag{4.33}$$

Hence, combining eqs. 4.30, 4.31 and 4.33, the resulting equations below can be analytically solved to obtain the equivalent fractions, i.e.

$$R_1 = \xi_{(>NaX)} - K_{Na\backslash Ca}\left(\frac{\xi_{(>CaX_2)}}{\gamma_{Ca} m_{Ca}}\right)^{0.5} \gamma_{Na} m_{Na} \tag{4.34}$$

$$R_2 = \xi_{(>MgX_2)} - \left(\frac{K_{Na\backslash Ca}}{K_{Na\backslash Mg}}\right)^2 \frac{\gamma_{Mg} m_{Mg}}{\gamma_{Ca} m_{Ca}}\, \xi_{(>CaX_2)} \tag{4.35}$$

$$R_3 = \left(1 + \left(\frac{K_{Na\backslash Ca}}{K_{Na\backslash Mg}}\right)^2 \frac{\gamma_{Mg} m_{Mg}}{\gamma_{Ca} m_{Ca}}\right)\xi_{(>CaX_2)} + K_{Na\backslash Ca}\frac{\gamma_{Na} m_{Na}}{(\gamma_{Ca} m_{Ca})^{0.5}}\xi_{(>CaX_2)}^{0.5} - 1 \tag{4.36}$$

4.2.4.2 Surface complexation reactions.

The surface sorption model may be too simplistic to mimic the complex interaction between the aqueous solution and the surface site. The main disadvantage is that it does not take into consideration the electric state of the rock surface, which is known to vary considerably with pH, ionic strength and composition. In contrast, SCMs consider adsorption on the surface together with the formation of the EDL. The main advantage of the SCM is its ability to account for electrostatic interaction separately and variation of pH due to protonation/deprotonation reactions (R19-R20). The aqueous phase during brine-dependent recovery contained a wide variety of PDIs such as Mg^{2+}, Ca^{2+}, SO_4^{2-} and HCO_3^-, while the most dominant are Mg^{2+}, Ca^{2+}, and SO_4^{2-} because of their

relatively higher concentrations. When the aqueous solutions contact the rock surface sites, the typical surface reactions that are to be considered are protonation/deprotonation (reactions R19 and R20), cations affinity (reactions R21 and R22) and anions affinity (reactions R23 and R24), leading to formation of surface species, such as $>CO_3^-$, $>CaOH_2^+$, $>CO_3Ca^+$, $>CO_3Mg^+$, $>CaSO_4^-$, and $>CaCO_3^-$. Each of these reactions has a corresponding mass action equation as below:

$$K_{C1} = \frac{a_{[>CO_3^-]}\, a_{H^+}}{a_{[>CO_3H^o]}}\chi^{-1} = \frac{\beta_{[>CO_3^-]}\, a_{H^+}}{\beta_{[>CO_3H^o]}}\chi^{-1} \tag{4.37}$$

$$K_{C2} = \frac{a_{[>CaOH_2^+]}}{a_{[>CaOH^o]}\, a_{H^+}}\chi^{-1} = \frac{\beta_{[>CaOH_2^+]}}{\beta_{[>CaOH^o]}\, a_{H^+}}\chi^{-1} \tag{4.38}$$

$$K_{C3} = \frac{a_{[>CO_3Ca^+]}\, a_{H^+}}{a_{[>CO_3H^o]}\, a_{Ca^{2+}}}\chi^{-1} = \frac{\beta_{[>CO_3Ca^+]}\, a_{H^+}}{\beta_{[>CO_3H^o]}\, a_{Ca^{2+}}}\chi^{-1} \tag{4.39}$$

$$K_{C4} = \frac{a_{[>CO_3Mg^+]}\, a_{H^+}}{a_{[>CO_3H^o]}\, a_{Mg^{2+}}}\chi^{-1} = \frac{\beta_{[>CO_3Mg^+]}\, a_{H^+}}{\beta_{[>CO_3H^o]}\, a_{Mg^{2+}}}\chi^{-1} \tag{4.40}$$

$$K_{C5} = \frac{a_{[>CaSO_4^-]}\, a_{H_2O}}{a_{[>CaOH_2^+]}\, a_{SO_4^{2-}}}\chi^{-1} = \frac{\beta_{[>CaSO_4^-]}\, a_{H_2O}}{\beta_{[>CaOH_2^+]}\, a_{SO_4^{2-}}}\chi^{-1} \tag{4.41}$$

$$K_{C6} = \frac{a_{[>CaCO_3^-]}\, a_{H_2O}}{a_{[>CaOH^o]}\, a_{HCO_3^-}}\chi^{-1} = \frac{\beta_{[>CaCO_3^-]}\, a_{H_2O}}{\beta_{[>CaOH^o]}\, a_{HCO_3^-}}\chi^{-1} \tag{4.42}$$

where K_{C1}, K_{C2}, K_{C3}, K_{C4}, K_{C5}, and K_{C6} are temperature-dependent stability constants for surface complexation reactions R19-R24. In eqs. 4.37-4.42, the surface species activities are also expressed in terms of the surface mole fractions, which are defined as:

$$\beta_i = \frac{N_{[>i]}}{\phi CEC} \tag{4.43}$$

Moreover, the summation of the surface species mole fractions with the free species mole fractions must equal unity on each surface site. Particularly, eq. 4.44 sums up surface mole fractions for the hydroxylated cationic surface site, while eq. 4.45 sums up those at the protonated anionic surface site:

$$\sum_i \beta_i = \beta_{>CaOH^o} + \beta_{>CaOH_2^+} + \beta_{>CaSO_4^-} + \beta_{>CaCO_3^-} = 1 \tag{4.44}$$

$$\sum_i \beta_i = \beta_{>CO_3H^o} + \beta_{>CO_3^-} + \beta_{>CO_3Ca^+} + \beta_{>CO_3Mg^+} = 1 \tag{4.45}$$

Similar to SSM, the surface potential is related to the rock surface charge by the Grahame equation (eq. 4.19) derived from the Gouy-Chapman theory. If the rock surface has a positive potential, as it is the case for purely calcite carbonate rock, then negatively charged aqueous species, such as SO_4^{2-}, will have a higher activity close to the surface and vice versa. Meanwhile, the electrostatic term, $\chi = \exp(-z\mathcal{F}\psi_o/RT)$, will decrease the activities of ions having the same sign as the charge at the surface, and increase the activities of ions with opposite charge. The presence of charged complexes on the surface site results in non-zero surface charge density, which is the summation of the charge of all the surface complexes as:

$$\sigma_o = \frac{\mathcal{F}\phi CEC}{A_\beta \rho_b}\sum_i z_i\beta_i = \frac{\mathcal{F}\phi CEC}{A_\beta \rho_b}\left(\beta_{>CaOH_2^+} + \beta_{>CO_3Ca^+} + \beta_{>CO_3Mg^+} - \beta_{>CO_3^-} - \beta_{>CaSO_4^-} - \beta_{>CaCO_3^-}\right) \quad (4.46)$$

Combining eqs. 4.37 – 4.42, the equations to solve can be expressed as:

$$R_j = -\log K_j + \log Q_j + \log \chi^{-1} = -\log K_j + \log Q_j + \frac{z\mathcal{F}\psi_o}{\ln 10\, RT} \quad for\ j = 1, \ldots\ldots, N_x \quad (4.47)$$

where j is the j-th equation representing mass action equation for N_x surface reactions, Q_j is the activity product for the j-th mass action equation and ψ_o in eq. 4.47 can be expressed in the form of eq. 4.19 and 4.46 as:

$$\psi_o = \frac{2RT}{\mathcal{F}} sinh^{-1}\left[\frac{\mathcal{F}\phi CEC}{A_\beta \rho_b\sqrt{8000\varepsilon\varepsilon_0 RTI}}\left(\beta_{>CaOH_2^+} + \beta_{>CO_3Ca^+} + \beta_{>CO_3Mg^+} - \beta_{>CO_3^-} - \beta_{>CaSO_4^-} - \beta_{>CaCO_3^-}\right)\right] \quad (4.48)$$

4.3 Coupled Flow and Reaction Model

In this section, all equations that describe all the identified effects are coupled and a numerical solution is provided.

<u>*Governing equations*</u>: For this isothermal process, the number of moles, N_i, of each species is characterized as a function of the gradients in terms of the advective-dispersion transfer, chemical reaction rate variables analogous to the various reactions given in Table 4.1 and external sources/sinks given by the rate of change in the number of moles of species added or subtracted.

The rate of change in the number of moles of each species must satisfy the general conservation equation for all components, N_t, written as:

$$V_b \frac{\partial N_i}{\partial t} + V_b \sum_{j=o,g,aq} \vec{\nabla} \cdot \left(\xi_j y_{ij} u_j - \phi s_j \xi_j D_{ij} \nabla y_{ij}\right) - V_b \frac{\partial \sigma_{i,eq}}{\partial t} - V_b \frac{\partial \sigma_{i,m}}{\partial t} - q_i = 0 \quad for\ i = 1, \ldots\ldots, N_t \quad (4.49)$$

where eq. 4.49 is written in terms of moles per unit time; N_i is the moles per unit bulk volume of the *i*-th component (mol./m^3); N_t is the total number of components/species; V_b is the bulk volume (m^3); q_i is the molar rate of source/sink term for the *i*-th component (mol./s); t is the time (s); ξ_j, s_j and u_j are the molar densities (mol./m^3); saturation (fraction) and Darcy velocity (m/s) of the *j*-th phase; y_{ij} and D_{ij} are the molar fractions and dispersion/diffusion coefficients (m^2/s) of the *i*-th component in the *j*-th phase; $\sigma_{i,eq}$ and $\sigma_{i,m}$ are net moles per unit bulk volume due to equilibrium-controlled and kinetic-controlled reactions representing aqueous/sorption/complexation and mineral surface reactions (mol./m^3) of the *i*-th component respectively. In eq. 4.49, the first term represents the components mass accumulation; the second term represents components' transport that includes advection and dispersion; the third and fourth term represent the components' reaction, both equilibrium and rate dependent; and the last term is the source/sink. The flux component for each phase according to Darcy's law, as theoretically derived from Navier Stokes equation [265], is a function of the phase potential, Φ_j, as represented by:

$$u_j = -k\lambda_{ij} \nabla \Phi_j \qquad for\ j = o,\ g,\ aq \qquad (4.50)$$

with

$$\nabla \Phi_o = \nabla P_o - \gamma_o \nabla \mathrm{D}$$

$$\nabla \Phi_g = \nabla P_o + \nabla P_{cog} - \gamma_g \nabla \mathrm{D}$$

$$\nabla \Phi_{aq} = \nabla P_o - \nabla P_{caqo} - \gamma_{aq} \nabla \mathrm{D}$$

where D is the depth (m); P is the reference pressure (kPa); Φ_j is the pressure potential (kPa) of the *j*-th phase; P_{cj} and γ_j are the capillary pressure (kPa) and pressure gradient (kPa/m) of the *j*-th phase; k is the permeability (m^2) and λ_{ij} is the mobility of the *i*-th component in the *j*-th phase. Inserting eq. 4.50 into eq. 4.49, the new equation becomes:

$$V_b \frac{\partial N_i}{\partial t} - V_b \sum_{j=o,g,aq} \vec{\nabla} \cdot \left(\xi_j y_{ij} k \lambda_{ij} \nabla \Phi_j + \phi s_j \xi_j D_{ij} \nabla y_{ij}\right) - V_b \frac{\partial \sigma_{i,eq}}{\partial t} - V_b \frac{\partial \sigma_{i,m}}{\partial t} - q_i = 0 \qquad (4.51)$$

The above equation is solved by splitting the whole system into finite numbers of spatially discrete subsystems. Large spatial dimensions of each subsystem were applied to capture the macroscopic properties such as the number of moles of each species, saturation, pressure, porosity, permeability, though small enough to avoid characteristic changes in properties of these physical variables within each subsystem. Then, eq. 4.51 can be discretized using finite-difference techniques to provide the solution to the equation in an adaptive-implicit approach. The following general discretized conservation equation can be derived from eq. 4.51.

$$\frac{V_b}{\nabla t}\left({N_i}^{n+1} - {N_i}^{n}\right) - \sum_{j=o,g,aq} \left[\Delta {T_j}^u {y_{ij}}^u \Delta {\Phi_j}^u + \Delta {D_{ij}}^u \Delta {y_{ij}}^u\right] - V_b {r_{i,eq}}^{n+1} - V_b {r_{i,m}}^{n+1} - {q_i}^{n+1} = 0 \qquad for\ i = 1, \dots, N_t \qquad (4.52)$$

with

$$\Delta {\Phi_o}^u = \Delta {P_o}^{n+1} - {\gamma_o}^u \Delta \mathrm{D}$$

$$\Delta {\Phi_g}^u = \Delta {P_o}^{n+1} + \Delta {P_{cog}}^u - {\gamma_g}^u \Delta \mathrm{D}$$

$$\Delta {\Phi_{aq}}^u = \Delta {P_o}^{n+1} - \Delta {P_{caqo}}^u - {\gamma_{aq}}^u \Delta \mathrm{D}$$

where T_j is the transmissibility of j-th phase (mol./kPa/s); $r_{i,eq}$ and $r_{i,m}$ are the equilibrium and mineral surface reaction rates (mol./m^{3}s) of the i-th component, respectively. The subscript n implies the old time step; $n+1$ denotes the new time step; when $u = n$, it denotes explicit gridblocks; while when $u = n+1$, it denotes implicit gridblocks. The discretized equation for hydrocarbon components is expressed as follows:

$$R_i = \frac{V_b}{\nabla t}\left({N_i}^{n+1} - {N_i}^{n}\right) - \sum_{j=o,g,aq} \left[\Delta {T_j}^u {y_{ij}}^u \nabla {\Phi_j}^u + \Delta {D_{ij}}^u \Delta {y_{ij}}^u\right] - V_b {r_{i,eq}}^{n+1} - {q_i}^{n+1} \qquad for\ i = 1, \dots\dots, N_c \qquad (4.53)$$

The discretized equation for aqueous components is:

$$R_i = \frac{V_b}{\nabla t}\left({N_i}^{n+1} - {N_i}^{n}\right) - \Delta {T_{aq}}^u {y_{iaq}}^u \left(\Delta P^{n+1} - \Delta {P_{caqo}}^u - {\gamma_{aq}}^u \Delta \mathrm{D}\right) - \Delta {D_{ij}}^u \Delta {y_{iaq}}^u - V_b {r_{i,eq}}^{n+1} - V_b {r_{i,m}}^{n+1} - {q_i}^{n+1} \qquad for\ i = 1, \dots\dots, N_a \qquad (4.54)$$

The solid phase is considered immobile and hence, the flux of components (transport term) at the surface by surface sorption or complexation reactions is zero. The discretized equation for components at the surface site is expressed as:

$$R_i = \frac{V_b}{\nabla t}\left({N_i}^{n+1} - {N_i}^{n}\right) - V_b {r_{i,eq}}^{n+1} - {q_i}^{n+1} \qquad for\ i = 1, \ldots\ldots, N_x \qquad (4.55)$$

where N_x is the number of surface reactions either surface sorption (4 reactions) or complexation (6 reactions). The rate of formation or consumption of different aqueous component during mineral dissolution or precipitation is given by:

$$r_{i,m} = s_w \sum_{\beta=1}^{R_m} \nu_{i\beta}\ r_\beta \qquad for\ i = 1, \ldots\ldots, N_m + N_{aq} \qquad (4.56)$$

where s_w is the water saturation (fraction) and $\nu_{i\beta}$ is the the stoichiometry coefficient of the i-th component in mineral reaction β. The same equation as eq. 4.56 can be written for the rate of production or destruction of an aqueous component from an equilibrium reaction, α. However, the rate law in eq. 4.56 does not directly apply to equilibrium reactions because they are considered extremely fast. An approximate description of the equilibrium reaction would require an infinite rate constant. The application of eq. 4.56 will result in an infinite reaction rate for the components engaged in equilibrium reactions. Therefore, the equilibrium term, $r_{i,aq}$, in eq. 4.52 is often handled by the application of a linear transformation known as *Equilibrium Rate Annihilation* (ERA) matrix. Application of ERA matrix eliminates the equilibrium reaction terms and reduces the number of equations sets by the number of equilibrium reactions. Detailed explanation can be found in Nghiem *et al.* [252] and Nghiem *et al.* [253]. The discretized equation for mineral components can be expressed as:

$$R_i = \frac{V_b}{\nabla t}\left({N_i}^{n+1} - {N_i}^{n}\right) - V_b {s_w}^{n+1} \sum_{\beta=1}^{R_m} \nu_{i\beta}\ {r_\beta}^{n+1} \qquad for\ i = 1, \ldots\ldots, N_m \qquad (4.57)$$

It is crucial to ensure that the difference between the sum of phase volumes and the pore volumes be equal to zero by employing the volume constraint equation

$$\sum_{j=o,g,aq}\left[\frac{\sum_{i=1}^{N_t} N_{ij}^{\;\;n+1}}{\left(\rho_j\, s_j\right)^{n+1}}\right]-\phi^{n+1}=0 \tag{4.58}$$

The phase saturation is calculated using eq. 4.59 while satisfying the normalization condition in eq. 4.60.

$$s_j=\frac{\frac{\sum_{i=1}^{N_t} N_{ij}}{\rho_j}}{\sum_{j=o,g,aq}\left[\frac{\sum_{i=1}^{N_t} N_{ij}}{\rho_j}\right]} \tag{4.59}$$

$$\sum_{j=o,g,aq} s_j=1 \tag{4.60}$$

Initial and Boundary Conditions: The initial conditions are set by an appropriate choice of variables such as pressure, saturation, and concentrations at the initial time. A typical choice of the initial conditions representing a laboratory water flood test is homogeneous initial saturation, pressure and species concentrations. The boundary conditions are specified such that the reservoir is surrounded by impermeable sides and no flow boundary condition applies. Meanwhile, the inner boundary conditions can be specified as injection/production rates or inlet well pressure, and the outer boundary condition is usually given by the outlet well pressure. For a typical laboratory test domain with a cylindrical shape, one facet corresponds to the injection surface (inlet), the other facet corresponds to the production surface (outlet), and the side surface is impermeable.

Numerical Solution Approach: The total components in the aqueous phase $\left(N_{aq}\right)$ consist of soluble hydrocarbon components (N_c) and aqueous components (N_a). The elimination of the equilibrium reactions term from eq. 4.54 using ERA matrix reduces the discretized for aqueous components to only primary aqueous components. Then, the number of all conservation equations including hydrocarbon and aqueous components becomes $N_{ia}+N_c$. The addition of N_x conservation equations for N_k surface sorbed/complexed species given by eq. 4.55 and $N_{ia}+N_c$ conservation equations eliminates the equilibrium term accounting for sorption/complexation reaction rates. Hence, the discretized equation for $N_{ia}+N_c$ components can be expressed as:

$$R_i = \frac{V_b}{\nabla t}\left(\left(N_i + \sum_{\alpha=N_{ia}+1}^{N_a} \nu_{i\alpha}\, N_\alpha + \sum_{k=1}^{N_x} \nu_{ik}\, N_k\right)^{n+1} - \left(N_i + \sum_{\alpha=N_{ia}+1}^{N_a} \nu_{i\alpha}\, N_\alpha + \sum_{k=1}^{N_x} \nu_{ik}\, N_k\right)^{n}\right)$$
$$- \sum\nolimits_{j=o,g,aq}\left[\Delta T_j{}^u\left(y_{ij} + \sum_{\alpha=N_{ia}+1}^{N_a} \nu_{i\alpha}\, y_{\alpha j}\right)^u \Delta\Phi_j{}^u\right.$$
$$\left. - \Delta D_{ij}{}^u\left(\Delta y_{ij} + \sum_{\alpha=N_{ia}+1}^{N_a} \nu_{i\alpha}\, \Delta y_{\alpha j}\right)^u\right] - V_b s_w{}^{n+1} \sum_{\beta=1}^{R_m} \nu_{i\beta}\; r_\beta{}^{n+1}$$
$$- q_i{}^{n+1} \qquad for\ i = 1, \ldots\ldots, N_{ia} + N_c \tag{4.61}$$

There are $N = N_{ia} + 3N_c + N_x + R_{aq} + N_m + 1$ nonlinear algebraic differential equations that can be used to find solutions to the same number of unknown variables as summarized below:

- $2N_c$ phase-equilibrium equations [eqs. 4.4 and 4.5]
- R_{aq} chemical equilibrium equations [eq. 4.7]
- N_x surface sorption [eqs. 4.25, 4.34 – 4.36] or complexation equations [eq. 4.47]
- $N_{ia} + N_c$ hydrocarbon and aqueous component conservation equations [eq. 4.61]
- N_m mineral component conservation equations [eq. 4.57]
- Volume-constraint equation [eq. 4.58]

The identified primary unknown variables are:

- Pressure
- Summed number of moles of hydrocarbon components in all phases, $N_i \quad for\ i = 1, \ldots\ldots, N_c$
- Number of moles of aqueous (primary and secondary) components, $N_i \quad for\ i = 1, \ldots\ldots, N_a$
- Number of moles of hydrocarbon components soluble in the aqueous phase, $N_{i,aq}$
- Number of moles of hydrocarbon components in the gaseous phase, $N_{i,g} \quad for\ i = 1, \ldots\ldots, N_c$
- Number of moles of minerals, $N_i \quad for\ i = 1, \ldots\ldots, N_m$
- Number of moles of sorbed or complexed species, $N_i \quad for\ i = 1, \ldots\ldots, N_x$

For more detailed information about the numerical solution approach used to solve the non-linear systems of algebraic equations, reference is made to the work of Behie *et al.* [266], Nghiem and

Rozon [267] and Nghiem *et al.* [252]. This solution method allows simultaneous convergence of the transport, phase-equilibrium, chemical equilibrium, reaction kinetic equations using Newton's iteration method at each time step of the form:

$$\vec{\xi}^{(k+1)} = \vec{\xi}^{(k)} - J_{\vec{R}}{}^{-1}\left(\overrightarrow{R(\xi)}\right)^{(k)} \tag{4.62}$$

where $\overrightarrow{R(\xi)}$ is the vector of all grid-block system of N algebraic equations including well constraints; $\vec{\xi}$ is the vector of N reservoir unknown variables including bottom-hole flowing pressure; $J_{\vec{R}} = \left(\frac{\partial \overrightarrow{R(\xi)}}{\partial \vec{\xi}}\right)^{k}$ is the Jacobian matrix of the system of N algebraic equations. The Jacobian matrix in eq. 4.62 is a sparse matrix that is solved by a preconditioned Incomplete LU (ILU) factorization method followed by the GMRES iterative method until the iterations converged. The convergence is achieved when the residual norm is less than the desired tolerance value. The development of this numerical model was carried out in CMG GEM^{TM}. The usage of an adaptive-implicit method for discretization means that some grid blocks are treated as implicit pressure, explicit compositions and saturations (IMPECS) blocks and others are treated as fully implicit. For both cases, the phase equilibrium equations (eq. 4.4 and 4.5), the chemical equilibrium equations (eq. 4.7), sorption/complexation reaction equations (eqs. 4.25, 4.34 – 4.36, 4.47), mineral material balance equations (eq. 4.57) and the volume constraint equation (eq. 4.58) do not involve variables in neighboring grid blocks and they are eliminated in a pre-processing step through a partial Gaussian elimination. The partial Gaussian elimination decouples all equations except the conservation equation to solve pressure and moles of $N_{ia} + N_c$ components for implicit blocks, while other variables are calculated through back substitution. In the case of IMPECS blocks, only the pressure variable is solved from the conservation equations and other variables are explicitly calculated. During each time step calculation, the phase saturations are calculated using eq. 4.60, while the flow functions are updated as described below.

4.4 Summary of Experimental Data

The model was validated by comparing its performance with independently-sourced experimental data. Here, single-phase flow-through tests conducted on similar rock type were used to study the

surface chemistry and retrieve thermodynamic parameters. The linear 1-D simulations considered for all core experiments were discretized uniformly into 200 × 1 × 1 grid blocks to reduce numerical dispersion effects with the properties described in Table 4.2. As previously mentioned, one major challenge is the uncertainty in the input parameters for the surface reactions and to overcome this challenge, validation of the model with the observed experimental trend was conducted, and the output was used in predicting different brine-dependent recovery cases in Chapter 5. The reported effluent concentrations of PDIs were used to track surface composition changes with fluid compositions listed in Table 4.3.

Table 4.2—Summary of core properties used in simulating different single-phase flow through experiments to retrieve thermodynamic parameters for intact carbonate rocks.

Property	**Core 2-21[a]**	**Core CM-1[b]**	**Core 1/4[a]**	**Core 7/1[c]**	**LSSK#5[d]**	**SCC#1[d]**
Core type material	Middle Eastern reservoir limestone	Stevns Klint outcrop chalk	Stevns Klint outcrop chalk	Stevns Klint outcrop chalk	Stevns Klint outcrop chalk	Stevns Klint outcrop chalk
Porosity (%)[f]	24.7	47.1	45	48.9	46	45
Mineral Volume (%)						
Calcite	69.2	52.9	55	51	54	55
Dolomite	6.1					
Permeability (mD)	2.7	1.2	2.5	2.5	2	2
Saturation fluids						
Initial water		ZP	SW-U	SW-U	SW-0T	SW-0T
Saturation (%)	ZP	100	100	100	10	100
AN (mg KOH/g oil)	100				1.90	
Operating conditions						
Pressure (psi)	101.5	101.5	101.5	101.5	101.5	101.5
Temperature (ºC)	20,70,100,130	23, 130	23	23,70,100,130	23	23
Flow Rate (cm^3/min)	0.1	0.2	0.2	0.2	0.2	0.2
Core Dimensions						
Diameter (cm)	3.78	3.57	3.78	3.81	3.81	3.81
Length (cm)	4.91	6.23	7.30	8.00	7.00	7.00
Pore Volume (cm^3)	13.6	29.3	36.9	44.7	36.7	35.9

Note: The specific surface area for calcite in limestone and chalk cores were retrieved from Shariatpanahi *et al.* [112] as 0.29 m^2/g and 1.70 m^2/g respectively. Sources: [a] Data retrieved from Strand *et al.* [53], [b] Data retrieved from Zhang *et al.* [32], [c] Data retrieved from Strand *et al.* [54], and [d] Data retrieved from Fathi *et al.* [38]. [f] The porosity values used for simulating chalk experiments were approximated from the range of porosity given in the respective references.

With the intention of analyzing the interplay between the PDI cations (Ca^{2+} and Mg^{2+}), the data reported by Strand *et al.* [53] and Zhang *et al.* [32] at different temperatures was examined, even though they belong to different rock lithology. In the work by Zhang *et al.* [32] on outcrop chalk cores, core plugs were initially fully saturated with ZP brine and flooded with CF-M brine at 23 and 130 °C. It was emphasized that production of both ions was delayed as compared to the tracer ion (SCN^-), and Ca^{2+} was adsorbed more on the surface at 23 °C, while at 130°C, Mg^{2+} was adsorbed more and it substituted Ca^{2+} at the surface. Likewise, Strand *et al.* [53] used similar brines at a lower injection rate on Middle Eastern limestone cores at 20, 70, 100 and 130 °C. More comprehensive observations were made similar to that of Zhang *et al.* [32], where Mg^{2+} adsorbed more than $Ca^{2+,}$ and no substitution at the surface was reported. However, this interplay was reported to behave differently in the presence of PDI anion (SO_4^{2-}).

Table 4.3—Fluid compositions and properties used in the simulation.

Ions (M)	**ZP**	**CF-M**	**SW-U**	**SW-½M**	**SW-M**	**SW-0T**	**SW-1T**
Na^+	0.573	0.504	0.500	0.475	0.450	0.460	0.393
K^+	0	0	0.010	0.022	0.034	0.010	0.034
Li^+	0	0	0	0	0	0	0.024
Ca^{2+}	0	0.013	0.013	0.013	0.013	0.013	0.013
Mg^{2+}	0	0.013	0.045	0.045	0.045	0.045	0.045
HCO_3^-	0	0	0.002	0.002	0.002	0.002	0.002
Cl^-	0.573	0.556	0.623	0.574	0.525	0.583	0.492
SCN^-	0	0.013	0	0.012	0.024	0	0.024
SO_4^{2-}	0	0	0	0.012	0.024	0	0.024
TDS (g/L)	33.39	33.40	35.71	35.68	35.72	33.39	33.39
Ionic Strength	0.573	0.589	0.684	0.680	0.682	0.644	0.649

Note: ZP brine contains 0.573M NaCl—similar ionic strength with seawater (SW); CF-M brine contains equal amount of Ca^{2+} and Mg^{2+} and SCN^-—also similar ionic strength with SW; SW-U/SW-0T, seawater-like brine with no SO_4^{2-} and SCN^-; SW-½M, seawater-like brine with equal amount of SO_4^{2-} and SCN^-, but half of SO_4^{2-} in SW; SW-M/SW-1T, seawater-like brine with equal amounts of SO_4^{2-} and SCN^-, but same amount as SO_4^{2-} in SW; and CF-M, NaCl solution with equal amounts of Ca^{2+}, Mg^{2+} and SCN^-, but same amount as Ca^{2+} in SW. Sources: Data with ZP, CF-M retrieved from Zhang *et al.* [32] and Strand *et al.* [53]; SW-U, SW-M retrieved from Strand *et al.* [54]; SW-0T and SW-1T retrieved from Fathi *et al.* [38]. The pH was not reported in these studies references, but was adapted after pH values reported for brines with similar ionic strength in the work of Gupta *et al.* [61] at 95 ºC, pH 6 — ionic strength of about 3.63 for a typical reservoir FW and pH of 6.7 — ionic strength about 0.66 for typical SW.

In the work of Strand *et al.* [54], the cores initially saturated with SW-U were flooded with SW-M at 23, 40, 70, 100 and 130 °C to evaluate the inherent behavior in the presence of SO_4^{2-}. A delay

in the concentration of SO_4^{2-} in the effluent was observed as compared to the tracer ion and the delay increased with temperature. Meanwhile, in the presence of increased SO_4^{2-} adsorption, Ca^{2+} concentration in the effluent also decreased with temperature (though Mg^{2+} effluent concentrations were not reported). This trend indicates that the interplay between the PDI cations is reversed as compared to the trend observed in the absence of PDI anion. On the contrary, considering other studies by Zhang *et al.* [32], Strand *et al.* [53] and Shariatpanahi *et al.* [112], where changes in molar concentrations of PDIs were monitored with temperature during seawater flooding in seawater-saturated cores. It was observed that SO_4^{2-} affinity and PDI cations interplay (where Mg^{2+} adsorbed more than Ca^{2+}) increased with temperature. However, it was only evident, at temperatures above 100 °C, that Mg^{2+} substituted Ca^{2+}.

4.5 Validation of Surface Sorption Model

For the wide range values for site capacity, 3 sites/nm^2 equivalent to 4.98 μmol./m^2 or μeq/m^2 was assumed in this validation. Therefore, all obtained thermodynamic parameters are based on this specific value of site capacity. The dispersion/diffusion coefficient was determined by reproducing the effluent concentration curves of the tracer ions (SCN^-) from each flow-through experiment.

4.5.1 Temperature-Dependent Competition between PDI cations:

Limestone: At first, the competition between Ca^{2+} and Mg^{2+} in the absence of PDI anion documented in the study by Strand *et al.* [53] was modeled at different temperatures with experimental details as listed in Table 4.2. The results, in terms of relative concentrations of the effluent to those injected, are shown in Figure 4.2, where the simulated concentration profiles fit well with that of the experiments. The simulated profiles were obtained without considering the surface adsorption reaction R16 and mineral reactions R13-R15. The fact that the relative concentrations of Ca^{2+} and Mg^{2+} reached one later than that of SCN^- at all considered temperature indicates that SCN^- did not participate in the surface chemistry and it behaved as inert. The tracer ion travels with no retention as it breakthroughs sooner compared to the retarded PDI cations. At the low temperatures of 20 and 70 °C, both Ca^{2+} and Mg^{2+} showed nearly similar affinity towards the rock surface; however, Ca^{2+} adsorbed more at 20 °C while Mg^{2+} adsorbed more at 70 °C.

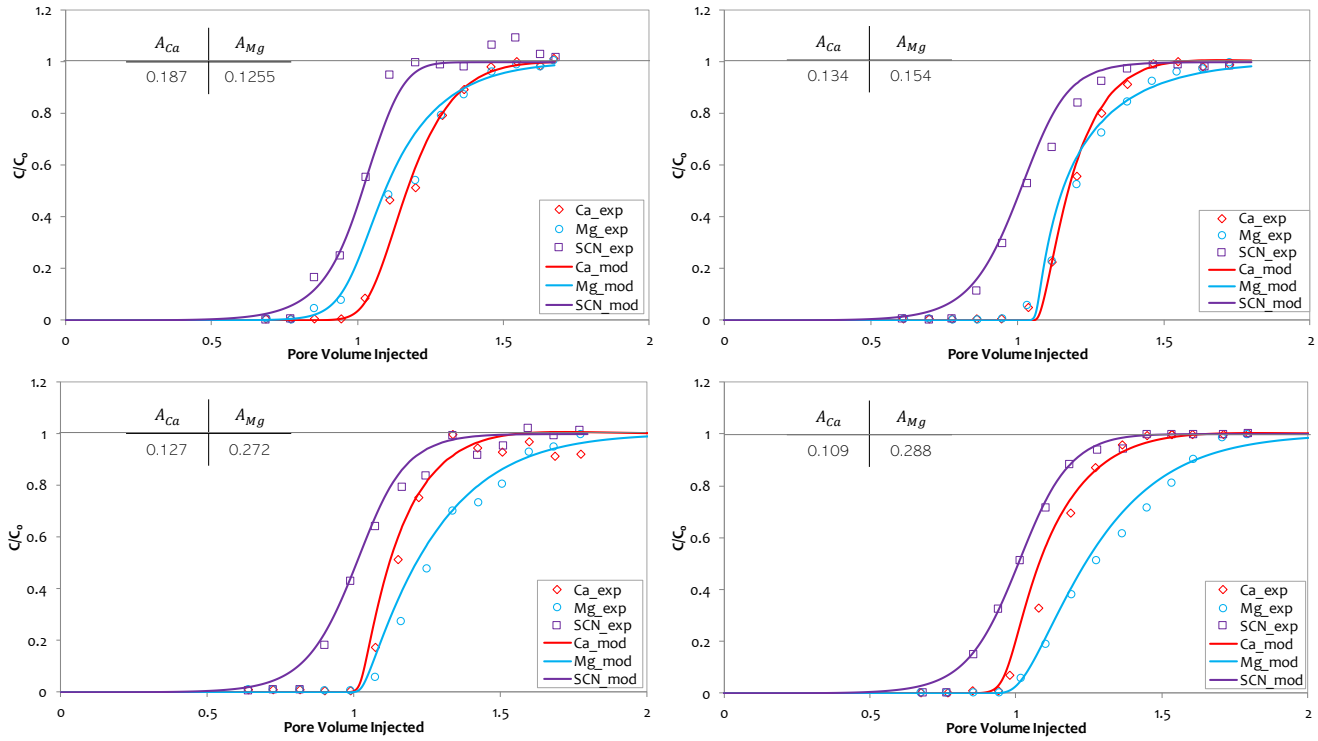

Figure 4.2—Simulated and experimental breakthrough curves of Ca^{2+} and Mg^{2+} from CF-M brine on limestone core 2-21 at various experimental temperatures: 20 °C (*top left*), 70 °C (*top right*), 100 °C (*bottom left*), and 130 °C (*bottom right*). Data points connote measured datasets, and solid-lines represent the model results; subscripts "*exp*" and "*mod*" in the legend are the experimental (Strand *et al.* [53]) and predicted values

When the temperature was increased to 100 and 130 °C, Mg^{2+} became more strongly adsorbed compared to Ca^{2+} as indicated by the larger adsorption area in Figures 4.2. This trend was captured by interpolating between exchange coefficients ratios (ratio of exchange coefficient for reaction R17 over that of R18) reported in Table 4.4 for the considered temperature. The exchange coefficient ratio is less than one at 20 °C because Ca^{2+} adsorbed comparably more than Mg^{2+} and exponentially increased as temperature increased indicating increased Mg^{2+} adsorption (see Figure 4.3). Consequently, the set of exchange coefficients so obtained has been proven to be valid by perfectly reproducing the breakthrough curves at 100 °C. Similarly, the areas between Ca^{2+} and Mg^{2+} simulated curves and SCN^- simulated curve (known as the adsorption area) was also calculated at the different temperatures. It was noted that when the temperature is increased, an increase in the Mg^{2+} adsorption area is accompanied by a simultaneous decrease in the adsorption area for Ca^{2+} (see the calculated areas in Figure 4.2). The impact of the increased exchange

coefficient ratios with temperature could also be seen on the equivalent fractions of Ca^{2+} and Mg^{2+} on the rock surface in Figure 4.4. The difference between the two ions adsorbed on the rock becomes larger as temperature increased beyond 70 °C. As previously highlighted in Chapter 3 (see Table 3.1), Mg^{2+} has a lower ionic radius and it becomes strongly hydrated because of its lower hydration energy compared to Ca^{2+}, which is why at an elevated temperature Mg^{2+} partly dehydrates and becomes more reactive.

Table 4.4—Surface reactions and summary of equilibrium constants at different temperatures. These values were obtained from the best-matched simulation run after conducting a series of simulation

		$\mathbf{Log}\, K_{ex}$		
Surface Sorption Reactions		$T = 20$ ℃	$T = 70$ ℃	$T = 130$ ℃
$Na^+ + \frac{1}{2} > CaX_2 \Leftrightarrow \frac{1}{2}Ca^{2+} + > NaX$	(1)	-1.208	-1.444	-1.237
$Na^+ + \frac{1}{2} > MgX_2 \Leftrightarrow \frac{1}{2}Mg^{2+} + > NaX$	(2)	-1.125	-1.468	-1.398
Exchange coefficient ratios		0.833	1.058	1.450
Exchange coefficient ratios with maximum sulfate adsorbed		0.416	0.417	1.000
$> X^+ + SO_4{}^{2-} \Leftrightarrow \quad > XSO_4{}^-$	(3)	2.477	2.778	3.130

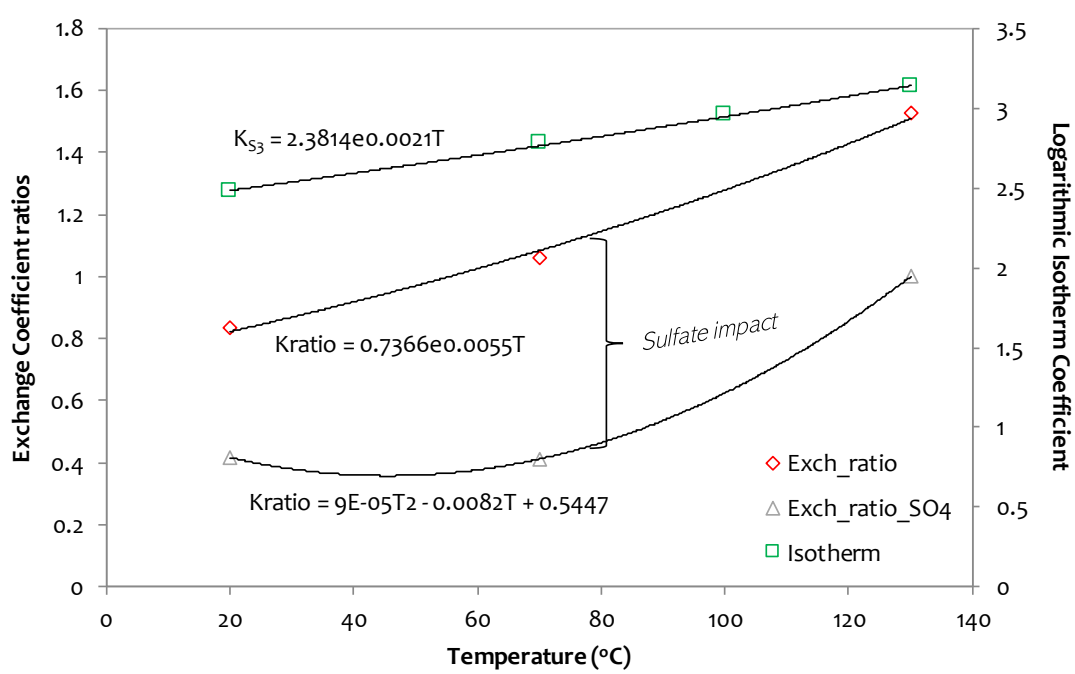

Figure 4.3—Relationship of exchange and isotherm coefficients with temperature

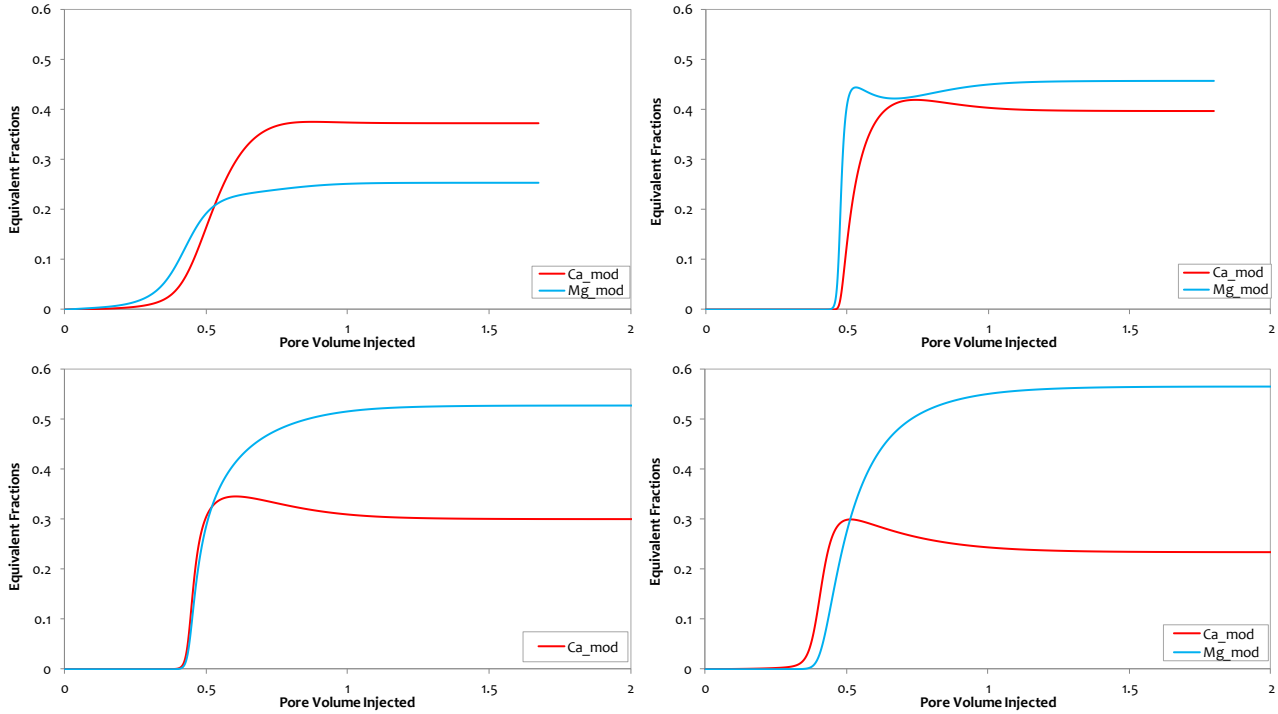

Figure 4.4—Simulated surface fractions of Ca^{2+} ($> CaX_2$) and Mg^{2+} ($> MgX_2$) along the mid-section of the limestone core 2-21 at various experimental temperatures: 20 °C (*top left*), 70 °C (*top right*), 100 °C (*bottom left*), and 130 °C (*bottom right*)

Chalk: Chalks are often considered to have a higher surface area and reactivity compared to limestones. A similar study conducted on Stevns Klint chalk by Zhang *et al.* [32] was examined to see if similar exchange coefficients listed in Table 4.4 could be used to replicate the experimental concentration profiles. Figure 4.5 shows that the experimental data at 23 and 130 °C could be fitted into the model with similar exchange coefficient values and ratios, which further validates the exchange coefficient. The breakthrough curve of chalk at 23 °C showed a wider gap between Ca^{2+} and Mg^{2+} curves compared to the limestone breakthrough curve at 20 °C in Figure 4.2. The systematic differences between the predicted and experimental curves (Figure 4.5) could be because the exact porosity for this experiment was not reported, hence the exact exchange capacity could not be used. However, the breakthrough curve of chalk in Figure 4.5 was nevertheless fairly reproduced by the same exchange coefficients. Meanwhile, the breakthrough curve at 130 °C showed a much more Mg^{2+} adsorption and possible substitution of Ca^{2+} by Mg^{2+}, which the model captured reasonably well. Modeling of different rock lithologies with same exchange coefficients suggests that there is no significant discrepancy with respect to the interplay

between Ca^{2+} and Mg^{2+} at the different rock surfaces even though they have different diagenesis and surface area.

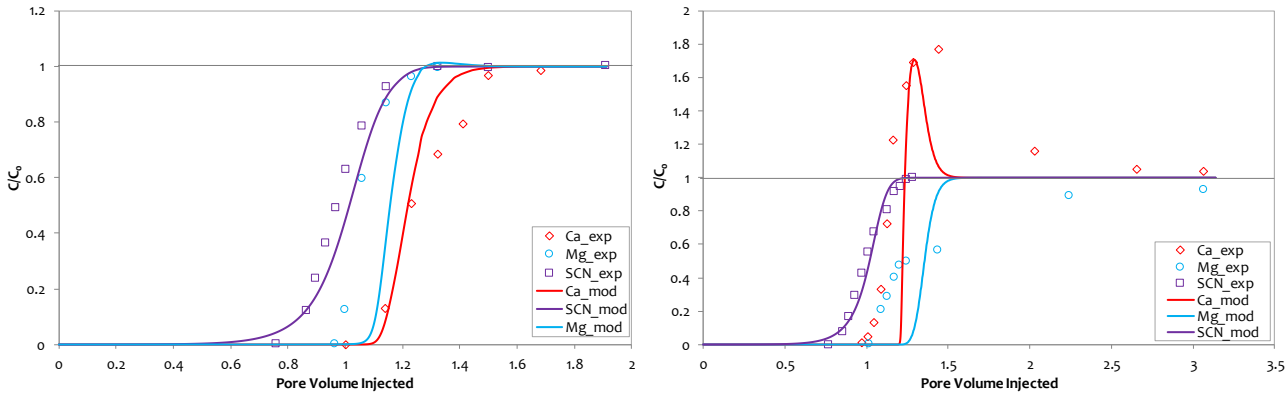

Figure 4.5—Simulated and experimental breakthrough curves of Ca^{2+} and Mg^{2+} from CF-M brine on chalk core CM-1 23 °C (*left*) and 130 °C (*right*). Data points connote measured datasets from Zhang *et al.* [32], and lines represent the model results.

4.5.2 Competition between PDI cations in the presence of PDI anion:

The next step in the surface chemistry study was to consider the interplay between the cations in the presence of SO_4^{2-}. It was further demonstrated that no significant difference exists between the interplay at chalk and limestone surfaces by analyzing the room-temperature data of Strand *et al.* [127] on chalk cores and Strand *et al.* [53] on limestone cores. It is to be noted that in both sets of experiments, the rock was initially saturated with SW-U. In the study by Strand *et al.* [53], the pore fluid was displaced by SW-½M, which is a similar seawater-like brine but containing 0.012M of SO_4^{2-} and SCN^-. As shown in Figure 4.6, the concentration of Ca^{2+} and Mg^{2+} were comparably close to the initial pore fluid concentration, and both concentrations remained consistent until the breakthrough of SO_4^{2-} at the core outlet. It is noted yet again that SO_4^{2-} is delayed compared to the tracer ion SCN^- indicating the affinity of SO_4^{2-} to the rock surface. Because of SO_4^{2-} adsorption, Ca^{2+} was co-adsorbed, resulting in its decreased effluent concentration as compared to Mg^{2+}. The interplay observed between the PDI cation is quite like what was observed when both ions were present in equal concentrations at 20 °C (see Figure 4.2). Therefore, the first modeling attempt was to use the exchange coefficients previously established. However, as evident from Figure 4.6 (dotted line), this attempt failed to replicate the experiment results. This suggests that the

established exchange coefficients used were not enough to capture the dynamic interplay triggered by the presence of SO_4^{2-}. However, SO_4^{2-} and SCN^- breakthrough curves were reasonably replicated using isotherm coefficient reported in Table 4.4.

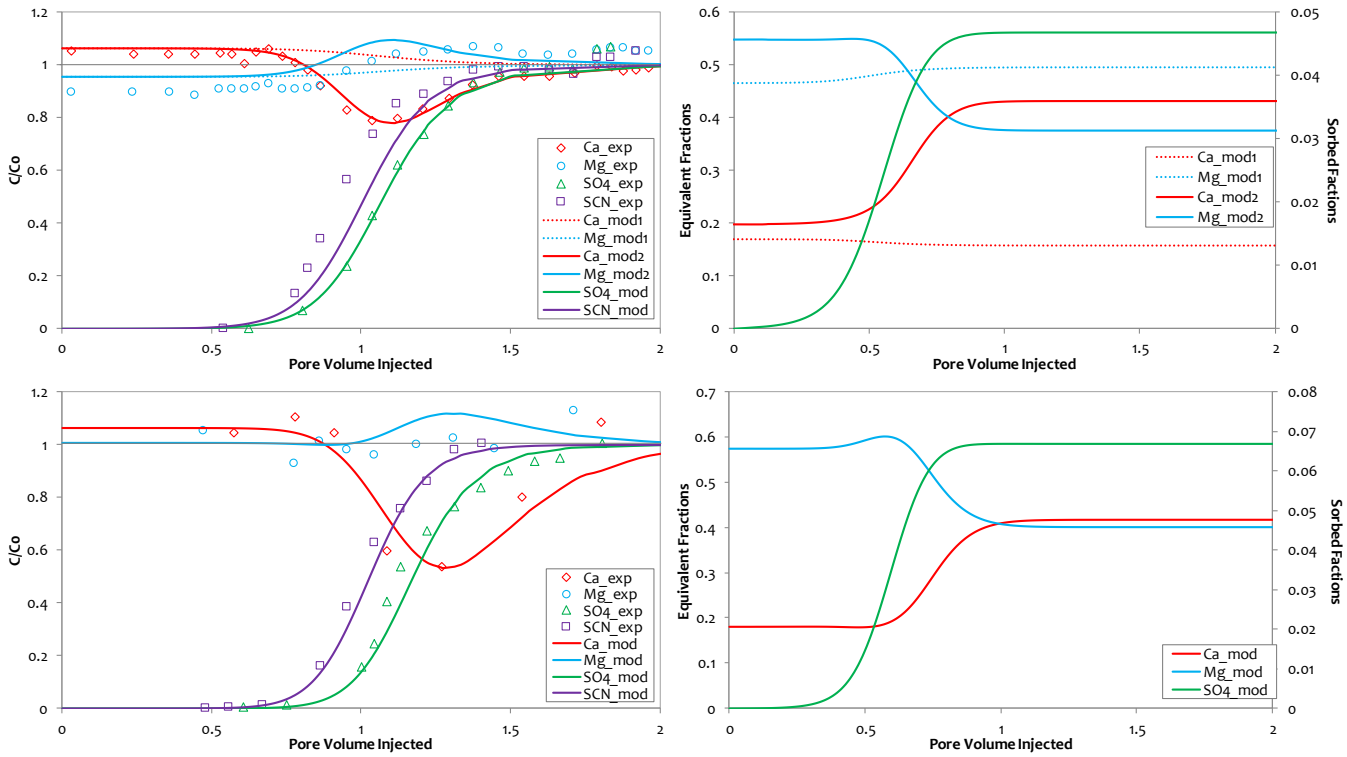

Figure 4.6—Simulated and experimental breakthrough curves of Ca^{2+}, Mg^{2+} and SO_4^{2-} at room temperature from SW-½M brine on limestone core 2-21 (*top left*), SW-M brine on chalk core ¼ (*bottom left*), and simulated surface fractions of Ca^{2+} ($> CaX_2$), Mg^{2+} ($> MgX_2$) and SO_4^{2-} ($> XSO_4^-$) along the core mid-section of the limestone core 2-21 (*top right*) and chalk core ¼ (*bottom right*). Data points connotes measured datasets from Strand *et al.* [53] as plotted in the *top left* panel and from Strand *et al.* [127] as plotted in the *top right* panel, lines represent the model results and the dotted lines represent the first attempt at modeling the experimental data

On further consideration, an interpolation technique was used where the upper boundary is the established exchange coefficients when SO_4^{2-} is absent and the lower boundary is the exchange coefficient ratios at maximum SO_4^{2-} adsorption as illustrated in Figure 4.3. The corresponding exchange coefficient ratio is obtained by interpolation between these boundary values using the corresponding amount of adsorbed SO_4^{2-} (see Table 4.4). Key steps adopted in obtaining the representative thermodynamic parameters are explained using below conceptual flow diagram.

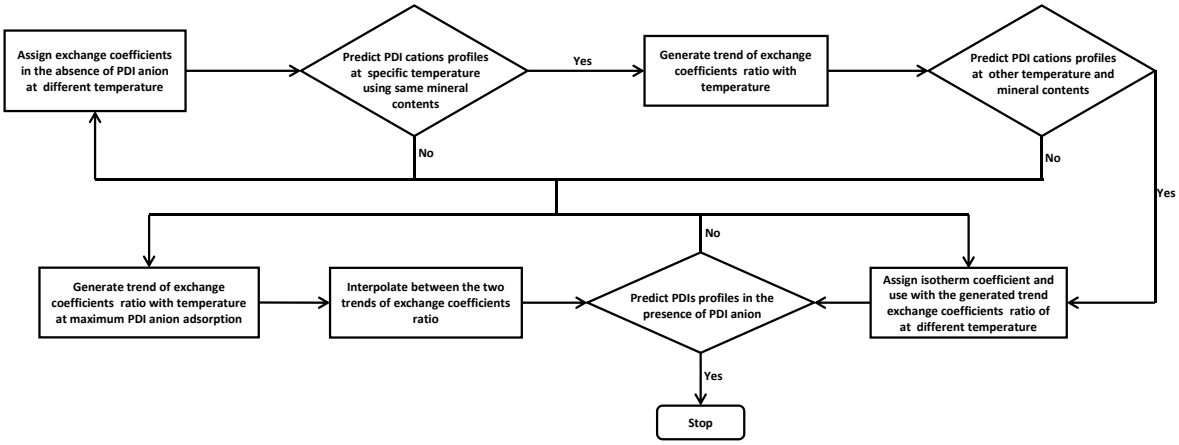

Figure 4.7—Flow chart algorithm used to investigate thermodynamic parameters

A lower exchange coefficient ratio suggests that Ca^{2+} maintains stronger affinity to the rock surface compared to Mg^{2+}. With this interpolation technique, the co-adsorption of Ca^{2+} as SO_4^{2-} adsorbed was well replicated (see the *top left* panel in Figure 4.6 denoted by the solid lines). The impact of the decreased exchange coefficient ratio could be seen on the surface fractions of Ca^{2+}, Mg^{2+} and SO_4^{2-}. In both the injected and initial pore brines, Mg^{2+} concentration quadrupled Ca^{2+} concentration, which accounted for Mg^{2+} overriding Ca^{2+} at the surface, even though Mg^{2+} is strongly hydrated at a lower temperature. In addition, SO_4^{2-} only occupied less than 5% of the positively charged surface site. In the first model, denoted by the dotted line in Figure 4.6, no significant interplay occurred between Mg^{2+} and Ca^{2+}; however, the second model reasonably captured the interplay responsible for Ca^{2+} co-adsorption. Using similar exchange and isotherm coefficients, the model was able to capture similar observed experimental trend in chalk cores as reported by Strand *et al.* [127] (see the *bottom* panels in Figures 8). Further emphasis was therefore placed on the fact the model could simulate surface chemistry of chalk and limestone cores with similar thermodynamic parameters.

Temperature-Dependent Interplay: Just as elucidated above, the presence of SO_4^{2-} considerably changed the dynamics of the interplay at room temperature. Therefore, it was deemed essential to examine the effect of temperature variation on the dynamics of the interplay. This was achieved by analyzing the study by Strand *et al.* [54] where chalk core initially saturated with SW-U was flooded at different temperatures (23, 40, 70, 100 and 130 °C) with SW-M (containing an equal

amount of SO_4^{2-} and SCN^-). At 23 °C, the observed trend is similar to that reported by Strand *et al.* [127], which the model excellently captured in Figure 4.6. The experimental and simulated breakthrough curves at various temperatures (40, 70, 100 and 130 °C) are shown in Figure 4.8. The areas between the tracer and SO_4^{2-} breakthrough curves (known as SO_4^{2-} adsorption area) increased as the temperature increased, which indicates that SO_4^{2-} adsorption to the positively charged surface site steadily increased with temperature. This increase in SO_4^{2-} adsorption appears to be more pronounced as the temperature is raised above 100 °C. The trend of increased SO_4^{2-} adsorption is captured by the increasing isotherm coefficient presented in Figure 4.3.

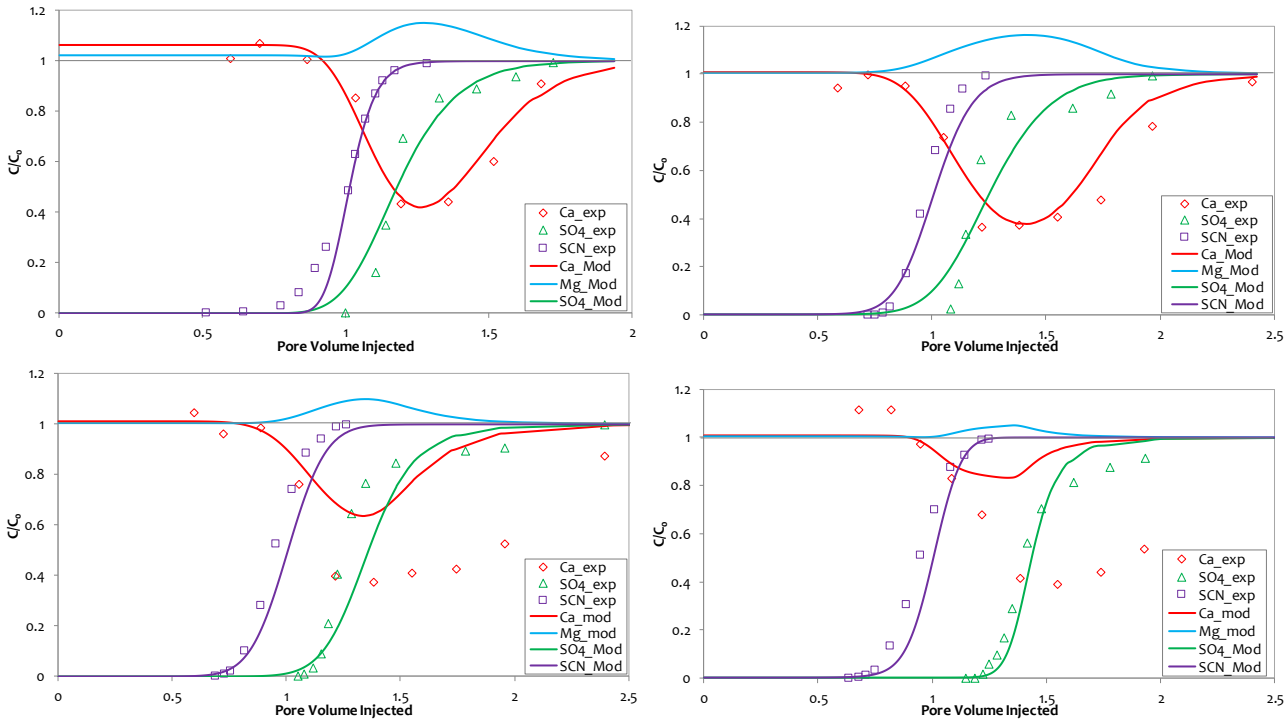

Figure 4.8—Simulated and experimental breakthrough curves of Ca^{2+}, Mg^{2+}, SCN^-, and SO_4^{2-} from SW-M brine on chalk core 7/1 at various experimental temperatures: 40 °C (*top left*), 70 °C (*top right*), 100 °C (*bottom left*), and 130 °C (*bottom right*). Experimental data are taken from Strand *et al.* [54].

A similar approach used to capture the interplay between PDI cations at room temperature was also applied to capture the interplay at 70 °C. This was also tested to predict the interplay at 40 °C. The resulting simulated breakthrough curves perfectly reproduced the experimental curves as shown in Figure 4.8. Same exchange coefficient ratio was maintained to capture the increased co-adsorption of Ca^{2+} as SO_4^{2-} adsorption increased with temperature. However, at higher

temperature, it has been reported that Mg^{2+} adsorbed more and even substituted Ca^{2+} at the rock surface [32, 53, 112], an observation not captured by Strand *et al.* [54] in their study. Furthermore, the authors mentioned that the co-adsorption of Ca^{2+} decreased as temperature goes beyond 70 °C. Accordingly, an exchange coefficient ratio of one was maintained to imply that both Ca^{2+} and Mg^{2+} have a similar affinity towards the rock surface because Mg^{2+} is strongly dehydrated and becomes reactive at higher temperatures. This is validated by predicting the experimental breakthrough curves at 100 and 130 °C as presented in the *bottom* panels of Figure 4.8, where a reduced co-adsorption of Ca^{2+} was observed as mentioned by Strand *et al.* [54]. With this conjecture, the model provides a solution with a reasonable agreement to other experimental datasets as will be discussed subsequently.

4.5.3 Competition between PDIs in the presence of oil

Having obtained a complete set of thermodynamic parameters to describe the surface sorption reactions, the effect of oil saturation on the interplay between the PDIs was then analyzed. In a chromatographic wettability experiment conducted by Fathi *et al.* [38], a reference water-wet core (SCC#1) was flooded with seawater (I = 0.657M) and the oil-wet core (LSSK#5) aged in oil of acid number 1.90 mg of KOH/g initially saturated with Valhall formation water (I = 1.112M). Afterwards, both cores were flooded with SW0T, and residual oil saturation was established in the oil-wet core. For the wettability comparison, SW1T was flooded through both saturated cores containing no SO_4^{2-} and tracer ions (SCN^- and Li^+).

Using this data, two models were constructed to account for both cases using the established set of thermodynamic parameters. As shown in Figure 4.9, a good agreement was obtained with the experimental result. Surface sorption reactions, as well as other geochemical reactions considered in this model, occurred only at the rock-brine interface. Therefore, the presence of oil was not anticipated to influence the final aqueous phase composition, but the transport of PDIs back and forth the rock-brine interface through the water film layer keeping the oil-brine interface apart. As it is the case presented here in Figure 4.9, the oil-aged core gave an earlier breakthrough of SO_4^{2-} and SCN^-, and a smaller adsorption area compared to the reference core because of the presence of oil competing with the adsorbed PDIs at the rock surface. Their predicted Mg^{2+} and Ca^{2+}

breakthrough curves looked similar to those plotted in Figure 4.6 with the oil-aged core showing an earlier breakthrough of these ions. The surface fractions of Ca^{2+}, Mg^{2+} and SO_4^{2-} for both cases are compared in the *right* panel of Figure 4.9. The reference core appears to have a slower mass transfer because there was more surface area to interact with the rock compared to the oil-aged core. Aside from the delay, SO_4^{2-} adsorption was more for the reference core than the oil-aged core, as evident by the larger adsorption area and higher surface fractions. Considering the oil-aged core, which typically represents an oil-wet condition, the water film covering the surface becomes very thin or unstable, and therefore the polar components in the crude oil can directly adsorb onto the rock surface.

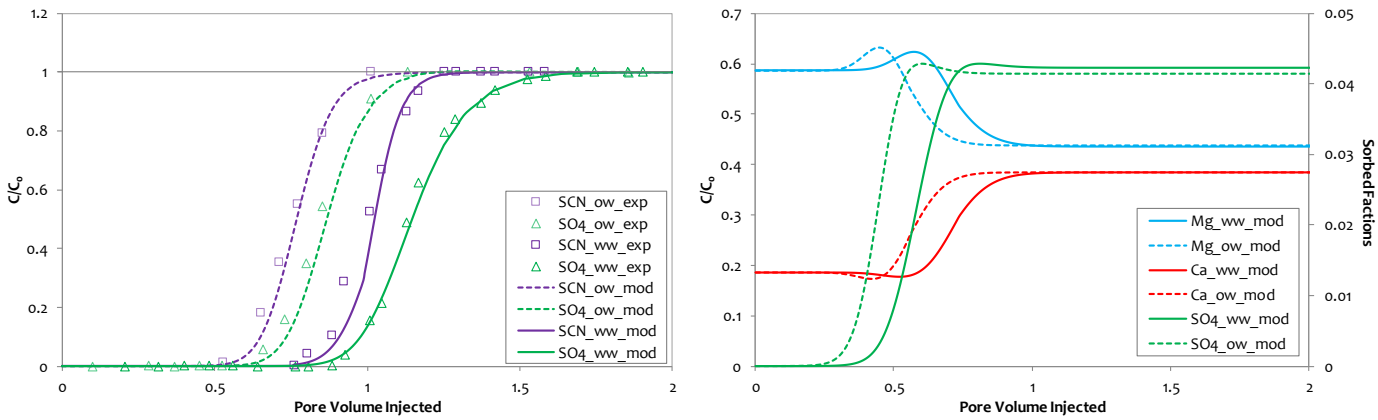

Figure 4.9—Simulated and experimental breakthrough curves of SCN^- and SO_4^{2-} at room temperature from SW-1T brine flood (*left*). Simulated surface fractions of Ca^{2+} ($> CaX_2$), Mg^{2+} ($> MgX_2$) and SO_4^{2-} ($> XSO_4^-$) along the mid-section (*right*), on aged chalk core LSSK#5 (with oil at S_{orm} = 0.29) and unaged chalk core SCC#1 (with no oil present). Data points connotes measured datasets (Fathi *et al.* [38]) and lines represent the model results.

4.6 Validation of Surface Complexation Model

Because SCM considers electrostatic interaction, the model can be validated by comparing its performance with ζ–potential experimental data. Unlike SSM where thermodynamic parameters do not exist, the thermodynamic equilibrium constants at the surface for SCM was initially taken same as those their corresponding aqueous phase reactions and then derived by utilizing SCM to fit surface charge data and pH at the isoelectric point for pure crystalline calcite in lower ionic strength solution by various authors [260, 262, 263]. Meanwhile, the temperature-dependence of these equilibrium constants often use the similar temperature-dependent relationship of aqueous

phase reactions [47]. Table 4.5 shows various widely-used equilibrium stability constants for the surface reactions R19-R24 reported in the literature at room temperature.

Table 4.5—Reported stability constants for the rock−brine surface reactions at room temperature

Stability Constants	$\mathbf{Log}\, K_{ex}$ 25 ℃					
	Van Cappellen *et al.* [262]	Pokrovsky *et al.* [263]	Hiorth *et al.* [47]	Brady and Thyne [198]	Qiao *et al.* [84]	Mean ± SD
K_{C1}	-4.9	-5.1	-4.9	-5.1	-5.1	-5.02 ± 0.11
K_{C2}	12.2	11.5	12.9	11.85	11.8	12.05 ± 0.54
K_{C3}	-2.8	-1.7	-3.16[a]	-2.6	-2.6[a]	-2.57 ± 0.54
K_{C4}	N/R	-2.2	-3.17[a]	-2.6	-2.6[a]	-2.64 ± 0.40
K_{C5}	N/R	N/R	2.1	2.1	2.1	2.1
K_{C6}	3.35[a]	5.6[a]	3.32[a]	4.28[a]	6	4.51 ± 1.25

[a]Note: these constant values are not exactly reported in the cited publications but were estimated from the combination of surface and aqueous reactions reported in these references. "N/R" connotes "no value is reported or could be estimated" and SD connotes standard deviation.

4.6.1 Surface chemistry prediction comparison with zeta potential experiments

However, carbonate reservoir rocks are composed of calcite and other impurities and in a slightly higher saline environment, which tends to affect the stability constants for surface complexation reactions. Therefore, a more representative stability constant need to be derived for the SCM to represent the carbonate rock-brine interactions. To begin with, the stability constants of the surface reactions R19-R24 were optimized to fit the measured ζ–potential data of suspension of pulverized Stevns Klint chalk reported by Austad and colleagues [32, 55]. The chalk suspension was prepared by mixing 4 wt.% pulverized chalk with 0.573M NaCl solution and PDI concentrations in the suspension were adjusted by gradually adding $CaCl_2$, $MgCl_2$, or Na_2SO_4 concentrated solutions. The authors did not specify the pre-equilibration procedures, however, the equilibrium between calcite in carbonate minerals and aqueous solution exposed to CO_2 is achieved when most of the carbonate ions (CO_3^{2-}) formed during calcite dissolution are turned into bicarbonate ions (HCO_3^-), according to eqs. 4.63 and 4.64. For carbonate/water/CO_2 equilibrium conditions, the aqueous pH increases as hydroxide (OH^-) ions are formed (eq. 4.63), and decreases as the hydroxide ions are used up (eq. 4.64) until an equilibrium pH is achieved. Hence, in a simple open system, aqueous

solutions exposed to CO_2 in the presence of calcite at 25 °C is reported to have an equilibrium pH of 8.3–8.4 [104, 268].

$$CaCO_{3\,(s)} + H_2 \Leftrightarrow Ca^+ + HCO_3^- + OH^- \tag{4.63}$$

$$CO_2 + OH^- \Leftrightarrow HCO_3^- \tag{4.64}$$

Instead, Austad and colleagues [32, 54, 55] fixed the pH at 8.4 by the addition of HCl or NaOH concentrated solutions to ensure the rock suspension achieve equilibrium prior to starting the experimental measurements. For this reason, dissolution of atmospheric CO_2 was not considered because the pH was kept constant throughout the experimental measurement. For the fact that pulverized samples were used, to eliminate rock porosity, the rock site capacity according to eq. 4.32 was taken as:

$$CEC = \delta_s A_\beta \rho_b \tag{4.65}$$

As earlier stated, the surface potential is directly calculated from the SCM, and the ζ-potential can be indirectly calculated through: $\zeta = \psi_o(\Delta) = \psi_o e^{-\kappa\Delta}$. Meanwhile, various authors [32, 55, 104, 120, 170] have shown that ζ-potential obtained from using particles suspension with electrophoretic mobility measurement (EPM) differed from that obtained from intact rock cores with streaming potential measurement (SPM). The contrast is associated with the difference in the shear plane relative position to the charged mineral surface of particle suspension and natural porous media [104]. For EPM with pulverized rock suspension, it has been demonstrated that the shear plane corresponds to the Stern plane, hence $\xi = \psi_o$ [104, 170]. With the intention of fitting the predicted ζ-potential from SCM to ζ-potential experimental data, the objective function is minimized such that:

$$\min_x \|f(x)\|, \qquad x \in \mathcal{F} = \{x : l < x < u\} \tag{4.66}$$

with

$$f(x) = \sum_i \left(\zeta_{i,\ exp} - \zeta_{i,\ mod}\right)^2 \qquad for\ i = 1, \ldots\ldots, N_\zeta \tag{4.67}$$

where N_ζ is the total number of ζ-potential data points, l and u are the lower and upper bounds on the stability constants and the subscripts "exp" and "mod" are the experimental and predicted ζ

potential values, respectively. The objective function with the batch calculation of the SCM by solving eq. 4.47 using Newton's iteration method is programmed in MATLAB. The output of the batch calculation also compared well with same calculation conducted with PHREEQC reaction module, as illustrated below. For the minimization of the objective function (eq. 4.66), the Trust-region-reflective algorithm was utilized for nonlinear unconstrained optimization from the MATLAB Optimization Toolbox package.

Similar to SSM, a wide range of surface site densities exist for SCM ranging from 2 to 8 sites/nm^2 for carbonate rocks [261, 262]. Hiorth *et al.* [47] and Eftekhari *et al.* [220] stated that 2 sites/nm^2 gave a better fit to the measured ζ-potential while Megawati *et al.* [161] stated that using 5 sites/nm^2 gave a much better fit for all tested core types as compared to 2 sites/nm^2. Hence, in this research study, the effect of site densities on the stability constant optimization was tested by utilizing 2—6 sites/nm^2. The specific surface area of chalk is reported as about 2.0 m^2/g in the study by Zhang and Austad [55], but Shariatpanahi *et al.* [112] gave the exact value as 1.7 m^2/g. The upper and lower bounds of the stability constant for the minimization operation was taken as no more than twice of the standard deviations of the mean values reported in Table 4.5. Since CO_3^{2-} and CO_2 are not included in the aqueous solution, the equilibrium constants for reactions R24, K_{C6}, is not modified by the optimization operation. The stability constant results of fitting the SCM to the ζ-potential data for varying site densities are compared in Table 4.6.

Table 4.6—Optimized stability constants derived from fitting pulverized carbonate ζ-potential

	Log K_{ex} 25 ℃				
S_d (sites/nm^2)	**2**	**3**	**4**	**5**	**6**
K_{C1}	-3.95	-3.85	-3.76	-3.72	-3.77
K_{C2}	9.97	10.16	10.29	10.39	10.57
K_{C3}	-3.14	-3.23	-3.26	-3.33	-3.50
K_{C4}	-2.73	-2.82	-2.86	-2.93	-3.09
K_{C5}	1.63	1.44	1.31	1.21	1.20
Residual Norm[a]	85.313	83.967	83.339	82.975	95.531
Relative Resnorm[a]		0.984	0.977	0.973	1.119

[a]Note: The norm of the residuals is the measure of the deviation between the estimated value and the experimental data. The relative residual norm is calculated as the deviation of estimated and experimental value relative to the site density of 2 sites/nm^2.

It can be observed that from Table 4.3 that as the site density increased, the measure of deviation between measured and predicted ζ-potential values (also referred to as residual norm) decreased, while the relative value of the residual norm compared to the residual norm at 2 sites/nm^2 reduced as the site density increased. This implies that increasing site density slightly decreased the deviations but did not significantly improved the fit to the experimental data. As such, the relative residual norm for 3 sites/nm^2 was much higher as compared to other higher site densities, implying that 3 sites/nm^2 gave a better and optimized fit to the data as presented in Figure 4.10.

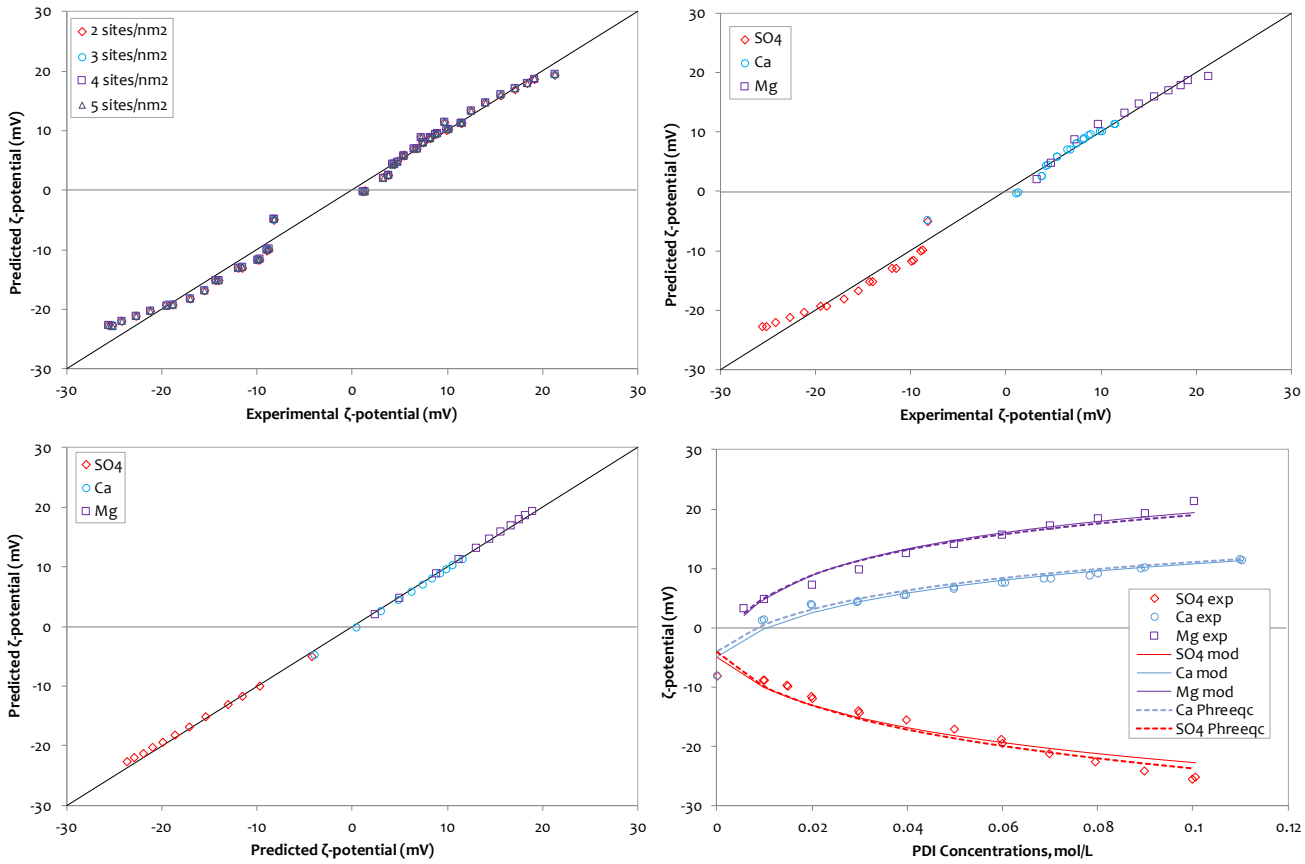

Figure 4.10—Comparison of measured and predicted ζ-potential for all PDI concentrations and varying surface site densities (*top left*) and 3 sites/nm^2, showing the variation with PDIs (*top right*), the contrast between the prediction from this model and PHREEQC reaction module (*bottom left*). The solid black diagonal line is 1:1 zero error line, i.e. $\zeta_{i,\ exp} = \zeta_{i,\ mod}$, which shows the contrast between measured and predicted values. ζ-potential measured by Austad and colleagues [32, 55] with stepwise addition of $MgCl_2$, $CaCl_2$ or Na_2SO_4 to 0.573 M NaCl brine solution in 4 wt.% pulverized chalk suspension with pH maintained at 8.4, compared against the predicted ζ-potential from SCM with optimized stability constants for 3 sites/nm^2 as shown by solid lines (*bottom right*). The top (*squares* and *circles*) curves and data points is for Mg^{2+} and Ca^{2+} additions, respectively; the bottom (*diamonds*) curve and data points is for SO_4^{2-} additions. PHREEQC prediction was plotted in dotted lines.

There is no much difference in the variation observed for the considered site densities in Figure 4.10, which implies that site densities do not significantly affect the surface potential inasmuch the corresponding stability constants are applied. Figure 4.10 also presents the variation in the measured and predicted ζ-potential as the PDI compositions in the aqueous solution is changed. The increment of SO_4^{2-} resulted in more negatively charged carbonate surface while the addition of Ca^{2+} and Mg^{2+} led to a positive surface and ζ-potential. The fit between the compared values in Figures 4.10 is excellent, showing that the optimized stability constants at 3 sites/nm^2 can predict PDI adsorption and the surface potential of calcite very well.

Considering that the experiments carried out by Austad and colleagues [32, 54, 55] were conducted using pulverized samples and mostly chalk formation, which is pure calcite, the obtained thermodynamic constants might not be necessarily applicable to rock-brine interactions in natural intact carbonates. This is because natural carbonates are often composed of various forms of mineral impurities. In order to confirm this theory, the experimental data of Alroudhan *et al.* [104] was utilized, where the ζ-potential of natural intact carbonate rock (limestone) was measured in NaCl brine with different ionic strength and compositions. A pre-equilibration step was carried out in an open system, as discussed above, where the core sample was saturated with the aqueous solution as exposed to atmospheric CO_2 to achieve equilibrium pH of 8.2±0.2 for 0.05 M and 0.5 M NaCl brines. After that, the ζ-potential measurement was carried out in a closed system where the brine solution was repeatedly pumped through the sample until a new equilibrium is established.

This study considered PDI cations variation in 0.05M NaCl brine conducted with both EPM and SPM technique and PDI anions in 0.5M NaCl brine with SPM technique. Alroudhan *et al.* [104] claimed that increment in injected concentrations of Ca^{2+} or Mg^{2+} reduced the pH to the range 7.2–8, while SO_4^{2-} caused a smaller change in the pH range of 7.9–8.1. For the SCM, the pH was assumed to remain constant in the range specified above, as the experiments were conducted under closed conditions. Besides, the pH was varied during the optimization operation to study the effect of pH variation on stability constants. The specific surface area of limestone is reportedly less than that of chalk, and Shariatpanahi *et al.* [112] reported a value of 0.29 m^2/g. However, the effect of

the specific surface area on the optimization of limestone rock was studied by varying the surface area from 0.1 to 0.75 m^2/g with a site density of 3 sites/nm^2. A run of the optimization routine was performed for each pair of the specific surface area of chalk and equilibrium pH. In this case of intact carbonate rock, the rock site capacity calculation considered rock porosity as defined by eq. 4.32. Meanwhile, Alroudhan *et al.* [104] stated that the relative position of the shear plane from the charged surface is 0.245 nm for SPM and 0 nm for EPM. These values were considered in the model as the shear plane position, and the optimized stability constants obtained from pulverized chalk suspension was applied to fit the model as illustrated in Figure 4.11.

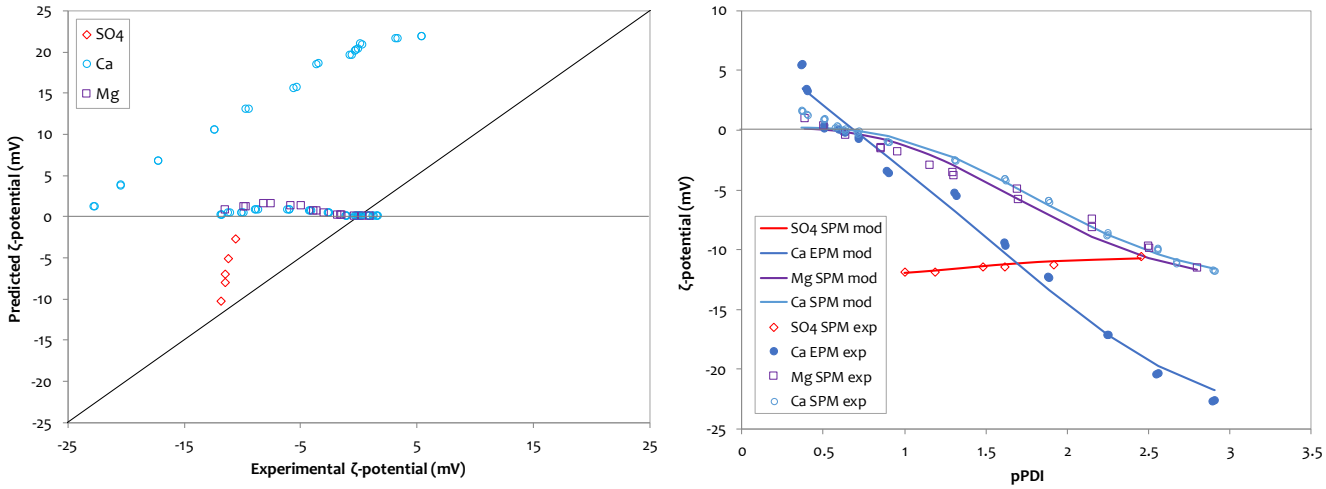

Figure 4.11—Comparison of ζ-potential measured and predicted for PDI concentrations with optimized stability constants for surface site densities of 3 sites/nm^2 (*left*). ζ-potential predicted by optimized stability constants for intact rock compared against measured ζ-potential (*right*) by Alroudhan *et al.* [104] with PDI variations in 0.5M (*red lines and data points*) and 0.5M (*other colored lines aside red*) NaCl brine. EPM data for Ca^{2+} variation in 0.05M NaCl brine is plotted in "*light-blue*" on the right graph. The concentration is plotted in terms of negative logarithmic value (pPDI) instead of molar concentrations. The specific surface area was taken 0.29 m^2/g. The fixed pH of cation and anion variation was taken as 7.2 and 7.9, respectively.

As illustrated in Figure 4.11 (*left figure*), the stability constants for pulverized chalk failed to fit the ζ-potential values for intact carbonate rock. The reason could be that the stability constants of chalk differ from that of limestone due to mineralogical differences and/or surface area; this will be further discussed below. The shear plane position of 0.245 nm and 0 nm suggested for SPM and EPM also failed to give a better fit of experimental ζ-potential values, and the shear plane position was included in the optimization routine. Then, the optimization routine was applied to

capture the stability constant and a much better fit is presented in 4.11 (*right figure*). The sensitivity of stability constants and shear plane position with the specific surface area of chalk and equilibrium pH are presented in Table 4.7 and illustrated in Figure 4.12.

Table 4.7—Optimized stability constants derived from fitting natural intact carbonate ζ-potential

				Log K_{ex} 25 ℃			
A_β (m²/g)		0.1	0.29	0.75	0.1	0.29	0.75
pH cations[a]		7.2	7.2	7.2	8	8	8
pH anions[a]		7.9	7.9	7.9	8.1	8.1	8.1
K_{C1}		-3.07	-3.07	-3.07	-3.10	-3.10	-3.17
K_{C2}		8.42	8.42	8.42	9.21	9.21	9.20
K_{C3}		-3.21	-3.21	-3.21	-3.22	-3.22	-3.28
K_{C4}		-3.45	-3.45	-3.45	-3.46	-3.46	-3.44
K_{C5}		1.72	1.72	1.71	1.20	1.20	1.21
Δ (nm)	0.05M	0.695	0.695	0.694	0.708	0.707	0.702
	0.5M	0.399	0.398	0.398	0.170	0.166	0.172
Resnorm		50.4214	50.4467	50.5095	57.8744	57.9371	59.1544

[a]Note: pH sensitivity due to changes in cations and anions in the injected brine solution; the upper and lower limit of the pH changes was used as a fixed pH in the optimization routine. The residual norm is as described in Table 4.6.

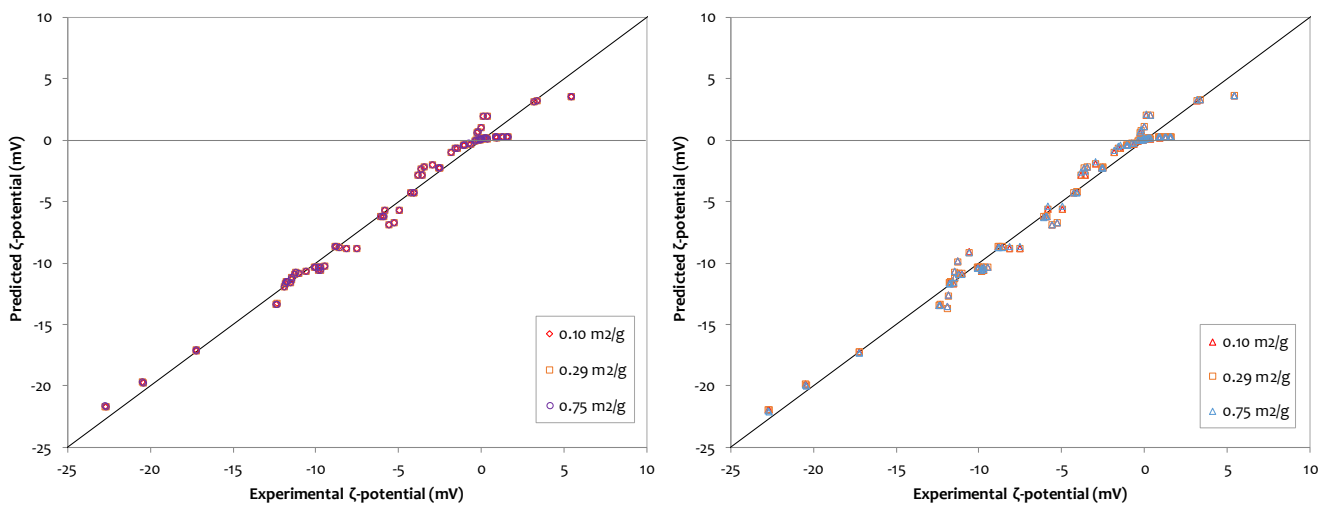

Figure 4.12—Optimized ζ-potential predicted against measured ζ-potential for pH of 7.2 and 7.9 (*left*) and 7.9 and 8.1 (*right*) for PDI cations and anions additions, respectively. Experimental data are taken from Alroudhan *et al.* [104].

The variation in the surface area of the intact limestone rock did not have a significant effect on the stability constants as much as the variation in equilibrium pH, though using 0.75 m^2/g resulted in the higher residual norm as compared to other surface areas. The slight change in equilibrium pH for SO_4 addition slightly worsen the fit as illustrated in Figure 4.12 and influenced the stability constants values for reactions R20 (K_{C2}) and R23 (K_{C5}) with higher residual norm reported in Table 4.7. Meanwhile, every attempt to use the same shear plane position for both brine ionic strength failed, and the experimental ζ-potential could only be replicated by a higher shear plane position as the brine salinity decreased. This implies that the relative position of the shear plane is a function of the brine salinity, which is in contrary to Alroudhan *et al.* [104] but in agreement with Korrani and Jerauld [215]. This could be related to increased double layer thickness with reduced brine salinity, which could result in an increase in the shear plane relative position. The fact that the optimized stability constants for pulverized chalk could not fit ζ-potential for intact limestone will be further evaluated by comparing both stability constants to fitting single-phase flow through experiments below.

4.6.2 Comparison of surface chemistry prediction to single-phase flooding experiments

The experimental breakthrough data obtained from single-phase flooding experiments were also used to investigate the interface chemistry and compare with reactive-transport parameters retrieved using ζ-potential. The competition between Ca^{2+} and Mg^{2+} as documented in the study by Strand *et al.* [53] was modeled at various temperatures with experimental details as listed in Table 4.2. The comparison between the predicted and measured relative effluent ion concentrations to injected ion concentrations is shown in Figure 4.13. For all temperatures, predicted breakthrough profiles fit well with the experimental profiles. Similar to earlier explanation, the involvement of Ca^{2+} and Mg^{2+} in the surface chemistry compared to the tracer ion (SCN^-) triggered their retention and delayed their breakthrough in the effluent. At lower temperatures of 20 and 70 °C, both Ca^{2+} and Mg^{2+} showed similar affinity towards the rock surface. However, Ca^{2+} adsorbed more at 20 °C while Mg^{2+} adsorbed more at 70 °C, as highlighted by the surface fractions presented in Figure 4.14. Meanwhile, at higher temperatures above 100 °C, Mg^{2+}

became dehydrated, highly reactive and strongly adsorbed to the rock surface in comparison to Ca^{2+} as evident by the higher surface fractions in Figures 4.14.

Neither of the optimized stability constants for pulverized chalk nor intact limestone could provide the best fit for the experimental breakthrough profiles as indicated by the corresponding stability constants obtained for reactions at the protonated anion site (K_{C1}, K_{C3} and K_{C4}) during the flow through the experiment (see Table 4.8). The temperature-dependent competition between Ca^{2+} and Mg^{2+} was also evident in the stability constants derived for their corresponding surface complexation reactions. The stability constants for R21 (K_{C3}) increased with temperature and that of R22 (K_{C3}) decreased with temperature, the difference between the stability constants became larger with temperature.

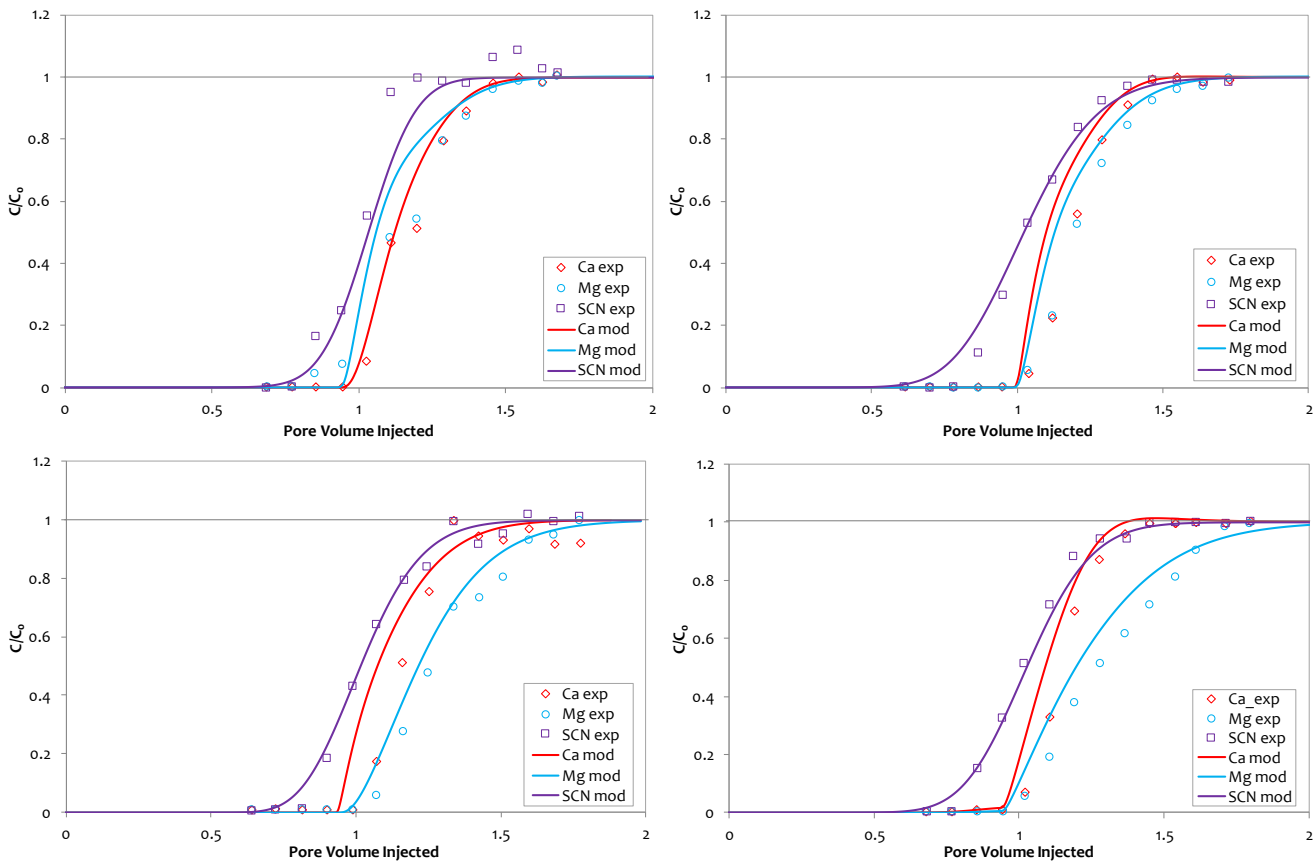

Figure 4.13—Predicted compared against experimental breakthrough curves of SCN^-, Ca^{2+} and Mg^{2+} from CF-M brine flow through limestone core 2-21 at various experimental temperatures: 20 °C (*top left*), 70 °C (*top right*), 100 °C (*bottom left*), and 130 °C (*bottom right*). Experimental data are taken from Strand *et al.* [53].

Table 4.8—Corresponding equilibrium constants at various temperatures and pressure of 7 bar

	Log K_{ex}				Temperature-dependent Empirical Parameters					
	20 °C	70 °C	100 °C	130 °C	A_0	A_1	A_2 (10^4)	A_3	A_4 (10^6)	A_5 (10^{-4})
K_{C1}	-5.10	-5.80	-5.85	-6.00	278.85	0.401	-4.106	-115.71	6.609	-4.194
K_{C2}	11.60	10.00	9.75	9.50	293.22	-0.141	3.208	-129.61	-6.325	3.873
K_{C3}	-1.25	-1.35	-1.50	-2.00	277.36	0.341	-3.490	-118.19	5.030	-3.512
K_{C4}	-1.50	-1.30	-1.25	-1.20	282.94	0.345	-3.366	-116.10	4.299	-3.965
K_{C5}	1.25	1.60	1.75	2.30	287.11	0.120	-0.354	-122.54	-0.580	-0.323

Note: these are the adjusted stability constant values that match the produced ion histories from the chromatographic experiments by Austad and colleagues [32, 53, 54]. The temperature-dependent empirical parameters are developed based on the analytical polynomial expression defined by eq. 4.9 to obtain stability constants at various temperatures.

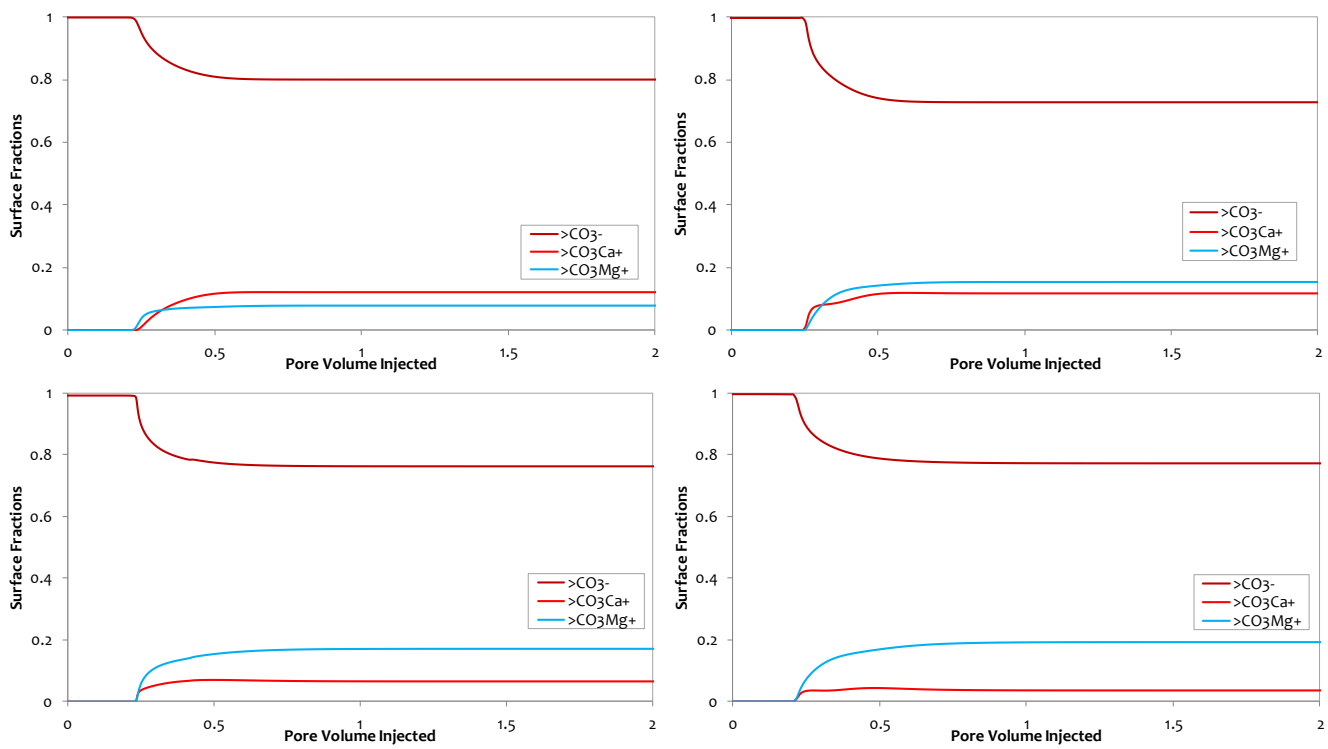

Figure 4.14—Predicted surface fractions of $>CO_3^-$, $>CO_3Ca^+$ and $>CO_3Mg^+$ along the mid-section of the limestone core 2-21 at various experimental temperatures: 20 °C (*top left*), 70 °C (*top right*), 100 °C (*bottom left*), and 130 °C (*bottom right*).

The stability constants derived for limestones were also applied to simulate the flow-through experiment conducted by Zhang *et al.* [32] using Stevns Klint chalk with similar initial and injected brines as used by Strand *et al.* [53]. Figure 4.15 shows that the SCM predictions with similar stability constants fit well with experimental data at 23 and 130 °C, which further proves the

validity of the stability constants. Just as observed for SSM, the breakthrough curve of chalk at 23 °C showed a broader gap between Ca^{2+} and Mg^{2+} curves compared to the limestone breakthrough curve at 20 °C in Figure 4.13, which could be because the actual chalk core porosity was not reported in the study by Zhang *et al.* [32]**.** Meanwhile, the breakthrough curve at 130 °C showed a high concentration of produced Ca^{2+} attributed to a possible replacement of Ca^{2+} at the rock surface by Mg^{2+}, which the SCM also reasonably captured. In addition, the surface fractions of Ca^{2+} and Mg^{2+} presented in Figure 4.13 is higher compared to that reported for limestones in Figure 4.14, which is due to higher total surface capacity for chalk. This effort confirmed that similar stability constants could be used to model different carbonate rock lithologies and the discrepancy associated with the model prediction of ζ-potential between chalk and limestone could be associated with uncontrolled experimental conditions.

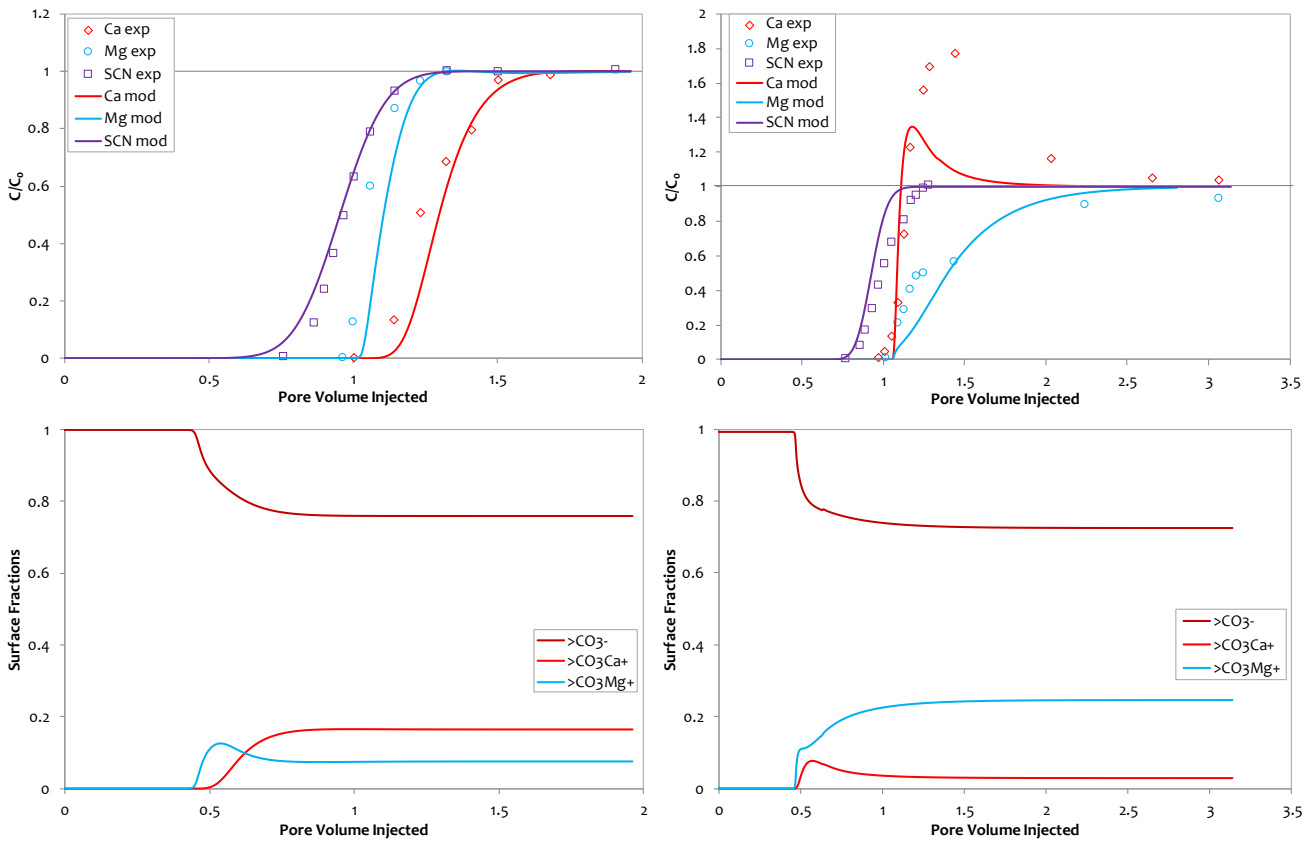

Figure 4.15—Predicted compared against experimental breakthrough curves of SCN^-, Ca^{2+} and Mg^{2+} from CF-M brine flow through chalk core (CM-1) at 20 °C (*top left*) and 130 °C (*top right*). Predicted surface fractions of $>CO_3^-$, $>CO_3Ca^+$ and $>CO_3Mg^+$ along the mid-section of the core at 20 °C (*bottom left*) and 130 °C (*bottom right*). Experimental data are taken from Zhang *et al.* [32].

The stability constants describing the reactions at the hydroxylated cation site (K_{C2} and K_{C5}) was derived by predicting flow-through experiments by on chalk core saturated initially with SW-U and flooded with SW-M at 23, 70, 100 and 130 °C. The comparison between the predicted and experimental breakthrough profiles demonstrates a good fit at various temperatures as shown in Figure 4.16. As stated earlier, SO_4^{2-} adsorption to the positively charged surface site increased as the temperature increased and the increase in adsorption becomes more pronounced as the temperature is raised above 100 °C. The trend is well captured by the increasing stability constants, K_{C5} as presented in Table 4.8. The delayed production of SO_4^{2-} as compared to SCN^- indicate the affinity of SO_4^{2-} to the rock surface, which increased as the temperature increased as evident in surface fraction of SO_4^{2-} plotted in Figure 4.17. The derived stability constants for K_{C2} and K_{C5} are within the range of optimized predicted stability constants for intact limestone rock.

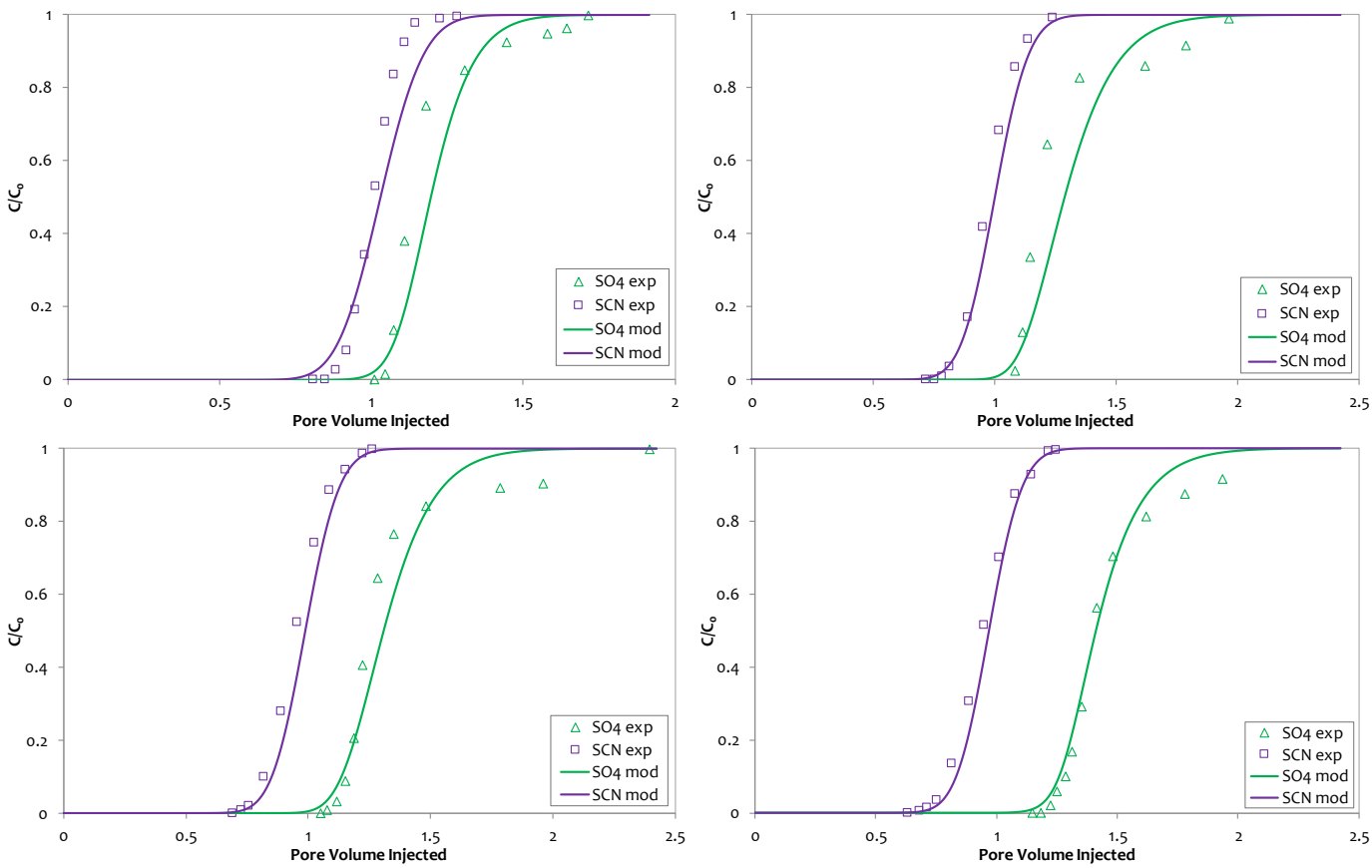

Figure 4.16—Predicted and experimental breakthrough curves of SCN^- and SO_4^{2-} from SW-M brine flow through chalk core (7/1) at various experimental temperatures: 23 °C (*top left*), 70 °C (*top right*), 100 °C (*bottom left*), and 130 °C (*bottom right*). Experimental data are taken from Strand *et al.* [54].

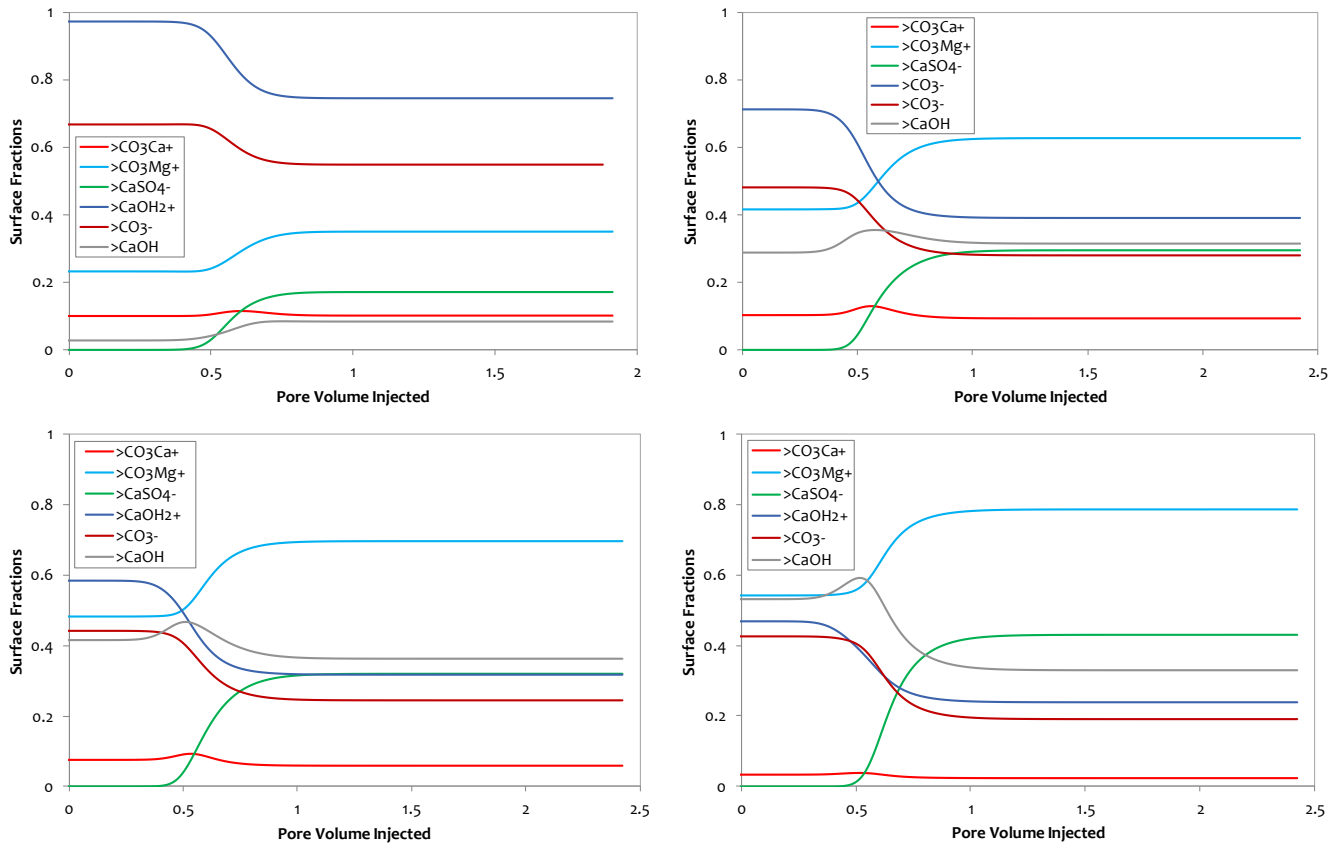

Figure 4.17—Predicted surface fractions of $>CaOH_2^+$, $>CaSO_4^-$, $>CaOH^0$, $>CO_3^-$, $>CO_3Ca^+$ and $>CO_3Mg^+$ along the mid-section of the limestone core (7/1) at various experimental temperatures: 23 °C (*top left*), 70 °C (*top right*), 100 °C (*bottom left*), and 130 °C (*bottom right*)

Hitherto, it has been shown that the coupled transport and geochemical model can predict PDI adsorption and interplay at the rock surface irrespective of the rock lithology, and surface and ζ-potential, as there are excellent agreements between predicted and experimental results. The model with its derived thermodynamic parameters will be used extensively in subsequent Chapters to investigate diverse brine-dependent recovery processes.

4.7 Chapter Summary

This Chapter presents the approaches used for numerical modeling of the problems associated with coupled multicomponent transport and geochemical interactions. The governing system of equations is represented by a set of material balance equations for the phases and chemical species. The numerical model was developed to account for the interactions between the PDIs at the rock

surface during brine-dependent recovery processes. The results presented in this study shows that this model can quantitatively reproduce the interplay between ions and rock surface during brine-dependent recovery in different carbonate lithologies. This study identifies and establishes a unique set of thermodynamic parameters that can model brine-dependent recovery processes by fitting ζ-potential data and produced ion histories. Hence, the following conclusions are drawn from this study:

- The transient period, as well as the late steady-state period of single-phase flow experiments were captured by the model and the important thermodynamic equilibrium constants, were captured.
- The relative interplay between Ca^{2+}, Mg^{2+}, and SO_4^{2-} varies with temperature. Although there are inconsistencies in the experimental datasets with respects to Ca^{2+} and Mg^{2+}, the model indicates that Ca^{2+} is strongly adsorbed at temperatures below 100 °C in the presence of sulfate.
- Produced ion histories during the two-phase experiments exhibited a trend similar to that of single-phase experiments, except that the presence of oil impacts ion transports. This rationale suggests that surface composition changes can be tracked efficiently by analyzing single-phase flow experiments.
- The mostly used equilibrium constants for the surface complexation reactions reported in the literature are not suitable to replicate the experimental ζ-potential of intact limestone rock and pulverized chalk suspension. The equilibrium constants that fit the measured ζ-potential of chalks differ from those that fit intact limestone ζ-potential, and neither is suited to predict the reactive transport of brine in chalk and limestone.
- Though chalk and limestones differ by surface area and reactivity, the same thermodynamic parameter can be used in modeling brine-dependent recovery in the respective reservoirs.
- The presence of either Ca^{2+} and SO_4^{2-} or Mg^{2+} and SO_4^{2-} in the injection brine can modify wettability towards water-wetness during brine-dependent recovery processes.

Chapter 5 Prediction of Brine-Dependent Recovery

This Chapter demonstrates the investigation of brine-dependent recovery explored on two-major frontlines, including brine-dilution and compositional variation, by utilizing the surface sorption model developed and validated in Chapter 4. At first, the link between the geochemical changes with wettability alteration leading to oil recovery improvement needed to be established; in so doing, various governing parameters were described to link the observed interfacial phenomenon to changes in oil recovery characteristics.

5.1 Geochemical Interactions and Wettability Modification Relationship

Generally, wettability alteration is modeled in EOR processes through the interpolation of flow functions, particularly the relative permeability and capillary pressure, based on a controlling parameter. Meanwhile, in laboratory water flood experiments cases where high pressure-drop drives fluid flow, capillary pressure becomes negligible and can be ignored. One important technique to control the flow functions is to establish the relationship that exists between the surface energies, wettability indicator (contact angle) and the surface specie fractions. Wettability of the rock surface is often quantified by the contact angle of the liquid drop resting on the surface. Hence, the contact angle can be derived from surface force balance and relates to the surface tensions between rock/brine/oil as described by Young's equation:

$$\cos\theta = \frac{\gamma_{ro} - \gamma_{rb}}{\gamma_{bo}} \tag{5.1}$$

where γ_{ro}, γ_{rb}, and γ_{bo} are the rock/oil, rock/brine and brine/oil interfacial energies (mN/m) respectively. Many studies [45, 57, 58, 59, 60] have shown that the change in γ_{bo} is not considered significant during brine-dependent recovery process. Meanwhile the change in either γ_{ro} or γ_{rb} is related to the changes in surface component fractions through the Gibbs adsorption isotherm for multicomponent systems:

$$d\gamma = -\sum_i \Gamma_i d\mu_i \tag{5.2}$$

where Γ_i and μ_i are the surface excess and chemical potential of the *i*-th component, respectively. As a typical example, the surface excess can be taken as the *i*-th surface species fractions, i.e. $\Gamma_i = \xi_\mathrm{i}$, in eq. 5.2. While, the chemical potential of the *i*-th surface species depends on the surface fractions as follows:

$$\mu_i = {\mu_i}^0 + RT \ln \xi_\mathrm{i} \tag{5.3}$$

where ${\mu_i}^0$ is the chemical potential of the *i*-th surface species at a reference state. Then differentiation of eq. 5.3 with respect to surface fraction becomes:

$$d\mu_i = RT \frac{d\xi_i}{\xi_i} \tag{5.4}$$

Replacing $d\mu_i$ in eq. 5.2 with eq. 5.4 gives:

$$d\gamma = -\sum\nolimits_i \xi_i \, RT \frac{d\xi_i}{\xi_i} = -\sum\nolimits_i RT \, d\xi_i \tag{5.5}$$

Eq. 5.5 demonstrates the linear dependence of the changes in interfacial energies on the changes in the *i*-th surface species fractions. Then considering the relationship of contact angle with interfacial energies as stated in eq. 5.1, changes in the contact angle of the liquid drop on the surface can be expressed as:

$$d\cos\theta = \frac{d(\gamma_{ro} - \gamma_{rb})}{\gamma_{bo}} = \frac{RT}{\gamma_{bo}} \sum\nolimits_i d\xi_i \tag{5.6}$$

The expression in eq. 5.6 shows that changes in wettability indicator do have a linear relationship with changes in the fractions of surface species. This implies that a linear dependency can be used to modify the flow functions based on surface species fractions on the water-wet and oil-wet surfaces. The modification of the flow function can be used to capture the wettability alteration from oil-wetting towards water-wetting. Hence, linear interpolation, as will be utilized later, can be used to model the flow function to capture wettability alteration. For multiphase transport, the dimensionless form of Brooks-Corey's type correlation can be used to describe the relative permeability functions (eqs. 5.7 and 5.8), and simplified power-law form of Brooks and Corey is used to describe the capillary pressure functions (eq. 5.9) [269] for $s_{wr} \leq s_w \leq 1 - s_{or}$ as:

$$k_{row} = k_{row}^{*}\left(\frac{1 - s_w - s_{or}}{1 - s_{or} - s_{wr}}\right)^{n_o} \tag{5.7}$$

$$k_{rw} = k_{rw}^{*}\left(\frac{s_w - s_{wr}}{1 - s_{or} - s_{wr}}\right)^{n_w} \tag{5.8}$$

$$P_c = \frac{P_{th,w}}{\left(\frac{s_w - s_{wr}}{1 - s_{wr}}\right)^{\alpha_w}} + \frac{P_{th,o}}{\left(\frac{1 - s_w - s_{or}}{1 - s_{or}}\right)^{\alpha_o}} \tag{5.9}$$

where k_{rw} and k_{row} are the relative permeabilities to water and oil in water-oil displacement, respectively; s_{wr} and s_{or} are the irreducible water saturation and residual oil saturation respectively; k_{row}^{*} and k_{rw}^{*} are the endpoint relative permeabilities to oil and water respectively; $P_{th,w}$ and $P_{th,o}$ are the entry pressures to (positive) water and (negative) oil respectively; n_o and n_w are the Corey exponents for oil and water respectively; and α_o and α_w are the power-law indices for oil and water respectively.

In most water flood cases considered in this study, the endpoint water relative permeabilities were obtained when the differential pressure stabilized towards the end of each flooding cycle. Meanwhile, the residual oil saturation was determined by taking the material balance of both the remaining and recovered fluid. This is because the flow functions were not measured in many of the independently-sourced data that have been used in this study. For this reason, the following workflow was used to obtain the relative permeability and capillary pressure functions to simulate core flooding experiments:

- Use the predetermined s_{or}, k_{ro}^{*} and k_{rw}^{*}, tune n_o and n_w at the original state to fit measured oil recovery of the injection cycle where wettability alteration has not occurred.
- Tune $P_{th,w}$, $P_{th,o}$, α_o and α_w at the original state to fit measured pressure differential of the injection cycle where wettability alteration has not occurred.
- Adjust the relative permeability and capillary pressure obtained through steps 1 and 2, by tuning the n_o, n_w and $P_{th,o}$ to fit the measured oil recoveries and capillary pressure to determine flow functions for the new wetting state. Skjaeveland *et al.* [270] reported that $P_{th,o}$ is an important parameter that account for the change in wettability in capillary imbibition process.

Unlike chemical flooding, the identification of the specific parameter to control the interpolation of the flow functions is quite a challenge in modeling brine dependent-recovery processes. In an attempt to overcome this hurdle, the geochemical response of the different experimental system was investigated to determine which mechanism(s) would better correlate with the available results in terms of oil recovery profiles, pressure differential and breakthrough curves. Linear interpolation was employed, as stated in eqs. 5.10 - 5.22, to estimate the altered relative permeability, capillary pressure and residual oil saturation functions at every time step based on the extent of the alteration in geochemical properties, akin to the fact that these flow functions are shifting from the initial oil-wetting state towards water wetness. Such a shift can only be achieved by defining a process dependent interpolation function, which depends on the geochemical properties.

$$k_{rj}{}^{altered} = \omega k_{rj}{}^{intial} + [1-\omega]k_{rj}{}^{final} \tag{5.10}$$

$$P_c{}^{altered} = \omega P_c{}^{intial} + [1-\omega]P_c{}^{final} \tag{5.11}$$

$$s_{or}{}^{altered} = \omega\, s_{or}{}^{intial} + [1-\omega]s_{or}{}^{final} \tag{5.12}$$

where ω is the process dependent interpolation function and k_{rj} is the relative permeability for the j-th phase. Hence, when $\omega = 1$, it implies that $k_{rl}{}^{altered} = k_{rl}{}^{intial}$, $P_c{}^{altered} = P_c{}^{intial}$ and $s_{or}{}^{altered} = s_{or}{}^{intial}$, which reflects the initial wetting conditions. However, as ω reduces, it implies that wettability alteration is taking place until it has completely taken place when $\omega \approx 0$, i.e. $k_{rl}{}^{altered} = k_{rl}{}^{final}$, $P_c{}^{altered} = P_c{}^{final}$ and $s_{or}{}^{altered} = s_{or}{}^{final}$ as the new more water-wetting state is reached. For the process dependent interpolation function, different scenarios were considered and tested in different simulations runs as will be discussed below.

5.2 Oil Recovery Prediction for Brine Dilution Approach

The brine dilution approach, widely known as "*low-salinity-waterflooding*", has shown remarkable improvement in oil recovery in experimental studies with clay-rich sandstone rocks. Many studies reported an incremental recovery as high as 30% oil-originally-in-place (OOIP) [13, 23, 41, 271]. Although, similar improvements (up to 19% OOIP) have been observed in carbonate rocks at much higher salinities compared to sandstones. The term "*low salinity*" is still applied

because the injected brines are generally of lower salinity compared to the initial reservoir brine. Brine dilution approach with its fundamental physicochemical mechanisms has been reported to have a higher order of complexity in carbonate rocks than sandstone rocks [30, 36, 48, 57, 101]. Carbonate rocks often undergo diagenesis and different post-depositional chemical and physical changes, which varies with respect to pore pressure, temperature, and fluid chemistry [272]. This results in corresponding changes in the rock petrophysical properties, such as permeability, porosity, faults, fractures, and wettability. The resulting large-scale heterogeneity often generates complex fluid flow paths, which is one of the major challenges encountered in managing and exploiting such reservoirs.

Furthermore, carbonate rocks are positively charged over a wide range of pH, while heavy carboxylic fractions (such as resin and asphaltene) present in crude oil, makes the oil surface strongly negatively charged at higher pH, especially typical reservoir pH (7-9) [65]. Thus, adsorption of the negatively charged oil polar component onto the positively charged carbonate rock, cause the oil to cover the rock surface and create higher bonding energy between the oil and carbonate rocks that often renders the rocks oil-wet to mixed-wet [29]. The relative contribution of rock wettability dictates the corresponding flow functions, like relative permeability, capillary pressure and residual oil saturation, which impact the amount of oil recovered [273]. In this context, water-wet rocks benefit from faster oil recovery over oil-wet because of increased oil mobility resulting from the lower affinity of oil to the rock surface. Thus, the combination of these factors is the primary possible explanation for the differences in the reported oil recovery range and physicochemical mechanisms between carbonate and sandstone rocks.

Various published results suggest that diluted brine can change the rock wettability toward the more water-wetting state. The wettability alteration process in sandstone rocks has been associated with the presence of clay minerals and the injected water salinity level as less as 2000 ppm [14, 56]. However, the alteration process was not anticipated in carbonate rocks as they lack or has a minute amount of clay minerals. Instead, carbonate rocks are purely calcite (calcium carbonate) and dolomite with/without other minerals like magnesite (magnesium source), gypsum/anhydrite (sulfate source), apatite (phosphate source), glauconite, quartz, ankerite, pyrite, siderite, etc. These

mineralogical differences between sandstone and carbonate rock is another possible explanation for the differences in the reported oil recovery range [274]. For instance, chalk is purely calcite, and no incremental oil recovery was observed with brine dilution; whereas limestones (mostly calcite with dolomite/magnesite/anhydrite/pyrite) and dolomites demonstrated considerable variance in the magnitude of incremental oil recovery [36, 101]. Consequently, brine dilution-dependent recoveries for carbonate rocks vary greatly depending on the injected brine salinity and the rock mineralogy.

A series of experiments on middle-eastern carbonate cores containing about 5% anhydrite was carried out to unravel the positive effects of brine dilution [57, 102]. The authors reported an incremental recovery up to 19% OOIP and indicated that surface charge alteration was more important than dissolution in the wettability alteration process. Elsewhere, Austad *et al.* [48] injected sulfate-free diluted brine into carbonate cores containing anhydrite and reported an incremental recovery of 5% OOIP. The authors explained that sulfate was continually generated *in-situ* because of anhydrite dissolution and this led to the wettability alteration process. Romanuka *et al.* [101] carried out spontaneous imbibition experiments on different mineralogical carbonate cores and showed that brine dilution contributed to an incremental recovery up to 20% OOIP. In the same way, Zahid *et al.* [36] conducted another series of experiment on carbonate cores free of dolomite/anhydrite and reported incremental recovery up to 18% OOIP. The authors proposed fines migration and rock material dissolution as the plausible mechanisms for wettability alteration. Chandrasekhar [275] observed that the multi-ion exchange between the active multivalent ions (Ca^{2+}, Mg^{2+} and SO_4^{2-}) and mineral dissolution was the mechanism responsible for wettability alteration when the brine dilution approach was applied to carbonate cores containing dolomite. However, in a few other cases, very little or negligible results were observed during brine dilution as highlighted in Chapter 2. Furthermore, several authors suggested that wettability alteration could not depend on the bulk mineral dissolution due to aqueous solution buffering and equilibration on field-scale [194, 195]. Though incremental oil recoveries as measured in the laboratory core experiments are usually greater than those from the field pilot tests, a single-well tracer test conducted by Yousef *et al.* [24] using diluted seawater indicates a decrease in the residual oil saturation by about 7%.

It is clear from the published studies that the brine chemistry, especially the PDIs, plays a more essential role than its level of salinity in carbonates. A probable explanation for the observed wettability alteration is that the PDIs are higher in the imbibing brine compared to the formation brine and molecularly diffuse into the water film separating the crude oil and the rock. This leads to a non-equilibrium state in the oil-brine-rock interaction that prompts aqueous phase reactions along with likely rock-brine reactions in the form of surface interactions and/or mineral dissolution/precipitation. More dilution of the imbibing brine would lead to the reduction in the amount of non-active ions and increased activity of the PDIs that would make this interplay more effective. This is coupled with the fact that brine dilution increases the size of the double layer, thereby thickening the water film layer between oil/rock. Consequently, this leads to alterations in the rock wettability to less oil wetting state. The different mechanisms that have been proposed [7, 32, 47, 56] can be expressed as:

- Dissolution of *in-situ* rock minerals can expose fresh water-wet sites by removing oil-wet sites and/or precipitation of new rock minerals with water-wet properties can overlay the surface.
- Surface interaction with PDIs can increase the electrostatic repulsive forces between oil/rock leading to the substitution of attached oil polar components at the surface.

In this case, the predictive model was developed on the basis that the specific brine composition is highly essential, especially when the total brine salinity is reduced in the presence of different mineralogical content. In an attempt to use this tool to explain how various features identified above influence oil recovery by changes in water chemistry, the model was launched to investigate how the different phenomena relate to brine dilutions. For the process dependent interpolating parameter to estimate the altered relative permeability, capillary pressure and residual oil saturation functions through linear interpolation as stated in eq. 5.10 – 5.12, two different scenarios were considered and tested in different simulations runs.

<u>Sim A</u>: Just as previously mentioned, the exchange reactions are involved in wettability alteration towards the less oil-wet state. During diluted brine injection, the initial equilibrium established between crude oil/brine/rock is disturbed, such that the carboxylic components attached to the rock surface are desorbed as a result of sulfate ions adsorption and exchange between the divalent cations on the rock surface sites. This exchange eventually results in the increase in surface

equivalent fractions of either or both Ca^{2+} and Mg^{2+}, leading to a reduction in the concentration of the free charged surface anionic sites ($> NaX$). This concept is captured by using the equivalent fraction of the free charged anionic surface as the interpolant:

$$\omega(\psi_{Na-X}) = \frac{\psi_{(>NaX)}{}^{final} - \psi_{(>NaX)}(x, y, z, t)}{\psi_{(>NaX)}{}^{final} - \psi_{(>NaX)}{}^{initial}} \tag{5.13}$$

The initial equivalent fractions, $\psi_{(>NaX)}{}^{initial}$, at the beginning of the injection period, which is the fraction of the charged anionic surface when there was no wettability alteration and the final equivalent fractions, $\psi_{(>NaX)}{}^{final}$, at the end of the injection period, which signifies the fractions at which enough alteration has occurred are the parameters on which the interpolation is calculated based on the equivalent fractions at any point with time, $\psi_{(>NaX)}(x, y, z, t)$. When $\omega = 1$, it implies no exchange had taken place and the fractions of the charged anionic surface remained the same while when $\omega \approx 0$, this implies that there had been a sorbed process.

<u>Sim B</u>: As diluted brine is injected with lower salinity and different ionic compositions as compared to the initial formation brine, the ions are transported such that the equilibrium state between the mineral and the aqueous phase is disturbed. Consequently, rate-dependent chemical reactions evolved in the form of mineral dissolution/precipitation that changes the rock surface and as a result alter the porosity as earlier mentioned. As the mineral dissolves, the absorbed oil is liberated from the surface while fresh water wet surface sites are created. This simulation scenario did not consider the surface sorption reactions, because changes at the rock surface in terms of dissolution/precipitation was dynamically linked to altering the wetting state by:

$$\omega(\Delta\phi) = 1 - \frac{\Delta\phi^{final} - \Delta\phi(x, y, z, t)}{\Delta\phi^{final} - \Delta\phi^{initial}} \tag{5.14}$$

$$\Delta\phi = \phi_{initial} - \phi_{altered}^{n} \tag{5.15}$$

The porosity modification, $\Delta\phi$, is used as a measure for the dissolved and/or precipitated minerals, which can be calculated by subtracting the initial porosity, $\phi_{initial}$, from the altered porosity, $\phi_{altered}$, at time n. Then, the initial porosity modification, $\Delta\phi^{initial}$, at the beginning of the injection cycle, which is the value at which no wettability alteration has occurred and the final porosity modification, $\Delta\phi^{final}$, at the end of the injection cycle, which is the value at which

enough minerals have dissolved to create more water-wet surfaces are the matching parameters. When $\omega = 1$, it implies that no mineral alteration has taken place while when $\omega \approx 0$, this implies that enough minerals have dissolved, and new equilibrium state is established.

Table 5.1—Reservoir core properties used for simulating the different core experiments.

Property	**Chandrasekhar [275]**	**Austad *et al.* [48]**	**Yousef *et al.* [57]**
Porosity	26.4%	18%	25.1%
Mineral Volume Fraction	70% Calcite, 3.6% Dolomite	79% Calcite, 3% Anhydrite	64% Calcite, 10% Dolomite, 2% Anhydrite
Permeability (mD)	7.60	1.20	39.60
Diameter (cm)	3.79	3.80	3.80
Length (cm)	5.81	8.10	16.24
Pore Volume (cm^3)	17.3	16.5	36.6
Cross Sectional Area (cm^2)	11.28	11.34	11.34
Initial water saturation	0.32	0.07	0.10
Initial pressure (psi)	50	145	3000
Reservoir temperature (°C)	120	110	100
Injection Sequence	SW→SW/2	FW→FW/100	SW→SW/2→SW/10
Injection Rate (cm^3/min)	0.045	0.01	1.0

5.2.1 Simulation portfolio for different mineralogical carbonate rocks

Different cases of linear one-dimensional (1-D) simulations were run with the various core and flow parameters, and mineralogical contents listed in Table 5.1. The relative permeability and capillary pressure functions are also presented in Figure 5.1. The carbonate cores used by Chandrasekhar [275] contained calcite with 5% rock volume fractions of dolomite. While carbonate cores from Austad *et al.* [48] contained calcite and 3% rock volume fractions of anhydrite, in contrast to that of Yousef *et al.* [57] containing calcite, dolomite and anhydrite. The specific surface area considered for calcite, dolomite and anhydrite are 0.29 m^2/g, 2.8 m^2/g and 1 m^2/g respectively [70, 112]. Various sorption capacities, equilibrium constants, rate constants, selectivity factors, and isotherm coefficients for all reactions were kept constant as discussed in Chapter 4. The flow domain was uniformly discretized into 100 grid blocks. A horizontal configuration was utilized for simulation of all experiments except for Chandrasekhar [275] where

the vertical configuration was used similar to their experimental flooding configuration with the producer at the top and injector at the bottom (Figure 5.2). Table 5.2 lists the properties of the crude oil, formation and injected brine compositions. More detailed explanation about these experiments can be found in the references cited in Table 5.1. A synthetic oil composition was used which reproduced the reported oil viscosity listed in Table 5.2. The dispersion/diffusion coefficient (8.13 x 10^{-5} cm^2/s) was determined by reproducing the effluent concentration curves of the non-active ions (Na^+ and Cl^-) from the experiment by Chandrasekhar [275]. Similarly, the reaction sets, and tuned reaction and transport parameters obtained from the 1-D core simulations was used to simulate and evaluate a two-dimensional (2-D) quarter of a five-spot pattern.

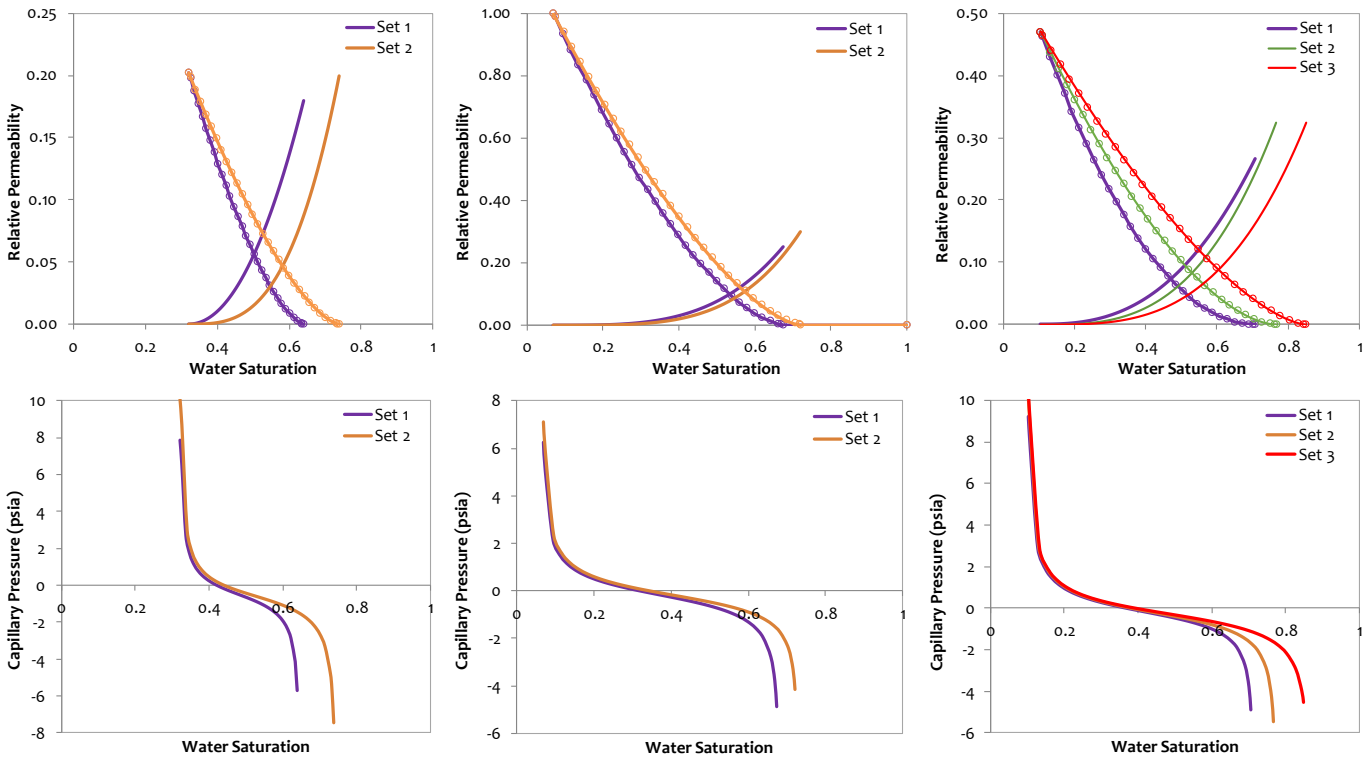

Figure 5.1—Relative permeabilities (*top panels*) and capillary pressure (*bottom panels*) used in simulating core flooding experiment of Chandrasekhar [275] (*left*), Austad *et al.* [48] (*middle*), Yousef *et al.* [57] (*right*). The solid lines with markers correspond to the relative permeability to oil while the solid lines without markers correspond to relative permeability to water. The initial flow functions (*set 1*) correspond to the initial wetting state, and the subsequent flow functions correspond to cases where the wetting state has shifted towards more water wetness. The changes in k_{rj}, P_c and s_{or} values in *middle panel* is smaller than in *left panel* and *right panel* because the cores used by Austad *et al.* [48] is more water-wet than those used by Chandrasekhar [275] and Yousef *et al.* [57].

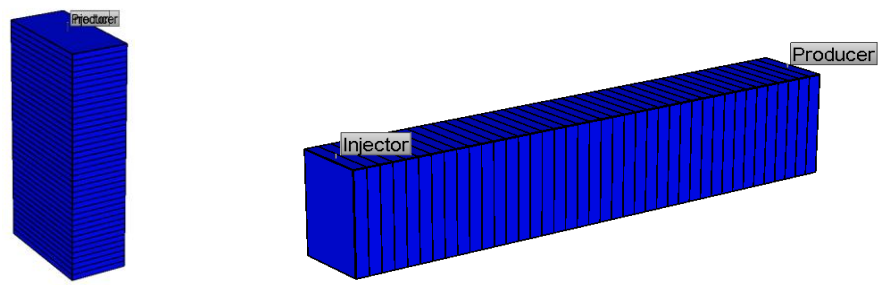

Figure 5.2—Core flood experiment design Vertical (*left*) and Horizontal (*right*) simulation model

Table 5.2—Fluid compositions and Properties used in the simulation

Chandrasekhar [275]									
Brine (mg/L)	Na^+	Ca^{2+}	Mg^{2+}	SO_4^{2-}	HCO_3^-	Cl^-	Total Salinity	Ionic Strength (M)	Debye Length κ^{-1} (nm)
Formation Water	49933	14501	3248	234	-	111810	179726	3.161	0.158
Seawater	13700	521	1620	3310	-	24468	43619	0.757	0.323
Twice Diluted Seawater	6850	260.5	810	1655	-	12234	21809.5	0.379	0.456
Viscosity (cP) at 120 °C	Oil	Formation water		Seawater		Twice Diluted Seawater			
Acid number of 2.45 mg KOH/g	1.05	0.3382		0.2505		0.2418			
Austad *et al.* [48]									
Brine (mg/L)	Na^+	Ca^{2+}	Mg^{2+}	SO_4^{2-}	HCO_3^-	Cl^-	Total Salinity	Ionic Strength (M)	Debye Length κ^{-1} (nm)
Formation Water	60168	17468	1814	0	183	129308	208942	3.664	0.149
Diluted Formation water	601.68	174.68	18.14	0	1.83	1293.08	2089.42	0.036	1.486
Viscosity (cP) at 110 °C	Oil	Formation water		Diluted Formation water					
Acid number of 0.70 mg KOH/g	0.76	0.39			0.26				
Yousef *et al.* [57]									
Brine (mg/L)	Na^+	Ca^{2+}	Mg^{2+}	SO_4^{2-}	HCO_3^-	Cl^-	Total Salinity	Ionic Strength (M)	Debye Length κ^{-1} (nm)
Formation Water	59491	19040	2439	350	354	132060	213734	3.764	0.148
Seawater	18300	650	2110	4290	120	32200	57670	1.008	0.285
Twice Diluted Seawater	9150	325	1055	2145	60	16100	28835	0.504	0.404
Ten times Diluted Seawater	1830	65	211	429	12	3220	5767	0.101	0.903
Viscosity (cP) at 100 °C	Oil	Formation water		Seawater		Twice Diluted Seawater			
Acid number of 0.25 mg KOH/g	0.691	0.476		0.321		0.304			

5.2.2 Laboratory simulation results

For the investigation of laboratory brine-dependent recovery, not only ultimate oil recovery was considered, but also other available data, most notably, the effluent ion concentrations and pressure differential. The analysis of the produced ions was also performed to give a robust understanding of the thermodynamic parameters used in describing the complex oil-brine-rock interactions. It is worth mentioning that the comparison between the simulated and experimental breakthrough curves of the produced ions is plotted on a semi-log scale due to the order of magnitude difference between initial and injected brine concentrations. Furthermore, the final recovery and the shape of recovery for each core simulation differed due to the degree of oil/mixed wettability of the core as represented by the relative permeability curves in Figure 5.1. The reaction sets considered for Sim B excluded surface reactions, while Sim A considered all reactions.

5.2.2.1 Core material with calcite and dolomite minerals

Chandrasekhar [275] reported several coreflood experiments investigating brine dilution on carbonate cores at a reservoir temperature of 120 °C and atmospheric pressure. In one of the vertical corefloods, the core was saturated with formation water and aged in dead oil at the initial water saturation. Then, the core was first flooded with seawater followed by various dilutions (twice, 10 times, and 20 times diluted) of seawater. Seawater (SW) injection was reported to recover 47% OOIP after 5 PV injections and during the first 3 PV injection of twice diluted seawater (SW/2), an additional 10% OOIP was recovered. The rock lithology is composed of calcite (95%) and dolomite (5%). They presented associated mechanisms supported through the effluent ion and pH analysis. Here, the focus was to model these two injection cycles. Figures 5.3—5.5 compare the simulated and experimental results of the effluent ion concentration, oil recovery, pressure differential and pH, and a good agreement is evident among these results, which indicates that this model could capture the slow and fast transient responses observed during the flooding experiments. The model replication of the reported Mg^{2+} was initially poor and every attempt to do so tend to poorly replicate the reported Ca^{2+}. The process involves dolomite precipitation, which requires the consumption of Mg^{2+} and Ca^{2+} as indicated by reaction R14 in Chapter 4. It was suspected that either there was an experimental error in the reported values or

another mineral was present such as magnesite that the authors did not report. However, reduced concentrations (932 ppm for SW and 624 ppm for SW/2) were used in the simulation instead of the actual reported concentrations (1620 ppm for SW and 810 ppm for SW/2) to obtain a good agreement between simulated and experimental Mg^{2+} as presented in Figure 5.3. Meanwhile, Sim B shows a similar trend with Sim A, except that the dip at the start of each injection cycle was better captured in the latter. The dip at the start of each injection cycle was because of the surface sorption process that reduced Mg^{2+} concentration in the effluents. The surface sorption occurred because Mg^{2+} was exchanged at the surface site during the period of improved production. Meanwhile, as no more oil production was observed, Mg^{2+} in the effluent returned to the injection level.

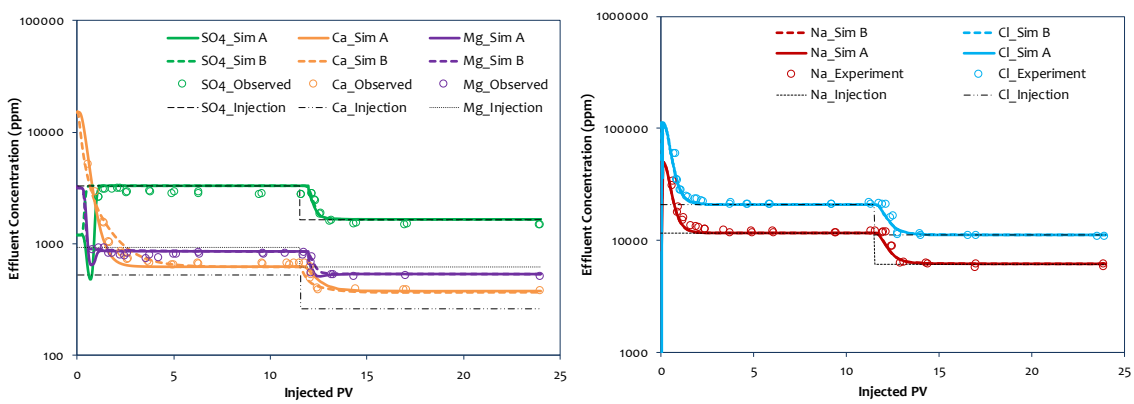

Figure 5.3—Simulated and experimental breakthrough curves of Mg^{2+}, Ca^{2+} and SO_4^{2-} (*left*) and Na^+ and Cl^- (*right*). Experimental data obtained from Chandrasekhar [275]

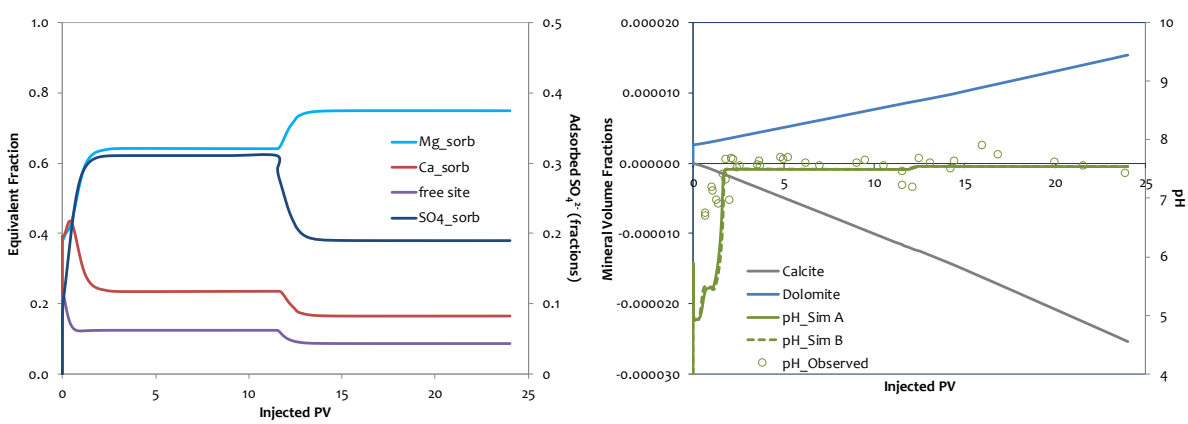

Figure 5.4—Sim A prediction at the center of the simulation domain for exchangeable fraction of Ca^{2+} ($> CaX_2$), Mg^{2+} ($> MgX_2$), free anionic site ($> NaX$), and amount of SO_4^{2-} adsorbed (*left*); mineral volume alteration and simulated and experimental pH comparison (*right*)

Likewise, in Figure 5.3, calcite dissolution, which had spiked Ca^{2+} in the effluent, and adsorption of SO_4^{2-} were captured as both models replicated the reported concentrations from the experiments. However, Sim A better captured the earlier dip in SO_4^{2-} concentration when SW flooding was conducted with higher SO_4^{2-} content than in the initial formation water. It is well documented that there is a high tendency for Mg^{2+} to displace Ca^{2+} from the surface site at a high temperature [53, 55], which is the case presented here based on further analysis of Sim A predictions in Figure 5.4. The inclusion of surface sorption reactions only in Sim A captured this fact that was further supported by the evidence that more Ca^{2+} (abundant due to calcite dissolution) and less Mg^{2+} was found in the effluent at the point where improved production was observed. Similarly, SW contained less Ca^{2+} and more Mg^{2+} compared to the initial formation water, as and when SW had contacted the surface site, more Mg^{2+} had adsorbed and replaced the adsorbed Ca^{2+}. This led to a reduction in the concentration of free anionic surface site, and because SW contained more SO_4^{2-}, there was also an increased SO_4^{2-} adsorption on the surface site (Figure 5.4). Lower concentration of Ca^{2+} in SW increased calcite dissolution to compensate for less Ca^{2+} in the aqueous phase, which consequently resulted in dolomite precipitation because of excess Ca^{2+} in the aqueous phase (see Figure 5.4). In this regard, Sim A and Sim B showed a similar trend in terms of dissolution/precipitation because they both account for rate-dependent reactions.

However, as SW/2 was injected with less SO_4^{2-}, there was less SO_4^{2-} adsorption as emphasized by Sim A predictions in Figure 5.4. A high sulfate adsorption has occurred in the previous cycle and introduction of diluted brine with reduced salinity led to an increase in the double layer thickness (evident from Table 5.2 as Debye length increased from 0.32 to 0.46) which enabled cations co-adsorption. The reduced concentration of Ca^{2+}, Mg^{2+} and Na^{+} in SW/2 was expected to result in less formation of aqueous complexes of $CaSO_4$, $MgSO_4$ and $NaSO_4^{-}$ according to reactions R5–R7 in Chapter 4. Because of the available surface site previously created by sulfate adsorption, increased double layer thickness and reduced surface charge, Mg^{2+} continued to be exchanged until a new equilibrium was reached and adsorbed oil continued to desorb until no more oil recovery (Figure 5.5). It is worth mentioning that the initial Na^{+} and Cl^{-} concentration of the seawater is 13,700 ppm and 24,468 ppm, respectively, however, the concentration produced was less (12,100 ppm and 21,090 ppm) as shown in Figure 5.3. Both Na^{+} and Cl^{-} are considered non-

active ions towards the carbonate rock surface, hence, they are not involved in any reaction that could reduce or decrease their concentration in the effluent. No substantial explanation was given by the authors to be responsible as such. Moreover, a similar observation was made during SW/2 injection, and the difference is not too large, which can be interpreted as an experimental error. Hence, the reduced concentration was considered rather than the actual reported concentration because using a higher concentration than observed in the effluent would increase the ionic strength, which would consequently decrease the activity of other ions. As shown in Figure 5.3, the predicted concentrations from both simulation scenarios gave a similar trend with concentrations from the experiments since Na^+ and Cl^- were non-active ions. Then, reduction of Na^+ and Cl^- in the injected brines resulted in lower total ionic strength and increased double layer thickness, such that surface reactivity of the PDIs leading to wettability alteration increased as discussed above.

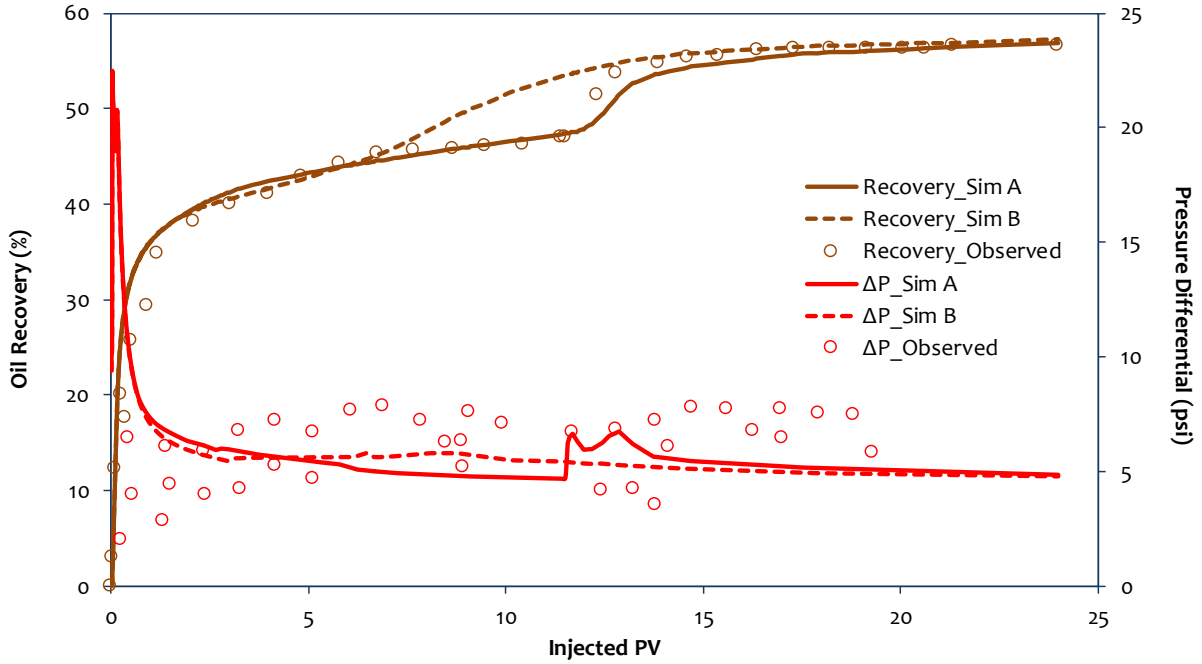

Figure 5.5—Comparison between simulated and experimental oil recovery and pressure differential. Experimental data obtained from Chandrasekhar [275]

Both simulation scenarios captured the experimental pH, which is predominantly dictated by the mineral alteration in terms of dissolution and precipitation. As calcite dissolution and dolomite precipitation occurred, there were loss and gain of H^+ protons respectively that influenced the

aqueous pH. However, a slight increase in effluent pH as seen in Figure 5.4 is the resultant effect which signifies that the dissolution occurred more than the precipitation. The slight increase in the pH as reported by the authors is not the mechanism responsible for the improved recovery as it would require a very high pH – exceeding 10 to generate a significant amount of *in-situ* surfactant that could improve recovery [56]. The process-dependent interpolation parameter was tuned using maximum and minimum thresholds to reproduce the reported oil recovery and pressure differential. Both simulation scenarios reproduced the experimental pressure differential. Considering Sim B with its effect on wettability, the simulation model could not capture the observed improved recovery as shown in the contrasts between the simulated and experimental oil recovery in Figure 5.5. The simulated oil recovery was more than the experimental values at the first injection cycle, though later replicated the ultimate cumulative oil recovery that is mainly dictated by the residual oil saturation. However, sim A showed a good match of cumulative oil recovery with wettability alteration as a function of the exchangeable fractions of the free anionic surface. The exchange of the divalent cations enhanced by adsorption of SO_4^{2-} was responsible for the alteration of the wetting state towards water-wetness and the resulting improved oil recovery was excellently reproduced similar to the experimental oil recovery in Figure 5.5.

5.2.2.2 Core material with calcite and anhydrite minerals.

A study was conducted by Austad *et al.* [48] to investigate brine dilution effects on carbonates as observed by Yousef *et al.* [57]. In their study, a carbonate core plug was saturated and aged in oil with an acid number of 0.7 mg KOH/g. Then, flooded with 6 PV of formation water (FW) followed by diluted formation water (FW/100), both without sulfate, and observed an incremental recovery of 5% OOIP at reservoir temperature of 110 °C. After that, the presence of anhydrite was confirmed by flooding the saturated core with deionized water, of which SO_4^{2-} production was observed in the effluent. They concluded that the continuous presence of SO_4^{2-} in the aqueous phase, due to anhydrite dissolution, was the key factor responsible for wettability alteration and improved recovery. The two simulation model scenarios were also implemented to test the hypothesis presented by Austad *et al.* [48] using a horizontal coreflood configuration with

producer and injector placed at either side of both ends (see Figure 5.2). The rock lithology, model dimensions and parameters used are listed in Table 5.1.

Figure 5.6 shows the comparison between the simulated and experimental result of the SO_4^{2-} effluent ion concentration, pressure differential and oil recovery. With the available experimental data for SO_4^{2-} effluent concentration in Figure 5.6, Sim A closely reproduced the experimental breakthrough curve than Sim B. Since injected brines did not contain SO_4^{2-}, the only source of the produced SO_4^{2-} was anhydrite dissolution and the amount produced served as an indication of the amount of anhydrite dissolved. Upon FW injection, anhydrite began to dissolve as shown in Figure 5.7, because of supersaturation of dissolvable anhydrite in the core. The dissolution continued because the reaction is a slow process and SO_4^{2-} continued to be produced as effluent as well as adsorbed onto the surface site until the adsorbed and produced amount remained constant after about 1 PV injection. At this point, considerable amounts of sulfate had adsorbed to the rock (Figure 5.7). Because of anhydrite dissolution, excess Ca^{2+} in the aqueous phase led to calcite precipitation as shown in Figure 5.7. However, during the FW/100 injection, there was a rapid increase in the amount of SO_4^{2-} adsorbed, which was because the brine dilution created more destabilization of the existing equilibrium and increased surface reactivity of the PDIs.

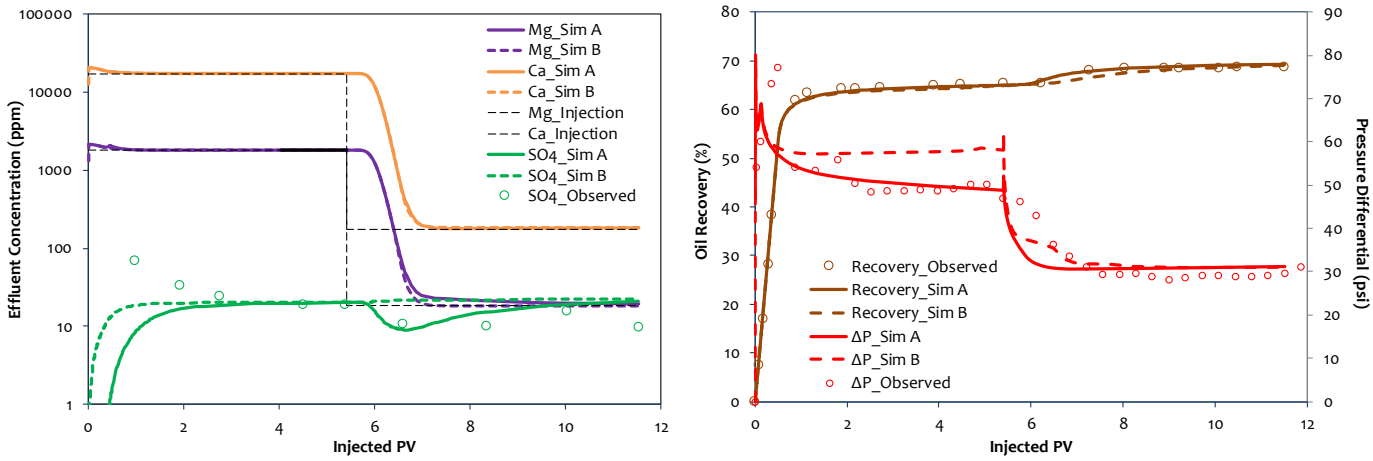

Figure 5.6—Comparison of predicted and experimental breakthrough curves of SO_4^{2-}, Mg^{2+}, and Ca^{2+} (*left*) and oil recovery and pressure differential (*right*). Experimental data obtained from Austad *et al.* [48]

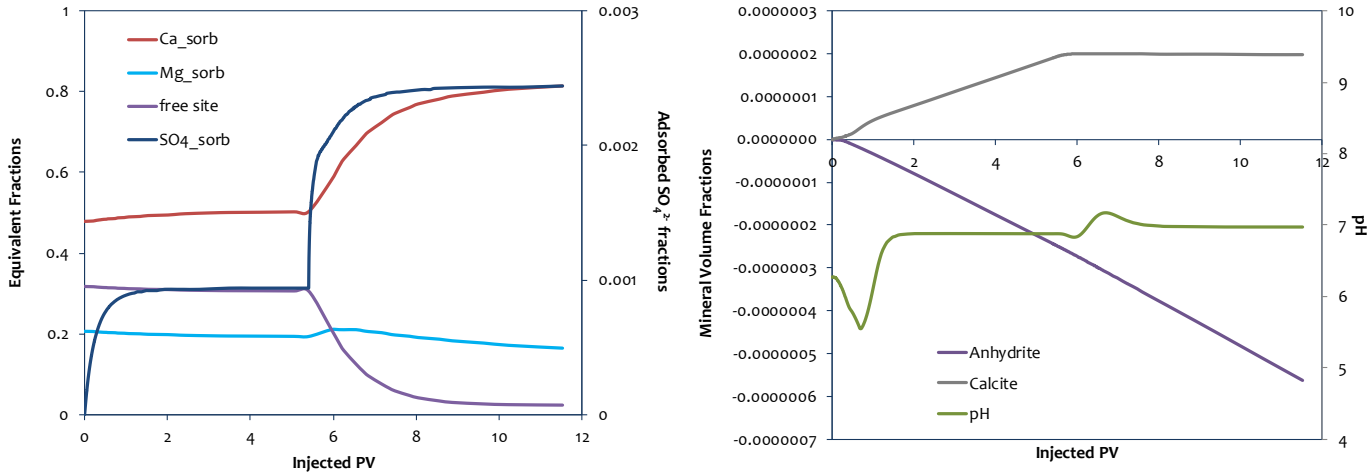

Figure 5.7—Sim A predictions at the center of the simulation domain for exchangeable fraction of Ca^{2+} ($> CaX_2$), Mg^{2+} ($> MgX_2$), free anionic site ($> NaX$), and amount of SO_4^{2-} adsorbed (*left*); mineral volume alteration and pH (*right*)

Once flooding commences, SO_4^{2-} in the effluent decreased as an indication of increased SO_4^{2-} adsorption. The dissolution rate of anhydrite remained constant and calcite precipitation slightly reduced to produce enough Ca^{2+} to compensate for the low Ca^{2+} in the injected brine. The net result is seen as SO_4^{2-} remained constant after about 1 PV until the end of the injection cycle. At the start of the injection cycle, SO_4^{2-} was lesser in Sim A as compared to Sim B (same with experiments), enabling SO_4^{2-} to adsorb more, reduce the surface charge, and replace adsorbed oil at the surface site. In another test, Austad *et al.* [48] injected deionized water into a core saturated with FW and reported production of Ca^{2+} and SO_4^{2-}. This means that anhydrite dissolution was responsible for the Ca^{2+} and SO_4^{2-} production while slight calcite dissolution added to the effluent concentration of Ca^{2+}. This explanation is synonymous to the author's claim as they observed that there was the dissolution of anhydrite in addition to that of calcite. In this present case, the dissolution of calcite is not as evident compared to that in the work of Chandrasekhar [275] because anhydrite dissolution compensated for the low Ca^{2+} during diluted brine injection. Figure 5.7 also presents the equivalent exchangeable cations and free anionic site for Sim A at the surface sites. An increase in sorbed Ca^{2+} was observed when more sulfate adsorbed because of the increased amount of Ca^{2+} in the aqueous phase. An improved recovery was achieved during the FW/100 injection cycle (see Figure 5.6) because of the co-adsorption process of the PDIs, which led to a reduction free anionic site concentration.

There is a good agreement between the Sim A and Sim B results for effluent concentration of Mg^{2+} and Ca^{2+}. The effluent concentration of Mg^{2+} remained same as injected because Ca^{2+} was the major ion exchanged. Since Na^{+} and Cl^{-} are considered as non-active ions, their concentration in the effluent remained similar to the injected concentration. They had a similar trend with those plotted for the previous case in Figure 5.3. However, their reduction in the injected brine decreased the ionic strength, increased the double layer thickness (from 0.15 to 1.49 as reported in Table 5.2 for reciprocal Debye length) and increased the activity coefficients of PDIs so they could easily promote wettability alteration through improved surface reactivity. From Figure 5.6, Sim A excellently reproduced the oil recovery and pressure differential than Sim B, with an indication that the process of exchange of Mg^{2+} and Ca^{2+} enhanced by the adsorption of SO_4^{2-} was responsible for the wettability alteration. Sim B reproduced the oil recovery but gave an underestimation of oil recovery during the FW/100 injection cycle and could not replicate the pressure differential. This signifies that dissolution alone, cannot explain the improved recovery observed during brine dilution: rather a process that integrates dissolution with surface sorption resulting in wettability alteration. The predicted pH is similar for both simulation scenarios (Figure 5.7), though slightly higher than what was obtained in the simulation of the experiment by Chandrasekhar [275]. This is because both calcite (slight) and anhydrite dissolution took place consecutively as compared to the resultant effect of dissolution and precipitation in the latter.

5.2.2.3 Core material with calcite, dolomite, and anhydrite minerals

Yousef *et al.* [57] conducted a series of study to investigate brine dilution effects on carbonates and reported about 20% incremental recovery on successful seawater dilution. In their experiment, the composite core plug was saturated and aged in live oil, and flooded with 10 PV of field seawater (SW) followed by 10 PV of various seawater dilutions at typical middle eastern reservoir conditions. In this case, the first three injection cycles were considered, which included seawater (SW), twice-diluted seawater (SW/2) and ten times diluted seawater (SW/10). The composite core comprised of four core plugs of average permeability of 36.5 mD. Each core plug was represented in the simulation by twenty-five (25) grid-blocks, making a hundred grid-blocks in total. The core is comprised of 85% calcite, 12% dolomite, and 3% anhydrite [102]. The authors highlighted

surface charge alteration as the key mechanism responsible for wettability alteration and improved recovery. Figure 5.8 shows that both simulation scenarios closely reproduced the experimental oil recovery and pressure differential, though Sim A gave better result than Sim B.

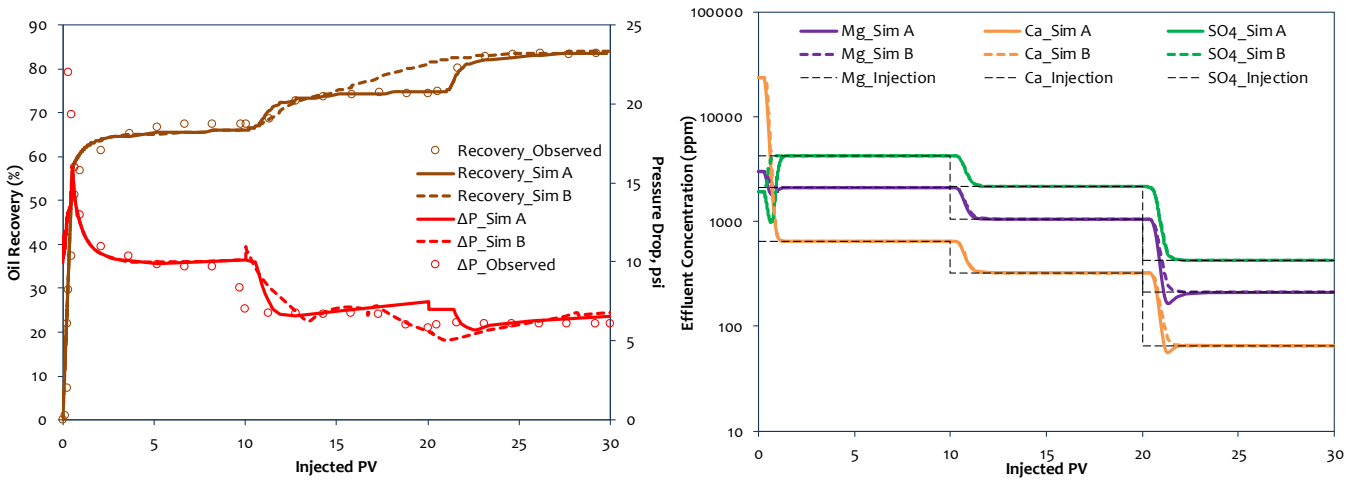

Figure 5.8—Comparison between simulated and experimental oil recovery, and pressure differential (*left*). Simulated breakthrough curves of SO_4^{2-}, Mg^{2+}, and Ca^{2+} (*right*). Experimental data obtained from Yousef *et al.* [57]

For the simulated breakthrough curves also presented in Figure 5.8, the trend is practically similar for both simulation scenarios except at the start of the injection cycle. The injected brine contained higher SO_4^{2-} than in the initial formation water, resulting in more adsorption of SO_4^{2-}. Sulfate adsorption desorbed the oil by altering the surface charge such that more cations were exchanged, leading to a reduction in the free surface site. At a high temperature, 100 °C, more Mg^{2+} exchanged than Ca^{2+} (Figure 5.9). Reduced concentration of Ca^{2+} in the aqueous phase due to brine injection with less Ca^{2+} resulted in both calcite and anhydrite dissolution and consequent dolomite precipitation (Figure 5.9), which continued through the injection of various diluted brines. Though the changes in mineral volumes were lower compared to what was obtained in previous simulation cases where either anhydrite or dolomite was absent. As mentioned earlier, it can be seen here that subsequent dilutions increased the double layer thickness and the reactivity of the PDIs such that they exchanged/adsorbed more at the surface sites and reduced the concentration of the free anionic surface site (Figure 5.9). In furtherance to the authors' conclusion, it can be stated here that injecting diluted brine destabilized the existing equilibrium and caused dissolution and/or

precipitation of some minerals, to re-establish equilibrium with the new brine. Even though the mineral alteration in terms of dissolution/precipitation could be microscopic, their effects are still felt with other corresponding process mechanisms.

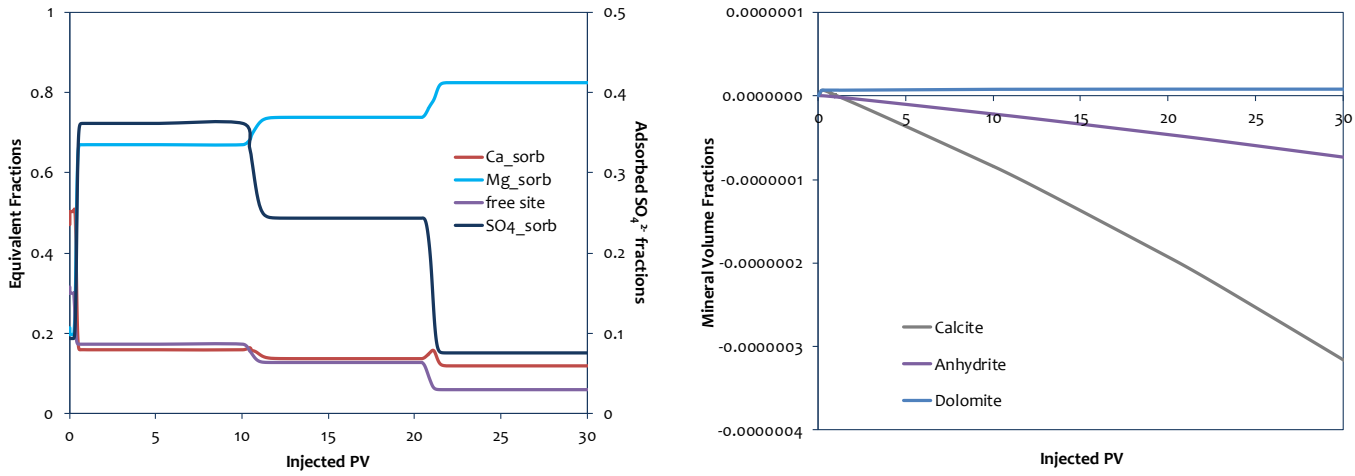

Figure 5.9—Simulation results at the center of the simulation domain for an exchangeable fraction of Ca^{2+} ($> CaX_2$) and Mg^{2+} ($> MgX_2$), free anionic site ($> NaX$), and amount of sulfate adsorbed (*left*); mineral volume alteration (*right*)

In the majority of the simulated experiments, the injected brine contained more SO_4^{2-}, which speedily adsorbed at early times and became relaxed at later periods. This adsorption results in a reduction of surface site charge and consequential desorption of oil as well as enhancing the co-adsorption of the potential determining cations, and continual dilution increased the double layer size and correspondingly increased the reactivity of the PDIs to co-adsorbed, leading to alteration of the wetting state.

5.2.3 Field-scale simulation

To this end, it has been proved that the model based on the hypothesis of integrating all surface interactions, can interpret brine dilution experimental results. In these flooding experiments, cores with different mineralogy have been used, all exhibiting varying improved recoveries. At this stage, investigation of the possibility of achieving similar incremental recovery with lower pore volume injected on field scale as achieved in the core scale flooding was proposed and to further examine the impact of different mineralogical content on the field production.

This was accomplished by using the model to simulate a quarter of a 2-D five-spot pattern with tuned reaction and transport parameters obtained from reproducing the experiment of Yousef *et al.* [57]. A homogeneous model shown in Figure 5.10, assuming a 10-acre well spacing with a permeability of 39.6 mD, and pattern size of 201 m × 201 m × 6 m discretized uniformly into different grid block sizes (30 × 30 × 1, 60 × 60 × 1, 100 × 100 × 1), was developed using the same input parameters as Yousef *et al.* [57]. The results plotted in Figure 5.11 shows the predicted oil recovery from the quarter of a five-spot pattern for the different grid-block sizes. There is no distinct difference in the oil recovery and water cut obtained from the different grid-block sizes, which means the considered grid sizes would have minimal impact on the sensitivity of the mineralogical content on oil recovery.

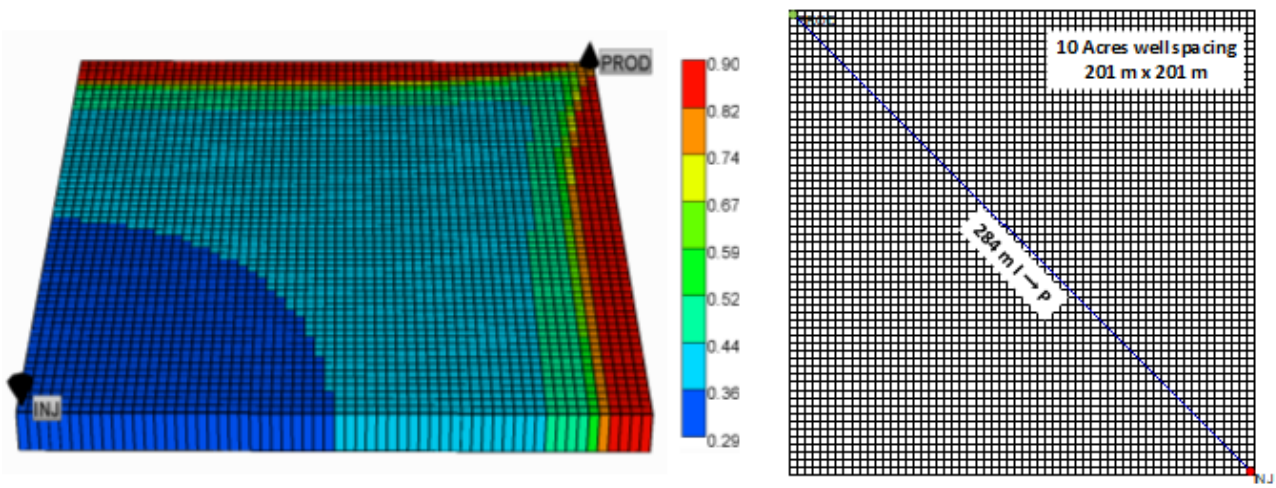

Figure 5.10—Simulation model for the quarter of a five-spot pattern used in this research showing oil saturation after about 1 PV injection (*left*) and grid-block - 60 × 60 × 1 with a block size of 3.35 m (*left*). The green dot at the upper-left corner is the producer while the injector is represented by the red dot at the lower-right. The diagonal blue line is the shortest streamline between the injector and producer, about 284 m long.

Meanwhile, grid-block cells of 3600 (60 x 60 x 1) and 10000 (100 x 100 x 1) showed a similar trend in oil recovery and water cut, as well in the adsorbed sulfate and available free sites fractions presented in Figure 5.12. This informed the decision to continue with 60 x 60 x 1 grid-blocks to ensure computation efficiency. Furthermore, comparison of the 2-D results with the 1-D results plotted in Figure 5.8 reveals that significant incremental recovery was achieved at a less injection pore volume typical of field-scale process. However, the recovery was lower as compared to the

core-scale because of early water breakthrough and poorer areal sweep as indicated in the curvature of the oil recovery curves. The field water cut was also presented to illustrate the immediate response of the injected diluted brines to improve oil recovery. The response was such that water production reduced as significant incremental recovery was obtained.

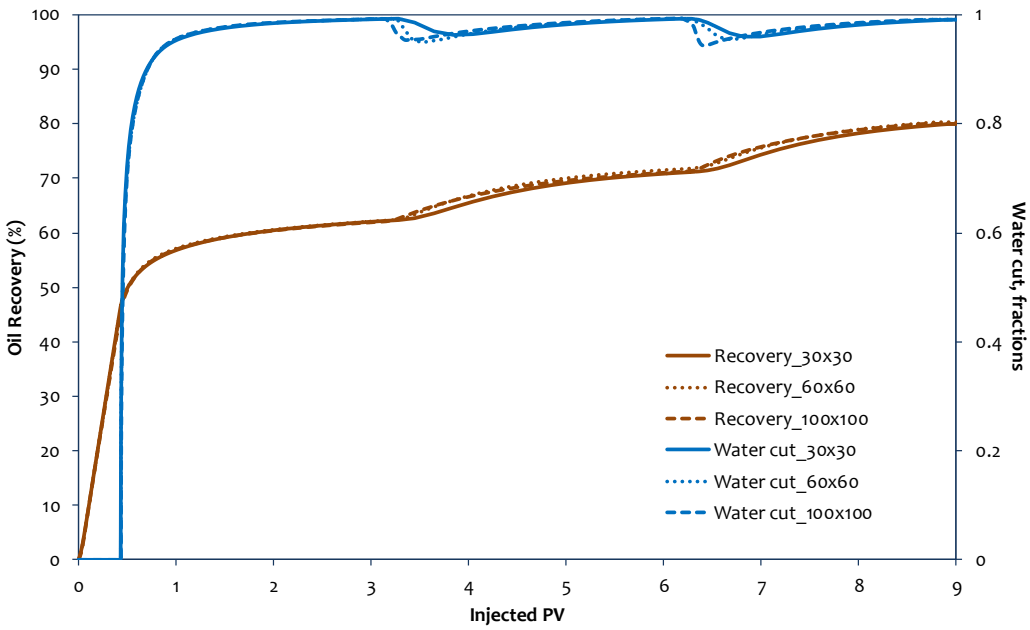

Figure 5.11—Predicted oil recovery and water cut for the quarter of a five-spot pattern with the different grid-block cells (900, 3600 and 10000) using core, flow and reaction parameters of Yousef *et al.* [57]

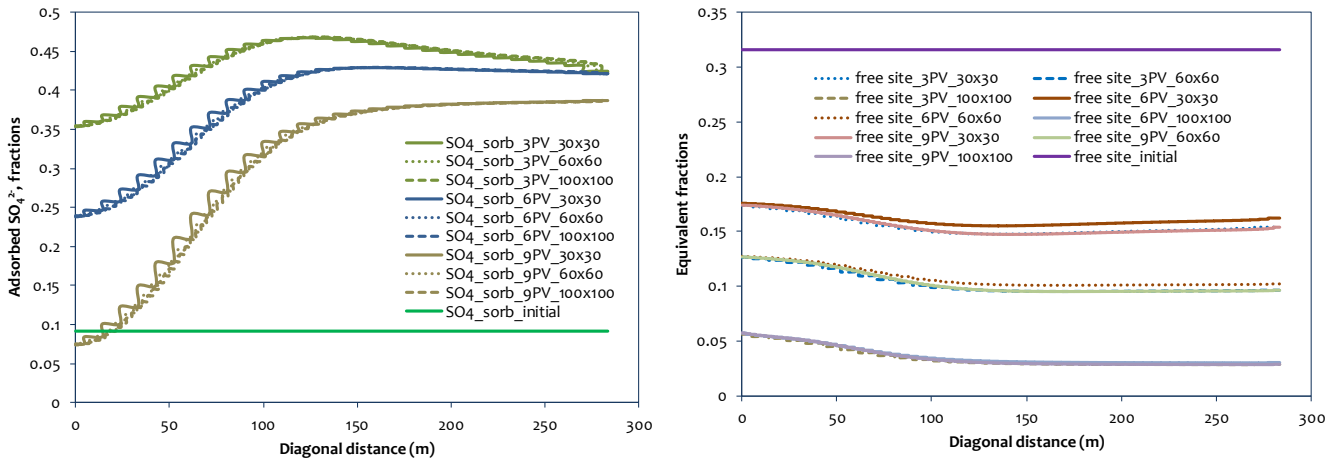

Figure 5.12—Profiles along the diagonal streamline of the quarter five-spot pattern for the different grid-block sizes after each injection cycle: adsorbed SO_4^{2-} (*left*) and free anionic surface site (*right*).

Similarly, using the same injection schemes and water compositions with varying rock mineral compositions, the predicted oil recovery was compared using the cases presented in Table 5.3. The base case contained the same proportion of minerals reported by Yousef *et al.* [57], and for other cases, the mineral proportions were slightly varied. Figure 5.13 compares the oil recoveries from different simulation cases. All the cases have similar ultimate oil recovery, however, during the first two injection cycles, their recovery trend deviated. The different responses of the different mineralogical contents to the same injected water indicate the significance of incorporating mineral alteration into the modeling of brine dilution-dependent recovery processes. Comparing the cases where anhydrite was absent, i.e. Case 1, the oil recovery was low compared to the other cases, because of less SO_4^{2-} adsorption. The cases that showed slightly higher recovery/lower water cut trend compared with the base case, i.e. Case 2, Case 3 and Case 4, was because of high presence of SO_4^{2-}, triggered by anhydrite dissolution, that could be adsorbed and enhanced the exchange of the cations at the surface site. This analysis is not intended to be quantitative but to emphasize the importance of rock mineralogical contents during brine-dilution dependent recoveries, which is consistent with various core experimental observations discussed previously. Hence, the kinetically controlled mineral reaction should not be discarded when modeling brine dilution.

Table 5.3—Mineralogical content for various cases simulated

Field Scale Cases	**Calcite**	**Dolomite**	**Anhydrite**
Base case	85%	12%	3%
Case 1	85%	15%	0%
Case 2	85%	0%	15%
Case 3	85%	7.5%	7.5%
Case 4	97%	0%	3%

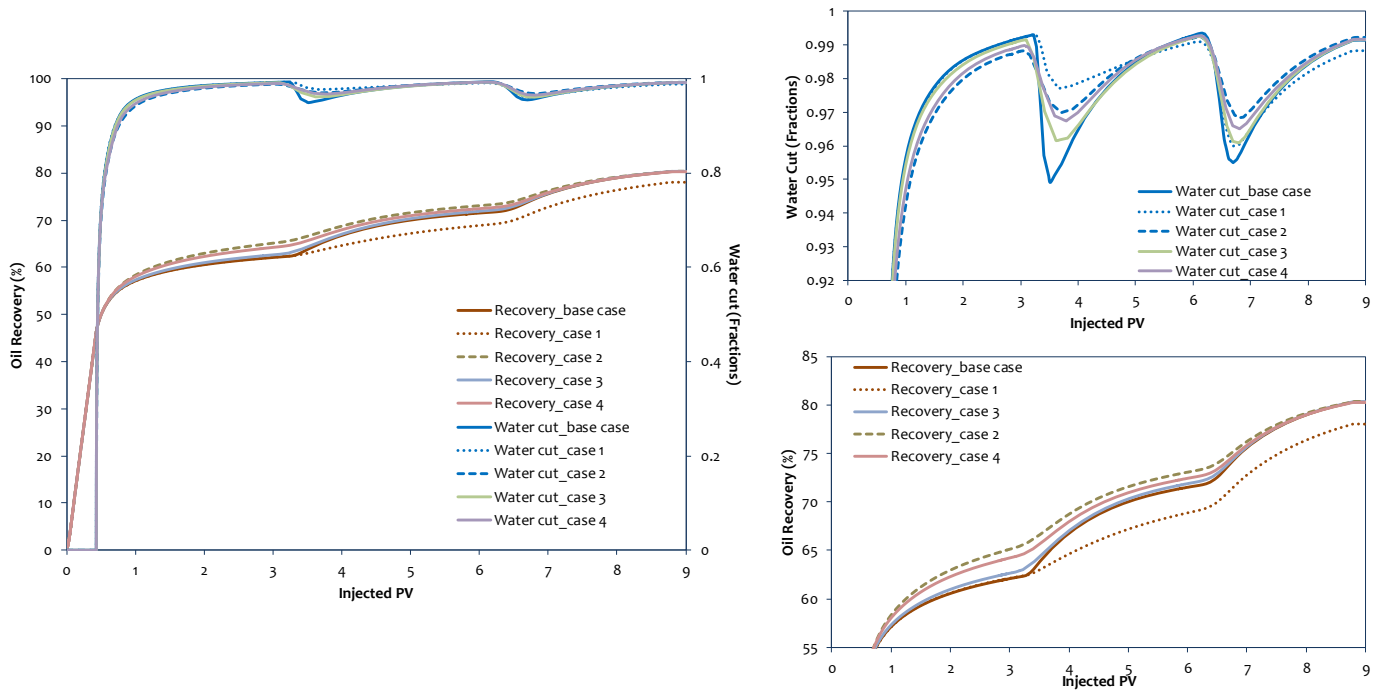

Fig. 5.13—Oil recovery and water cut fractions comparison of varying mineralogical contents with a collapsed view (*left*) and expanded view (*right*)

Next, the investigation of the compositional variation approach during brine-dependent recovery will be discussed, where the process dependent interpolation function described in Sim A was further utilized.

5.3 Oil Recovery Prediction for Compositional Variation Approach

Many studies on carbonate rocks have shown a positive response to injection of smart brines. Some of these studies, especially those performed by Austad and colleagues [32, 38, 51, 52, 54], have ascribed the improved recovery response to the influence of PDIs present in brines that serves as the main water source for waterflooding projects. Chalk formation was found to respond better than either limestone or dolomite formation because of its higher surface area. However, similar profound responses have been reported in limestone and dolomite formation by several other researchers [27, 29, 30, 46, 61, 99, 101]. Different studies have been conducted to identify the PDI that has the most dominant effect. The significant conclusion of these studies is that none of the PDIs could act alone, although in the different combinations that were investigated, SO_4^{2-} was found to be present. In addition, several studies have proved that a high SO_4^{2-} concentration did

not offer improved recovery; rather an upper limit existed beyond which no improved recovery could be observed [7, 46, 52, 138].

In some of these studies, it was hypothesized that wettability alteration is a consequence of a multi-ion exchange process that involves the PDI interactions with the rock surface. It was proposed that SO_4^{2-} is attached to the rock−brine interface, reducing or reversing the positive charge. This leads to the reduction of the electrostatic attraction between the interacting interfaces. Consequently, Ca^{2+} and Mg^{2+} adsorb more to the interacting interfaces because of reduced charge. Some ions combine with the carboxylic component at the oil−brine interface to release the oil, while others attach to the rock−brine interface to balance the electric charge. Meanwhile, another hypothesis suggests that the cause of the wettability alteration is mineral alteration in terms of dissolution and precipitation [47], even though, a few have classified this cause as more of a secondary mechanism [27, 56]. Recent work by Awolayo *et al.* [276] proved that both causes should be integrated in modeling the wettability alteration process as both are involved in re-establishing the new equilibrium state. In this section, the surface sorption model was used to investigate wettability alteration during smart brine injection at the core-scale. Single-phase flooding experiments that were reported in the literature were modeled and compared with the measured produced ion histories. Two-phase water-oil displacement tests were also modeled and compared with experimental data. Lastly, the model was utilized to demonstrate the potential of smart brine flooding at field-scale.

The descriptions of the equations and assumptions made in developing this SSM model are provided in Chapter 4. The model assumes that rock−brine interface becomes initially attracted to oil−brine interface because of the presence of the positively charged surface site ($> X^+$) that can attach to the oil acid-group. Meanwhile the surface fraction of $> X^+$ is reduced due to geochemical interactions between the interacting interfaces in the presence of smart brines. As previously explained, SO_4^{2-} interaction decreases the charge of the positive charge site, and consequently detaches the oil acid group and enables adsorption of Ca^{2+} and Mg^{2+}. This results in the reduction of surface fractions of $> X^+$ and $> NaX$. Then, the flow functions, in this case relative permeability (see Figure 5.14), were made to reflect wettability alteration by their dependency on

the fraction of unoccupied surface site using the linear interpolation technique proposed in eq. 5.10. This hypothesis was tested by predicting different smart brine flooding cases from independently-sourced experiments. The linear 1-D simulations for all core experiments were discretized uniformly into 100 × 1 × 1 grid blocks to reduce numerical dispersion effects with different core properties described in Table 5.4.

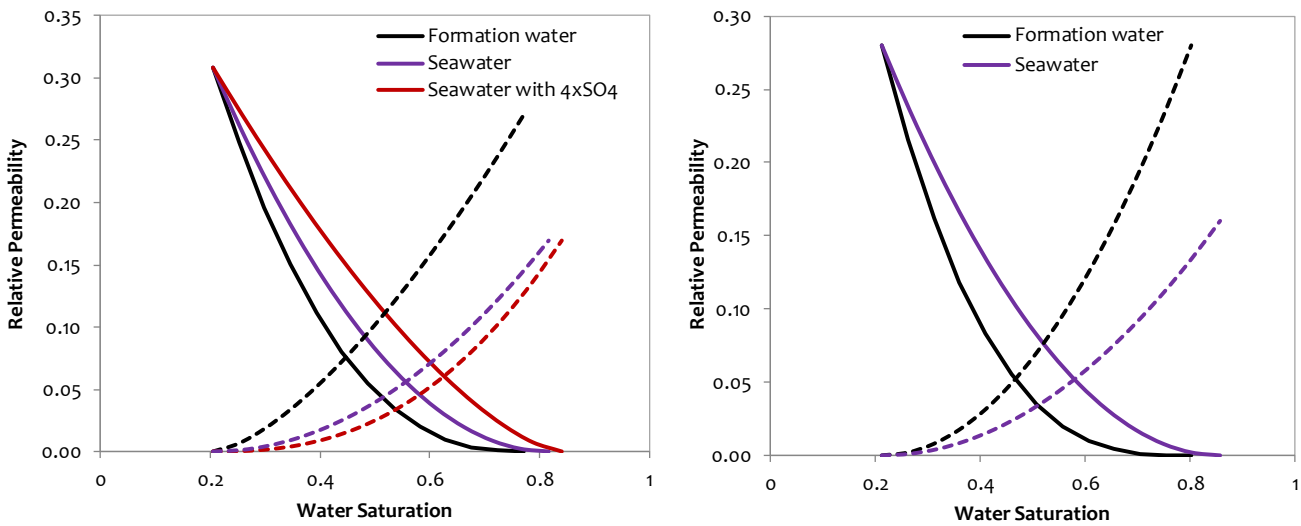

Figure 5.14—Water-oil relative permeability curves for *in-situ* and injected smart brines used in simulating the flooding experiments of S#42 (*left*) and S#9 (*right*). Broken lines indicate relative permeability to water and solid lines indicate relative permeability to oil.

5.3.1 Laboratory scale simulation

5.3.1.1 Single−phase modeling.

In furtherance to the testing of the hypothesis and, the established set of surface sorption parameters, single phase flow experiments using smart brines conducted by Chandrasekhar *et al.* [196] was evaluated. The experiment was carried out on a composite core initially equilibrated with formation water at 120 ºC. In the first experiment, the *in-situ* brine was displaced by about two pore volumes of seawater (SO_4^{2-} in seawater was ten times greater than that in formation water). While, for the second experiment, the *in-situ* brine was displaced with the same pore volumes of seawater with $4\times SO_4^{2-}$. The compositions of different brines *in-situ* and injected are given in Table 5.4. The experimental and simulated normalized ion concentration profiles are

presented in Figures 5.15 and 5.16 for the seawater and seawater with 4×SO_4^{2-} displacement, respectively. In both cases, until about 0.6 pore volume injection (PVI), the concentration of the *in-situ* brine was maintained. This concentration changed significantly until about 1.8 PVIs, which was captured by the model using a dispersion coefficient of 1.95×10^{-5} cm^2/s. Aside from the dispersion effect, the model captured the evolution of the ion profile excellently. Further delay in the production of the PDIs using the established surface sorption parameters in Chapter 4 was well captured as presented in Figures 5.15 and 5.16.

Table 5.4—Summary of fluid and core compositions and properties used in the simulation. Site capacity; was assumed as 3 sites/nm^2. I represents ionic strength and TDS represents total dissolved solids.

Chandrasekhar *et al.* [196] — 120 ºC								
Brine (M)	**Ca^{2+}**	**Mg^{2+}**	**SO_4^{2-}**	**Na^+**	**Cl^-**	**HCO_3^-**	**I**	**TDS** (g/L)
Formation Water	0.280	0.116	0.002	1.752	4.627	0.000	3.986	218.588
Seawater	0.013	0.063	0.036	0.561	0.750	0.000	0.878	44.981
Seawater with 4xSO_4^{2-}	0.006	0.060	0.126	0.423	0.379	0.000	0.785	36.957
Rock properties	*Length (cm)*	*Diameter (cm)*	*Mineral volume fraction*		*Permeability (mD)*	*Porosity (fraction)*	*Swi (%)*	*Flow rate (ml/min)*
	15.3	3.80	0.81 Calcite 0.02 Dolomite		25	0.17	100	0.02
Awolayo *et al.* [29] — 110 ºC								
Brine (M)	**Ca^{2+}**	**Mg^{2+}**	**SO_4^{2-}**	**Na^+**	**Cl^-**	**HCO_3^-**	**I**	**TDS** (g/L)
Formation Water	0.477	0.138	0.001	3.335	4.564	0.001	5.183	261.135
Seawater with 0.5xSO_4^2	0.013	0.067	0.017	0.639	0.701	0.000	0.864	43.365
Seawater with 1xSO_4^{2-}	0.010	0.071	0.030	0.593	0.695	0.000	0.865	43.267
Seawater with 2xSO_4^{2-}	0.014	0.077	0.069	0.531	0.573	0.000	0.873	43.877
Seawater with 4xSO_4^{2-}	0.016	0.083	0.148	0.521	0.423	0.000	0.966	43.877
Rock properties Oil viscosity (1.93 cP)	*Length (cm)*	*Diameter (cm)*	*Mineral volume fraction*		*Permeability (mD)*	*Porosity (fraction)*	*Swi (%)*	*Flow rate (ml/min)*
Core S#9	6.22	3.84	0.67 Calcite 0.08 Dolomite		7.31	0.25	21.42	0.25
Core S#42	9.93	3.86	0.71 Calcite 0.09 Dolomite		1.61	0.20	20.44	0.25

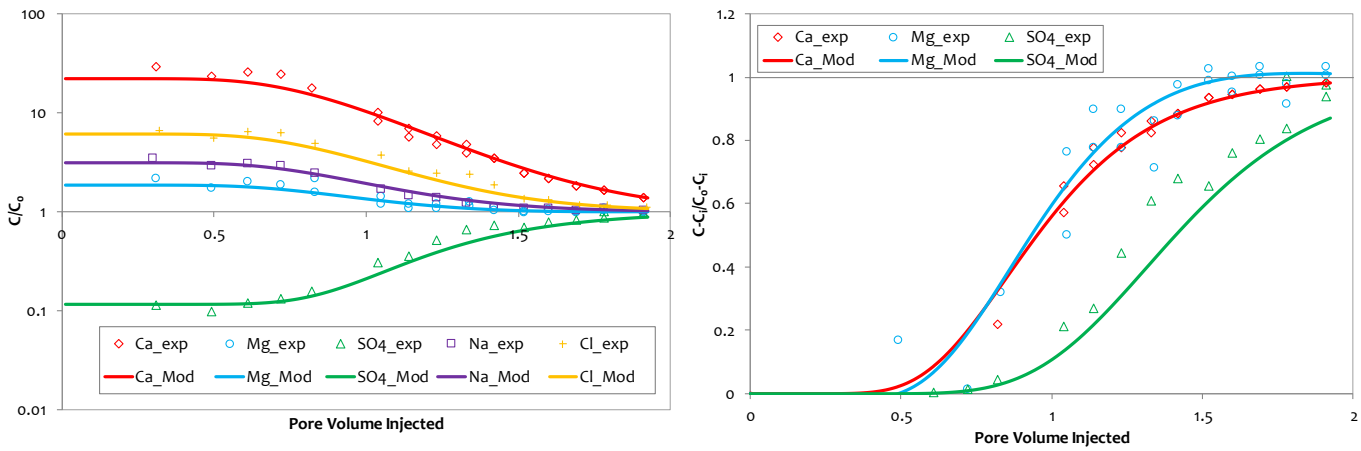

Figure 5.15—Comparison between observed and simulated normalized breakthrough curves for all ions (*left*) and relative breakthrough curves for PDIs (*right*) during seawater flooding. Experimental data obtained from Chandrasekhar *et al.* [196].

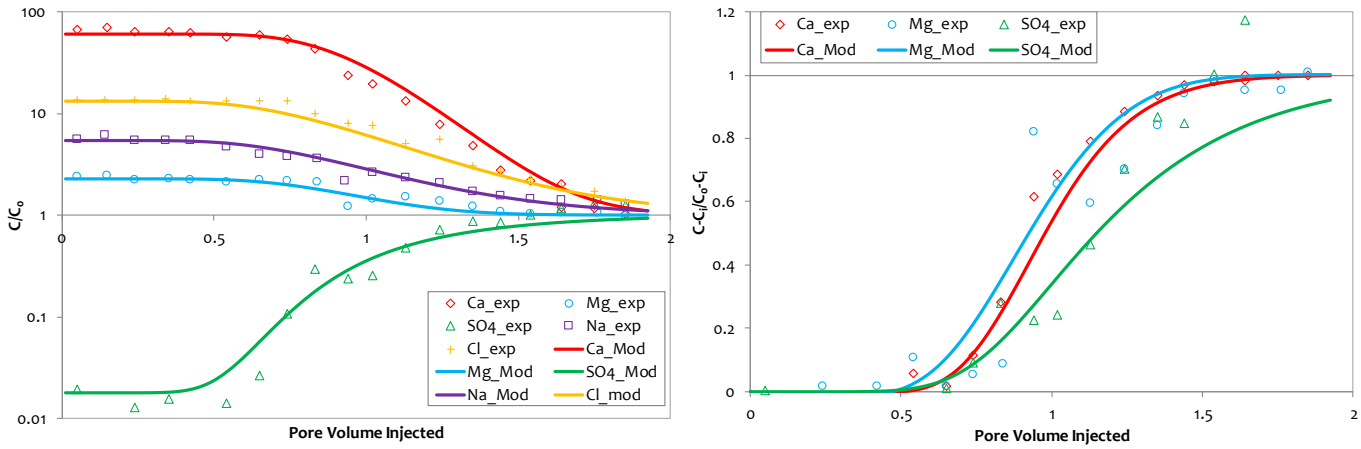

Figure 5.16—Comparison between observed and simulated [a] normalized breakthrough curves for all ions (*left*) and relative breakthrough curves for PDIs (*right*) during seawater with $4xSO_4^{2-}$ flooding. Experimental data obtained from Chandrasekhar *et al.* [196].

The results in the *right* panel of Figures 5.15 and 5.16 were plotted to reproduce the normalized ion profile relative to the *in-situ* concentrations. The delay in the transport of SO_4^{2-}, reaching a value of 1 later than other PDI cations, implied that SO_4^{2-} was sorbed to the rock–brine interface. A reduced interfacial charge enabled the competitive adsorption of Mg^{2+} and Ca^{2+} as earlier theorized. It is expected that Mg^{2+} should be more adsorbed than Ca^{2+} at this high temperature [32], however, because of very high Ca^{2+} concentration *in-situ*, their adsorption is more or less the same. Although SO_4^{2-} showed a similar delay in both experimental cases, the delay in the PDI cations was more in the second case (Figure 5.15) as compared to the first case (Figure 5.16). This

showed that with more SO_4^{2-} injected, more electrostatic repulsion consequently occurred, which enabled more PDI cation adsorption. A good agreement observed between various single-phase experimental ion profiles, and that of the simulation results suggests that the model accurately capture the rock−brine interactions. The simulation of these single-phase experiments showed preferential SO_4^{2-} adsorption to the core when flooded with sulfate-rich brines.

5.3.1.2 Two-phase modeling

It is expedient to evaluate the influence of smart brine on oil-water displacement experiments to investigate the changes in rock wettability. In the two-phase displacement experiments conducted by Awolayo *et al.* [29] at 110 ºC, the carbonate cores were initially saturated with the formation water and later displaced by dead oil to irreducible water saturation. Then, the reservoir *in-situ* brine was injected followed by different smart brines in the tertiary mode. More details about the experiment are discussed in the cited reference. The brine compositions and core properties used in modeling these experiments are presented in Table 5.4. In both experiments, relative permeability was not measured but rather inferred from the observed experimental recovery and pressure data with the method highlighted earlier in this Chapter.

In the composite coreflood test labelled as “S#42”, the *in-situ* formation water was first injected and recovered 71.13% oil−originally−in−core (OOIC). This flooding cycle was followed by an injection of seawater, which recovered an additional 5.7% OOIC. Lastly, SO_4^{2-} concentration was further spiked by the injection of seawater with $4\times SO_4^{2-}$ and additional recovery of 3.09% OOIC was observed. The authors emphasized that the additional oil could be observed when PDI concentrations in the injected brine are favorably modified while maintaining similar ionic strength. This trend was well captured by the model as presented in Figure 5.17. In addition, simulated changes in mineral volume fractions are reported alongside the oil recovery data plotted in Figure 5.17. The result showed that no significant mineral dissolution occurred during the *in-situ* brine injection. However, as brines of lower salinities were injected, the calcite dissolved to maintain the equilibrium concentration of Ca^{2+} in the aqueous solution. This effect can be seen in the comparison between simulated and experimental effluent concentration profiles plotted in Figure 5.17, where Ca^{2+} effluent concentration was continually higher than the injected

concentration during the tertiary injection mode. Meanwhile, SO_4^{2-} was quite higher in the subsequent injected cycle compared to the preceding cycle. As a result, increased SO_4^{2-} adsorption to the rock-brine interface was evident in sorbed fractions of sulfate. The resultant effect is an increased repulsion between the interacting media, enabling Mg^{2+} and Ca^{2+} to be co-adsorbed and thereby reducing the fractions of the free unoccupied site ($> NaX$) as presented in the *bottom left* panel of Figure 5.17. Hence, the model interpolated the relative permeability with respect to the $> NaX$ fractions to capture the wettability alteration leading to improved recovery. The simulated effluent concentration profile of Na^+ and Cl^- matched with the experimental data as both ions were not involved in any reaction at the interface, though present in the bulk electrolyte solution.

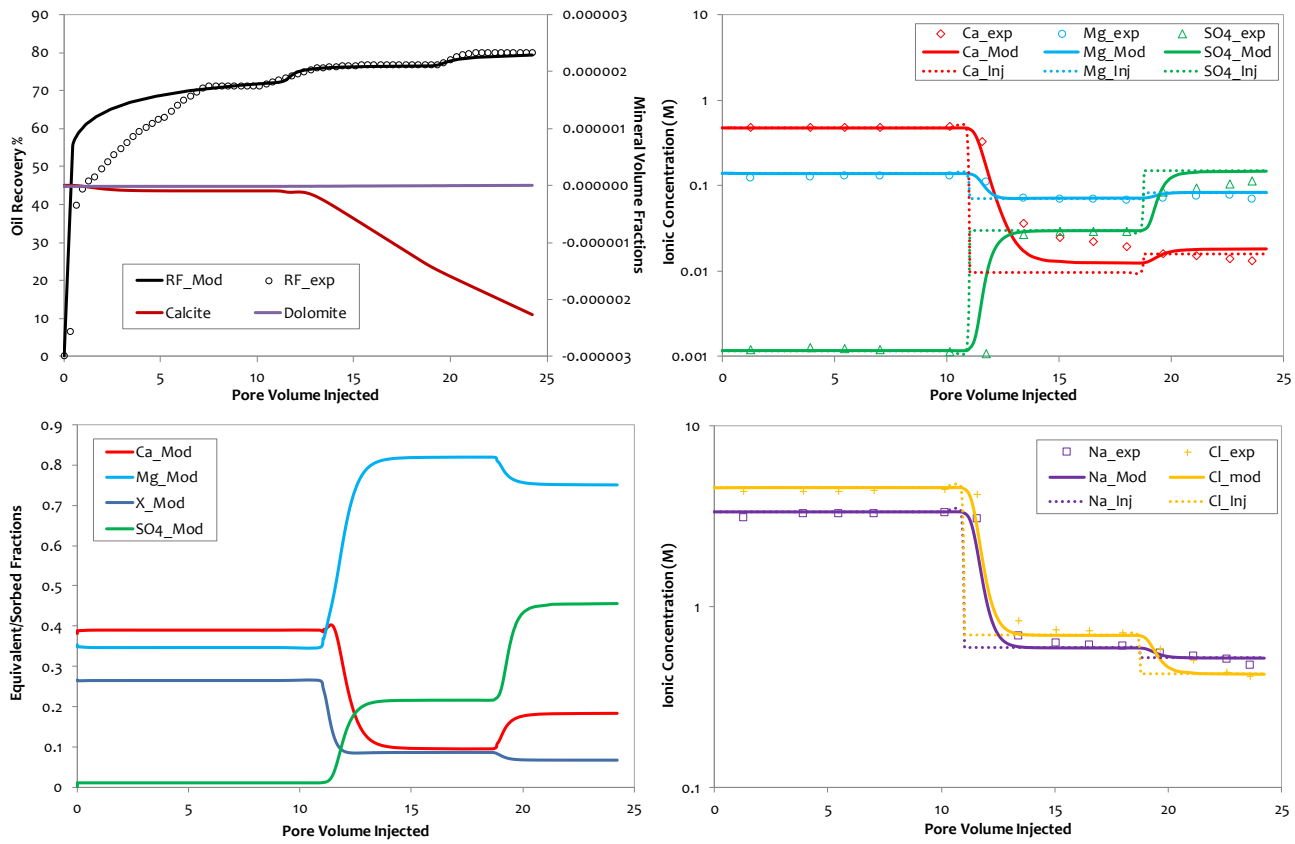

Figure 5.17—Results of formation water, seawater and seawater with $4xSO_4^{2-}$ flooding sequence comparison between two-phase simulated and experimental oil recovery, and simulated mineral volume changes (*top left*); simulated and experimental effluent ions concentration of PDIs (*top right*); simulated surface and equivalent fractions of PDIs along the mid-section of core S#42 (*bottom left*) and simulated and experimental effluent ions concentration of Na^+ and Cl^- (*bottom right*). Data-points indicate measured datasets (Awolayo *et al.* [29]), broken lines indicate injection concentration, and solid lines indicate the simulation results.

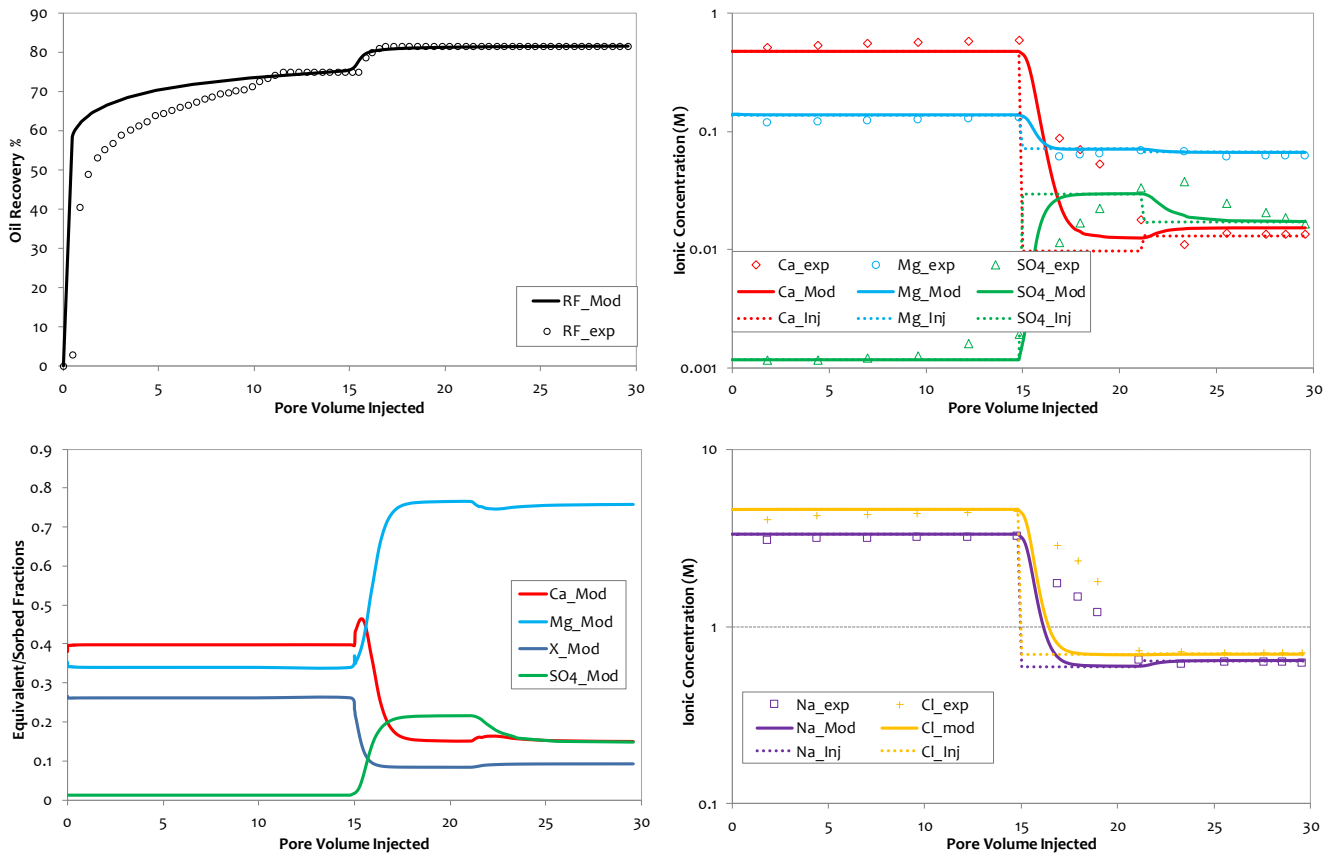

Figure 5.18—Prediction of formation water, seawater and seawater with 0.5xSO_4^{2-} flooding sequence: comparison between two-phase simulated and experimental oil recovery (*top left*); simulated and experimental effluent ions concentration of PDIs (*top right*); simulated surface and equivalent fractions of PDIs along the mid-section of core S#9 (*bottom left*); and simulated and experimental effluent ions concentration of Na^+ and Cl^- (*bottom right*). Experimental data obtained from Awolayo *et al.* [29].

Meanwhile, for the flood test S#9, the *in-situ* formation water recovered 75.6% OOIC, followed by an additional 6.86% OOIC recovered by injection of seawater. Lastly, seawater with 0.5×SO_4^{2-} was flooded through the core and no additional recovery was observed. The comparison between the simulated and experimental oil recovery is presented in Figure 5.18. Similar observation as highlighted earlier could be noted during seawater injection. Because of mineral dissolution, Ca^{2+} effluent concentration remained higher than injected. The adsorption of SO_4^{2-} increased and decreased during seawater and seawater with 0.5×SO_4^{2-} injection, respectively (see the *bottom left* panel of Figure 5.18). The impact of reduced sulfate adsorption was an increased electrostatic attraction between the interacting interfaces. This resulted in a slight increase in equivalent fractions of the free unoccupied site, which implied that no further wettability alteration towards

less oil-wetting state could occur. Hence, the model predicted no additional recovery during seawater with 0.5×SO_4^{2-} flooding cycle. This analysis showed that no additional oil could be recovered when PDI concentration in the injected brine is reduced, while similar ionic strength is maintained.

Table 5.5—Input parameters for the 2D synthetic simulation model

Parameters	**Values**
Well pattern	Quarter five-spot
Pattern size	183 m × 183 m × 10 m
Rock mineral volume	71% calcite, 9% dolomite and 20% pore space
Initial pressure	4695 psia
Reservoir temperature	110 ºC
Depth	2970 m
Average porosity	0.197
Average permeability	180 mD
Permeability anisotropy (K_V/K_H)	0.1
Oil viscosity at reservoir temperature	0.560 cP
Initial water saturation	0.214
Well injection rate	160 m^3/d
Well production condition	Constant bottom-hole pressure of 4600 psia

5.3.2 Field−scale modeling

In this section, 2D field-scale simulations were performed to illustrate the possible recovery improvement due to smart brine injection using a quarter five-spot waterflood pattern. Fluid properties and compositions of different injected brines are based on the previous laboratory coreflood (see Table 5.5 for the other input data). The sector is 183 m × 183 m × 10 m discretized into 40 × 40 × 1 grid cells. The reservoir is assumed heterogeneous and anisotropic in porosity and permeability with an arithmetic mean of 0.197 and 180 mD, respectively. The porosity and permeability are within the measured range for many carbonate reservoirs. Figure 5.19 shows the permeability field for the quarter five-spot reservoir model containing patches of high permeability channel. While the porosity field is normally distributed with a mean of 0.2 and a standard deviation of 0.029. The permeability-porosity correlation was taken from a typical carbonate

reservoir as shown in Figure 5.19 [277, 278]. The initial pressure is 4695 psi, and the temperature is 110 ºC. The well-to-well distance is 260 m. The injection well in the quarter five-spot is in the lower-left corner with a constant-reservoir volumetric rate of 160 m^3/d. The simulation of formation water, seawater and seawater with 4×SO_4^{2-} flooding was conducted using the relative permeability curves as shown in Figure 5.14 to account for the wettability alteration process.

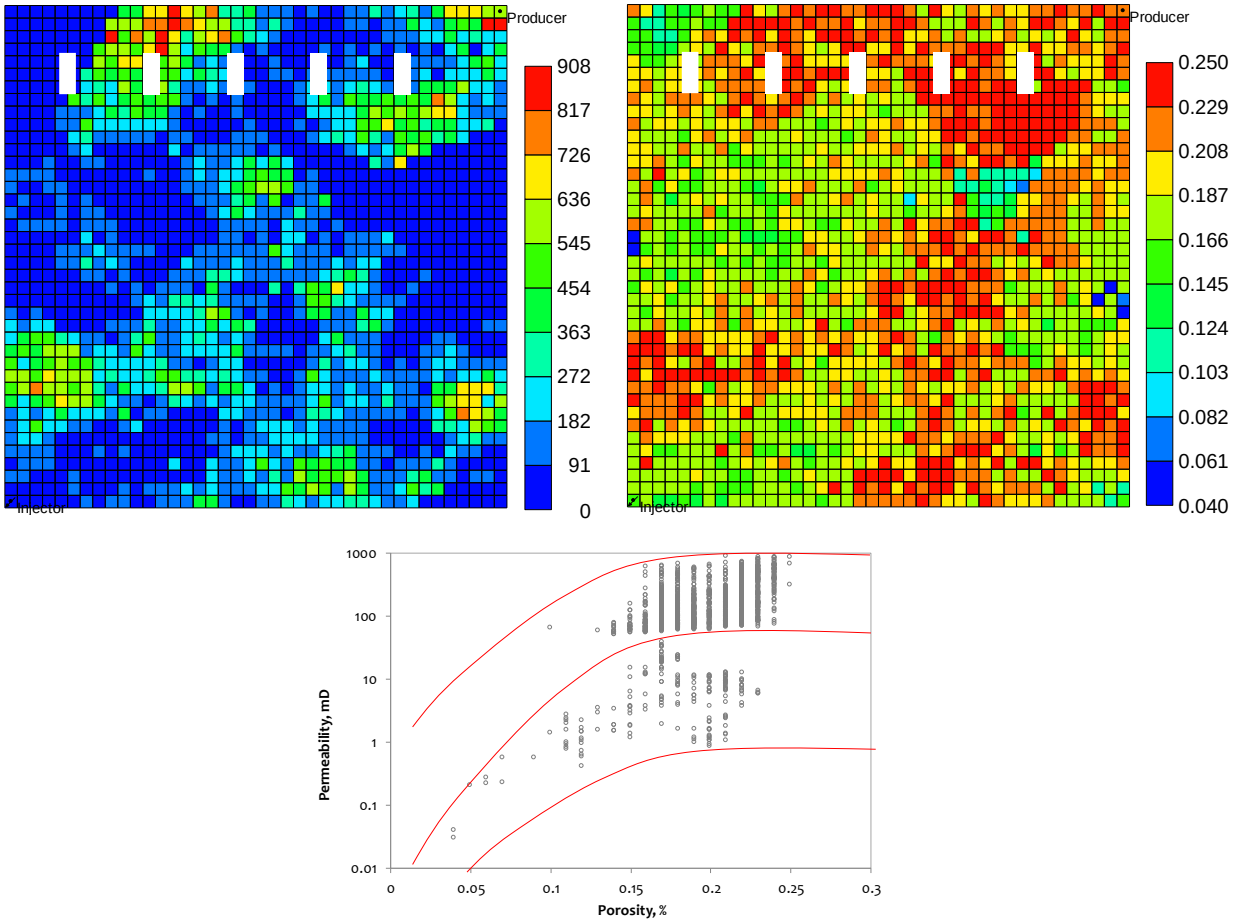

Figure 5.19—Simulation of 2-D synthetic quarter five-spot pattern with permeability distribution map (*top left*), porosity distribution map (*top right*) and permeability-porosity cross-plot (*bottom*) [277]. The block size is 15 ft. in every direction. The black dot at the upper-right corner is the producer, while the black dot with an arrow at the lower-left corner is the injector

A simulation run was conducted at secondary recovery mode, where 3 PV of *in-situ* and smart brines were separately injected as shown in Figure 5.20. Seawater and seawater with 4×SO_4^{2-} recovered about 8% and 13% additional oil, respectively, compared to formation waterflooding. The simulation results prove that the benefits of smart brine injection in the full field scale are very

similar to that of the laboratory-scale pilot tests. The saturation profiles in Figure 5.21 for secondary formation water, seawater and seawater with $4\times SO_4^{2-}$, further demonstrate the potential of smart brine injection. The seawater with $4\times SO_4^{2-}$ performed better because of the presence of high SO_4^{2-} concentration that reduced the electrostatic attraction between the interacting interfaces, which is consistent with previous discussions. The SO_4^{2-} adsorption led to a reduction in the fraction of unoccupied surface sites (Figure 5.22), promoting favorable wettability alteration, and ease of flow of mobile oil to the producing wells through the high permeable streaks. Because of the heterogeneous nature of the reservoir model, water breakthrough as early as 0.5PV and it appears that 2.5PV injection was enough to obtain a comparable laboratory oil recovery from the field-scale.

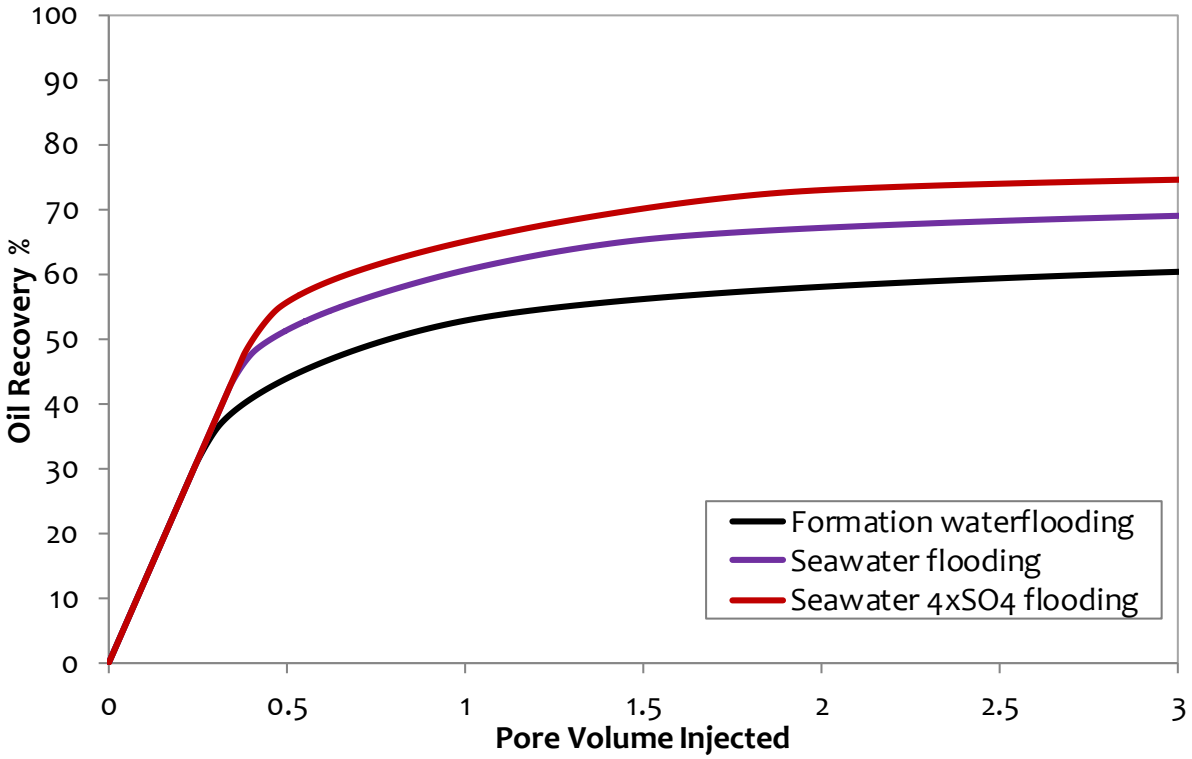

Figure 5.20—Comparison of oil recoveries by formation water and seawater in secondary mode

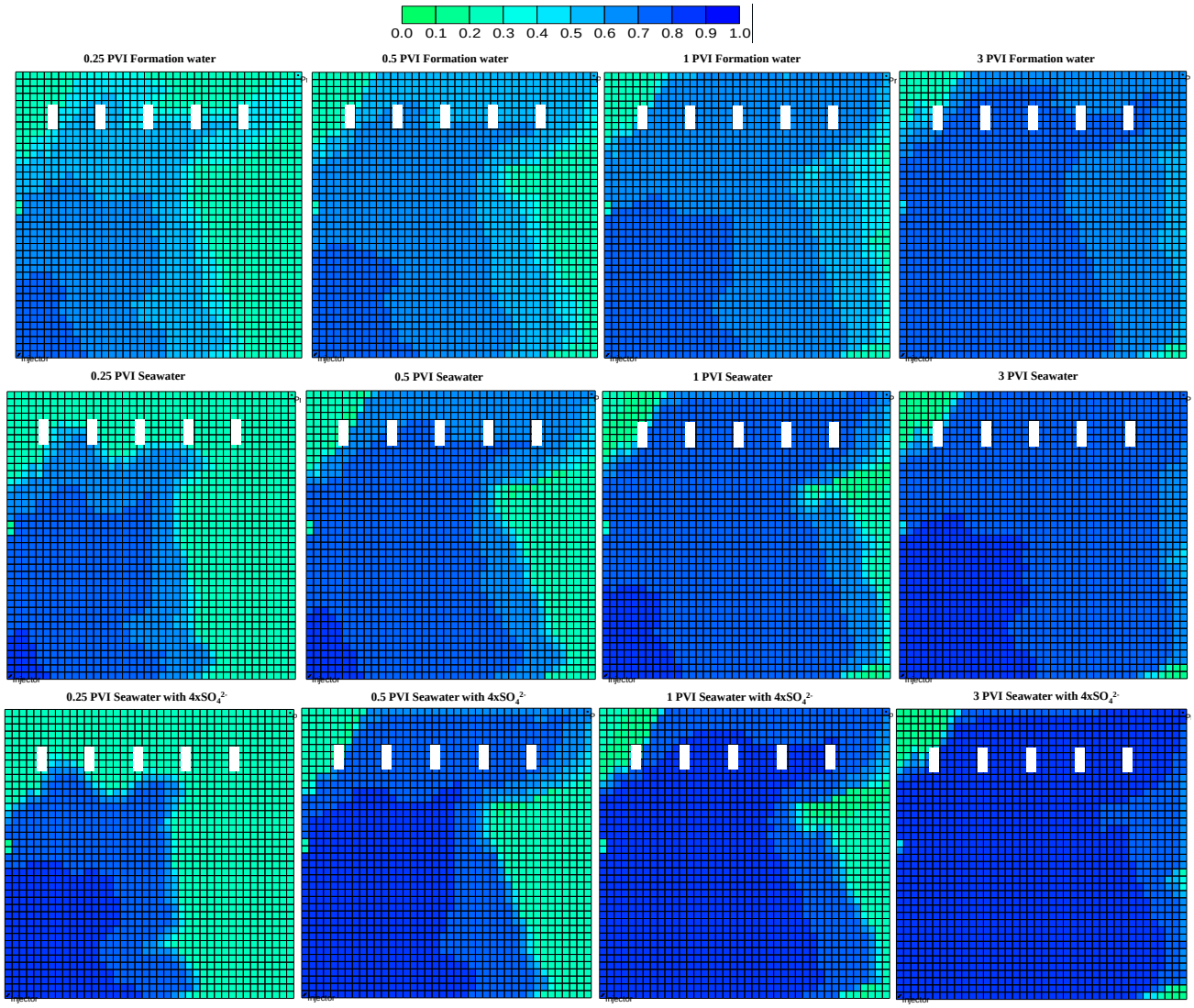

Figure 5.21—Comparison of the evolution of water saturation during secondary injection mode of formation water, seawater and seawater with $4\times SO_4^{2-}$

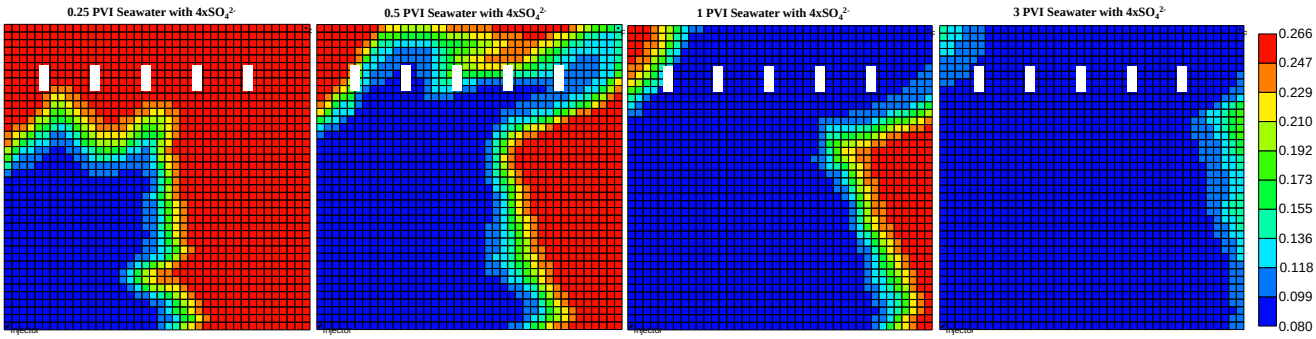

Figure 5.22—Evolution of equivalent fractions of unoccupied sites during secondary injection mode of seawater with $4\times SO_4^{2-}$

Meanwhile, in many cases, producing oil reservoirs are flooded conventionally with high saline formation water right after the primary production stage. This implies that smart brines would rather be injected as a tertiary recovery fluid. Hence, another simulation run was conducted to explore the potential of smart brine by first injecting the formation water for about 2.5 PV, followed by another 2.5 PV of smart brine injection. Figure 5.23 demonstrates that the tertiary flooding of seawater and seawater with $4\times SO_4^{2-}$ gave an additional oil recovery of 6% and 9% respectively, after the high saline formation waterflood. Besides, continuous injection of secondary mode seawater, seawater with $4\times SO_4^{2-}$ and formation water were presented in Figure 5.23 to compare with the tertiary injection mode. The comparison shows that continuously injecting a higher pore volume of formation water would not significantly improve recovery. Meanwhile, replacing the formation water with smart brine showed a higher recovery. Overall, the continuous injection of both seawater and seawater with $4\times SO_4^{2-}$ in secondary mode appears to be much more effective in terms of the waterflood project timeline and oil recovery. This option gives better oil recovery as well as lesser cost and complexity of the new operation and facility.

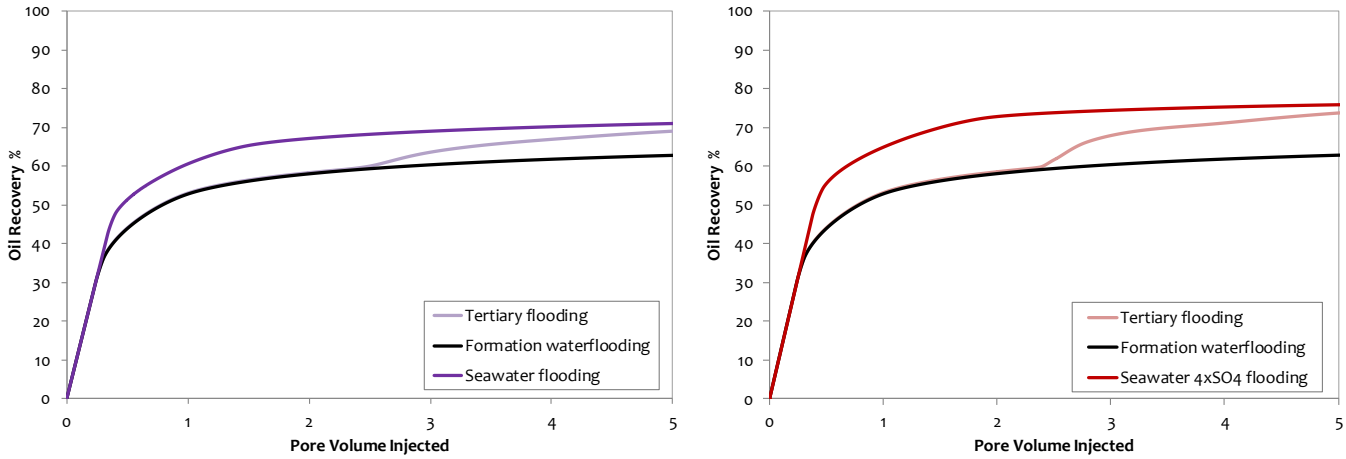

Figure 5.23—Oil recovery comparison between secondary and tertiary injection mode of formation water and seawater (*left*), and formation water and seawater with $4xSO_4^{2-}$ (*right*)

5.4 Chapter Summary

In this Chapter, the brine dilution dependent-oil recovery was investigated by applying the multicomponent multiphase geochemical model developed and validated in Chapter 4, to interpret ion transport and oil recovery behavior during core experiments, understand the dominant

mechanisms and their interplay. For the two-phase flow, the model justified that the reduction of the free surface site fractions and/or co-adsorption of PDIs can improve recovery by modifying flow functions, like relative permeability and capillary pressure. The model with previously established thermodynamic parameters was further validated with independently-sourced single-phase and two-phase flow experiments. These thermodynamic parameters can be used to predict various brine-dependent recovery processes as illustrated in this Chapter. Based on the results of this validation, a field-scale prediction was made, hence, the following conclusions are drawn:

- Single-phase and two-phase displacement experiments were simulated. The predicted effluent concentrations were consistent with experimental measurements. Moreover, the predicted oil recoveries matched well with the experimental measurements. The thermodynamic parameters that were utilized are widely applicable.
- It is proved that incorporating surface interactions in terms of surface adsorption reaction to capture SO_4^{2-} and the use of fractions of the free anionic surface site as the interpolant is sufficient to excellently reproduce the experimental data. In many cases, Mg^{2+} exchanged more than Ca^{2+} because of its high reactivity at high temperature and high concentration in the injected brine.
- It is evident that the model can replicate the early transient as well as the late steady-state trend noticed in the effluent concentrations. The reactivity of the PDIs increased with increased double layer thickness as the brine salinity is reduced and this became significant during the wettability alteration process.
- Mineral dissolution/precipitation is obvious at both core and lab scale in the pursuit of re-establishing equilibrium during diluted brine injection. The effect of carbonate mineral variation was explored, and the impact can be seen on the process mechanisms leading to improved recovery for different mineralogical carbonate rocks.
- In cases where sulfate was present in the injected brine, with reduced ion strength due to brine dilution, less aqueous complexes of sulfate with cations were formed. While the absence of sulfate, caused anhydrite dissolution from cores containing anhydrite. The resultant effect was that free SO_4^{2-} was available to adsorb, thereby improved the oil recovery.

- The model aptly explained the link between brine-dependent recovery process and wettability alteration on the two major frontlines involving brine-dilution and compositional variation in reference to the extent at which cations exchanged at the surface due to enhanced surface interaction enhanced by the adsorbed sulfate. The prediction of wettability alteration is linked to the relative permeability using the fractions of the occupied surface sites. This fraction is reduced as the adsorption of PDIs increases
- The interplay between surface charge alteration and mineral dissolution is vital to the improved recovery observed. Therefore, the relative contribution of these two depends on brine composition, mineral constituents, and temperature.
- Aqueous pH is controlled by the interaction between injected brine and minerals present. The pH may reach up to 8-9 in core experiments because of the resultant effect of mineral dissolution and precipitation.
- The simplistic field simulation study has demonstrated oil recovery similar to those of the 1D core simulation, using sequential seawater dilutions and PDI anions additions. However, it is a function of the number of pore volumes of brine injected. The field-scale model confirmed that significant incremental recovery could be obtained at representative field pore volumes injected.
- Further and more detailed site-specific field-scale simulation studies are needed to firm up the above observations made from the limited simulation study.

Chapter 6 Prediction of Low-Salinity-Water-CO_2 Recovery Process

In this Chapter, the investigation of low-salinity-water-CO_2 (LSWCO_2) recovery by utilizing the surface complexation model (SCM) developed and validated in Chapter 4 was presented. Carbon dioxide flooding is the most viable enhanced oil recovery (EOR) process in intermediate and light oil reservoirs, both in sandstone and carbonate reservoirs. While low-salinity waterflood is an emerging new EOR process. By combining the two EOR processes, the possibility of additional oil mobilization by LSWCO_2 was investigated.

6.1 Introduction

The key to the success of the design, evaluation and implementation of various EOR projects around the globe is dictated by the favorable economics in the availability of suitable injection fluids [2, 4]. In this regard, brine-dependent recovery process appears to have a better advantage compared to other EOR techniques in terms of environmental footprints, costs, and field implementation [62]. Several pieces of evidence have been presented to suggest that there are even more significant advantages in the combination of brine-dependent recovery with other proven EOR techniques, like chemical and gas flooding, which tends to benefit from synergies between these different techniques. While low saline/smart brines improve recovery by alteration of rock wettability; chemicals like polymer improves recovery by increasing the sweep efficiency; surfactant and alkali by reduction of IFT; and gases like CO_2, N_2, hydrocarbon, etc., improves recovery by increasing oil mobility either through first or multiple contact process resulting in IFT reduction, oil swelling and viscosity reduction [88, 279].

However, chemical flooding appears to be comparatively uneconomical because some of these chemicals are lost due to either retention or adsorption to the rock. Remarkably, high salinity conditions have been reported to lead to higher polymer adsorption and negatively influence polymer gel strength [280]. The earliest attempt at combining several EOR technique was to combine low salinity waterflooding with low-tension surfactant flooding. Surfactant solubility are improved as surfactant are less retained in low salinity brine [93]. A significant incremental recovery was obtained by Kozaki [93] during the low-salinity-water-surfactant flooding in

sandstone rocks, and the proposition was that the surfactant formed micro-emulsion in the aqueous phase as opposed to being trapped at high salinity conditions. Similarly, with low-salinity-water-polymer flooding, coreflood experiments showed significant improvements in oil recovery with fairly lower polymer quantity required for the target viscosity [93]. This was reported to consequently reduce the costs of chemical required to improve recovery.

On the other hand, gas flooding is a commercially proven EOR technique to recover light oil, however, gravity segregation, viscous fingering, early gas breakthrough and rock heterogeneity are factors that tend to decrease oil displacement efficiency [1]. A technique that has been developed to ensure mobility control and reduce the required quantity of injected gas is water alternating gas (WAG) which alternates cycles of water and gas injection. The primary purpose of WAG is to increase the sweep efficiency by reducing mobility ratio between the reservoir oil and the injected fluids. Residual oil saturation in WAG process is always lower compared to that in gas flooding because of higher trapped gas saturation, which results in less water blocking and oil trapping [281]. WAG operates similar to gas flooding in miscible, immiscible or near-miscible recovery mode, and the process can fluctuate between these modes in the reservoir production life depending on reservoir oil properties, temperature, and pressure. The preferred mode is miscible process because of its potential to achieve higher hydrocarbon recoveries compared to the other modes. Though, one key issue associated with WAG in field application is reduced injectivity caused by the presence of more than two phases near the wellbore and the associated pressure drop and relative permeability effects [282]. Hence, low-saline-water-alternating-gas (LSWAG) flooding promotes the synergy between mechanisms of wettability alteration and mobility control. LSWAG is also capable of overcoming the issue of injectivity associated with WAG as will be discussed below.

Decades of research and field experiences have attested to the success of CO_2 injection. CO_2 behaves uniquely compared to other injection gases due to its special properties. It can coexist as liquid and gas at its critical temperature and pressure and above this critical condition, exist in a supercritical state. At its supercritical state, it assumes a dense phase with a density as close to that of a liquid with low viscosity and mostly injected into the reservoir in this form [283]. Unlike other

gases, CO_2 undergoes both vaporization gas-drive process – where intermediate-weight hydrocarbons vaporize into the injected gas from the reservoir oil and condensation gas-drive process – where the injected gas dissolves in the oil to achieve dynamic miscibility such that the two fluids become completely miscible. Then oil recovery is improved by oil swelling, viscosity reduction and IFT reduction. In an immiscible mode, the injected gas and reservoir oil will not mix, though the gas will still dissolve in the oil leading to oil swelling and viscosity reduction [284]. However, optimal mobilization of the residual oil only occurs when the injected gas and the reservoir oil becomes miscible. In comparison to available commercial injected gases, such as nitrogen and light-weight hydrocarbon, CO_2 is reported to have a lower minimum miscibility pressure (MMP) with any reservoir oil [2, 285, 286]. On the grounds of its lower MMP, CO_2 is often preferred to other injection gases and also offers a better economic advantage as it is less costly compared to hydrocarbon gases, and environmentally advantageous by sequestering a significant amount of greenhouse gases.

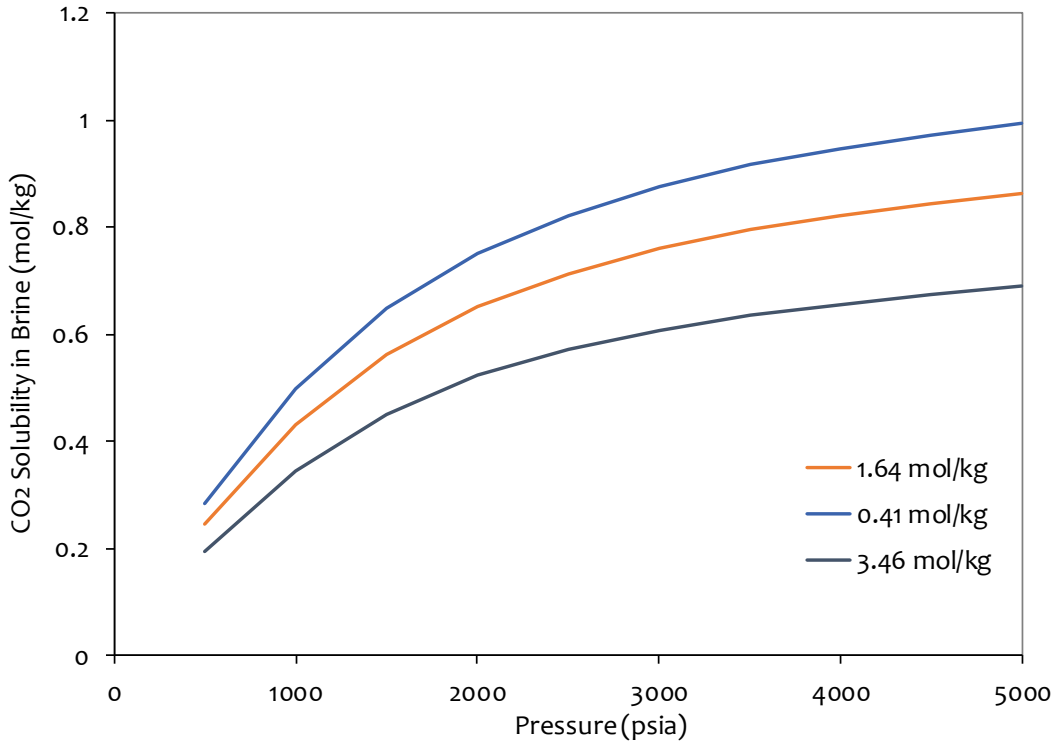

Figure 6.1—CO_2 solubility in different brine salinity brine at 195 ºF (90.5 ºC) and a wide range of pressure using Li and Nghiem [287] solubility model in CMG WINPROP™

Unlike other gases, CO_2 is soluble in brine and its solubility increases slightly linearly as brine salinity reduces (Figure 6.1), which implies that more CO_2 could be lost to the brine during $LSWCO_2$ injection. Similarly, its increased amount in the aqueous phase could enhance CO_2 diffusion and increase brine acidity. Because of this acidity, CO_2 can react with rock minerals like limestone and dolomite, resulting in either higher or lower permeability as the case may be either dissolution or precipitation. The density of CO_2 also increases linearly with brine salinity. The implication is that during $LSWCO_2$ injection, the reduction in IFT between CO_2 and brine as brine salinity reduces would diminish the gravity difference between reservoir fluids, and lead to low flow resistance and enhanced injectivity [88, 288].

6.2 Simulation of $LSWCO_2$

In the case of $LSWCO_2$, the mechanism has been documented to be as a result of the formation of *in-situ* carbonated water with increased saturation of CO_2 in the aqueous phase. Experimental findings have shown that the process is a highly effective and significant improvement in recovery has been recorded compared to the conventional high-salinity-brine-gas flooding in sandstone and carbonate reservoirs [85, 86, 87, 88]. Meanwhile, simulation studies conducted by researchers, such as Dang *et al.* [83], Al-Shalabi *et al.* [89], Qiao *et al.* [289] and Lee *et al.* [279], have provided further proof through synthetic cases and there has not been any such study that has predicted experimental $LSBCO_2$. This is what this study hopes to achieve and further evaluate the process by considering different injection strategies. The performance of $LSWCO_2$ in terms of oil production, relative injectivity, and CO_2 storage was further evaluated on a quarter of a five-spot pattern (same as shown in Figure 5.10) using field-specific injection parameters. With the aim of evaluating the synergy between low saline brine and CO_2, a coreflood experiment conducted by Teklu *et al.* [88] was simulated with reservoir fluid and rock properties listed in Table 6.1. The middle-eastern carbonate core was flooded with a sequential dilution of seawater at a reservoir temperature of 195 ºF and a pressure of 1800 psi. Then, the waterflooding was followed by CO_2 injection at an injection pressure of 2500 psi to achieve a miscible flood process. The oil sample was characterized with the Peng Robinson EOS, which was tuned to match oil sample properties as in Table 6.1.

Table 6.1—Summary of fluid and core compositions and properties used in the LSBCO_2 simulation. The total dissolved solids is denoted as TDS, ionic strength (M) is denoted as I, reservoir oil is denoted as RO and injected gas is denoted as IG

Brine (M)	**Ca^{2+}**	**Mg^{2+}**	**SO_4^{2-}**	**Na^+**	**Cl^-**	**HCO_3^-**	**I**	**TDS (g/L)**	**pH**
Formation Water	0.15265	0.050595	0.009052	1.41104	1.839111	0.001	2.050	105.92	7.170
Seawater	0.01725	0.142315	0.034434	0.59913	0.849403	0.000	1.112	51.35	6.600
Twice diluted seawater	0.00863	0.07116	0.01722	0.29957	0.42470	0.000	0.556	25.67	6.53
Four times diluted seawater	0.00431	0.03558	0.00861	0.14978	0.21235	0.000	0.278	12.84	6.31
Fifty times diluted seawater	0.00035	0.00285	0.00069	0.01198	0.01699	0.000	0.022	1.03	6
Rock properties	*Length (cm)*	*Diameter (cm)*	*Mineral volume fraction*		*Permeability (mD)*	*Porosity (fraction)*	*Swi (%)*	*Flow rate (ml/min)*	
Oil viscosity (3 cP)	13.87	3.81	0.698 Calcite 0.078 Dolomite		1.49	0.221	0.296	0.1	0.3
Components	*Mole % (RO)*	*Mole % (IG)*	*Model dimension:*		Δx=0.23cm Δy=3.37cm Δz=3.37cm	*MMP, psia*	2470		
CO_2	1.05	100							
C_1	13.78	0							
C_2	5.46	0							
C_3	6.58	0							
C_4	5.72	0							
C_5	5.27	0							
C_{6+}	62.14	0							

The MMP of CO_2 gas is estimated to ensure that the CO_2 injected at reservoir pressure of 2500 psi achieve miscibility with the reservoir oil as carried out in the experimental work of Teklu *et al.* [88]. The miscibility calculation is performed with WINPROP using the method of multicell EOS-based MMP calculation. The input for calculations is PR-EOS, reservoir oil and injected gas compositions listed in Table 6.1, and temperature of 195 ºF (90.5 ºC). For this method, the results showed condensing/vaporizing drive for miscibility developed between the reservoir fluid and injected gas with MMP of 2450 psia. In addition, displacement of reservoir oil by CO_2 in a slim tube was simulated using GEM; the length and porosity of the slim tube was taken as in Table 6.1 and discretized into different grid block sizes – 500 cells, 1000 cells and 2000 cells. The model was designed in such a way that during gas injection the pressure drop along the tube is less than 5 psia, as such the displacement and multi-contact miscibility can occur at the specific constant

pressure. The composition, temperature and the EOS used in the slime tube displacement simulation is similar to that used in the multicell calculation in WINPROP. The simulation of the injection of 1.2 PV of CO_2 is performed for a range of pressures as plotted in Figure 6.2. The MMP is observed from the oil recovery at 1.2 PV versus pressure plot to be in the range of 2450 to 2500 psia for the slim tube simulation and close to the value obtained with EOS multicell calculation. This implies that there is a good consistency between multicell calculation and slim tube simulations; hence for the rest of the study, MMP of 2450 psi is used, which is close to the experimental MMP of 2470 psia.

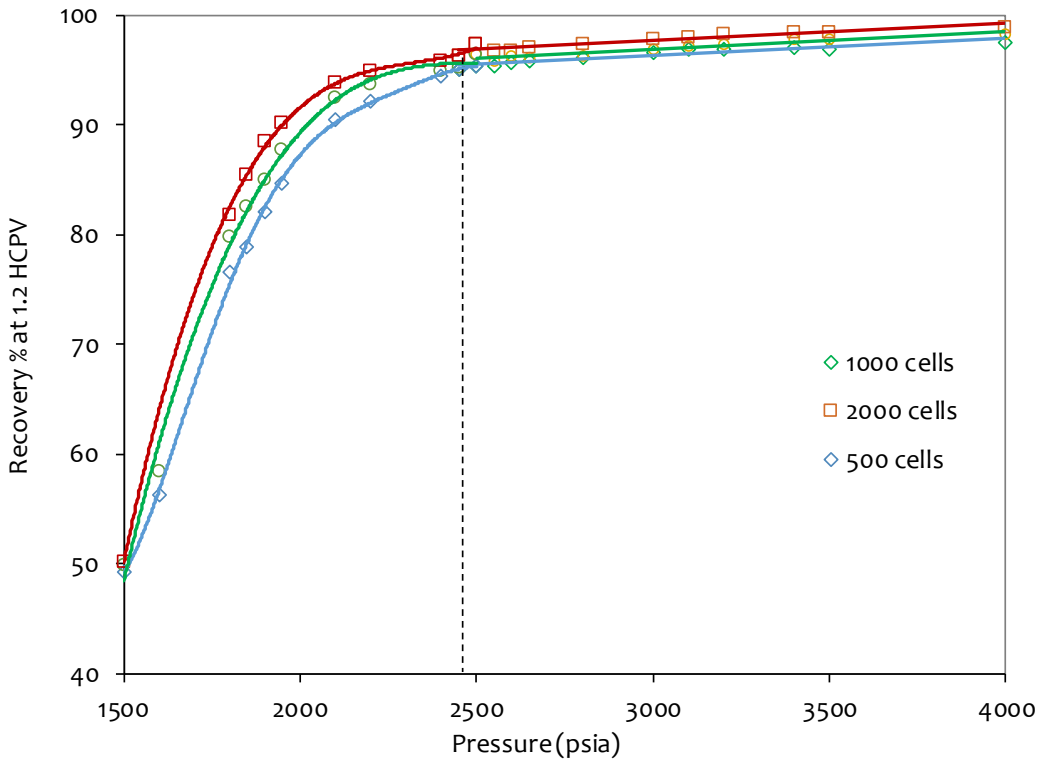

Figure 6.2—Estimation of CO_2 MMP from slim tube simulations with different number of cells

The SCM model and its thermodynamic constants, as described and validated in Chapter 4, is utilized to simulate the experiment by discretizing the flow domain into 60 x 1 x 1 with grid sizes stated in Table 6.1. Meanwhile, for the combined effect of low saline brine and CO_2, the three-phase flow functions were described using Stone II model. The three-phase water relative permeability, which is identical to water relative permeability in water-oil displacements, can be

described by eq. 5.8. Similarly, the three-phase gas relative permeability, which is also identical to gas relative permeability in gas-oil displacements at an irreducible water saturation, can be expressed as:

$$k_{rg} = k_{rg}^{*}\left(\frac{s_g - s_{gr}}{1 - s_{org} - s_{wr} - s_{gr}}\right)^{n_g} \tag{6.1}$$

where s_g, s_{gr} and s_{org} are the gas saturation, residual gas saturation and residual oil saturation for a gas-oil displacement, respectively; k_{rg}^{*} and n_g are the endpoint relative permeability to gas and Corey exponent for gas in gas-oil displacements, respectively. While the three-phase oil relative permeability, which depends nonlinearly on water and gas saturations, can be expressed as:

$$k_{ro} = k_{row}^{*}\left[\left(\frac{k_{row}}{k_{row}^{*}} + k_{rw}\right)\left(\frac{k_{rog}}{k_{row}^{*}} + k_{rg}\right) - \left(k_{rw} + k_{rg}\right)\right] \tag{6.2}$$

where k_{rog} is the relative permeability for oil in gas-oil displacement, which is expressed as:

$$k_{rog} = k_{rog}^{*}\left(\frac{1 - s_g - s_{wr} - s_{org}}{1 - s_{org} - s_{wr} - s_{gr}}\right)^{n_{og}} \tag{6.3}$$

where k_{rog}^{*} is the endpoint relative permeability to oil in gas-oil displacement and n_{og} is the Corey exponent for oil in gas-oil displacement. The three-phase oil relative permeability is calculated using eq. 6.2 with water-oil and gas-oil relative permeabilities plotted in Figure 6.3. The same linear interpolation of the flow functions in terms of relative permeability was used here as described by eq. 5.10 – 5.12. However, for SCM, the surface charge density was used as the interpolating parameter, defined by eq. 6.4. The rationale for such is that the model assumes that the rock−brine interface becomes initially attracted to oil−brine interface because of a high amount of the positively charged surface sites (such as $>CaOH_2^+$, $>CO_3Ca^+$, and $>CO_3Mg^+$) in the presence of high saline water, which can attach to the negatively charged oil acid-group. Then, as low saline/smart brine approach the surface, the PDIs present engage with the surface in such a way as to reduce the surface charge and allow the desorption of adsorbed oil acid.

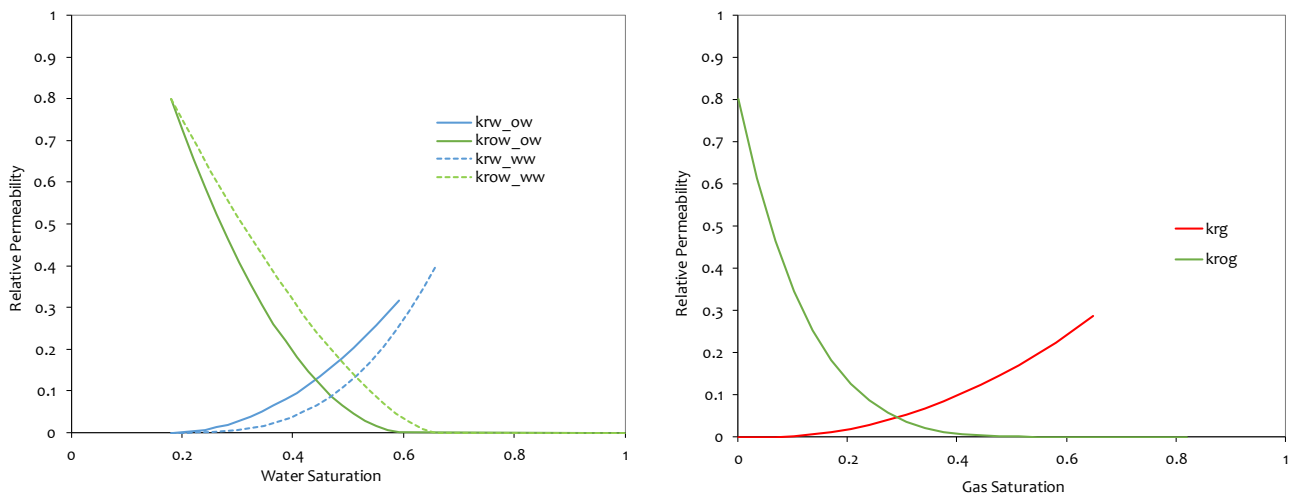

Figure 6.3—Water-oil relative permeability curves (*left*) and gas-oil relative permeability curves (*right*) used in simulating the flooding experiments of Teklu *et al.* [88]. Broken lines indicate final-wetting state relative permeability and solid lines indicate initial wetting relative permeability

$$\omega(\psi_{Na-X}) = \frac{{\sigma_s}^{final} - \sigma_s(x,y,z,t)}{{\sigma_s}^{final} - {\sigma_s}^{initial}} \tag{6.4}$$

Similarly, the initial surface charge density, ${\sigma_s}^{initial}$, at the beginning of the injection period, which is the amount of charge at the surface due to different surface reactions when there was no wettability alteration and the final surface charge density, ${\sigma_s}^{final}$, at the end of the injection period, which signifies the amount of charge at which enough alteration has occurred are the parameters on which the interpolation is calculated based on the surface charge at any point and time, $\sigma_s(x,y,z,t)$. When $\omega = 1$, it implies the surface has maintained its original surface charge and the surface charge density remained the same while when $\omega \approx 0$, this implies that the surface charge has been reduced because of the surface interaction of the PDIs as well as double layer expansion. Another performance indicator used to evaluate LSWCO_2 is injectivity, which can be defined in various ways, however in this Chapter, it is calculated as:

$$Injectivity = \frac{Q_{inj}}{P_{bh} - P_{avg}} \tag{6.5}$$

where Q_{inj} is the injection rate (ft^3), P_{bh} is the bottom-hole pressure (psia) of the injection well and P_{avg} is the domain average pressure (psia). The definition given in eq. 6.5 is to ensure that the injectivity is considered as a global effect on the reservoir domain. The relative magnitude between

injectivity in tertiary and secondary injection modes is calculated by normalizing injectivity at any time with the injectivity at the end of the secondary waterflood as:

$$Relative\ Injectivity\ = \frac{Injectivity}{Secondary\ Waterflood\ Injectivity} \tag{6.6}$$

The simulation of the experiment follows a similar procedure on which the experiments were carried out. The experiment was performed on a composite of three carbonate cores with a total length of 13.8 cm and a pore volume of 30 cm^3. The flooding sequence was – seawater, twice diluted seawater, four times diluted seawater, and fifty times diluted seawater, followed by miscible CO_2 flood. The comparison between the experimental and simulated oil recovery and pressure drop is presented in Figure 6.4. The model gave an excellent reproduction of the experimental curves, where seawater recovered 52.8% OOIC, and sequential brine dilution resulted in the additional recovery of 5.6% OOIC. The authors only reported the final recovery of the CO_2 miscible flood, which the model also replicated as 25% OOIC after 10 PV continuous injection of CO_2.

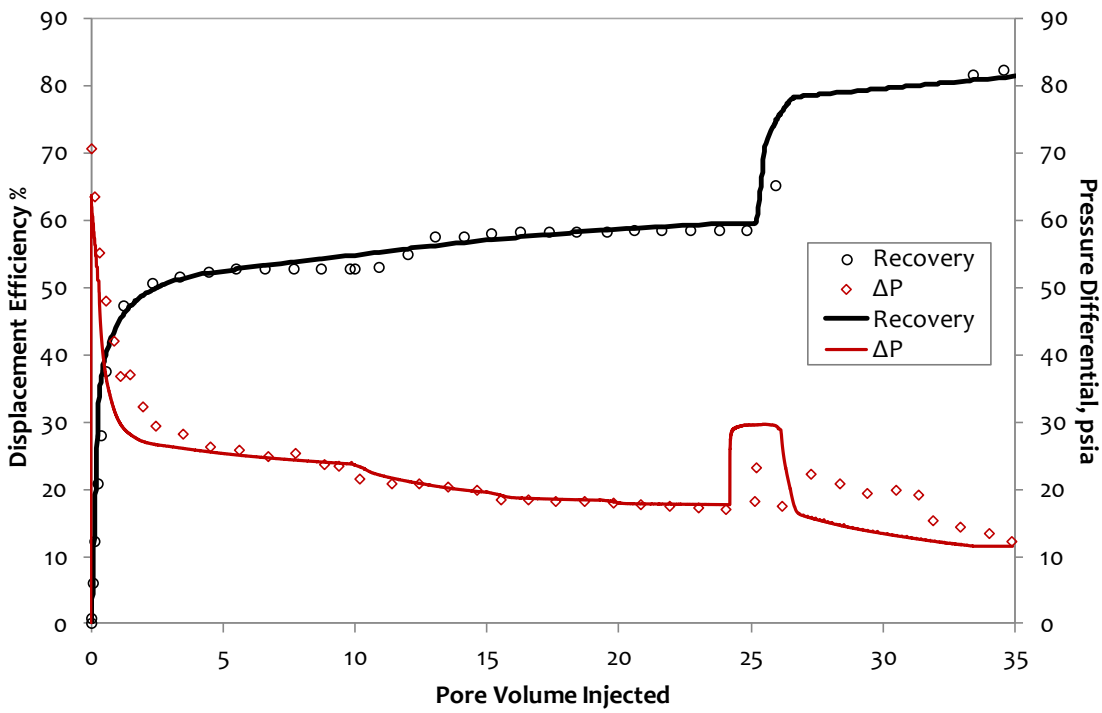

Figure 6.4—Comparison of experimental and simulated oil recovery and pressure differential. Experimental data obtained from Teklu *et al.* [88]

The model prediction for surface fractions is presented in Figure 6.5, surface fractions of SO_4^{2-} is reduced while surface fractions of Mg^{2+} and Ca^{2+} varied because of their reduced concentrations through the sequential injection process. Despite the variation in the surface fractions of the PDI, the surface charge continued to decrease as a result of reduced monovalent ions and ionic strength of the injected brine, leading to double layer expansion. The reduction in surface charge was utilized to excellently reproduce the experimental oil recovery and pressure differential dataset shown in Figure 6.4. As brine salinity reduces, calcite dissolution compensated for reduced Ca^{2+} in the injected brines and further dissolution can be seen in Figure 6.5 due to increased CO_2 solubility in the aqueous phase (see Figure 6.6). The relative injectivity shown in Figure 6.6 increased as the brine salinity reduced but became more pronounced during CO_2 injection. Similarly, oil density and viscosity reduced during CO_2 injection due to higher CO_2 diffusion into the oil phase. The simulation results show that the incremental recovery can be associated with increased CO_2 solubility leading to the *in-situ* formation of carbonated water to alter wettability and reduce interfacial tension.

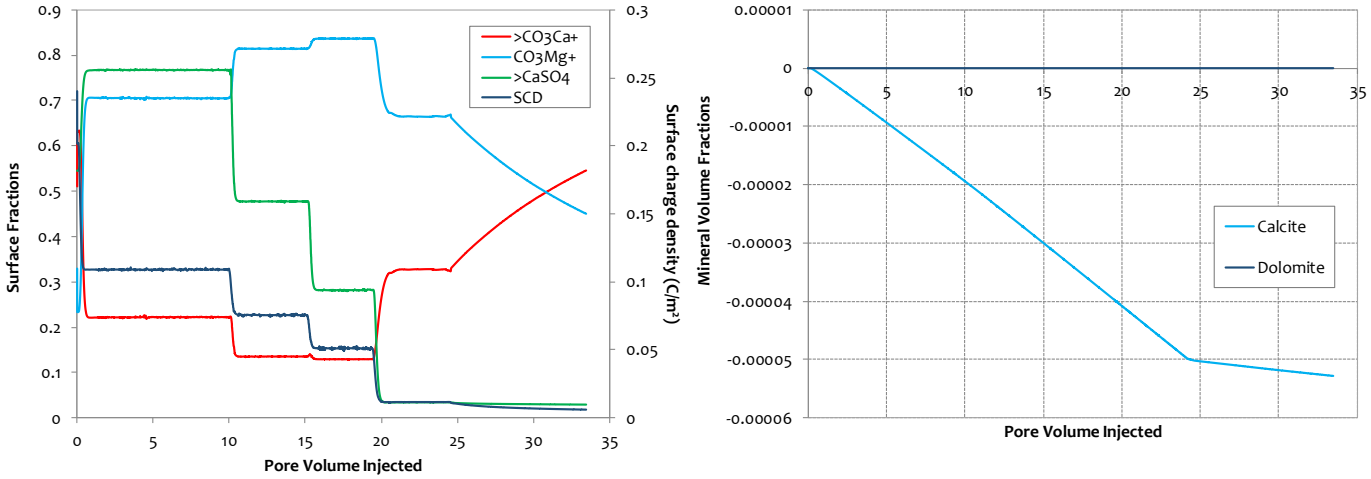

Figure 6.5—Simulation profiles at the mid-section of the flow domain for surface fractions of Ca^{2+} ($>CO_3Ca^+$), SO_4^{2-} ($>CaSO_4^-$) and Mg^{2+} ($>CO_3Mg^+$) and surface charge density (*left*) and fractional amounts of mineral volume alteration (*right*)

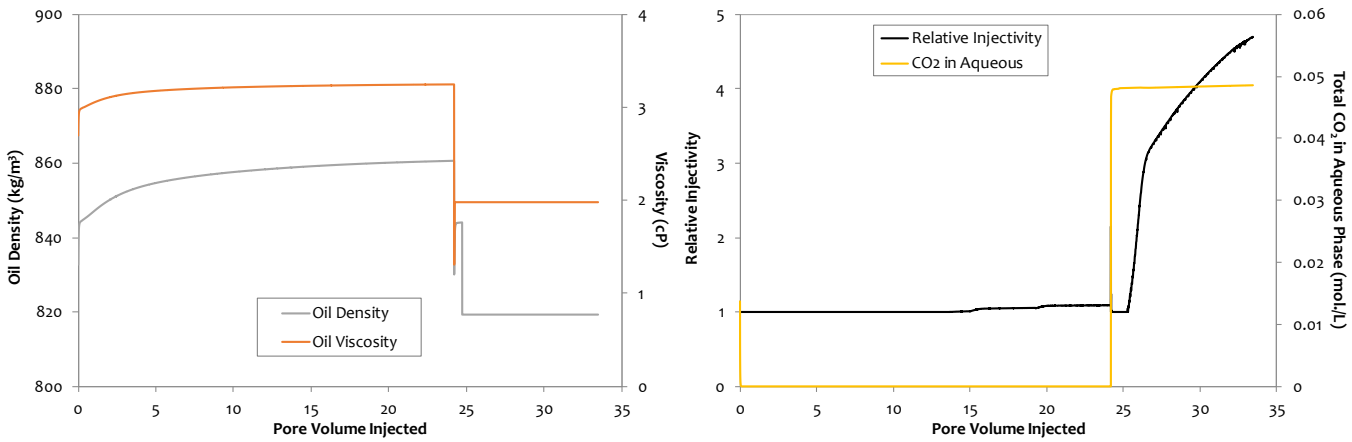

Figure 6.6—Predicted oil density and viscosity at the injection grid block (*left*); relative injectivity and the total amount of CO_2 dissolved in the aqueous brine solution (*right*)

To this end, the SCM has been successfully applied to investigate fluid-rock interaction at the core-scale and to examine the interaction at a larger scale and evaluate different injection strategies like carbonated water injection (CWI) and low-salinity-water-alternating-CO_2 gas (LSWACO_2) injection, a similar quarter of a 2-D five-spot pattern as used in Sect. 5.1.3 was utilized with the rock and fluid properties described in Table 6.1. CWI is an injection scheme where the injected water is first saturated with CO_2, before being injected into the reservoir. The results plotted in Figures 6.7, and 6.8 shows the predicted oil recovery from the quarter of a five-spot pattern for conventional waterflooding, low saline waterflooding, CWI and LSWACO_2. The comparison presented in Figure 6.7 reveals that secondary mode injection of low saline brine can significantly improve oil recovery compared to conventional waterflooding. Meanwhile, CWI considerably improved recovery in both seawater and low saline brine, though recovery was higher in the latter because of higher CO_2 that could dissolve in low saline brine. The injectivity was also higher which increased with an increase in injection pore volume for low saline brine CWI as compared to seawater CWI. The increase in the amount of dissolvable CO_2 led to an increase in the amount of CO_2 diffusing into the oil phase, resulting in lower oil viscosity and density as shown in Figure 6.7. For the LSWACO_2 injection, the injectivity was significantly greater than that of WAG (see Figure 6.8), mainly because there is a higher CO_2-saturated-brine that the rock surface is exposed to during LSWACO_2 injection. As a result, more oil production was achieved with water-alternating-gas using low saline brine.

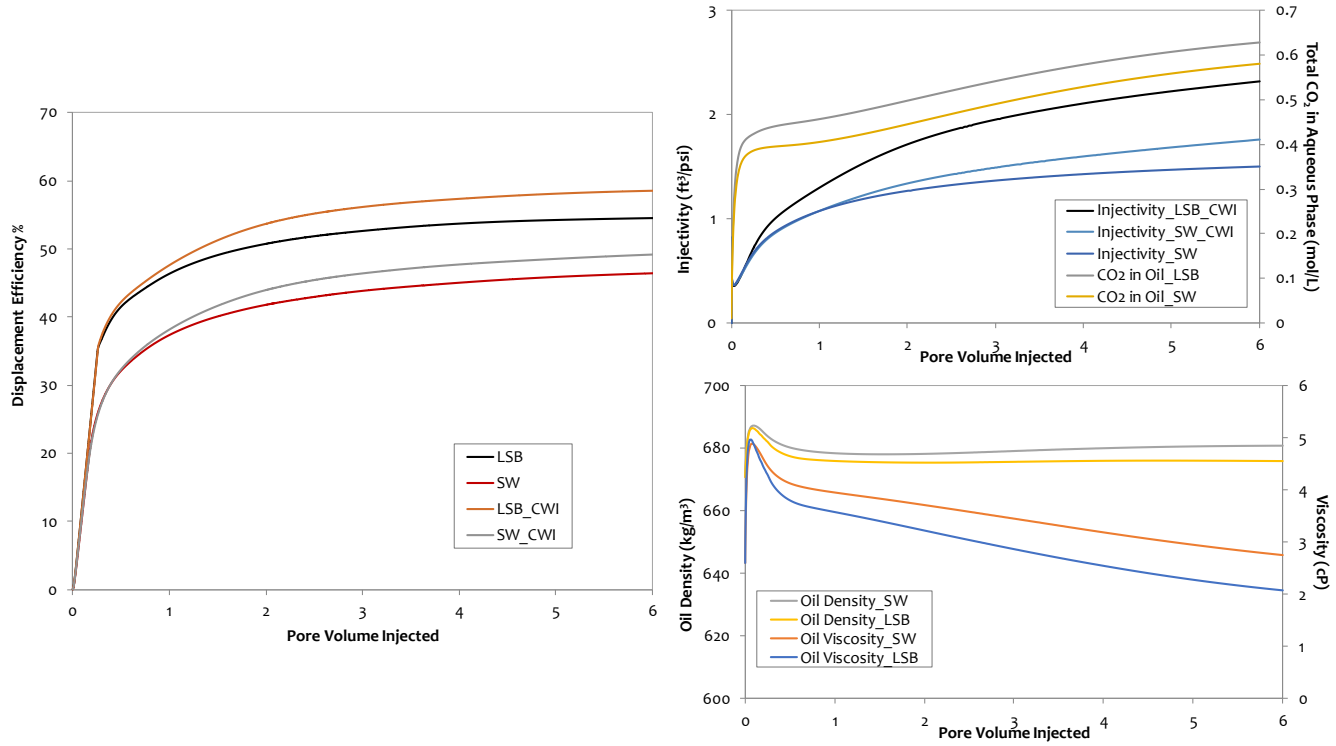

Figure 6.7—Predicted oil recovery for different injection schemes in a quarter of a five-spot pattern (*left*), comparison of injectivity and amount of dissolvable CO_2 (*top right*) and oil density and viscosity (*bottom right*). Here, carbonated water injection is compared with low saline brine and seawater injection in terms of oil recovery, injectivity and CO_2 solubility.

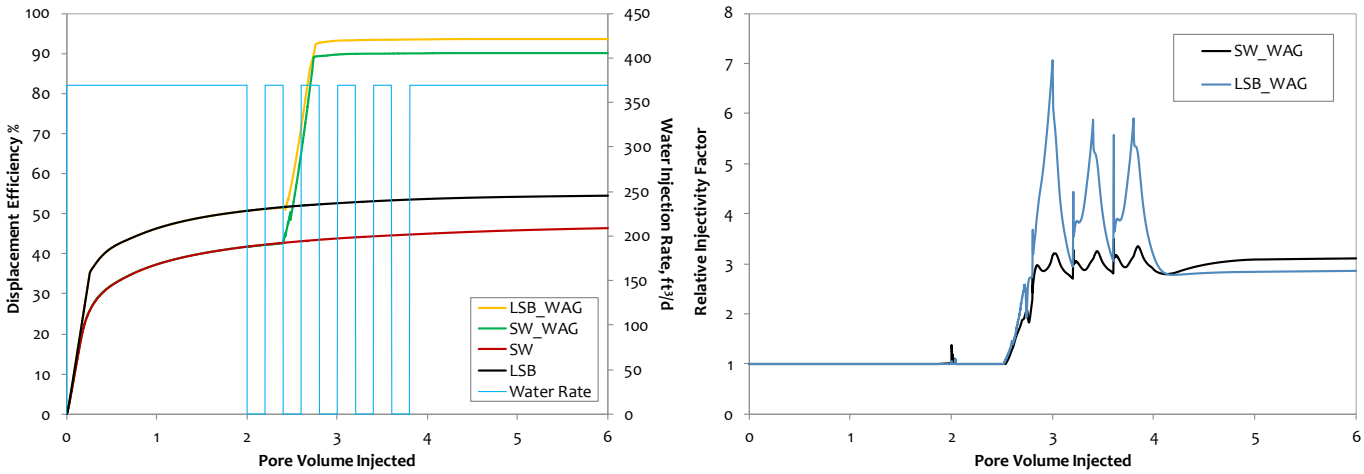

Figure 6.8—Predicted oil recovery comparison for $LSWACO_2$, conventional seawater WAG and normal waterflooding (*left*); comparison of their relative injectivity (*right*)

6.3 Chapter Summary

This Chapter demonstrates the significance of modeling fluid-rock interactions in investigating, designing and optimizing schemes for low saline water-CO_2 flooding as an enhanced oil recovery candidate in carbonate reservoirs. The profound influence of low salinity brine flooding is primarily based on wettability alteration, while that of CO_2 flooding is based on oil swelling, viscosity reduction, and interfacial tension reduction. Low saline brine, when combined with CO_2, leads to higher CO_2 solubility and diffusion, and increases brine acidity. Hence, the following conclusions are drawn:

- The mechanistic model captures the trends observed during the oil-brine-rock interactions in laboratory tests by providing an excellent match with the experiment.
- Simulation results show that the incremental recovery can be associated with increased CO_2 solubility leading to the formation of carbonated water *in-situ* to alter wettability and reduce interfacial tension.
- The increased CO_2 solubility as salinity reduces, increase mineral dissolution and CO_2 diffusion in the oil phase to reduce oil viscosity and density.
- The injectivity was significant for LSWACO_2 injection, mainly because there is an increase in the amount of CO_2 dissolved and exposure time on the rock surface to CO_2-saturated-brine.
- Though the amount of CO_2 that can dissolve in carbonated water is small, CWI shows greater injectivity compared to seawater and low-salinity-brine.

Chapter 7 Conclusions and Recommendations

7.1 Conclusions

The main aim of this research is to fill existing gaps in the literature, unravel the discrepancy between different studies, further implement representative modeling techniques and evaluate the benefits of the brine-CO_2 recovery system. This was achieved by first providing an integrative review on the systematic investigation of brine-dependent recovery across the different scale of investigations from laboratory experiments to field studies, various proposed fundamental mechanisms, the major modeling attempts and water injection compatibility issues. This was followed by the application of the theory of surface forces and water film stability to rationalize the relationship between carbonate rocks wetting state and the corresponding oil recovery characteristics. After developing a comprehensive understanding of the process mechanisms, a numerical model that which considered various reaction mechanisms was developed, in particular, the two distinct surface reactions, surface sorption and complexation reactions. The numerical model was validated against independently sourced electrokinetic and single-phase experimental data and was further used to investigate brine-dependent recovery and the brine-CO_2 process. Therefore, based on the various data analyzed and assumptions made, the following conclusions have been drawn:

- The injected brine is more effective at improving recovery when it contains potential determining ions, depleted in NaCl, and wettability alteration is much more effective at high temperatures.
- Though brine-dependent recovery has been explored on two frontlines, potential determining ion concentrations play a more significant role as compared to brine salinity reduction.
- Although the wettability alteration is widely accepted as the consequence of the brine-dependent recovery process, this study proves that a combination of surface charge and mineral alteration is the probable cause.
- The magnitude of the contribution of the electrostatic force to sustaining a stable water film increases with decreasing ionic strength (either through reduction of NaCl, Ca^{2+} or brine dilution) and/or increasing SO_4^{2-} concentration.

- When the energy barrier, required to be overcome for the interacting interfaces to attract, increases as a result of potential determining ion interactions or ionic strength reduction, the pre-existing oil-wetting condition is reversed to generate a more stable water film between the two interfaces, leading to improvements in oil recovery.
- The reported equilibrium constants for the surface complexation reactions in the literature are not able to predict the zeta potential and single-phase flow-through experiments. The optimized equilibrium constants are derived from fitting the produced ion history of the reactive transport of brine in chalk and limestone and have been demonstrated to be widely applicable.
- Though chalk and limestone differ by surface area and reactivity, the same thermodynamic parameters can be used in modeling brine-dependent recovery in their respective reservoir rocks
- Mineral dissolution/precipitation is obvious at both core and lab scale in the pursuit of re-establishing equilibrium during brine-dilution dependent recovery and should not be ignored in modeling different mineralogical carbonate rocks.
- Fluid-rock interaction during brine-CO_2 recovery results in increased CO_2 solubility as brine salinity reduces, increase in brine acidity and causing mineral dissolution, and higher CO_2 diffusion in the oil phase to reduce oil viscosity and density.
- There is a significant increase in relative injectivity for brine-CO_2 recovery, either carbonated water or low-salinity-water-alternating-CO_2 gas injection, mainly due to more exposure to a higher amount of CO_2-saturated-brine

7.2 Recommendations for Further Study

Based on the findings from this research, the following recommendations are made for further study:

- Hitherto, the models developed have been effective in interpreting the process mechanisms during brine-dependent recoveries. These models do have a few limitations that may affect its predictive capability, particularly because only a few of the independently source experimental data used in this study had the detailed geochemical data on the produced brine. Likewise,

further understanding of wettability alteration mechanisms can be achieved by more robust interpretation and measurements of the chemical composition of injected and effluent brines.

- In addition, measurement of the flow functions data, particularly the relative permeability and capillary pressure at the initial and final wetting state, specific to the core experiments will also lead to more conclusive model validation.
- The inconsistencies in modeling zeta potential data for pulverized suspension and intact rocks could be resolved by conducting experiments at controlled conditions. In addition, while conducting single phase flooding with different potential determining ion variations, the zeta potential could be measured, and both datasets used to improve the calibrating of the surface complexation model thermodynamic constants.
- Many studies quantified polar oil components using acid and base number, which might not be able to give a robust description for type and structure of polar oil components contributing to increased oil adhesion. This is one of the reasons why less emphasis is placed on oil surface interaction.
- More detailed site-specific field-scale simulation studies are recommended to firm up the observations made from the limited field-scale simulation study carried out.
- There are various other operational parameters and design strategies for field application of the process that were not explored in this study; incorporation of such aspects will complement this study.
- As with most enhanced oil recovery project evaluations, a pilot test is recommended with brine-dependent and brine-CO_2 recovery process before full field implementation. The application of this simulation model to the different single-well chemical tracer tests will improve the predictability of the model.
- Brine-dependent recovery has proved effective in carbonate reservoirs, and most carbonates are highly heterogeneous and naturally fractured. Therefore, it is vital to extend this model to accurately capture individual species interactions in fractured carbonate reservoirs.

Appendix A: Aqueous Reaction Thermodynamic Parameters

This Appendix presents the temperature-dependence analytical empirical parameters for the estimation of reaction thermodynamic constant as found in Lawrence Livermore National Laboratory (LLNL) database using eq. 4.9 in Section 4.2.2.

Aqueous reactions	A_0	A_1	A_2 (10^4)	A_3	A_4 (10^3)	A_5 (10^{-5})
$CO_{2(aq)} + H_2O \Leftrightarrow H^+ + HCO_3{}^-$	682.16	0.1143	-3.8165	-246.59	2513.64	
$H_2O \Leftrightarrow H^+ + OH^-$	293.29	0.1361	-1.0577	-123.73	0.0000	-6.9965
$HCO_3{}^- \Leftrightarrow H^+ + CO_3^{2-}$	-69.96	-0.0335	-0.0071	28.22	-0.0011	
$CaSO_4 \Leftrightarrow Ca^{2+} + SO_4{}^{2-}$	286.18	0.0841	-0.7688	-114.49	-0.1201	
$MgSO_4 \Leftrightarrow Mg^{2+} + SO_4{}^{2-}$	1692.30	0.2670	-9.1846	-614.81	5309.20	
$NaSO_4{}^- \Leftrightarrow Na^+ + SO_4{}^{2-}$	935.88	0.1444	-5.3023	-338.40	3306.39	
$CaCO_3 + H^+ \Leftrightarrow Ca^{2+} + HCO_3{}^-$	695.43	0.1163	-3.6153	-256.84	174.026	
$MgCO_3 + H^+ \Leftrightarrow Mg^{2+} + HCO_3{}^-$	234.65	0.0555	-0.8395	-93.10	0.0002	
$NaCO_3{}^- + H^+ \Leftrightarrow Na^+ + HCO_3{}^-$	169.39	0.0005	-0.7677	-62.08	-0.0120	
$CaHCO_3{}^+ \Leftrightarrow Ca^{2+} + HCO_3{}^-$	868.61	0.1458	-4.8281	-316.73	308.32	
$MgHCO_3{}^+ \Leftrightarrow Mg^{2+} + HCO_3{}^-$	38.46	0.0301	0.0098	-18.87	0.0002	
$NaHCO_3{}^+ \Leftrightarrow Na^+ + HCO_3{}^-$	-90.67	-0.0299	0.2795	36.52	0.0047	
$CaCl^+ \Leftrightarrow Ca^{2+} + Cl^-$	81.49	0.0384	-0.1376	-35.97	-0.0022	
$MgCl^+ \Leftrightarrow Mg^{2+} + Cl^-$	43.36	0.0329	0.0119	-21.69	0.0002	
Mineral reactions						
$Calcite + H^+ \Leftrightarrow Ca^{2+} + HCO_3{}^-$	-149.78	-0.0484	0.4897	60.46	0.0076	
$Dolomite + 2H^+ \Leftrightarrow Ca^{2+} + 2HCO_3{}^- + Mg^{2+}$	-317.82	-0.0982	1.0845	126.57	0.0169	
$Anhydrite + H^+ \Leftrightarrow Ca^{2+} + SO_4{}^{2-}$	-209.86	-0.0788	0.5097	85.64	0.0080	

Appendix B: Supplementary Material (Journal Permission License)

This Appendix presents permission/license for reuse of the published work included in this dissertation.

Copyright Clearance Center RightsLink®

Home | Account Info | Help

ACS Publications
Most Trusted. Most Cited. Most Read.

Title: Thermodynamic Modeling of Brine Dilution-Dependent Recovery in Carbonate Rocks with Different Mineralogical Content

Author: Adedapo Noah Awolayo, Hemanta Kumar Sarma, Long X. Nghiem

Publication: Energy & Fuels

Publisher: American Chemical Society

Date: Sep 1, 2018

Copyright © 2018, American Chemical Society

Logged in as:
Adedapo Awolayo
Account #:
3001347302
LOGOUT

PERMISSION/LICENSE IS GRANTED FOR YOUR ORDER AT NO CHARGE

This type of permission/license, instead of the standard Terms & Conditions, is sent to you because no fee is being charged for your order. Please note the following:

- Permission is granted for your request in both print and electronic formats, and translations.
- If figures and/or tables were requested, they may be adapted or used in part.
- Please print this page for your records and send a copy of it to your publisher/graduate school.
- Appropriate credit for the requested material should be given as follows: "Reprinted (adapted) with permission from (COMPLETE REFERENCE CITATION). Copyright (YEAR) American Chemical Society." Insert appropriate information in place of the capitalized words.
- One-time permission is granted only for the use specified in your request. No additional uses are granted (such as derivative works or other editions). For any other uses, please submit a new request.

Copyright Clearance Center RightsLink®

Home Create Account Help

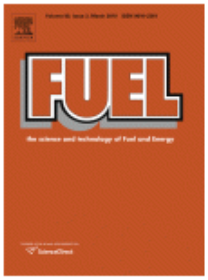

Title: Modeling the characteristic thermodynamic interplay between potential determining ions during brine-dependent recovery process in carbonate rocks

Author: Adedapo N. Awolayo,Hemanta K. Sarma,Long X. Nghiem

Publication: Fuel

Publisher: Elsevier

Date: 15 July 2018

Crown Copyright © 2018 Published by Elsevier Ltd. All rights reserved.

LOGIN

If you're a copyright.com user, you can login to RightsLink using your copyright.com credentials.

Already **a RightsLink user** or want to learn more?

Please note that, as the author of this Elsevier article, you retain the right to include it in a thesis or dissertation, provided it is not published commercially. Permission is not required, but please ensure that you reference the journal as the original source. For more information on this and on your other retained rights, please visit: https://www.elsevier.com/about/our-business/policies/copyright#Author-rights

BACK CLOSE WINDOW

Copyright © 2018 Copyright Clearance Center, Inc. All Rights Reserved. Privacy statement. Terms and Conditions.
Comments? We would like to hear from you. E-mail us at customercare@copyright.com

Copyright Clearance Center RightsLink®

Home | Account Info | Help

SPRINGER NATURE

Title: The Impact of Pore Water Chemistry on Carbonate Surface Charge and Oil Wettability

Author: A. Hiorth, L. M. Cathles, M. V. Madland

Publication: Transport in Porous Media

Publisher: Springer Nature

Date: Jan 1, 2010

Copyright © 2010, Springer Science Business Media B.V.

Logged in as:
Adedapo Awolayo
Account #:
3001347302

LOGOUT

Order Completed

Thank you for your order.

This Agreement between Mr. Adedapo Awolayo ("You") and Springer Nature ("Springer Nature") consists of your license details and the terms and conditions provided by Springer Nature and Copyright Clearance Center.

Your confirmation email will contain your order number for future reference.

printable details

License Number	4523121296388
License date	Feb 06, 2019
Licensed Content Publisher	Springer Nature
Licensed Content Publication	Transport in Porous Media
Licensed Content Title	The Impact of Pore Water Chemistry on Carbonate Surface Charge and Oil Wettability
Licensed Content Author	A. Hiorth, L. M. Cathles, M. V. Madland
Licensed Content Date	Jan 1, 2010
Licensed Content Volume	85
Licensed Content Issue	1
Type of Use	Thesis/Dissertation
Requestor type	academic/university or research institute
Format	print and electronic
Portion	figures/tables/illustrations
Number of figures/tables/illustrations	1
Will you be translating?	no
Circulation/distribution	>50,000
Author of this Springer Nature content	no
Title	Geochemical Modeling of Oil-Brine-Rock Interactions during Brine-Dependent and Brine-CO2 Recovery Technique in Carbonate Petroleum Reservoirs
Institution name	University of Calgary
Expected presentation date	Apr 2019
Portions	Figure 7
Requestor Location	Mr. Adedapo Awolayo 369 ROCKY VISTA PARK NORTHWEST

Copyright Clearance Center RightsLink®

Home | Account Info | Help

Title: Wettability alteration and improved oil recovery by spontaneous imbibition of seawater into chalk: Impact of the potential determining ions Ca2+, Mg2+, and SO4 2−

Author: Peimao Zhang,Medad T. Tweheyo,Tor Austad

Publication: Colloids and Surfaces A: Physicochemical and Engineering Aspects

Publisher: Elsevier

Date: 5 July 2007

Copyright © 2006 Elsevier B.V. All rights reserved.

Logged in as:
Adedapo Awolayo
Account #:
3001347302

LOGOUT

Order Completed

Thank you for your order.

This Agreement between Mr. Adedapo Awolayo ("You") and Elsevier ("Elsevier") consists of your license details and the terms and conditions provided by Elsevier and Copyright Clearance Center.

Your confirmation email will contain your order number for future reference.

printable details

License Number	4523120872254
License date	Feb 06, 2019
Licensed Content Publisher	Elsevier
Licensed Content Publication	Colloids and Surfaces A: Physicochemical and Engineering Aspects
Licensed Content Title	Wettability alteration and improved oil recovery by spontaneous imbibition of seawater into chalk: Impact of the potential determining ions Ca2+, Mg2+, and SO4 2−
Licensed Content Author	Peimao Zhang,Medad T. Tweheyo,Tor Austad
Licensed Content Date	Jul 5, 2007
Licensed Content Volume	301
Licensed Content Issue	1-3
Licensed Content Pages	10
Type of Use	reuse in a thesis/dissertation
Portion	figures/tables/illustrations
Number of figures/tables/illustrations	2
Format	both print and electronic
Are you the author of this Elsevier article?	No
Will you be translating?	No
Original figure numbers	Figure 5, 8
Title of your thesis/dissertation	Geochemical Modeling of Oil-Brine-Rock Interactions during Brine-Dependent and Brine-CO2 Recovery Technique in Carbonate Petroleum Reservoirs
Expected completion date	Apr 2019
Estimated size (number of pages)	200
Requestor Location	Mr. Adedapo Awolayo

Copyright Clearance Center RightsLink®

Home | Account Info | Help

Title: Wettability alteration in chalk 1. Preparation of core material and oil properties

Author: Dag C Standnes,Tor Austad

Publication: Journal of Petroleum Science and Engineering

Publisher: Elsevier

Date: November 2000

Copyright © 2000 Elsevier Science B.V. All rights reserved.

Logged in as:
Adedapo Awolayo
Account #:
3001347302

LOGOUT

Order Completed

Thank you for your order.

This Agreement between Mr. Adedapo Awolayo ("You") and Elsevier ("Elsevier") consists of your license details and the terms and conditions provided by Elsevier and Copyright Clearance Center.

Your confirmation email will contain your order number for future reference.

printable details

License Number	4523120015667
License date	Feb 06, 2019
Licensed Content Publisher	Elsevier
Licensed Content Publication	Journal of Petroleum Science and Engineering
Licensed Content Title	Wettability alteration in chalk 1. Preparation of core material and oil properties
Licensed Content Author	Dag C Standnes,Tor Austad
Licensed Content Date	Nov 1, 2000
Licensed Content Volume	28
Licensed Content Issue	3
Licensed Content Pages	11
Type of Use	reuse in a thesis/dissertation
Portion	figures/tables/illustrations
Number of figures/tables/illustrations	1
Format	both print and electronic
Are you the author of this Elsevier article?	No
Will you be translating?	No
Original figure numbers	Figure 8
Title of your thesis/dissertation	Geochemical Modeling of Oil-Brine-Rock Interactions during Brine-Dependent and Brine-CO2 Recovery Technique in Carbonate Petroleum Reservoirs
Expected completion date	Apr 2019
Estimated size (number of pages)	200
Requestor Location	Mr. Adedapo Awolayo 369 ROCKY VISTA PARK NORTHWEST CALGARY, AB T3G5K7 Canada Attn: Mr. Adedapo Awolayo

Copyright Clearance Center

Note: Copyright.com supplies permissions but not the copyrighted content itself.

1 PAYMENT — 2 REVIEW — 3 CONFIRMATION

Step 3: Order Confirmation

Thank you for your order! A confirmation for your order will be sent to your account email address. If you have questions about your order, you can call us 24 hrs/day, M-F at +1.855.239.3415 Toll Free, or write to us at info@copyright.com. This is not an invoice.

Confirmation Number: 11788956
Order Date: 02/06/2019

If you paid by credit card, your order will be finalized and your card will be charged within 24 hours. If you choose to be invoiced, you can change or cancel your order until the invoice is generated.

Payment Information

Adedapo Awolayo
adedapo.awolayo@ucalgary.ca
+1 (403) 397-7639
Payment Method: n/a

Order Details

Oil and gas facilities

Order detail ID:	71798150
Order License Id:	4523120366540
ISSN:	2224-4514
Publication Type:	Journal
Volume:	
Issue:	
Start page:	
Publisher:	Society of Petroleum Engineers
Author/Editor:	Society of Petroleum Engineers (U.S.)

Permission Status:	Granted
Permission type:	Republish or display content
Type of use:	Republish in a thesis/dissertation
Requestor type	Author of requested content
Format	Print, Electronic
Portion	chart/graph/table/figure
Number of charts/graphs/tables/figures	1
The requesting person/organization	Adedapo Awolayo / University of Calgary
Title or numeric reference of the portion(s)	Table 1-pros and cons of reviewed water-chemistry
Title of the article or chapter the portion is from	A Critical Review of Alternative Desalination Technologies for Smart Waterflooding

Copyright Clearance Center

Note: Copyright.com supplies permissions but not the copyrighted content itself.

1 PAYMENT — 2 REVIEW — 3 CONFIRMATION

Step 3: Order Confirmation

Thank you for your order! A confirmation for your order will be sent to your account email address. If you have questions about your order, you can call us 24 hrs/day, M-F at +1.855.239.3415 Toll Free, or write to us at info@copyright.com. This is not an invoice.

Confirmation Number: 11788963
Order Date: 02/06/2019

If you paid by credit card, your order will be finalized and your card will be charged within 24 hours. If you choose to be invoiced, you can change or cancel your order until the invoice is generated.

Payment Information

Adedapo Awolayo
adedapo.awolayo@ucalgary.ca
+1 (403) 397-7639
Payment Method: n/a

Order Details

SPE JOURNAL -RICHARDSON-

Order detail ID:	71798157
Order License Id:	4523121005362
ISSN:	1086-055X
Publication Type:	Journal
Volume:	
Issue:	
Start page:	
Publisher:	THE SOCIETY,
Author/Editor:	SOCIETY OF PETROLEUM ENGINEERS (U.S.)

Permission Status:	Granted
Permission type:	Republish or display content
Type of use:	Republish in a thesis/dissertation
Requestor type	Author of requested content
Format	Print, Electronic
Portion	chart/graph/table/figure
Number of charts/graphs/tables/figures	1
The requesting person/organization	Adedapo Awolayo/University of Calgary
Title or numeric reference of the portion(s)	Figure 9 — Comparison of zeta potential of dolomite, calcite, Figure 10 — Comparison of zeta potential of limestone, calcite, chalk, and dolomite particles

References

[1] Green, D. W., and Willhite, G. P. (1998). *Enhanced oil recovery*. Henry L. Doherty Memorial Fund of AIME, Society of Petroleum Engineers: Richardson, TX.

[2] Alvarado, V., and Manrique, E. (2010). Enhanced oil recovery: an update review. *Energies, 3*(9), 1529-1575. doi: 10.3390/en3091529

[3] Rod, S. (2003). *Quantification of uncertainty in recovery efficiency predictions: lessons learned from 250 mature carbonate fields.* In Proceedings of the SPE Annual Technical Conference and Exhibition, Denver, Colorado, 5-8 October.

[4] Sheng, J. (2013). *Enhanced oil recovery field case studies*. Gulf Professional Publishing.

[5] Muggeridge, A., Cockin, A., Webb, K., Frampton, H., Collins, I., Moulds, T., and Salino, P. (2014). Recovery rates, enhanced oil recovery and technological limits. *Phil. Trans. R. Soc. A, 372*(2006), 20120320. doi: 10.1098/rsta.2012.0320

[6] Kokal, S., and Al-Kaabi, A. (2010). Enhanced oil recovery: challenges & opportunities. *World Petroleum Council: Official Publication*, 64-69.

[7] Awolayo, A. N., Sarma, H. K., and Al-sumaiti, A. M. (2014). *A Laboratory Study of Ionic Effect of Smart Water for Enhancing Oil Recovery in Carbonate Reservoirs.* In Proceedings of the SPE EOR Conference at Oil and Gas West Asia, Muscat, Oman, 31 March-2 April.

[8] Buckley, S. E., and Leverett, M. C. (1942). Mechanism of fluid displacement in sands. *Transactions of the AIME, 146*(01), 107-116. doi: 10.2118/942107-g

[9] Welge, H. J. (1952). A simplified method for computing oil recovery by gas or water drive. *Journal of Petroleum Technology, 4*(04), 91-98. doi: 10.2118/124-g

[10] Bernard, G. (1967). *Effect of floodwater salinity on recovery of oil from cores containing clays.* In Proceedings of the SPE California Regional Meeting, Los Angeles, California, 26-27 October.

[11] Martin, J. (1959). *The Effects of Clay on the Displacement of Heavy Oil by Water.* In Proceedings of the Venezuelan Annual Meeting.

[12] Jadhunandan, P. P. (1990). *Effects of brine composition, crude oil, and aging conditions on wettability and oil recovery.* Department of Petroleum Engineering, New Mexico Institute of Mining & Technology.

[13] Jadhunandan, P. P., and Morrow, N. R. (1995). Effect of wettability on waterflood recovery for crude-oil/brine/rock systems. *SPE Reservoir Eval. Eng., 10*(1), 40-46. doi: 10.2118/22597-PA

[14] Tang, G. Q., and Morrow, N. R. (1997). Salinity, temperature, oil composition, and oil recovery by waterflooding. *SPE Reservoir Eval. Eng., 12*(4), 269-276. doi: 10.2118/36680-PA

[15] Tang, G. Q., and Morrow, N. R. (1999). Influence of brine composition and fines migration on crude oil/brine/rock interactions and oil recovery. *Journal of Petroleum Science and Engineering, 24*(2), 99-111. doi: 10.1016/s0920-4105(99)00034-0

[16] Yildiz, H. O., and Morrow, N. R. (1996). Effect of brine composition on recovery of Moutray crude oil by waterflooding. *Journal of Petroleum Science and Engineering, 14*(3), 159-168. doi: 10.1016/0920-4105(95)00041-0

[17] Zhou, X., Morrow, N. R., and Ma, S. (2000). Interrelationship of wettability, initial water saturation, aging time, and oil recovery by spontaneous imbibition and waterflooding. *SPE Journal, 5*(02), 199-207. doi: 10.2118/62507-pa

[18] Sulak, R. (1991). Ekofisk field: the first 20 years. *Journal of Petroleum Technology, 43*(10), 1265-1271. doi: 10.2118/20773-pa

[19] Sylte, J., Hallenbeck, L., and Thomas, L. (1988). *Ekofisk formation pilot waterflood.* In Proceedings of the SPE Annual Technical Conference and Exhibition, Houston, Texas, 2-5 October.

[20] Hallenbeck, L. D., Sylte, J. E., Ebbs, D. J., and Thomas, L. K. (1991). Implementation of the Ekofisk field waterflood. *SPE Formation Evaluation, 6*(03), 284-290. doi: 10.2118/19838-pa

[21] Hermansen, H., Thomas, L., Sylte, J., and Aasboe, B. (1997). *Twenty five years of Ekofisk reservoir management.* In Proceedings of the SPE Annual Technical Conference and Exhibition, San Antonio, Texas, US, 5-8 October.

[22] Callegaro, C., Masserano, F., Bartosek, M., Buscaglia, R., Visintin, R., Hartvig, S. K., and Huseby, O. K. (2014). *Single Well Chemical Tracer Tests to Assess Low Salinity Water and Surfactant EOR Processes in West Africa.* In Proceedings of the International Petroleum Technology Conference, Kuala Lumpur, Malaysia, 2014/12/10/.

[23] McGuire, P., Chatham, J., Paskvan, F., Sommer, D., and Carini, F. (2005). *Low Salinity Oil Recovery: An Exciting New EOR Opportunity for Alaska's North Slope.* In Proceedings of the SPE Western Regional Meeting, Irvine, California, 30 March-1 April.

[24] Yousef, A., Liu, J., Blanchard, G., Al-Saleh, S., Al-Zahrani, T., Al-Zahrani, R., Tammar, H., and Al-Mulhim, N. (2012). *Smart Waterflooding: Industry's First Field Test in Carbonate Reservoirs.* In Proceedings of the SPE Annual Technical Conference and Exhibition, San Antonio, Texas, USA, 8-10 October.

[25] Lager, A., Webb, K. J., and Black, C. J. J. (2007). *Impact of brine chemistry on oil recovery.* In Proceedings of the 14th European Symposium on Improved Oil Recovery, Cairo, Egypt, 22–24 April.

[26] Tang, G. Q., and Morrow, N. R. (1999). *Oil recovery by waterflooding and imbibition—invading brine cation valency and salinity.* In Proceedings of the International Symposium of the Society of Core Analysts, Golden, Colorado, USA, 1–4 August

[27] Chandrasekhar, S., and Mohanty, K. (2013). *Wettability Alteration with Brine Composition in High Temperature Carbonate Reservoirs.* In Proceedings of the SPE Annual Technical Conference and Exhibition, New Orleans, Louisiana, USA, 30 September - 2 October.

[28] Awolayo, A. N., Sarma, H. K., and AlSumaiti, A. M. (2014). *Impact of Ionic Exchanges between Active and Non-active Ions on Displacement Efficiency in Smart Waterflood Application.* In Proceedings of the 76th EAGE Conference and Exhibition 2014, Amsterdam, Netherlands, 16 - 19 June.

[29] Awolayo, A. N., Sarma, H. K., and AlSumaiti, A. M. (2015). An Experimental Investigation into the Impact of Sulfate Ions in Smart Water to Improve Oil Recovery in Carbonate Reservoirs. *Transport in Porous Media, 111*(3), 649-668. doi: 10.1007/s11242-015-0616-4

[30] Zhang, Y., and Sarma, H. (2012). *Improving Waterflood Recovery Efficiency in Carbonate Reservoirs through Salinity Variations and Ionic Exchanges: A Promising Low-Cost" Smart-Waterflood" Approach.* In Proceedings of the Abu Dhabi International Petroleum Conference and Exhibition, Abu Dhabi, UAE, 11-14 November.

[31] Yousef, A., Al-Saleh, S., Al-Kaabi, A., and Al-Jawfi, M. (2010). *Laboratory investigation of novel oil recovery method for carbonate reservoirs.* In Proceedings of the Canadian Unconventional Resources and International Petroleum Conference, Calgary, Alberta, Canada, 19-21 October.

[32] Zhang, P., Tweheyo, M. T., and Austad, T. (2007). Wettability alteration and improved oil recovery by spontaneous imbibition of seawater into chalk: Impact of the potential determining ions Ca^{2+}, Mg^{2+}, and SO_4^{2-}. *Colloids and Surfaces A: Physicochemical and Engineering Aspects, 301*(1), 199-208. doi: 10.1016/j.colsurfa.2006.12.058

[33] Austad, T., Strand, S., Høgnesen, E. J., and Zhang, P. (2005). *Seawater as IOR fluid in fractured chalk.* In Proceedings of the SPE International Symposium on Oilfield Chemistry, The Woodlands, Texas, 2-4 February.

[34] Sharma, M. M., and Filoco, P. R. (2000). Effect of Brine Salinity and Crude-Oil Properties on Oil Recovery and Residual Saturations. *SPE Journal, 5*(3), 293-300. doi: 10.2118/65402-pa

[35] Skrettingland, K., Holt, T., Tweheyo, M. T., and Skjevrak, I. (2011). Snorre Low-Salinity-Water Injection — Coreflooding Experiments and Single-Well Field Pilot. *SPE Reservoir Eval. Eng., 14*(02), 182-192. doi: 10.2118/129877-pa

[36] Zahid, A., Shapiro, A., and Skauge, A. (2012). *Experimental studies of low salinity water flooding in carbonate reservoirs: A new promising approach.* In Proceedings of the SPE EOR Conference at Oil and Gas West Asia, Muscat, Oman, 16-18 April.

[37] Winoto, W., Loahardjo, N., Xie, S., Yin, P., and Morrow, N. (2012). *Secondary and Tertiary Recovery of Crude Oil from Outcrop and Reservoir Rocks by Low Salinity Waterflooding.* In Proceedings of the SPE Improved Oil Recovery Symposium, Tulsa, Oklahoma, USA, 14-18 April.

[38] Fathi, S. J., Austad, T., and Strand, S. (2010). “Smart Water” as a Wettability Modifier in Chalk: The Effect of Salinity and Ionic Composition. *Energy & Fuels, 24*(4), 2514-2519. doi: 10.1021/ef901304m

[39] Awolayo, A. N., and Sarma, H. K. (2016). Impact of Multi-ion Interactions on Oil Mobilization by Smart Waterflooding in Carbonate Reservoirs. *Journal of Petroleum & Environmental Biotechnology, 7*(278), 1-8. doi: 10.4172/2157-7463.1000278

[40] Rivet, S., Lake, L. W., and Pope, G. A. (2010). *A coreflood investigation of low-salinity enhanced oil recovery.* In Proceedings of the SPE Annual Technical Conference and Exhibition Florence, Italy, 19-22 September.

[41] Lager, A., Webb, K. J., Collins, I., and Richmond, D. (2008). *LoSal enhanced oil recovery: Evidence of enhanced oil recovery at the reservoir scale.* In Proceedings of the SPE/DOE Symposium on Improved Oil Recovery, Tulsa, Oklahoma, USA, 20-23 April.

[42] Vo, L. T., Gupta, R., and Hehmeyer, O. J. (2012). *Ion Chromatography Analysis of Advanced Ion Management Carbonate Coreflood Experiments.* In Proceedings of the Abu Dhabi International Petroleum Conference and Exhibition, Abu Dhabi, UAE, 11-14 November.

[43] Omekeh, A. V., Evje, S., and Friis, H. A. (2012). Modeling of low salinity effects in sandstone oil rocks. *International Journal of Numerical Analysis and Modelling, 1*(1), 1-18.

[44] RezaeiDoust, A., Puntervold, T., Strand, S., and Austad, T. (2009). Smart water as wettability modifier in carbonate and sandstone: A discussion of similarities/differences in the chemical mechanisms. *Energy & Fuels, 23*(9), 4479-4485. doi: 10.1021/ef900185q

[45] Okasha, T. M., and Alshiwaish, A. (2009). *Effect of brine salinity on interfacial tension in Arab-D carbonate reservoir, Saudi Arabia.* In Proceedings of the SPE Middle East Oil and Gas Show and Conference, Manama, Bahrain, 15-18 March.

[46] Al-Attar, H. H., Mahmoud, M. Y., Zekri, A. Y., Almehaideb, R., and Ghannam, M. (2013). Low-salinity flooding in a selected carbonate reservoir: experimental approach. *Journal of Petroleum Exploration and Production Technology, 3*(2), 139-149. doi: 10.1007/s13202-013-0052-3

[47] Hiorth, A., Cathles, L. M., and Madland, M. V. (2010). The impact of pore water chemistry on carbonate surface charge and oil wettability. *Transport in Porous Media, 85*(1), 1-21. doi: 10.1007/s11242-010-9543-6

[48] Austad, T., Shariatpanahi, S. F., Strand, S., Black, C. J. J., and Webb, K. J. (2011). Conditions for a Low-Salinity Enhanced Oil Recovery (EOR) Effect in Carbonate Oil Reservoirs. *Energy & Fuels, 26*(1), 569-575. doi: 10.1021/ef201435g

[49] Pu, H., Xie, X., Yin, P., and Morrow, N. R. (2010). *Low-salinity waterflooding and mineral dissolution.* In Proceedings of the SPE Annual Technical Conference and Exhibition, Florence, Italy, Sept 19−22.

[50] Zhang, P., Tweheyo, M. T., and Austad, T. (2006). Wettability alteration and improved oil recovery in chalk: The effect of calcium in the presence of sulfate. *Energy & Fuels, 20*(5), 2056-2062. doi: 10.1021/ef0600816

[51] Austad, T., Strand, S., Madland, M. V., Puntervold, T., and Korsnes, R. I. (2008). Seawater in Chalk: An EOR and Compaction Fluid. *SPE Journal Paper, 11*(04), 648 - 654. doi: 10.2118/118431-PA

[52] Høgnesen, E., Strand, S., and Austad, T. (2005). *Waterflooding of preferential oil-wet carbonates: Oil recovery related to reservoir temperature and brine composition.* In Proceedings of the SPE Europec/EAGE Annual Conference, Madrid, Spain, 13-16 June.

[53] Strand, S., Austad, T., Puntervold, T., Høgnesen, E. J., Olsen, M., and Barstad, S. M. F. (2008). "Smart Water" for Oil Recovery from Fractured Limestone: A Preliminary Study. *Energy & Fuels, 22*(5), 3126-3133. doi: 10.1021/ef800062n

[54] Strand, S., Høgnesen, E. J., and Austad, T. (2006). Wettability alteration of carbonates—Effects of potential determining ions (Ca^{2+} and SO_4^{2-}) and temperature. *Colloids and Surfaces A: Physicochemical and Engineering Aspects, 275*(1), 1-10. doi: 10.1016/j.colsurfa.2005.10.061

[55] Zhang, P., and Austad, T. (2006). Wettability and oil recovery from carbonates: Effects of temperature and potential determining ions. *Colloids and Surfaces A: Physicochemical and Engineering Aspects, 279*(1), 179-187. doi: 10.1016/j.colsurfa.2006.01.009

[56] Mahani, H., Keya, A. L., Berg, S., Bartels, W.-B., Nasralla, R., and Rossen, W. R. (2015). Insights into the mechanism of wettability alteration by low-salinity flooding (LSF) in carbonates. *Energy & Fuels, 29*(3), 1352-1367. doi: 10.1021/ef5023847

[57] Yousef, A. A., Al-Saleh, S. H., Al-Kaabi, A., and Al-Jawfi, M. S. (2011). Laboratory investigation of the impact of injection-water salinity and ionic content on oil recovery from carbonate reservoirs. *SPE Reservoir Eval. Eng., 14*(05), 578-593. doi: 10.2118/137634-PA

[58] Meng, W., Haroun, M. R., Sarma, H. K., Adeoye, J. T., Aras, P., Punjabi, S., Rahman, M. M., and Al Kobaisi, M. (2015). *A Novel Approach of Using Phosphate-spiked Smart Brines to Alter Wettability in Mixed Oil-wet Carbonate Reservoirs.* In Proceedings of the Abu Dhabi International Petroleum Exhibition and Conference, Abu Dhabi, UAE, 9-12 November.

[59] Lashkarbolooki, M., Ayatollahi, S., and Riazi, M. (2014). Effect of salinity, resin, and asphaltene on the surface properties of acidic crude oil/smart water/rock system. *Energy & Fuels, 28*(11), 6820-6829. doi: 10.1021/ef5015692

[60] Alameri, W., Teklu, T. W., Graves, R. M., Kazemi, H., and AlSumaiti, A. M. (2014). *Wettability alteration during low-salinity waterflooding in carbonate reservoir cores.* In Proceedings of the SPE Asia Pacific Oil & Gas Conference and Exhibition, Adelaide, Australia, 14–16 October.

[61] Gupta, R., Smith Jr, P., Willingham, T., Lo Cascia, M., Shyeh, J., and Harris, C. (2011). *Enhanced Waterflood for Middle East Carbonate Cores–Impact of Injection Water Composition.* In Proceedings of the SPE Middle East Oil and Gas Show and Conference, Manama, Bahrain, 25-28 September.

[62] Awolayo, A., Sarma, H., and Nghiem, L. (2018). Brine-Dependent Recovery Processes in Carbonate and Sandstone Petroleum Reservoirs: Review of Laboratory-Field Studies, Interfacial Mechanisms and Modeling Attempts. *Energies, 11*(11). doi: 10.3390/en11113020

[63] Al-Shalabi, E. W., Sepehrnoori, K., Delshad, M., and Pope, G. (2014). A Novel Method to Model Low-Salinity-Water Injection in Carbonate Oil Reservoirs. *SPE Journal, 20*(05), 1,154 - 151,166. doi: 10.2118/169674-PA

[64] Andersen, P. Ø., Evje, S., Madland, M. V., and Hiorth, A. (2012). A geochemical model for interpretation of chalk core flooding experiments. *Chemical engineering science, 84*, 218-241. doi: 10.1016/j.ces.2012.08.038

[65] Awolayo, A. N., Sarma, H. K., and Nghiem, L. X. (2018). Modeling the characteristic thermodynamic interplay between potential determining ions during brine-dependent recovery process in carbonate rocks. *Fuel, 224*, 701-717. doi: 10.1016/j.fuel.2018.03.070

[66] Dang, C. T. Q., Nghiem, L. X., Chen, Z. J., and Nguyen, Q. P. (2013). *Modeling Low Salinity Waterflooding: Ion Exchange, Geochemistry and Wettability Alteration.* In Proceedings of the SPE Annual Technical Conference and Exhibition, New Orleans, Louisiana, USA, 30 September-2 October.

[67] Evje, S., and Hiorth, A. (2010). A mathematical model for dynamic wettability alteration controlled by water-rock chemistry. *Networks and Heterogenous Media, 5*(2), 217-256. doi: 10.3934/nhm.2010.5.217

[68] Jerauld, G. R., Webb, K. J., Lin, C.-Y., and Seccombe, J. C. (2008). Modeling low-salinity waterflooding. *SPE Reservoir Eval. Eng., 11*(06), 1,000-001,012. doi: 10.2118/102239-PA

[69] Omekeh, A. V., Friis, H. A., Fjelde, I., and Evje, S. (2012). *Modeling of Ion-Exchange and Solubility in Low Salinity Water Flooding.* In Proceedings of the SPE Improved Oil Recovery Symposium, Tulsa, Oklahoma, USA, 214-18 April.

[70] Qiao, C., Li, L., Johns, R. T., and Xu, J. (2015). A Mechanistic Model for Wettability Alteration by Chemically Tuned Waterflooding in Carbonate Reservoirs. *SPE Journal, 20*(04), 767 - 783. doi: 10.2118/170966-PA

[71] Venkatraman, A., Hesse, M. A., Lake, L. W., and Johns, R. T. (2014). Analytical solutions for flow in porous media with multicomponent cation exchange reactions. *Water Resources Research, 50*(7), 5831-5847. doi: 10.1002/2013wr015091

[72] Zeinijahromi, A., Nguyen, T. K. P., and Bedrikovetsky, P. (2013). Mathematical Model for Fines-Migration-Assisted Waterflooding With Induced Formation Damage. *SPE Journal, 18*(03), 518-533. doi: 10.2118/144009-PA

[73] Adegbite, J. O., Al-Shalabi, E. W., and Ghosh, B. (2018). Geochemical modeling of engineered water injection effect on oil recovery from carbonate cores. *Journal of Petroleum Science and Engineering, 170*, 696-711. doi: 10.1016/j.petrol.2018.06.079

[74] Chandrasekhar, S., Sharma, H., and Mohanty, K. K. (2018). Dependence of wettability on brine composition in high temperature carbonate rocks. *Fuel, 225*, 573-587. doi: 10.1016/j.fuel.2018.03.176

[75] Awolayo, A. N., and Sarma, H. K. (2018). An analytical solution to interpret active ion transport during chemically-tuned waterflooding process in high-temperature carbonate rocks. *The Canadian Journal of Chemical Engineering*. doi: 10.1002/cjce.23183

[76] Borazjani, S., Behr, A., Genolet, L., Van Der Net, A., and Bedrikovetsky, P. (2017). Effects of fines migration on low-salinity waterflooding: analytical modelling. *Transport in Porous Media, 116*(1), 213-249. doi: 10.1007/s11242-016-0771-2

[77] Al-adasani, A., Bai, B., and Wu, Y.-S. (2012). *Investigating low-salinity waterflooding recovery mechanisms in sandstone reservoirs.* In Proceedings of the SPE Improved Oil Recovery Symposium, Tulsa, Oklahoma, USA, 14–18 April.

[78] Wu, Y.-S., and Bai, B. (2009). *Efficient simulation for low salinity waterflooding in porous and fractured reservoirs.* In Proceedings of the SPE Reservoir Simulation Symposium, The Woodlands, Texas, 2-4 February.

[79] Al-Shalabi, E. W., Sepehrnoori, K., and Pope, G. (2015). *Mechanistic Modeling of Oil Recovery Due to Low Salinity Water Injection in Oil Reservoirs.* In Proceedings of the SPE Middle East Oil & Gas Show and Conference, Manama, Bahrain, 8-11 March.

[80] Yu, L., Evje, S., Kleppe, H., Kårstad, T., Fjelde, I., and Skjaeveland, S. M. (2009). Spontaneous imbibition of seawater into preferentially oil-wet chalk cores—Experiments and simulations. *Journal of petroleum science and engineering, 66*(3), 171-179. doi: 10.1016/j.petrol.2009.02.008

[81] Andersen, P., and Evje, S. (2012). *A Mathematical Model for Interpretation of Brine-Dependent Spontaneous Imbibition Experiments.* In Proceedings of the ECMOR XIII-13th European Conference on the Mathematics of Oil Recovery, Biarritz, France, 10–13 September

[82] Korrani, A. K. N., Jerauld, G. R., and Sepehrnoori, K. (2014). *Coupled Geochemical-Based Modeling of Low Salinity Waterflooding.* In Proceedings of the SPE Improved Oil Recovery Symposium, Tulsa, Oklahoma, USA, 12-16 April.

[83] Dang, C. T. Q., Nghiem, L. X., Chen, Z., Nguyen, N. T. B., and Nguyen, Q. P. (2014). *CO_2 Low Salinity Water Alternating Gas: A New Promising Approach for Enhanced Oil Recovery.* In Proceedings of the SPE Improved Oil Recovery Symposium, Tulsa, Oklahoma, USA, 12-16 April.

[84] Qiao, C., Johns, R. T., and Li, L. (2016). Modeling Low Salinity Waterflooding in Chalk and Limestone Reservoirs. *Energy & Fuels, 30 (2),* pp 884-895. doi: 10.1021/acs.energyfuels.5b02456

[85] Zolfaghari, H., Zebarjadi, A., Shahrokhi, O., and Ghazanfari, M. H. (2013). An Experimental Study of CO_2-low Salinity Water Alternating Gas Injection in Sandstone Heavy Oil Reservoirs. *Iranian Journal of Oil & Gas Science and Technology, 2*(3), 37-47.

[86] Kilybay, A., Ghosh, B., Thomas, N. C., and Aras, P. (2016). *Hybrid EOR Technology: Carbonated Water and Smart Water Improved Recovery in Oil Wet Carbonate Formation*. Paper Volume presented at the SPE Annual Caspian Technical Conference & Exhibition, Astana, Kazakhstan, 1-3 November https://doi.org/10.2118/182567-MS

[87] Ruidiaz, E. M., Winter, A., and Trevisan, O. V. (2018). Oil recovery and wettability alteration in carbonates due to carbonate water injection. *Journal of Petroleum Exploration and Production Technology, 8*(1), 249-258. doi: 10.1007/s13202-017-0345-z

[88] Teklu, T. W., Alameri, W., Graves, R. M., Kazemi, H., and AlSumaiti, A. M. (2016). Low-salinity water-alternating-CO_2 EOR. *Journal of Petroleum Science and Engineering, 142*, 101-118. doi: https://doi.org/10.1016/j.petrol.2016.01.031

[89] Al-Shalabi, E. W., Sepehrnoori, K., and Pope, G. A. (2014). *Modeling the Combined Effect of Injecting Low Salinity Water and Carbon Dioxide on Oil Recovery from Carbonate Cores.* In Proceedings of the International Petroleum Technology Conference, Kuala Lumpur, Malaysia, 10–12 December.

[90] Khorsandi, S., Qiao, C., and Johns, R. T. (2016). *Displacement Efficiency for Low Salinity Polymer Flooding Including Wettability Alteration.* In Proceedings of the SPE Improved Oil Recovery Conference, Tulsa, Oklahoma, USA, 2016/4/11/.

[91] Mohammadi, H., and Jerauld, G. (2012). *Mechanistic modeling of the benefit of combining polymer with low salinity water for enhanced oil recovery.* In Proceedings of the SPE Improved Oil Recovery Symposium.

[92] Shaker , S. B., and Skauge, A. (2013). Enhanced oil recovery (EOR) by combined low salinity water/polymer flooding. *Energy & Fuels, 27*(3), 1223-1235.

[93] Kozaki, C. (2012). *Efficiency of low salinity polymer flooding in sandstone cores.* (Masters Thesis), University of Texas, Austin.

[94] Standnes, D. C., Nogaret, L. A. D., Chen, H.-L., and Austad, T. (2002). An evaluation of spontaneous imbibition of water into oil-wet carbonate reservoir cores using a nonionic and a cationic surfactant. *Energy & Fuels, 16*(6), 1557-1564.

[95] Tavassoli, S., Korrani, K. N. A., Pope, G. A., and Sepehrnoori, K. (2015). Low-Salinity Surfactant Flooding—A Multimechanistic Enhanced-Oil-Recovery Method. *SPE Journal Paper*. doi: 10.2118/173801-PA

[96] Aksulu, H., Håmsø, D., Strand, S., Puntervold, T., and Austad, T. (2012). Evaluation of low-salinity enhanced oil recovery effects in sandstone: Effects of the temperature and pH gradient. *Energy & Fuels, 26*(6), 3497-3503. doi: 10.1021/ef300162n

[97] Rezaeidoust, A., Puntervold, T., and Austad, T. (2010). *A Discussion of the Low-Salinity EOR Potential for a North Sea Sandstone Field.* In Proceedings of the SPE Annual Technical Conference and Exhibition, Florence, Italy, 19-22 September.

[98] Boussour, S., Cissokho, M., Cordier, P., Bertin, H. J., and Hamon, G. (2009). *Oil Recovery by Low-Salinity Brine Injection: Laboratory Results on Outcrop and Reservoir Cores.* In Proceedings of the SPE Annual Technical Conference and Exhibition, New Orleans, Louisiana, USA, 4-7 October.

[99] Ligthelm, D., Gronsveld, J., Hofman, J., Brussee, N., Marcelis, F., and van der Linde, H. (2009). *Novel Waterflooding Strategy By Manipulation Of Injection Brine Composition.* In Proceedings of the EUROPEC/EAGE Conference and Exhibition, Amsterdam, The Netherlands, 8-11 June.

[100] Loahardjo, N., Xie, X., Yin, P., and Morrow, N. R. (2007). *Low salinity waterflooding of a reservoir rock.* In Proceedings of the International Symposium of the Society of Core Analysts, Calgary, Canada, 10-12 September.

[101] Romanuka, J., Hofman, J., Ligthelm, D., Suijkerbuijk, B., Marcelis, F., Oedai, S., Brussee, N., van der Linde, H., Aksulu, H., and Austad, T. (2012). *Low Salinity EOR in Carbonates.* In Proceedings of the SPE Improved Oil Recovery Symposium, Tulsa, Oklahoma, USA, 14-18 April.

[102] Yousef, A., Al-Saleh, S., and Al-Jawfi, M. (2012). *Improved/Enhanced Oil Recovery from Carbonate Reservoirs by Tuning Injection Water Salinity and Ionic Content.* In Proceedings of the SPE Improved Oil Recovery Symposium, Tulsa, Oklahoma, USA, 14-18 April.

[103] Al Mahrouqi, D., Vinogradov, J., and Jackson, M. D. (2016). Temperature dependence of the zeta potential in intact natural carbonates. *Geophysical Research Letters, 43*(22). doi: 10.1002/2016gl071151

[104] Alroudhan, A., Vinogradov, J., and Jackson, M. (2016). Zeta potential of intact natural limestone: Impact of potential-determining ions Ca^{2+}, Mg^{2+} and SO_4^{2-}. *Colloids and Surfaces A: Physicochemical and Engineering Aspects, 493*, 83-98. doi: 10.1016/j.colsurfa.2015.11.068

[105] Austad, T., RezaeiDoust, A., and Puntervold, T. (2010). *Chemical mechanism of low salinity water flooding in sandstone reservoirs.* In Proceedings of the SPE Improved Oil Recovery Symposium, Tulsa, Oklahoma, USA, 24-28 April.

[106] Hilner, E., Andersson, M. P., Hassenkam, T., Matthiesen, J., Salino, P. A., and Stipp, S. L. S. (2015). The effect of ionic strength on oil adhesion in sandstone–the search for the low salinity mechanism. *Scientific reports, 5*, 9933. doi: 10.1038/srep09933

[107] Nasralla, R. A., and Nasr-El-Din, H. A. (2011). *Impact of Electrical Surface Charges and Cation Exchange on Oil Recovery by Low Salinity Water.* In Proceedings of the SPE Asia Pacific Oil and Gas Conference and Exhibition, Jakarta, Indonesia, 20-22 September.

[108] Vinogradov, J., Jaafar, M. Z., and Jackson, M. D. (2010). Measurement of streaming potential coupling coefficient in sandstones saturated with natural and artificial brines at high salinity. *Journal of Geophysical Research: Solid Earth, 115*(B12). doi: 10.1029/2010jb007593

[109] Morrow, N. R., Tang, G. Q., Valat, M., and Xie, X. (1998). Prospects of improved oil recovery related to wettability and brine composition. *Journal of Petroleum science and Engineering, 20*(3-4), 267-276. doi: 10.1016/s0920-4105(98)00030-8

[110] Morrow, N. R. (1990). Wettability and Its Effect on Oil Recovery. *Journal of Petroleum Technology, 42*(12), 1,476-471,484. doi: 10.2118/21621-pa

[111] Lager, A., Webb, K. J., Black, C. J. J., Singleton, M., and Sorbie, K. S. (2008). Low Salinity Oil Recovery - An Experimental Investigation 1. *Petrophysics, 49*(01).

[112] Shariatpanahi, S. F., Strand, S., and Austad, T. (2010). Evaluation of water-based enhanced oil recovery (EOR) by wettability alteration in a low-permeable fractured limestone oil reservoir. *Energy & Fuels, 24*(11), 5997-6008. doi: 10.1021/ef100837v

[113] Masalmeh, S. K. (2012). *Impact of capillary forces on residual oil saturation and flooding experiments for mixed to oil-wet carbonate reservoirs.* In Proceedings of the International Symposium of the Society of Core Analysts, Aberdeen, Scotland, UK, 27-30 August.

[114] Shehata, A. M., Alotaibi, M. B., and Nasr-El-Din, H. A. (2014). Waterflooding in carbonate reservoirs: Does the salinity matter? *SPE Reservoir Eval. Eng., 17*(03), 304-313. doi: 10.2118/170254-pa

[115] Al Harrasi, A., Al-maamari, R. S., and Masalmeh, S. K. (2012). *Laboratory investigation of low salinity waterflooding for carbonate reservoirs.* In Proceedings of the Abu Dhabi International Petroleum Conference and Exhibition, Abu Dhabi, UAE, 11-14 November.

[116] Standnes, D. C., and Austad, T. (2000). Wettability alteration in chalk: 1. Preparation of core material and oil properties. *Journal of Petroleum Science and Engineering, 28*(3), 111-121. doi: 10.1016/s0920-4105(00)00083-8

[117] Xie, X., and Morrow, N. R. (2001). Oil recovery by spontaneous imbibition from weakly water-wet rocks. *Petrophysics, 42*(04).

[118] Alotaibi, M. B., Azmy, R., and Nasr-El-Din, H. A. (2010). *A comprehensive EOR study using low salinity water in sandstone reservoirs.* In Proceedings of the SPE Improved Oil Recovery Symposium, Tulsa, Oklahoma, USA, 24-28 April.

[119] Jackson, M. D., Al-Mahrouqi, D., and Vinogradov, J. (2016). Zeta potential in oil-water-carbonate systems and its impact on oil recovery during controlled salinity water-flooding. *Scientific reports, 6*, 37363. doi: 10.1038/srep37363

[120] Mahani, H., Keya, A. L., Berg, S., and Nasralla, R. (2017). Electrokinetics of carbonate/brine interface in low-salinity waterflooding: Effect of brine salinity, composition, rock type, and pH on ζ-potential and a surface-complexation model. *SPE Journal, 22*(01), 53-68. doi: 10.2118/181745-pa

[121] Xie, Q., Liu, Y., Wu, J., and Liu, Q. (2014). Ions tuning water flooding experiments and interpretation by thermodynamics of wettability. *Journal of Petroleum Science and Engineering, 124*, 350-358. doi: 10.1016/j.petrol.2014.07.015

[122] Chen, Q., Mercer, D., and Webb, K. (2010). *NMR study on pore occupancy and wettability modification during low salinity waterflooding.* In Proceedings of the 2010 International Symposium of Core Analysts, Halifax, Canada, 4-7 October.

[123] Looyestijn, W. J., and Hofman, J. (2006). Wettability-Index Determination by Nuclear Magnetic Resonance. *SPE Reservoir Eval. Eng.*, *9*(02), 146-153. doi: 10.2118/93624-PA

[124] Hassenkam, T., Mitchell, A. C., Pedersen, C. S., Skovbjerg, L. L., Bovet, N., and Stipp, S. L. S. (2012). The low salinity effect observed on sandstone model surfaces. *Colloids and Surfaces A: Physicochemical and Engineering Aspects*, *403*, 79-86. doi: 10.1016/j.colsurfa.2012.03.058

[125] Lebedeva, E., Senden, T. J., Knackstedt, M., and Morrow, N. (2009). *Improved Oil Recovery from Tensleep Sandstone–Studies of Brine-Rock Interactions by Micro-CT and AFM.* In Proceedings of the IOR 2009-15th European Symposium on Improved Oil Recovery, Paris, France, 27-29 April.

[126] Sarma, H. K. (2015). *SPE Training Course on Chemical Enhanced Oil Recovery Methods*. Kuala Lumpur, Malaysia.

[127] Strand, S., Standnes, D. C., and Austad, T. (2006). New wettability test for chalk based on chromatographic separation of SCN^- and SO_4^{2-}. *Journal of Petroleum Science and Engineering*, *52*(1), 187-197. doi: 10.1016/j.petrol.2006.03.021

[128] Anderson, W. (1986). Wettability literature survey-part 1: rock/oil/brine interactions and the effects of core handling on wettability. *Journal of Petroleum Technology*, *38*(10), 1125-1144. doi: 10.2118/13932-pa

[129] Ding, H., and Rahman, S. (2017). Experimental and theoretical study of wettability alteration during low salinity water flooding-an state of the art review. *Colloids and Surfaces A: Physicochemical and Engineering Aspects*, *520*, 622-639. doi: 10.1016/j.colsurfa.2017.02.006

[130] Israelachvili, J. N. (2011). *Intermolecular and surface forces: revised third edition*. Academic press: New York City.

[131] Shariatpanahi, S. F., Strand, S., and Austad, T. (2011). Initial wetting properties of carbonate oil reservoirs: effect of the temperature and presence of sulfate in formation water. *Energy & fuels*, *25*(7), 3021-3028. doi: 10.1021/ef200033h

[132] Suijkerbuijk, B., Hofman, J., Ligthelm, D., Romanuka, J., Brussee, N., van der Linde, H., and Marcelis, F. (2012). *Fundamental investigations into wettability and low salinity flooding by parameter isolation.* In Proceedings of the SPE Improved Oil Recovery Symposium, Tulsa, Oklahoma, USA, 14-18 April.

[133] Lindlof, J. C., and Stoffer, K. G. (1983). A Case Study of Seawater Injection Incompatibility. *SPE Journal*, *35*(07), 1256 - 1262. doi: 10.2118/9626-PA

[134] Austad, T. (2013). Water-Based EOR in Carbonates and Sandstones: New Chemical Understanding of the EOR Potential Using “Smart Water”. In J. Sheng (Ed.), *Enhanced*

Oil Recovery Field Case Studies (1st ed., pp. 301-335). Waltham: Gulf Professional Publishing Elsevier

[135] Viksund, B. G., Morrow, N. R., Ma, S., Wang, W., and Graue, A. (1998). *Initial water saturation and oil recovery from chalk and sandstone by spontaneous imbibition.* In Proceedings of the International Symposium of Society of Core Analysts, The Hague, The Netherlands, 26–30 August.

[136] Puntervold, T., Strand, S., and Austad, T. (2007). Water flooding of carbonate reservoirs: Effects of a model base and natural crude oil bases on chalk wettability. *Energy & fuels, 21*(3), 1606-1616. doi: 10.1021/ef060624b

[137] Puntervold, T., Strand, S., and Austad, T. (2007). New method to prepare outcrop chalk cores for wettability and oil recovery studies at low initial water saturation. *Energy & Fuels, 21*(6), 3425-3430. doi: 10.1021/ef700323c

[138] Fernø, M. A., Grønsdal, R., Åsheim, J., Nyheim, A., Berge, M., and Graue, A. (2011). Use of sulfate for water based enhanced oil recovery during spontaneous imbibition in chalk. *Energy & fuels, 25*(4), 1697-1706. doi: 10.1021/ef200136w

[139] Shariatpanahi, S. F., Hopkins, P., Aksulu, H., Strand, S., Puntervold, T., and Austad, T. (2016). Water based EOR by wettability alteration in dolomite. *Energy & Fuels, 30*(1), 180-187. doi: 10.1021/acs.energyfuels.5b02239

[140] Dubey, S. T., and Doe, P. H. (1993). Base number and wetting properties of crude oils. *SPE Reservoir Eval. Eng., 8*(03), 195-200. doi: 10.2118/22598-pa

[141] Denekas, M. O., Mattax, C. C., and Davis, G. T. (1959). Effects of Crude Oil Components on Rock Wettability. *Petroleum Transactions, AIME 216*, 330-333.

[142] Buckley, J. S., Liu, Y., and Monsterleet, S. (1998). Mechanisms of wetting alteration by crude oils. *SPE Journal, 3*(01), 54-61. doi: 10.2118/37230-PA

[143] Cuiec, L. (1984). *Rock/Crude-Oil Interactions and Wettability: An Attempt To Understand Their Interrelation.* In Proceedings of the SPE Annual Technical Conference and Exhibition, Houston, Texas, 16-19 September.

[144] Ehrlich, R. (1974). *Wettability alteration during displacement of oil by water from petroleum reservoir rock*. Paper Volume presented at the 48th National Colloid Symposium ACS preprints, Austin, Texas, 24-26 June.

[145] Block, A., and Simms, B. B. (1967). Desorption and exchange of adsorbed octadecylamine and stearic acid on steel and glass. *Journal of Colloid and Interface Science, 25*(4), 514-518. doi: 10.1016/0021-9797(67)90062-8

[146] Strassner, J. E. (1968). Effect of pH on interfacial films and stability of crude oil-water emulsions. *Journal of Petroleum Technology, 20*(03), 303-312. doi: 10.2118/1939-pa

[147] Lowe, A. C., Phillips, M. C., and Riddiford, A. C. (1973). On the wetting of carbonate surfaces by oil and water. *Journal of Canadian Petroleum Technology, 12*(02). doi: 10.2118/73-02-04

[148] Benner, F. C., and Bartel, F. E. (1941). *The effect of polar impurities upon capillary and surface phenomena in petroleum production.* In Proceedings of the Drilling and production practice, New York, USA, 1 January.

[149] Morrow, N. R., Cram, P. J., and McCaffery, F. G. (1973). Displacement Studies in Dolomite With Wettability Control by Octanoic Acid. *Society of Petroleum Engineers Journal, 13*(04), 221-232. doi: 10.2118/3993-PA

[150] Shimoyama, A., and Johns, W. D. (1972). Formation of alkanes from fatty acids in the presence of CaCO3. *Geochimica et Cosmochimica Acta, 36*(1), 87-91. doi: 10.1016/0016-7037(72)90122-6

[151] Zhang, P., and Austad, T. (2005). *The relative effects of acid number and temperature on chalk wettability.* In Proceedings of the SPE International Symposium on Oilfield Chemistry, The Woodlands, Texas, 2-4 February.

[152] Zhang, P., and Austad, T. (2005). *Waterflooding in chalk: Relationship between oil recovery, new wettability index, brine composition and cationic wettability modifier.* In Proceedings of the SPE Europec/EAGE Annual Conference, Madrid, Spain, 2005/1/1/.

[153] Thomas, M. M., Clouse, J. A., and Longo, J. M. (1993). Adsorption of organic compounds on carbonate minerals: 1. Model compounds and their influence on mineral wettability. *Chemical geology, 109*(1), 201-213. doi: 10.1016/0009-2541(93)90070-y

[154] Mwangi, P., Thyne, G., and Rao, D. (2013). *Extensive Experimental Wettability Study in Sandstone and Carbonate-Oil-Brine Systems: Part 1–Screening Tool Development.* In Proceedings of the International Symposium of the Society of Core Analysts, Napa Valley, California, USA, 16-19 September.

[155] Mwangi, P., Brady, P. V., Radonjic, M., and Thyne, G. (2018). The effect of organic acids on wettability of sandstone and carbonate rocks. *Journal of Petroleum Science and Engineering, 165*, 428-435. doi: 10.1016/j.petrol.2018.01.033

[156] Gomari, K. R., and Hamouda, A. A. (2006). Effect of fatty acids, water composition and pH on the wettability alteration of calcite surface. *Journal of petroleum science and engineering, 50*(2), 140-150. doi: 10.1016/j.petrol.2005.10.007

[157] Fathi, S. J., Austad, T., Strand, S., and Puntervold, T. (2010). Wettability alteration in carbonates: The effect of water-soluble carboxylic acids in crude oil. *Energy & Fuels, 24*(5), 2974-2979. doi: 10.1021/ef901527h

[158] Fathi, S. J., Austad, T., and Strand, S. (2011). Effect of water-extractable carboxylic acids in crude oil on wettability in carbonates. *Energy & fuels, 25*(6), 2587-2592. doi: 10.1021/ef200302d

[159] Awolayo, A., Sarma, H., and Nghiem, L. (2018). Thermodynamic Modeling of Brine Dilution-Dependent Recovery in Carbonate Rocks with Different Mineralogical Content. *Energy & Fuels, 32*(9), 8921–8943. doi: 10.1021/acs.energyfuels.8b01080

[160] Mazzullo, S. J., Chilingarian, G. V., and Bissell, H. J. (1992). Carbonate rock classifications. *Developments in petroleum science, 30*, 59-108. doi: 10.1016/s0376-7361(09)70125-6

[161] Megawati, M., Hiorth, A., and Madland, M. V. (2013). The impact of surface charge on the mechanical behavior of high-porosity chalk. *Rock mechanics and rock engineering, 46*(5), 1073-1090. doi: 10.1007/s00603-012-0317-z

[162] Korsnes, R. I., Madland, M. V., Austad, T., Haver, S., and Røsland, G. (2008). The effects of temperature on the water weakening of chalk by seawater. *Journal of Petroleum Science and Engineering, 60*(3-4), 183-193. doi: 10.1016/j.petrol.2007.06.001

[163] Korsnes, R. I., Strand, S., Hoff, Ø., Pedersen, T., Madland, M. V., and Austad, T. (2006). *Does the chemical interaction between seawater and chalk affect the mechanical properties of chalk.* In Proceedings of the International Symposium of the International Society for Rock Mechanics, Liège, Belgium, 9-12 May.

[164] Awolayo, A. N., Sarma, H. K., and AlSumaiti, A. M. (2014). *An Experimental Study of Smart Waterflooding on Fractured Carbonate Reservoirs.* In Proceedings of the ASME 2014 33rd International Conference on Ocean, Offshore and Arctic Engineering, San Francisco, USA, 8 - 12 June.

[165] Pierre, A., Lamarche, J. M., Mercier, R., Foissy, A., and Persello, J. (1990). Calcium as potential determining ion in aqueous calcite suspensions. *Journal of Dispersion Science and Technology, 11*(6), 611-635. doi: 10.1080/01932699008943286

[166] Strand, S., Standnes, D. C., and Austad, T. (2003). Spontaneous imbibition of aqueous surfactant solutions into neutral to oil-wet carbonate cores: Effects of brine salinity and composition. *Energy & fuels, 17*(5), 1133-1144. doi: 10.1021/ef030051s

[167] Fathi, S. J., Austad, T., and Strand, S. (2011). Water-based enhanced oil recovery (EOR) by "smart water": Optimal ionic composition for EOR in carbonates. *Energy & fuels, 25*(11), 5173-5179. doi: 10.1021/ef201019k

[168] Kasha, A., Al-Hashim, H., Abdallah, W., Taherian, R., and Sauerer, B. (2015). Effect of Ca^{2+}, Mg^{2+} and SO_4^{2-} ions on the zeta potential of calcite and dolomite particles aged with stearic acid. *Colloids and Surfaces A: Physicochemical and Engineering Aspects, 482*, 290-299. doi: 10.1016/j.colsurfa.2015.05.043

[169] Ravari, R. R., Strand, S., and Austad, T. (2010). *Care must be taken to use outcrop limestone cores to mimic reservoir core material in SCAL linked to wettability alteration.* In Proceedings of the 11th Intenational Symposium on Reservoir Wettability, Calgary, Canada, 7 - 9 September.

[170] Al Mahrouqi, D., Vinogradov, J., and Jackson, M. D. (2016). Zeta potential of artificial and natural calcite in aqueous solution. *Advances in Colloid and Interface Science, 240*, 60-76. doi: 10.1016/j.cis.2016.12.006

[171] Vdović, N., and Bišćan, J. (1998). Electrokinetics of natural and synthetic calcite suspensions. *Colloids and Surfaces A: Physicochemical and Engineering Aspects, 137*(1-3), 7-14. doi: 10.1016/s0927-7757(97)00179-9

[172] Karimi, M., Al-Maamari, R. S., Ayatollahi, S., and Mehranbod, N. (2015). Mechanistic study of wettability alteration of oil-wet calcite: The effect of magnesium ions in the presence and absence of cationic surfactant. *Colloids and Surfaces A: Physicochemical and Engineering Aspects, 482*, 403-415. doi: 10.1016/j.colsurfa.2015.07.001

[173] Buckley, J. S., and Liu, Y. (1998). Some mechanisms of crude oil/brine/solid interactions. *Journal of Petroleum Science and Engineering, 20*(3), 155-160. doi: 10.1016/s0920-4105(98)00015-1

[174] Rao, D. N. (1999). Wettability Effects in Thermal Recovery Operations. *SPE Reservoir Eval. Eng., 2*(05), 420-430. doi: 10.2118/57897-PA

[175] Heidari, M. A., Habibi, A., Ayatollahi, S., Masihi, M., and Ashoorian, S. (2014). *Effect of time and temperature on crude oil aging to do a right surfactant flooding with a new approach.* In Proceedings of the Offshore Technology Conference-Asia, Kuala Lumpur, Malaysia, 25-28 March.

[176] Mahani, H., Menezes, R., Berg, S., Fadili, A., Nasralla, R., Voskov, D., and Joekar-Niasar, V. (2017). Insights into the impact of temperature on the wettability alteration by low salinity in carbonate rocks. *Energy & Fuels, 31*(8), 7839-7853. doi: 10.1021/acs.energyfuels.7b00776

[177] Webb, K., Black, C., and Tjetland, G. (2005). *A laboratory study investigating methods for improving oil recovery in carbonates.* In Proceedings of the International Petroleum Technology Conference, Doha, Qatar, 21-23 November.

[178] Alshakhs, M. J., and Kovscek, A. R. (2016). Understanding the role of brine ionic composition on oil recovery by assessment of wettability from colloidal forces. *Advances in colloid and interface science, 233*, 126-138. doi: 10.1016/j.cis.2015.08.004

[179] Nyström, R., Lindén, M., and Rosenholm, J. B. (2001). The Influence of Na^{+}, Ca^{2+}, Ba^{2+}, and La^{3+} on the ζ-Potential and the Yield Stress of Calcite Dispersions. *Journal of colloid and interface science, 242*(1), 259-263. doi: 10.1006/jcis.2001.7766

[180] Thomas, L. K., Dixon, T. N., Evans, C. E., and Vienot, M. E. (1987). Ekofisk waterflood pilot. *Journal of petroleum technology, 39*(02), 221-232. doi: 10.2118/13120-pa

[181] Hermansen, H., Landa, G. H., Sylte, J. E., and Thomas, L. K. (2000). Experiences after 10 years of waterflooding the Ekofisk Field, Norway. *Journal of Petroleum Science and Engineering, 26*(1-4), 11-18. doi: 10.1016/s0920-4105(00)00016-4

[182] Barkved, O., Heavey, P., Kjelstadli, R., Kleppan, T., and Kristiansen, T. G. (2003). *Valhall field-still on plateau after 20 years of production.* In Proceedings of the Offshore Europe, Aberdeen, United Kingdom, 2-5 September.

[183] Griffin, T. A., Best, K. D., Thingvoll, T. T., Stockden, I. L., and Tjetland, G. (2007). *Monitoring Waterflood Performance in a Depleted Fractured Chalk Reservoir.* In Proceedings of the Offshore Europe.

[184] Tjetland, G., Kristiansen, T. G., and Buer, K. (2007). *Reservoir management aspects of early waterflood response after 25 years of depletion in the Valhall field.* In Proceedings of the International Petroleum Technology Conference, Dubai, U.A.E., 4-6 December.

[185] Webb, K. J., Black, C. J. J., and Al-Ajeel, H. (2004). *Low Salinity Oil Recovery-Log-Inject-Log.* In Proceedings of the SPE/DOE Symposium on Improved Oil Recovery, Tulsa, Oklahoma, USA, 17-21 April.

[186] Seccombe, J. C., Lager, A., Webb, K. J., Jerauld, G., and Fueg, E. (2008). *Improving wateflood recovery: LoSal^{TM} EOR field evaluation.* In Proceedings of the SPE Symposium on Improved Oil Recovery, Tulsa, Oklahoma, USA, 20-23 April.

[187] Vledder, P., Gonzalez, I., Carrera Fonseca, J., Wells, T., and Ligthelm, D. (2010). *Low Salinity Water Flooding: Proof Of Wettability Alteration On A Field Wide Scale.* In Proceedings of the SPE Improved Oil Recovery Symposium, Tulsa, Oklahoma, USA, 24-28 April.

[188] Al-Qattan, A., Sanaseeri, A., Al-Saleh, Z., Singh, B. B., Al-Kaaoud, H., Delshad, M., Hernandez, R., Winoto, W., Badham, S., Bouma, C., *et al.* (2018). *Low Salinity Waterflood and Low Salinity Polymer Injection in the Wara Reservoir of the Greater Burgan Field.* In Proceedings of the SPE EOR Conference at Oil and Gas West Asia, Muscat, Oman, 26-28 March.

[189] Callegaro, C., Bartosek, M., Nobili, M., Masserano, F., Pollero, M., Baz, D. M. M., and Kortam, M. M. (2015). *Design and Implementation of Low Salinity Waterflood in a North African Brown Field.* In Proceedings of the Abu Dhabi International Petroleum Exhibition and Conference, Abu Dhabi, UAE, 2015/11/9/.

[190] Akhmetgareev, V., and Khisamov, R. (2015). *40 Years of Low-Salinity Waterflooding in Pervomaiskoye Field, Russia: Incremental Oil.* In Proceedings of the SPE European Formation Damage Conference and Exhibition, Budapest, Hungary, 3-5 June.

[191] Agbalaka, C. C., Dandekar, A. Y., Patil, S. L., Khataniar, S., and Hemsath, J. R. (2009). Coreflooding studies to evaluate the impact of salinity and wettability on oil recovery efficiency. *Transport in Porous Media, 76*(1), 77-94. doi: 10.1007/s11242-008-9235-7

[192] Karoussi, O., and Hamouda, A. A. (2007). Imbibition of sulfate and magnesium ions into carbonate rocks at elevated temperatures and their influence on wettability alteration and oil recovery. *Energy & fuels, 21*(4), 2138-2146. doi: 10.1021/ef0605246

[193] Austad, T., Strand, S., and Puntervold, T. (2009). *Is wettability alteration of carbonates by seawater caused by rock dissolution.* In Proceedings of the International Symposium of the Society of Core Analysts, Noordwijk, The Netherlands, 27-30 September, 2009.

[194] Den Ouden, L., Nasralla, R., Guo, H., Bruining, H., and van Kruijsdijk, C. (2015). *Calcite dissolution behaviour during low salinity water flooding in carbonate rock.* In Proceedings

of the IOR 2015-18th European Symposium on Improved Oil Recovery, Dresden, Germany, 14 April.

[195] Nasralla, R. A., Snippe, J. R., and Farajzadeh, R. (2015). *Coupled Geochemical-Reservoir Model to Understand the Interaction Between Low Salinity Brines and Carbonate Rock.* In Proceedings of the SPE Asia Pacific Enhanced Oil Recovery Conference, Kuala Lumpur, Malaysia, 11–13 August.

[196] Chandrasekhar, S., Sharma, H., and Mohanty, K. K. (2016). *Wettability Alteration with Brine Composition in High Temperature Carbonate Rocks.* In Proceedings of the SPE Annual Technical Conference and Exhibition, Dubai, UAE, 26-28 September

[197] Takamura, K., and Chow, R. S. (1985). The electric properties of the bitumen/water interface Part II. Application of the ionizable surface-group model. *Colloids and surfaces, 15*, 35-48. doi: 10.1016/0166-6622(85)80157-8

[198] Brady, P. V., and Thyne, G. (2016). Functional wettability in carbonate reservoirs. *Energy & Fuels, 30*(11), 9217-9225. doi: 10.1021/acs.energyfuels.6b01895

[199] Goldberg, S., and Forster, H. S. (1991). Boron sorption on calcareous soils and reference calcites. *Soil Science, 152*(4), 304-310. doi: 10.1097/00010694-199110000-00009

[200] Sø, H. U., Postma, D., Jakobsen, R., and Larsen, F. (2011). Sorption of phosphate onto calcite; results from batch experiments and surface complexation modeling. *Geochimica et Cosmochimica Acta, 75*(10), 2911-2923. doi: 10.1016/j.gca.2011.02.031

[201] Lemon, P., Zeinijahromi, A., Bedrikovetsky, P., and Shahin, I. (2011). Effects of injected-water salinity on waterflood sweep efficiency through induced fines migration. *Journal of Canadian Petroleum Technology, 50*(9/10), 82-94. doi: 10.2118/140141-pa

[202] Zeinijahromi, A., Ahmetgareev, V., Badalyan, A., Khisamov, R., and Bedrikovetsky, P. (2015). Case study of low salinity water injection in Zichebashskoe field. *Journal of Petroleum Science Research*. doi: 10.12783/jpsr.2015.0401.03

[203] Zeinijahromi, A., Ahmetgareev, V., and Bedrikovetsky, P. (2015). *Case Study of 25 Years of Low Salinity Water Injection.* In Proceedings of the SPE/IATMI Asia Pacific Oil & Gas Conference and Exhibition, Nusa Dua, Bali, Indonesia, 2015/10/20/.

[204] Rahbar, M., Ayatollahi, S., and Ghatee, M. H. (2010). *The Roles of Nano-Scale Intermolecular Forces on the Film Stability during Wettability Alteration Process of the Oil Reservoir Rocks.* In Proceedings of the Trinidad and Tobago Energy Resources Conference, Port of Spain, Trinidad, 2010/1/1/.

[205] Xie, Q., Saeedi, A., Pooryousefy, E., and Liu, Y. (2016). Extended DLVO-based estimates of surface force in low salinity water flooding. *Journal of Molecular Liquids, 221*, 658-665. doi: 10.1016/j.molliq.2016.06.004

[206] Brady, P. V., Morrow, N. R., Fogden, A., Deniz, V., and Loahardjo, N. (2015). Electrostatics and the low salinity effect in sandstone reservoirs. *Energy & Fuels, 29*(2), 666-677. doi: 10.1021/ef502474a

[207] Awolayo, A., Sarma, H., Nghiem, L., and Emre, G. (2017). *A Geochemical Model for Investigation of Wettability Alteration during Brine-Dependent Flooding in Carbonate Reservoirs.* In Proceedings of the SPE Abu Dhabi International Petroleum Exhibition & Conference Abu Dhabi, UAE, 13-16 November.

[208] Tripathi, I., and Mohanty, K. K. (2008). Instability due to wettability alteration in displacements through porous media. *Chemical Engineering Science, 63*(21), 5366-5374. doi: 10.1016/j.ces.2008.07.022

[209] Fjelde, I., Asen, S. M., and Omekeh, A. V. (2012). *Low salinity water flooding experiments and interpretation by simulations.* In Proceedings of the SPE Improved Oil Recovery Symposium, Tulsa, Oklahoma, USA, 14-18 April.

[210] Brady, P. V., and Krumhansl, J. L. (2012). A surface complexation model of oil–brine–sandstone interfaces at 100 °C: Low salinity waterflooding. *Journal of Petroleum Science and Engineering, 81*, 171-176. doi: 10.1016/j.petrol.2011.12.020

[211] Brady, P. V., Krumhansl, J. L., and Mariner, P. E. (2012). *Surface Complexation Modeling for Improved Oil Recovery.* In Proceedings of the SPE Improved Oil Recovery Symposium, Tulsa, Oklahoma, USA, 14-18 April.

[212] Elakneswaran, Y., Shimokawara, M., Nawa, T., and Takahashi, S. (2017). *Surface Complexation and Equilibrium Modelling for Low Salinity Waterflooding in Sandstone Reservoirs.* In Proceedings of the Abu Dhabi International Petroleum Exhibition & Conference, Abu Dhabi, UAE, 2017/11/13/.

[213] Erzuah, S., Fjelde, I., and Omekeh, A. V. (2017). *Wettability Estimation by Surface Complexation Simulations.* In Proceedings of the SPE Europec featured at 79th EAGE Conference and Exhibition, Paris, France, 2017/6/12/.

[214] Lima, S. A., Murad, M. A., and Domingues, R. (2017). *A New Multiscale Computational Model for Low Salinity Alkaline Waterflooding in Clay-Bearing Sandstones.* In Proceedings of the SPE Reservoir Simulation Conference, Montgomery, Texas, USA, 20–22 February.

[215] Korrani, A. K. N., and Jerauld, G. R. (2018). *Modeling Wettability Change in Sandstones and Carbonates Using a Surface-Complexation-Based Method.* In Proceedings of the SPE Improved Oil Recovery Conference, Tulsa, Oklahoma, USA, 2018/4/14/.

[216] Evje, S., Hiorth, A., Madland, M. V., and Korsnes, R. I. (2009). A mathematical model relevant for weakening of chalk reservoirs due to chemical reactions. *Networks and Heterogenous Media, 4*(4), 755-788. doi: 10.3934/nhm.2009.4.755

[217] Al-Shalabi, E. W., Delshad, M., and Sepehrnoori, K. (2013). *Does the Double Layer Expansion Mechanism Contribute to the LSWI Effect on Hydrocarbon Recovery from Carbonate Rocks?* In Proceedings of the SPE Reservoir Characterization and Simulation Conference and Exhibition, Abu Dhabi, UAE, 16–18 September.

[218] Al-Shalabi, E. W., Sepehrnoori, K., and Pope, G. (2015). Geochemical Interpretation of Low-Salinity-Water Injection in Carbonate Oil Reservoirs. *SPE Journal, 20*(06), 1,212 - 211,226. doi: 10.2118/169101-PA

[219] Korrani, A. K. N., Fu, W., Sanaei, A., and Sepehrnoori, K. (2015). *Mechanistic Modeling of Modified Salinity Waterflooding in Carbonate Reservoirs.* In Proceedings of the SPE Annual Technical Conference and Exhibition, Houston, Texas, USA, 28–30 September.

[220] Eftekhari, A. A., Thomsen, K., Stenby, E. H., and Nick, H. M. (2017). Thermodynamic Analysis of Chalk–Brine–Oil Interactions. *Energy & Fuels, 31*(11), 11773-11782. doi: 10.1021/acs.energyfuels.7b02019

[221] Abdou, M., Carnegie, A., Mathews, S. G., McCarthy, K., O'Keefe, M., Raghuraman, B., Wei, W., and Xian, C. (2011). Finding value in formation water. *Oilfield Review, 23*(1), 24-35.

[222] Crabtree, M., Eslinger, D., Fletcher, P., Miller, M., Johnson, A., and King, G. (1999). Fighting scale—removal and prevention. *Oilfield review, 11*(3), 30-45.

[223] Vetter, O. J., Farone, W. A., Veith, E., and Lankford, S. (1987). *Calcium carbonate scale considerations: A practical approach.* In Proceedings of the SPE Production Technology Symposium, Lubbock, Texas, 16-17 November.

[224] Puntervold, T., Strand, S., and Austad, T. (2009). Coinjection of seawater and produced water to improve oil recovery from fractured North Sea chalk oil reservoirs. *Energy & Fuels, 23*(5), 2527-2536. doi: 10.1021/ef801023u

[225] Kajenthira, A., Siddiqi, A., and Anadon, L. D. (2012). A new case for promoting wastewater reuse in Saudi Arabia: Bringing energy into the water equation. *Journal of environmental management, 102,* 184-192. doi: 10.1016/j.jenvman.2011.09.023

[226] Burnett, D. (2005). Desalinating brine from oil and gas operations in Texas. *Southwest Hydrology,* 24-25.

[227] Burnett, D. B., and Siddiqui, M. (2006). Recovery of fresh water resources from desalination of brine produced during oil and gas production operations. College Station, TX, USA: Texas Engineering Experiment Station.

[228] Ayirala, S. C., Uehara-Nagamine, E., Matzakos, A. N., Chin, R. W., Doe, P. H., and van den Hoek, P. J. (2010). *A designer water process for offshore low salinity and polymer flooding applications.* In Proceedings of the SPE Improved Oil Recovery Symposium, Tulsa, Oklahoma, USA, 24-28 April.

[229] Collins, I. R. (2008). United States Patent No. US7455109B2. U.S. Patent and Trademark Office.

[230] Henthorne, L., and Movahed, B. (2013). United States Patent No. US 20130213892A1 U. S Patent.

[231] Curole, M. A., and Greene, E. B. (2014). United States Patent No. US008 789594B2 U.S. Patent and Trademark Office.

[232] Ligthelm, D. J., Romanuka, J., and Suijkerbuijk, B. M. J. M. (2012). United States Patent No. US 20120090833A1. U.S. Patent.

[233] Ayirala, S. C. B., Chin, R. W.-Y., Matzakos, A. N., and Uehara-Nagamine, E. (2016). United States Patent No. US9234413B2. U.S. Patent.

[234] Yousef, A. A., and Ayirala, S. C. (2014). *A novel water ionic composition optimization technology for SmartWater flooding application in carbonate reservoirs.* In Proceedings of the SPE Improved Oil Recovery Symposium, Tulsa, Oklahoma, USA, 12-16 April.

[235] Ayirala, S. C., and Yousef, A. A. (2016). A Critical Review of Alternative Desalination Technologies for Smart Waterflooding. *Oil and Gas Facilities*. doi: 10.2118/179564-PA

[236] Sohal, M. A., Thyne, G., and Søgaard, E. G. (2016). Review of recovery mechanisms of ionically modified waterflood in carbonate reservoirs. *Energy & Fuels, 30*(3), 1904-1914. doi: 10.1021/acs.energyfuels.5b02749

[237] Drummond, C., and Israelachvili, J. (2004). Fundamental studies of crude oil–surface water interactions and its relationship to reservoir wettability. *Journal of Petroleum Science and Engineering, 45*(1), 61-81.

[238] Stipp, S. L. S. (1999). Toward a conceptual model of the calcite surface: hydration, hydrolysis, and surface potential. *Geochimica et Cosmochimica Acta, 63*(19), 3121-3131. doi: 10.1016/S0016-7037(99)00239-2

[239] Wolthers, M., Charlet, L., and Van Cappellen, P. (2008). The surface chemistry of divalent metal carbonate minerals; a critical assessment of surface charge and potential data using the charge distribution multi-site ion complexation model. *American journal of science, 308*(8), 905-941. doi: 10.2475/08.2008.02

[240] Foxall, T., Peterson, G. C., Rendall, H. M., and Smith, A. L. (1979). Charge determination at calcium salt/aqueous solution interface. *Journal of the Chemical Society, Faraday Transactions 1: Physical Chemistry in Condensed Phases, 75*, 1034-1039. doi: 10.1039/F19797501034

[241] Smith, A. L. (1976). Electrokinetics of the oxide — solution interface. *Journal of Colloid and Interface Science, 55*(3), 525-530. doi: 10.1016/0021-9797(76)90062-X

[242] Revil, A., Pezard, P. A., and Glover, P. W. J. (1999). Streaming potential in porous media: 1. Theory of the zeta potential. *Journal of Geophysical Research: Solid Earth (1978–2012), 104*(B9), 20021-20031. doi: 10.1029/1999JB900089

[243] Hirasaki, G. J. (1991). Wettability: fundamentals and surface forces. *SPE Formation Evaluation, 6*(02), 217-226.

[244] Hirasaki, G., and Zhang, D. L. (2004). Surface chemistry of oil recovery from fractured, oil-wet, carbonate formations. *SPE Journal, 9*(02), 151-162. doi: 10.2118/88365-PA

[245] Geissbühler, P., Fenter, P., DiMasi, E., Srajer, G., Sorensen, L. B., and Sturchio, N. C. (2004). Three-dimensional structure of the calcite–water interface by surface X-ray scattering. *Surface Science, 573*(2), 191-203.

[246] Tansel, B. (2012). Significance of thermodynamic and physical characteristics on permeation of ions during membrane separation: Hydrated radius, hydration free energy and viscous effects. *Separation and purification technology, 86*, 119-126.

[247] Gregory, J. (1981). Approximate expressions for retarded van der waals interaction. *Journal of Colloid and Interface Science, 83*(1), 138-145. doi: 10.1016/0021-9797(81)90018-7

[248] Bergström, L. (1997). Hamaker constants of inorganic materials. *Advances in colloid and interface science, 70*, 125-169. doi: 10.1016/S0001-8686(97)00003-1

[249] Malmberg, C. G., and Maryott, A. A. (1956). Dielectric Constant of Water from 0 to 100 ^{o}C. *Journal of research of the National Bureau of Standards, 56*(1), 1-8.

[250] Gregory, J. (1975). Interaction of unequal double layers at constant charge. *Journal of Colloid and Interface Science, 51*(1), 44-51. doi: 10.1016/0021-9797(75)90081-8

[251] Buckley, J. S., Takamura, K., and Morrow, N. R. (1989). Influence of electrical surface charges on the wetting properties of crude oils. *SPE Reservoir Eval. Eng., 4*(03), 332-340. doi: 10.2118/16964-pa

[252] Nghiem, L., Sammon, P., Grabenstetter, J., and Ohkuma, H. (2004). *Modeling CO_2 storage in aquifers with a fully-coupled geochemical EOS compositional simulator.* In Proceedings of the SPE/DOE symposium on improved oil recovery, Tulsa, Oklahoma, 17-21 April.

[253] Nghiem, L. X., Shrivastava, V. K., and Kohse, B. F. (2011). *Modeling aqueous phase behavior and chemical reactions in compositional simulation.* In Proceedings of the SPE Reservoir Simulation Symposium, The Woodlands, Texas, USA, 21–23 February.

[254] Bethke, C. (1996). *Geochemical reaction modeling: Concepts and applications*. Oxford University Press Inc.: New York.

[255] Kharaka, Y. K., Gunter, W. D., Aggarwal, P. K., Perkins, E. H., and DeBraal, J. D. (1988). SOLMINEQ. 88: A computer program for geochemical modeling of water-rock interactions *US Geological Survey Water-Resources Investigations Report* (Vol. 88-4227, pp. 420). Menlo Park, California.

[256] Delany, J. M., and Lundeen, S. R. (1990). The LLNL thermochemical database. *Lawrence Livermore National Laboratory Report UCRL-21658. Lawrence Livermore National Laboratory*.

[257] Helgeson, H. C., Brown, T. H., and Leeper, R. H. (1969). *Handbook of theoretical activity diagrams depicting chemical equilibria in geologic systems involving an aqueous phase at one Atm and 0°to 300°C*. Freeman Cooper & Co.

[258] Takamura, K., and Chow, R. S. (1983). A mechanism for initiation of bitumen displacement from oil sand. *Journal of Canadian Petroleum Technology, 22*(06).

[259] Stipp, S. L., and Hochella, M. F. (1991). Structure and bonding environments at the calcite surface as observed with X-ray photoelectron spectroscopy (XPS) and low energy electron diffraction (LEED). *Geochimica et Cosmochimica Acta, 55*(6), 1723-1736.

[260] Pokrovsky, O. S., Mielczarski, J. A., Barres, O., and Schott, J. (2000). Surface speciation models of calcite and dolomite/aqueous solution interfaces and their spectroscopic evaluation. *Langmuir, 16*(6), 2677-2688.

[261] Pokrovsky, O. S., and Schott, J. (2002). Surface chemistry and dissolution kinetics of divalent metal carbonates. *Environmental science & technology, 36*(3), 426-432.

[262] Van Cappellen, P., Charlet, L., Stumm, W., and Wersin, P. (1993). A surface complexation model of the carbonate mineral-aqueous solution interface. *Geochimica et Cosmochimica Acta, 57*(15), 3505-3518. doi: 10.1016/0016-7037(93)90135-j

[263] Pokrovsky, O. S., Schott, J., and Thomas, F. (1999). Dolomite surface speciation and reactivity in aquatic systems. *Geochimica et Cosmochimica Acta, 63*(19), 3133-3143. doi: 10.1016/s0016-7037(99)00240-9

[264] Appelo, C. A. J., and Postma, D. (2005). *Geochemistry, groundwater and pollution* (Second ed.). CRC press: Boca Raton, FL, USA.pp. 668.

[265] Hubbert, M. K. (1957). Darcy's law and the field equations of the flow of underground fluids. *Hydrological Sciences Journal, 2*(1), 23-59. doi: https://doi.org/10.1080/02626665709493062

[266] Behie, A., Collins, D., Forsyth Jr, P. A., and Sammon, P. H. (1985). Fully coupled multiblock wells in oil simulation. *SPE Journal, 25*(04), 535-542. doi: 10.2118/11877-PA

[267] Nghiem, L. X., and Rozon, B. J. (1989). *A Unified and Flexible Approach for Handling and Solving Large Systems of Equations in Reservoir Simulation.* In Proceedings of the First and Second International Forum on Reservoir Simulation, Alpbach, Austria, September 1988 and I989.

[268] Stumm, W., and Morgan, J. J. (2012). *Aquatic chemistry: chemical equilibria and rates in natural waters* (3rd edition ed. Vol. 126). John Wiley & Sons: New York,.Vol. 126.

[269] Brooks, R. H., and Corey, A. T. (1966). Properties of porous media affecting fluid flow. *Journal of the Irrigation and Drainage Division, 92*(2), 61-90.

[270] Skjaeveland, S. M., Siqveland, L. M., Kjosavik, A., Hammervold, W. L., and Virnovsky, G. A. (2000). Capillary pressure correlation for mixed-wet reservoirs. *SPE Reservoir Eval. & Eng, 3*(1), 60-67.

[271] Webb, K., Black, C., and Edmonds, I. (2005). *Low salinity oil recovery-The role of reservoir condition corefloods.* In Proceedings of the 13th EAGE Symposium on Improved Oil Recovery, Budapest, Hungary.

[272] Akbar, M., Vissapragada, B., Alghamdi, A. H., Allen, D., Herron, M., Carnegie, A., Dutta, D., Olesen, J.-R., Chourasiya, R., and Logan, D. (2000). A snapshot of carbonate reservoir evaluation. *Oilfield Review, 12*(4), 20-41.

[273] Anderson, W. (1987). Wettability literature survey part 5: The effects of wettability on relative permeability. *Journal of Petroleum Technology, 39*(11), 1453-1468. doi: 10.2118/16323-PA

[274] Awolayo, A. N., Sarma, H. K., and Nghiem, L. X. (2017). *A Comprehensive Geochemical-Based Approach at Modeling and Interpreting Brine Dilution in Carbonate Reservoirs.* In Proceedings of the SPE Reservoir Simulation Conference, Montgomery, Texas, USA, 20-22 February.

[275] Chandrasekhar, S. (2013). *Wettability alteration with brine composition in high temperature carbonate reservoirs.* (Masters), The University of Texas at Austin, Austin. Retrieved from http://hdl.handle.net/2152/22657

[276] Awolayo, A. N., Sarma, H., and Nghiem, L. (2017). *A Comprehensive Geochemical-based Approach at Modeling and Interpreting Brine Dilution in Carbonate Reservoirs.* In Proceedings of the SPE Reservoir Simulation Conference, Montgomery, TX, USA, 20-22 February.

[277] Awolayo, A., Ashqar, A., Uchida, M., Salahuddin, A. A., and Olayiwola, S. O. (2017). A cohesive approach at estimating water saturation in a low-resistivity pay carbonate reservoir and its validation. *Journal of Petroleum Exploration and Production Technology, 7*(3), 637-657. doi: 10.1007/s13202-017-0318-2

[278] Salahuddin, A. A., Al-Seiari, J. M., and Al-Hammadi, K. E. (2016). *Hybrid Stochastic Algorithms: A Novel Application in Modeling Facies Cycles and Properties of Carbonate Platform, Onshore Abu Dhabi.* In Proceedings of the Abu Dhabi International Petroleum Exhibition & Conference, Abu Dhabi.

[279] Lee, J. H., Jeong, M. S., and Lee, K. S. (2017). *Geochemical Modelling of Carbonated Low Salinity Water Injection CLSWI to Improve Wettability Modification and Oil Swelling in Carbonate Reservoir*. Paper Volume presented at the SPE Latin America and Caribbean Mature Fields Symposium, Salvador, Bahia, Brazil, 15-16 March. https://doi.org/10.2118/184915-MS

[280] Sheng, J. J. (2013). Review of Surfactant Enhanced Oil Recovery in Carbonate Reservoirs. *Advances in Petroleum Exploration and Development, 6*(1), 1-10.

[281] Skauge, A., and Sorbie, K. (2014). *Status of Fluid Flow Mechanisms for Miscible and Immiscible WAG.* In Proceedings of the SPE EOR Conference at Oil and Gas West Asia, Muscat, Oman.

[282] Christensen, J. R., Stenby, E. H., and Skauge, A. (2001). Review of WAG Field Experience. *SPE Reservoir Evaluation & Engineering, 4*(02), 97 - 106. doi: 10.2118/71203-PA

[283] Verma, M. K. (2015). *Fundamentals of Carbon Dioxide-enhanced Oil Recovery (CO_2-EOR): A Supporting Document of the Assessment Methodology for Hydrocarbon Recovery Using CO_2-EOR Associated with Carbon Sequestration*. US Department of the Interior, US Geological Survey.

[284] Stalkup, F. I. (1983). Status of miscible displacement. *Journal of Petroleum Technology, 35*(04), 815-826.

[285] Christensen, J. R., Stenby, E. H., and Skauge, A. (1998). *Review of WAG field experience*. In Proceedings of the International Petroleum Conference and Exhibition of Mexico, Villahermosa, Mexico, 3-5 March.

[286] Stalkup, F. I. (1987). *Displacement behavior of the condensing/vaporizing gas drive process.* In Proceedings of the SPE Annual Technical Conference and Exhibition, Dallas, Texas, 27-30 September.

[287] Li, Y. K., and Nghiem, L. X. (1986). Phase equilibria of oil, gas and water/brine mixtures from a cubic equation of state and Henry's law. *The Canadian Journal of Chemical Engineering*, *64*(3), 486-496.

[288] Zhang, Y., and Sarma, H. K. (2013). *Modelling of Possible Impact of Reservoir Brine Salinity During CO_2 Injection.* In Proceedings of the SPE Enhanced Oil Recovery Conference, Kuala Lumpur, Malaysia.

[289] Qiao, C., Li, L., Johns, R. T., and Xu, J. (2016). Compositional modeling of dissolution-induced injectivity alteration during CO_2 flooding in carbonate reservoirs. *SPE journal*, *21*(03), 809-826. doi: https://doi.org/10.2118/170930-PA

Curriculum Vitae

Awolayo, Adedapo Noah

Dapo is a versatile and results-driven engineer/scientist with years of experience in oil and gas industry and research. He has continued to demonstrate success in using applied research and analytical skills to provide solutions to complex engineering problems as shown through independent innovation and multidisciplinary collaborations. He possesses excellent communication skills with proven ability to succinctly articulate technical issues and recommendations to relevant disciplines, through presentations, technical reports and published articles in recognized journals.

EDUCATION

Doctor of Philosophy (Ph.D.) Candidate in Petroleum Engineering — Sept. 2015 – Dec. 2018
University of Calgary, Calgary, Canada

Master of Science (M.Sc.) in Petroleum Engineering — Sept. 2012 – May 2014
Petroleum Institute, Abu Dhabi, U.A.E.

Bachelor of Technology (B.Tech.) in Chemical Engineering — Sept. 2005 – Dec. 2010
Ladoke Akintola University of Technology (LAUTECH), Nigeria

INDUSTRIAL & RESEARCH EXPERIENCE

Doctoral Research Scientist (Subsurface Tools Development) — Sept. 2015 – Dec. 2018
University of Calgary with Computer Modelling Group Ltd. (CMG), Calgary, Canada

Reservoir Engineer (Reservoir Strategy and Onshore Operations Team) — July 2014 – Sept. 2015
Abu Dhabi Company for Onshore Operations Petroleum Ltd. (ADCO), *Abu Dhabi, U.A.E.*

Research Assistant (Subsurface Tools Development) — Aug. 2012 – July 2014
Petroleum Institute, Abu Dhabi, U.A.E.

Facility Quality Control Chemist (Internship) — Apr. 2009 – Sep. 2009
Total Nigeria Plc. Lagos, Nigeria

TEACHING EXPERIENCE

Laboratory Instructor & Teaching Assistant — Jan. 2016 – Dec. 2017
University of Calgary, Calgary, Canada

Teaching Assistant — Aug. 2013 – May 2014
Petroleum Institute, Abu Dhabi, U.A.E.

HONORS AND AWARDS

Vanier Canada Graduate Scholarship - Most prestigious national Ph.D. scholarship in Canada — May 2017, 2018
Killam Doctoral Memorial Scholarship, Killam Trusts through University of Calgary — May 2017, 2018
1st Place Winner, SPE Canada Regional Student's Paper Contest (Ph.D. division) — Mar. 2017
Graduate Excellence Award, Chem. and Pet. Engineering Department, University of Calgary — Mar. 2016

Dean's Entrance Scholarship, Faculty of Graduate Studies, University of Calgary Jan. 2016
Eyes High International Recruitment Scholarship, Faculty of Graduate Studies, University of Calgary Sept. 2015

SELECTED PUBLICATION

Awolayo, A.N., Sarma, H.K., and Nghiem L.X. Modeling the Characteristic Interplay between Potential Determining Ions during Brine-Dependent Recovery Process in Carbonate Rocks. Fuel, 224: 701 - 717, (2018). DOI:10.1016/j.fuel.2018.03.070

Awolayo, A.N., Sarma, H.K., and Nghiem L.X. Thermodynamic Modeling of Brine Dilution-Dependent Recovery in Carbonate Rocks with Different Mineralogical Content. Energy & Fuels Journal, 32(9): 8921 – 8943, (2018). DOI:10.1021/acs.energyfuels.8b01080.

Awolayo, A.N., Sarma, H.K., and Nghiem L.X. "Brine-Dependent Recovery Processes in Carbonate and Sandstone Petroleum Reservoirs: Review of Laboratory-Field Studies, Interfacial Mechanisms and Modeling Attempts." Energies Journal, 11(11): 3020, (2018). DOI:10.3390/en11113020

Awolayo, A.N., Sarma, H.K. and Nghiem L.X. Numerical Modeling of Fluid-Rock Interactions during Low-salinity-brine-CO2 Flooding in Carbonate Reservoirs. In: Proceedings of the 2019 SPE Reservoir Simulation Conference, April 10 - 11, 2019. SPE Paper #193815

Awolayo, A.N., Sarma, H.K., Nghiem L.X. and Emre, G.A. Geochemical Model for Investigation of Wettability Alteration during Brine-Dependent Flooding in Carbonate Reservoirs. In: Proceedings of the 2017 Abu Dhabi International Petroleum Exhibition & Conference (ADIPEC 2017), November 13 - 16, 2017. DOI: 10.2118/188219-MS

Awolayo, A.N. Geochemical Modeling of the Interplay between Potential Determining Ions during Brine-Dependent Recovery in Carbonate Rocks. In: Proceedings of the 2017 SPE Annual Technical Conference and Exhibition (SPE ATCE 2017), October 9 - 11, 2017. DOI: 10.2118/189280-STU

Awolayo, A.N., Sarma, H.K. and Nghiem L.X. A Comprehensive Geochemical-based Approach at Modeling and Interpreting Brine Dilution in Carbonate Reservoirs. In: Proceedings of the 2017 SPE Reservoir Simulation Conference, February 20 - 22, 2017. DOI: 10.2118/182626-MS

Awolayo, A.N., Sarma, H.K., and Nghiem L.X. Mechanistic Modeling of Hybrid Low-Salinity-Brine-CO2 Injection in Carbonate Reservoirs. In: Global Petroleum Show - North America's Leading Exhibition & Conference, Calgary, Canada, June 12 - 14, 2018.

Awolayo, A.N. Geochemical modeling of brine dilution-dependent recovery in Carbonate Reservoirs. In: SPE Canada 2017 Regional Student Paper Contest, Vancouver, Canada, Feb. 25, 2017. **First Place for Best Paper at PhD Category**

*Awolayo, A.N***.** and Sarma, H.K. An Analytical Solution to Interpret Active Ion Transport during Chemically-Tuned Waterflooding Process in High-Temperature Carbonate Rocks. The Canadian Journal of Chemical Engineering, (2018). DOI:10.1002/cjce.23183

Awolayo, A.N., Sarma, H.K., and AlSumaiti, A.M. An Experimental Investigation into the Impact of Sulfate ion in Smart Water to Improve Oil Recovery in Carbonate Reservoirs. Transport in Porous Media, 111(3) : 649 - 668, (2015). DOI:10.1007/s11242-015-0616-4